THÈSE de DOCTORAT de l'UNIVERSITÉ PARIS 11

Spécialité :
Physique Quantique

présentée par

Thorsten SCHUMM

pour obtenir le grade de DOCTEUR de l'UNIVERSITÉ PARIS 11

Sujet de la thèse :

Bose-Einstein condensates in magnetic double well potentials

Soutenue le 20 Février 2005
devant le jury composé de :

M.	**F. Bretenaker**	Président du jury
M.	**M. Brune**	Rapporteur
M.	**M. Oberthaler**	Rapporteur
M.	**P. Schmelcher**	Examinateur
M.	**C. Westbrook**	Directeur de thèse
M.	**J. Schmiedmayer**	Directeur de thèse

Contents

III A double well realized by adiabatic dressed potentials

Annex: publications

References

Introduction

This year, the world's scientific community is celebrating the "Year of Albert Einstein", referring to the centennial of three of his most famous publications in 1905; his work on special relativity [1], about the Brownian motion [2] and on quantum theory [3]. Since then, quantum phenomena have become experimentally accessible in almost any physical system. Fundamental questions like the interpretation problem [4], the question of decoherence and the measurement process can now be addressed experimentally and are still the driving force behind research carried out today. Furthermore, quantum effects have become the building blocks for applied sciences and technology, most prominent examples being the laser as a coherent photon source, along with many many effect in solid state systems, which build the basis for our microelectronics. The enormous success of the laser and coherent optics in general has stimulated research towards similar applications in other well controlled quantum systems. In close "Anlehnung" to coherent optics with photons, the field of atom optics has developed. At its heart, based on Einsteins work of 1924/25 [5, 6, 7], the Bose-Einstein condensate (BEC) as coherent matter wave source .

The specific properties of neutral atoms make them a promising candidate for manipulation on the quantum level. Their weak coupling to the (uncontrolled) environment on the one hand allows for long lifetimes of the quantum state and therefore the storage and manipulation of information in external or internal atomic states. On the other hand, a rich toolbox for atom manipulation has been developed, ranging from laser cooling, over various sorts of conservative atom traps to evaporative cooling. The combination of these methods has enabled Bose-Einstein condensation in 1995. Different to photons, the inter atomic interaction plays an important role in the properties of the quantum state and can be manipulated at will by the use of Feshbach resonances. This high degree of control has enabled the use of atoms as a test scenario for other quantum systems, such as solid states or quantum liquids. The still growing field of cold atom research addresses ...QIPC und IFM.

In contrast to photons, atoms do carry significant mass, making the quantum system extremely sensitive to gravity, accelerations and rotations. Interferometers based external (motional) atomic states therefore....

Controlling external atomic quantum states and transporting atomic wave packets presents a major scientific challenge, as the system has to be manipulated on its intrinsic length scale, which is often below microns. Two approaches have demonstrated to provide sufficiently precise control on this level:

Optical potential based on the DC or AC Starck effect are able to create potential variations on the scale of their wavelength, either using focussed laser beams or optical interference patterns, making direct use of the coherent nature of the photon source. (geniale Experimente, schwer zu kontrollieren, adressability, die beiden, die schon geklappt haben.)

Magnetic micro potentials created by current carrying, microfabricated wires on atom chips allow for potential variations on the scale of their structure size. Sub-micron fabrication-... (Fussnote, das hier was neues kommt!)

This thesis was carried out as a joined project ("cotutelle de thèse") at the Institut d'Optique

in Orsay and the Physikalisches Institut in Heidelberg. Thanks to the direction of my two supervisors, C. Westbrook and J. Schmiedmayer, I had the opportunity to work on the two probably most promising approaches towards the experimental implementation of a quantum beam splitter on an atom chip.

When I started my thesis on October 2002, the first generation of chip experiments in Orsay was almost built up. From an existing surface magneto optical trap (MOT) a magnetic trap provided by a current carrying chip wire was loaded and Bose-Einstein condensation was achieved in May 2003. As almost any other group working with atom chips, we encountered the phenomenon of fragmentation; a cold atom cloud or BEC breaking up into lumps when brought close to the trapping structure. A careful study of the underlying magnetic trapping potential could explain this effect by current deviations in the chip wire due to fabrication defects. In order to create a stable magnetic double well to realize tunnelling and splitting of Bose condensates, the experimental setup was modified considerably in the beginning of 2004. The vacuum system was rebuild to fit into a multi layer magnetic field shielding. A new generation of atom chips was designed, employing a hybrid "sandwich" technology and including different methods of micro fabrication (optical lithographie followed by electroplating and direct electron beam lithographie followed by lift off). This chip carries large pattern submicron structures, involves patterned silicon etching, mechanical polishing and intra chip bonding. It's design, fabrication, loading with Bose condensed atoms and preliminary experiments constitute the main part of my thesis work in Orsay and will be described in the second part of this manuscript.

The experiments carried out in Heidelberg were performed with a conceptually similar setup, which was fully operational the time I joined the group. Only few electronic components had to be added and minor changes to the optical system were made to allow for imaging along the desired direction. Due to the simplicity of the beamsplitter concept used here, experimental results as coherent splitting of a BEC on an atom chip could be obtained in only 7 month time. Working out this concept, it's implementation and first experiments with split condensates constitute the main part of my thesis work in Heidelberg and will be described in the third part of this manuscript.

I. first list item Corresponding text.

II. Second list item Corresponding second text.

And a few nice words to close.

Part I

BEC, double wells and magnetic microtraps

Contents

Introduction

Introduction to first part.

Chapter 1

Bose-Einstein condensation

This chapter briefly reviews the theory of Bose-Einstein condensation in dilute gasses. Starting with the non-interacting Bose-gas, we describe the quantum phase transition and identify its critical temperature T_c in the hydrodynamic limit and in a realistic finite size system. Atom-atom interactions are taken into account by introducing a mean field approach, leading to the well known Gross-Pittaevskii equation. We apply the Thomas-Fermi approximation, which well describes the condensate wave function in an isotropic 3D system.

Magnetic micro traps formed on atom chips, as will be discussed in this manuscript, give rise to very elongated trapping geometries, where the Thomas-Fermi description fails in the transverse directions (Thomas-Fermi 1D regime). We describe the effect of trap anisotropy on the character of the BEC phase transition and the shape of the spatial wave function. Longitudinal phase fluctuations giving rise to a reduced coherence length, shorter than the condensate extension, are briefly resumed.

Considering two spatially separated Bose-Einstein condensates as sources of uniform phase, we describe interference phenomena that arise when the condensates are released from their traps and overlap. It is pointed out, that the observation of matter wave interference is not sufficient to unambiguously identify (phase) coherence between the sources, as even pure number states give rise to interference effects. We briefly resume the process of phase diffusion, which describes the loss of phase information in a coherent state due to number fluctuations, directly based on the uncertainty principle.

To demonstrate, that magnetic microchip traps are well suited to address fundamental topics discussed in this chapter, some points are illustrated with (preliminary) images of ongoing work, performed on the Orsay or the Heidelberg experiment, which will not be discussed in detail in this manuscript.

1.1 The non interacting Bose gas

We consider neutral atoms trapped in an external 3D harmonic potential:

$$V_{\text{trap}} = \frac{m}{2}\left(\omega_x^2 x^2 + \omega_y^2 y^2 + \omega_z^2 z^2\right) \tag{1.1}$$

where m is the atomic mass and ω_i the trap oscillation frequencies in the three spacial directions $i = \{x, y, z\}$. Assuming an ideal (non interacting) gas, the many-particle Hamiltonian can be written as the sum of single-particle Hamiltonians with the well known eigenenergies:

$$\epsilon_{n_x,n_y,n_z} = \sum_{i=x,y,z}\left(n_i + \frac{1}{2}\right)\hbar\omega_i, \tag{1.2}$$

with $\{n_x, n_y, n_z\}$ non negative integers. The N particle ground state of non interacting bosons in a harmonic potential is the product state $\phi_0(\mathbf{r}_1, ..., \mathbf{r}_N) = \Pi_i \phi_0(\mathbf{r}_i)$ of the single particle ground states

$$\phi_0(\mathbf{r}) = \left(\frac{m\omega_{\rm ho}}{\pi\hbar}\right)^{3/4} \exp\left(-\frac{m}{2\hbar}\left(\sum_{i=x,y,z} \omega_i i^2\right)\right), \tag{1.3}$$

where $\omega_{\rm ho} = (\omega_x\omega_y\omega_z)^{1/3}$ is the geometrical mean of the harmonic trap oscillation frequencies. The atomic density distribution is $n(\mathbf{r}) = N|\phi_0(\mathbf{r})|^2$, the spacial extension of the ground state wave function is independent of N and derives from the width of the gaussian distribution (1.3):

$$a_{ho} = \sqrt{\frac{\hbar}{m\omega_{\rm ho}}}. \tag{1.4}$$

The size of the ground state wave function $a_{\rm ho}$ fixes an important length scale of the system; it is usually of the order of $a_{\rm ho} \approx 0,1 - 1\,\mu m$. At finite temperature, only a certain fraction of the atoms populate the ground state, the others being thermally distributed among exited states. The size of the thermal cloud is usually much larger than $a_{\rm ho}$. Assuming a harmonic trapping potential like (1.1) and a classical Boltzmann distribution, we obtain a gaussian width of $R_{\rm therm} = a_{\rm ho}(k_BT/\hbar\omega_{\rm ho})^{1/2}$ for the thermal cloud, which largely exceeds the ground state size, as $k_BT \gg \hbar\omega_{\rm ho}$. Therefore the onset of Bose-Einstein condensation can be identified by a build up of a sharp peak in the central region of the density distribution [8, 9].

For strongly anisotropic (*e.g.* cigar shaped) traps, like wire traps, a description in cylindrical coordinates is convenient. We define an axial coordinate z and a radial coordinate $\rho = \sqrt{x^2 + y^2}$ with corresponding trap frequencies $\omega_\parallel = \omega_z$ and $\omega_\perp = \omega_x = \omega_y$. The ratio $\Re = \omega_\perp/\omega_\parallel$ describes the anisotropy of the trap. We can rewrite (1.3):

$$\phi_0(\mathbf{r}) = \frac{\Re^{1/4}}{\pi^{3/4}a_\perp^{3/2}} \exp\left(-\frac{1}{2a_\perp}(\rho^2 + \Re z^2)\right) \tag{1.5}$$

with $a_\perp = \sqrt{\hbar/(m\omega_\perp)}$. An anisotropic trap provides another characteristic signature of Bose-Einstein condensation based on the momentum distribution: The Fourier transform of wave function (1.5) gives $\tilde{\phi}_0(\mathbf{p}) \propto \exp[-a_\perp(p_\perp^2 + \Re^{-1}p_z^2)/2\hbar^2]$. From this one can calculate the average axial and radial width. Their ratio

$$\sqrt{\langle p_z^2\rangle/\langle p_\perp^2\rangle} = \sqrt{\Re} \tag{1.6}$$

is fixed by the asymmetry $\Re$ of the trap. Thus the shape of an expanding BEC reflects the trap anisotropy whereas a thermal component will expand isotropically [8, 10, 11]. For a quantitative analysis of the shape of an expanding condensate, the effect of interactions has to be taken into account [12, 13, 14].

1.1.1 Critical temperature and condensate fraction

In the grand-canonical ensemble, the total number of particles for a given temperature T is

$$N = \sum_{n_x,n_y,n_z} \frac{1}{e^{\beta(\epsilon_{n_x,n_y,n_z} - \mu)} - 1}, \tag{1.7}$$

where $\beta = 1/(k_BT)$, k_B being the Boltzmann constant and μ the chemical potential. The corresponding total energy is

$$E = \sum_{n_x,n_y,n_z} \frac{\epsilon_{n_x,n_y,n_z}}{e^{\beta(\epsilon_{n_x,n_y,n_z} - \mu)} - 1}. \tag{1.8}$$

Below a certain temperature T_c, the population of the lowest state becomes important, corresponding to the onset of Bose-Einstein condensation. In the following, we will therefore consider N_0, the number of atoms in the lowest energy Eigenstate ϵ_{000}. When the chemical potential approaches the ground state energy

$$\mu \to \mu_c = \frac{3}{2}\hbar\bar{\omega}, \tag{1.9}$$

with $\bar{\omega} = (\omega_x + \omega_y + \omega_z)/3$ the arithmetic mean trapping frequency, this number N_0 becomes macroscopic (on the order of N). For large total number of atoms N, the energy difference of neighboring energy eigenstates vanishes and we can replace the sum in equation (1.7):

$$N - N_0 = \int_0^\infty \frac{dn_x dn_y dn_z}{e^{\beta\hbar(\omega_x n_x + \omega_y n_y + \omega_z n_z)} - 1}, \tag{1.10}$$

or, equivalently, integrate over the density of states $\rho(\epsilon)$:

$$N - N_0 = \int_0^\infty \frac{\rho(\epsilon)d\epsilon}{e^{\beta\rho} - 1}. \tag{1.11}$$

This integration gives

$$N - N_0 = \zeta(3)\left(\frac{k_B T}{\hbar\omega_{\mathrm{ho}}}\right)^3 \tag{1.12}$$

with $\zeta(x)$ the Riemann Zeta function. By imposing $N_0 \to 0$ we can find the critical temperature for Bose-Einstein condensation:

$$T_c = \frac{\hbar\omega_{\mathrm{ho}}}{k_B}\left(\frac{N}{\zeta(3)}\right)^{1/3} = 0,94\frac{\hbar\omega_{\mathrm{ho}}}{k_B}N^{1/3}. \tag{1.13}$$

For this kind of system, the adequate thermodynamic limit is $N \to \infty$, $\omega_{ho} \to 0$ with $N\omega_{ho}^3$ constant, well defining the above critical temperature. With equation (1.10) and $T < T_c$ we obtain the condensate fraction in the thermodynamic limit:

$$\frac{N_0}{N} = 1 - \left(\frac{T}{T_c}\right)^3. \tag{1.14}$$

The system can be cooled, remaining in the normal gaseous phase, down to a temperature T_c which satisfies the condition $n(0)\lambda_{dB}^3 = \zeta(3/2) \approx 2,61$. Here $\lambda_{dB} = [2\pi\hbar^2/(mk_BT)]^{1/2}$ is the deBroglie wavelength and $n(0)$ the density at the trap center.

Critical temperature shift due to finite size effects

The thermodynamic limit $N \to \infty$, $\omega_{\mathrm{ho}} \to 0$ with constant $N\omega_{\mathrm{ho}}^3$, which was used to obtain expression (1.13) becomes incorrect for Bose condensates with small number of atoms ($10^4 - 10^5$), as they are typical for atom chip experiments. For small atom numbers, no abrupt thermodynamical phase transition occurs. Still, the transition takes place on a very narrow temperature region and the term of a (now slightly shifted) critical temperature still is meaningful. The shift in T_c following [15, 16, 17, 18] is:

$$\frac{\delta T_c}{T_c} = -\frac{\bar{\omega}\zeta(2)}{2\omega_{\mathrm{ho}}(\zeta(3))^{2/3}}N^{-1/3} \approx -0,73\frac{\bar{\omega}}{\omega_{\mathrm{ho}}}N^{-1/3}. \tag{1.15}$$

In anisotropic traps, the ratio of arithmetic to geometric mean $\bar{\omega}/\omega_{\mathrm{ho}} = (\Re + 2)/(3\Re^{1/3})$ can be large. Figure (1.1) compares the number of condensed atoms in the thermodynamical limit to

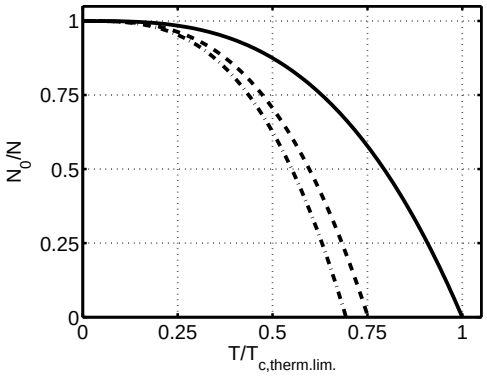

Figure 1.1: Condensate fraction N_0/N for $T < T_c$ in the thermodynamic limit (solid line) and taking into account finite size effects (dotted line) and interactions (dash dotted line) for typical experimental parameters (10^4 atoms in an anisotropic trap of $\Re = 100$).

a calculation for typical experimental parameters with 10^4 atoms in a highly anisotropic cigar shaped trap ($\Re = 100$).

So far, the properties of an ideal gas in three dimensional (though anisotropic) traps have been discussed. Fundamentally different behavior can be observed for systems in reduced dimensions (1D, 2D), when $k_B T$ is smaller than the oscillator energies $\hbar\omega_{x,y,z}$ in one or two directions. Due to their intrinsic elongated shape, chip traps are well suited to study 1D systems. In 1D, Bose-Einstein condensation does not occur in an ideal gas due to the logarithmic divergence of the integral (1.11); the critical temperature tends to zero in the thermodynamic limit. Nevertheless, one can obtain a large occupation of the lowest single particle state at finite particle number and finite temperature $T_{1\mathrm{D}}$ [17]:

$$k_B T_{1\mathrm{D}} = \hbar\omega_{1\mathrm{D}} \frac{N}{\ln(2N)}, \tag{1.16}$$

with $\omega_{1\mathrm{D}} \equiv \omega_{\|}$. For well chosen trap parameters, a two-step condensation at two distinct temperatures $T_{1\mathrm{D}} < T_{3\mathrm{D}}$ is predicted. In a first step, the radial degrees of freedom freeze out at $T < T_{3\mathrm{D}}$ and in a second step at $T < T_{1\mathrm{D}}$ also the axial ground state becomes macroscopically populated (see also section 1.3.1).

The above discussion describes the properties of an ideal Bose gas. Two particle interactions will strongly modify the nature of phase transitions in reduced dimensions [19] as will be discussed in section 1.3.

1.2 The interacting Bose gas

Bose condensed atoms do accumulate in the ground state of the trapping potential, so that the local density would increase to infinity, when adding more and more atoms. For interacting atoms, a repulsive interaction will limit the density in the trap center, whereas an attractive interaction will lead to a collapse of the condensate once exceeding a critical particle number [20].

The Hamiltonian for interacting particles in an external trapping potential V_{trap} in second quantization is

$$\begin{aligned}\hat{H} = & \int d\mathbf{r}\, \hat{\Psi}^\dagger(\mathbf{r}) \left(-\frac{\hbar^2}{2m}\nabla^2 + V_{\text{trap}}\right) \hat{\Psi}(\mathbf{r}) \\ & + \frac{1}{2}\int d\mathbf{r}\, d\mathbf{r}'\, \hat{\Psi}^\dagger(\mathbf{r})\hat{\Psi}^\dagger(\mathbf{r}')V(\mathbf{r}-\mathbf{r}')\hat{\Psi}^\dagger(\mathbf{r}')\hat{\Psi}^\dagger(\mathbf{r}).\end{aligned} \tag{1.17}$$

Here, $\hat{\Psi}(\mathbf{r})$ and $\hat{\Psi}^\dagger(\mathbf{r})$ are the bosonic creation and annihilation operators and $V(\mathbf{r}-\mathbf{r}')$ is the interaction potential for two atoms located at positions $\mathbf{r}$ and $\mathbf{r}'$.

1.2.1 The Gross-Pittaevskii equation

In 1947, Bogoliubov formed the basis of a *mean field theory* for dilute gasses by decomposing the field operator $\hat{\Psi}$ to a complex wave function $\Phi(\mathbf{r},t)$ describing the condensate wave function and the so called depletion $\hat{\Psi}'$, describing the non condensed fraction [21]:

$$\hat{\Psi}(\mathbf{r},t) = \Phi(\mathbf{r},t) + \hat{\Psi}'(\mathbf{r},t). \tag{1.18}$$

Assuming a macroscopic population of the ground state, $\Phi(\mathbf{r},t)$ is now a complex number and the condensate density distribution is given by $n_0(\mathbf{r},t) = |\Phi(\mathbf{r},t)|^2$. Combining the ansatz (1.18) and the Hamiltonian (1.17) and using the Heisenberg equation, we obtain

$$\begin{aligned} i\hbar\frac{\partial}{\partial t}\hat{\Psi}(\mathbf{r},t) &= \left[\hat{\Psi}, \hat{H}\right] \\ &= \Big[-\frac{\hbar^2\nabla^2}{2m} + V_{\text{trap}}(\mathbf{r}) \\ &\quad + \int d\mathbf{r}'\hat{\Psi}^\dagger(\mathbf{r}',t)V(\mathbf{r}'-\mathbf{r})\hat{\Psi}^\dagger(\mathbf{r}',t)\Big]\hat{\Psi}(\mathbf{r},t)\end{aligned} \tag{1.19}$$

In first approximation, we will set Φ for $\hat{\Psi}$. This is is justified since in Bose-Einstein condensates, the condensate fraction can easily be above 90 % (in contrast to ≈ 10 % in ^{4}He superfluid).

For ultracold atoms, scattering only occurs in the symmetric s-wave channel. Therefore, the atomic interaction can be described by a contact interaction with a delta function pseudo potential $g\delta^3(\mathbf{r}-\mathbf{r}')$ where g is a coupling constant, derived from the s-wave scattering length a:

$$g = \frac{4\pi\hbar^2 a}{m}. \tag{1.20}$$

Together with (1.19) we obtain the Gross-Pittaevskii equation for the condensate wave function:

$$i\hbar\frac{\partial}{\partial t}\Phi(\mathbf{r},t) = \left(-\frac{\hbar^2\nabla^2}{2m} + V_{\text{trap}}(\mathbf{r}) + g|\Phi(\mathbf{r},t)|^2\right)\Phi(\mathbf{r},t). \tag{1.21}$$

which is valid, once the s-wave scattering length is much smaller then the inter particle separation. To obtain the ground state of this approximation, we write $\Phi(\mathbf{r},t) = \phi(\mathbf{r})\exp(-i\mu t/\hbar)$, ϕ being real and normalized to the total particle number $\int \phi^2 d\mathbf{r} = N_0 = N$. By this the Gross-Pittaevskii equation (1.21) becomes

$$\left(-\frac{\hbar^2\nabla^2}{2m} + V_{\text{trap}}(\mathbf{r}) + g|\Phi(\mathbf{r},t)|^2\right)\phi(\mathbf{r}) = \mu\phi(\mathbf{r}), \tag{1.22}$$

a Schrödinger equation with a nonlinear interaction term, which is proportional to the local density $n(\mathbf{r}) = |\phi^2(\mathbf{r})|$. In the absence of interactions ($g = 0$), (1.22) reduces to the usual Schrödinger equation for a single particle.

1.2.2 The Thomas-Fermi approximation

As mentioned above, the Gross-Pittaevskii equation (1.22) can be applied, when the mean density n is much smaller than the number of atoms in a cube of volume a^3 (scattering length), or the so called *gas parameter* $a^3 n \ll 1$, which is clearly the case for all experimental conditions considered in this manuscript. Such a system is called *dilute* or *weakly interacting*, a term which has to be used with precaution: scaling equation (1.22) to natural units (lengths measured in a_{ho}, densities in a_{ho}^{-3} and energies in $\hbar\omega_{ho}$), we obtain

$$\Big(\underbrace{-\tilde{\nabla}^2}_{E_{\mathrm{kin}}} + \tilde{r}^2 + \underbrace{8\pi \frac{Na}{a_{ho}} \tilde{\phi}^2(\tilde{\mathbf{r}})}_{E_{\mathrm{int}}}\Big)\tilde{\phi}(\tilde{\mathbf{r}}) = 2\tilde{\mu}\tilde{\phi}(\tilde{\mathbf{r}}). \tag{1.23}$$

Written in this way, it becomes clear, that the atomic interactions and the kinetic energy scale as

$$\frac{E_{int}}{E_{kin}} \propto \frac{Na}{a_{ho}}. \tag{1.24}$$

In our experiments, this ratio varies between 50 and 5000, showing that we are in a dilute system, but in most cases, interactions determine the wave function properties. The term weakly interacting has historical significance, as it compares gaseous systems to quantum liquids like ^{4}He, which are referred to as *strongly interacting*.

As the interaction energy dominates over the kinetic energy in many configurations, one can simply neglect the (first) kinetic term in equation (1.22) and this way obtain the *Thomas-Fermi approximation* for $\phi(\mathbf{r})$:

$$n(\mathbf{r}) = |\phi^2(\mathbf{r})| = \frac{\mu - V_{trap}(\mathbf{r})}{g} \tag{1.25}$$

for $\mu > V_{trap}(\mathbf{r})$ and $n = 0$ elsewhere. For a harmonic trap, this approximation gives a density distribution of the shape of an inverted parabola with a maximal density

$$n(0) = \frac{\mu}{g} \tag{1.26}$$

at the center of the trap. The size of the condensate is described by the Thomas-Fermi radii:

$$R_\perp = \sqrt{\frac{2\mu}{m\omega_\perp^2}} \tag{1.27}$$

$$R_\parallel = \sqrt{\frac{2\mu}{m\omega_\parallel^2}}. \tag{1.28}$$

For rather isotropic traps, one can use a single Thomas-Fermi radius R, based on the geometric mean ω_{ho} of the trap frequencies. Together with the normalization of the wave function to density, we can calculate the chemical potential to

$$\mu = \frac{\hbar\omega_{ho}}{2}\left(\frac{15Na}{a_{ho}}\right)^{2/5}. \tag{1.29}$$

Inserting expression (1.29) into the expression for the Thomas-Fermi radius (1.28), we obtain

$$R = a_{ho}(15N)^{1/5}\left(\frac{a}{a_{ho}}\right)^{1/5} \gg a_{ho}, \tag{1.30}$$

which means, as $(a/a_{ho}) \gg N^{-1}$, that interactions increase the size of the condensate compared to the non interacting case, where the condensate extension is $\approx a_{ho}$ (see equation (1.3)). The Thomas-Fermi approximation is valid, when $\hbar\omega_{x,y,z} \ll ng$. In strongly anisotropic (cigar shaped) traps, this may well be the case in the longitudinal direction, whereas in the transverse direction, the confinement may be so strong, that the kinetic energy term may not be neglected. In this scenario, no simple solution for the Gross-Pittaevskii equation can be found, the condensate shape may deviate significantly from the parabolic shape as discussed in section 1.3.2.

Critical temperature shift due to interactions

As described by equation (1.26), in an interacting Bose gas, repulsive interactions decrease the density $n(0)$ at the trap center (see also figure (1.4)). As Bose condensations universally takes place at fixed phase space density $n(0)\lambda_{dB} \simeq 2,61$, this effect has an influence on the critical temperature [22]:

$$\frac{\delta T_c}{T_c} = -1,3\frac{a}{a_{\mathrm{ho}}}N^{1/6}. \tag{1.31}$$

Unlike the shift in T_c due to finite size (1.15), the effect of interactions does not depend on the shape of the trap as long as it stays three dimensional. Figure (1.1) illustrates the effect of interactions on the critical temperature for typical experimental conditions.

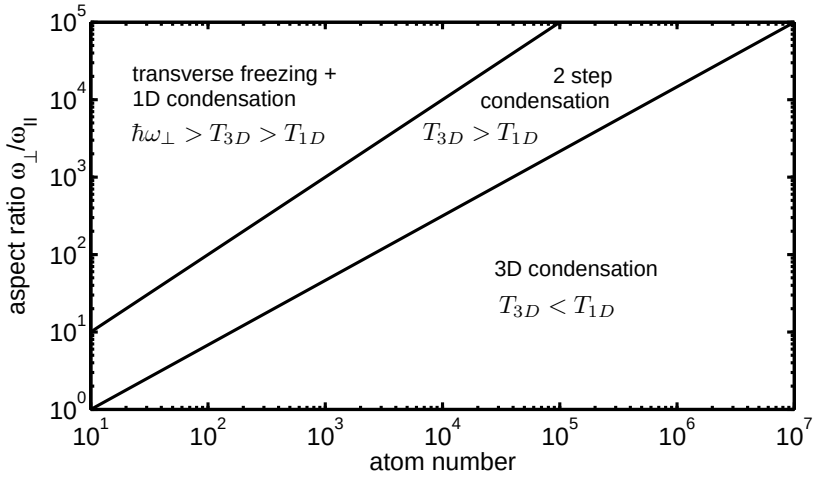

Figure 1.2: Phase transition regimes for an ideal Bose gas. For high atom numbers and isotropic traps, the usual phase transition to BEC takes place in 3D (lower right region). For more elongated systems, condensation occurs first at $T_{3\mathrm{D}}$ in the two transverse direction and at a lower $T_{1\mathrm{D}}$ in the longitudinal direction (two-step-condensation, central region). For extremely anisotropic traps end very low atom number, the transverse degrees of freedom freeze out even for a thermal sample, before any Bose condensation takes place (upper left region).

1.3 Bose-Einstein condensates in elongated traps

As mentioned in (1.5) and (1.6), most realizations of Bose-Einstein condensates in magnetic traps posses an axial symmetry, giving rise to an elongated, cigar shape of the cloud. The strength of the anisotropy is expressed in the aspect ratio of the trap $\Re = \omega_\perp/\omega_\parallel$. In magnetic traps formed by current carrying wires, this aspect ratio can easily reach values above 100, fundamentally altering the physical properties and energy scales of the system in the longitudinal and the transverse directions [23]. The above introduced Thomas-Fermi approximation may not be applicable to all three spatial directions, the shape of the wave function gets modified compared to an isotropic 3D system [24]. Elementary excitations of the system may become of 1D character, giving rise to a non-uniform phase in the longitudinal direction of the condensate, reducing its coherence length to below the extension of the cloud [25, 26, 27, 28].

Knowledge about the shape of the condensate wave function (*e.g.* an overlap with a neighboring wave function in a double well) as well as the coherence properties of the condensate are fundamental for the realization of tunnel coupling or interferometry in double wells and will therefore be discussed in the following sections.

1.3.1 Bose-Einstein condensation in 1D

Identifying the 1D regime

Cold atomic samples or Bose condensates in very elongated geometries are often referred to as being in the 1D regime. To avoid ambiguity, we clarify the criteria for an ideal and an interacting gas:

The ideal gas in 1D An ideal gas is considered to be in the 1D regime, once its transverse degrees of freedom are frozen out, but not the longitudinal motion of the particles: $k_B T \ll \hbar\omega_\perp$ and $k_B T \gg \hbar\omega_\parallel$. The particles are in the transverse (single particle) ground state, but populate many longitudinal modes. This regime could be named *thermodynamic 1D regime*.

The interacting gas in 1D The same criterion can be applied to a thermal gas of interacting particles. For a Bose condensate, not the temperature T predominantly defines the energy of the system, but the chemical potential μ. Consequently, the criterium for a condensate to be in the 1D regime is $\mu \ll \hbar\omega_\perp$. The degrees of freedom in the transverse and in the longitudinal direction are decoupled in the 1D regime. The transverse shape deviates significantly from the 3D Thomas-Fermi profile (see section 1.3.2), whereas the longitudinal shape is hardly modified. Therefore, this regime is referred to as the *Thomas-Fermi 1D regime* or the *1D mean field regime*.

A formal criterion to identify the dimensionality of an interacting system has been introduced by Menotti and Stringari in [29]. It is based in the parameter $\chi = N\Re a/a_\perp$, where N is the atom number, a the s-wave scattering length, $a_\perp$ the size of the transverse single particle ground state and $\Re$ the aspect ratio of the trap. For $\chi \gg 1$, the condensate is well described by a 3D theory, for $\chi \ll 1$ it is in the 1D regime.

Most experiments presented in this manuscript are at the 1D-3D crossover, where the chemical potential μ is comparable to the transverse ground state energy $\hbar\omega_\perp$ (1-3 kHz$\cdot h$), and $\chi \approx 1$.

The phase transition of an ideal gas in 1D

As discussed in section 1.1.1, Bose-Einstein condensation of a non-interacting gas does not occur in an ideal 1D trapping geometry. It has been shown by [17], that a macroscopic occupation of the ground state, which in many respects resembles the BEC phase transition, is nevertheless possible due to the finite size of the trap. As seen in (1.16), the critical temperature T_{1D} for this phenomenon gets shifted to lower values compared to the 3D system: $k_B T_{3D} > k_B T_{1D} \simeq N\hbar\omega_\parallel / \ln(2N)$ (see also figure (1.1)). As the degrees of freedom of a 1D condensate are decoupled, a 2-step-condensation is predicted: in a first step, at $T < T_{3D}$, the transverse degrees of freedom freeze out, where in a second step at $T < T_{1D}$ also the longitudinal ground state gets macroscopically populated. This happens preferably at high aspect ratios $\Re$ and low atom numbers, as can be seen in figure (1.2). Two-step-condensation has been observed very recently in our experiments in Orsay (see figure (1.3)) and is currently under investigation.

The phase transition of an interacting gas in 1D

For the interacting 1D Bose gas, the critical temperature T_c gets shifted according to (1.31). At this temperature, density fluctuations are suppressed, whereas the longitudinal phase still fluctuates, until a homogeneous phase establishes at an even lower temperature T_ϕ. This effect is described in more detail in section 1.3.3.

1.3.2 The shape of the condensate wave function

We will now concentrate on the transverse shape of the condensate wave function in a very elongated trap. We assume the longitudinal and the transverse degrees of freedom to be decoupled and restrict the analysis to the 2D transverse plane [30]. The condensate wave function can be determined by minimizing the energy functional

$$E = \langle\psi| \sum_{i=1}^{3} H_i |\psi\rangle + \frac{g}{2} \int |\psi|^4 d^3r, \tag{1.32}$$

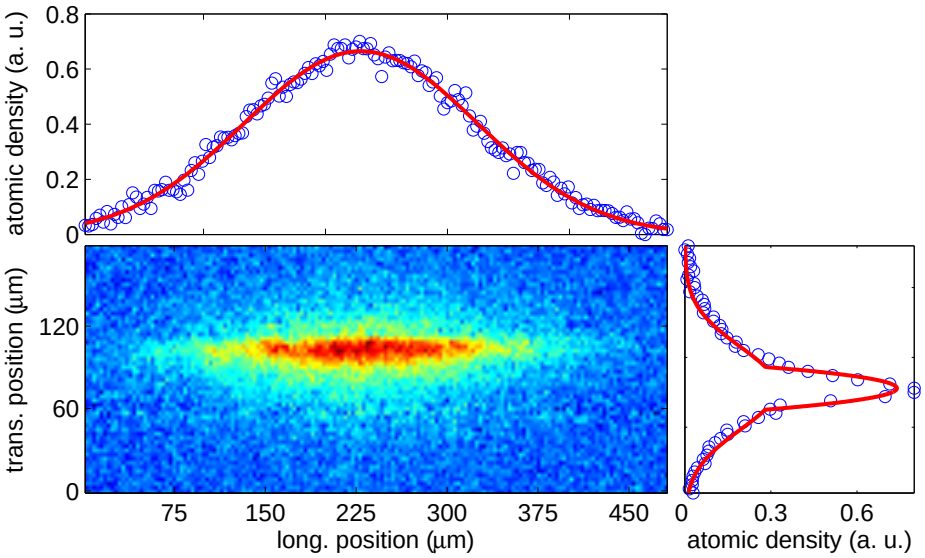

Figure 1.3: Signature of two-step-condensation in an absorption image after time-of-flight expansion (14 ms): the characteristic peak in the transverse density distribution indicates a macroscopic population of the transverse ground state, whereas in the longitudinal direction the level population is still completely thermal (preliminary data from the Orsay experiment).

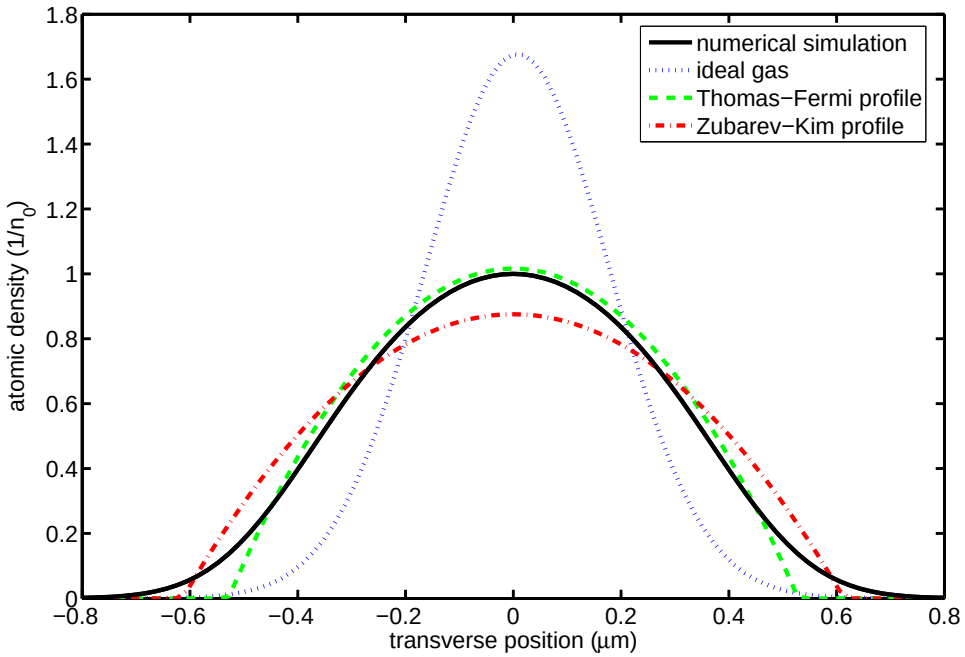

Figure 1.4: Transverse shape of the BEC wave function. The result of a numerical integration of the Gross-Pittaevskii equation (solid line) is compared the result of different analytical theories describing the condensate (details in the text).

where ψ is the condensate wave function, normalized to $\int |\psi|^2 d^3r = N$, N being the total number of (condensed) atoms and

$$H_i = -\frac{\hbar^2}{2m}\frac{\partial^2}{\partial x_i^2} + \frac{1}{2}m\omega_i^2 x_i^2, \tag{1.33}$$

where i denotes the spatial coordinates $\{x, y, z\}$.

Neglecting the (second) term in equation (1.32), describing the interactions, leads to the (single particle) ideal gas solution (1.3), which is of gaussian shape. Neglecting the (first) therm in equation (1.32), describing the kinetic energy, leads to the Thomas-Fermi approximation (see section 1.2.2) and to a parabola shaped wave function. At the 1D-3D crossover ($\mu \approx \hbar\omega_\perp$), both terms contribute comparably to the total energy of the system, giving rise to an intermediate behavior of the wave function concerning size and shape. The exact shape of the wave function (within the limitations of the mean field approach) can only be found by a numerical integration of the Gross-Pittaevskii equation.

The Zubarev-Kim Hamiltonian

An analytical approach to this problem has been proposed by Zubarev and Kim [24]: they introduce the vector $\gamma = \gamma_i, \quad i = \{x, y, z\}$ with $0 \leq \gamma_i < 1$ in order to adjust the contributions of interaction and kinetic term "by hand". The modified Hamiltonian is

$$\tilde{H}_i = \frac{\hbar\omega_i}{2}\sqrt{\gamma_i} + \frac{1}{2}m\omega_i^2(1-\gamma_i)x_i^2. \tag{1.34}$$

This Hamiltonian systematically underestimates the total energy of the system:

$$H_i - \tilde{H}_i = -\frac{\hbar^2}{2m}\frac{\partial^2}{\partial x_i^2} + \frac{1}{2}m\omega_i^2\gamma_i x_i^2 - \frac{\hbar\omega_i}{2}\sqrt{\gamma_i}, \tag{1.35}$$

where for all ψ, $\langle\psi|H_i - \tilde{H}_i|\psi\rangle \geq 0$ where 0 identifies the "correct" γ_i that well describes the ground state of the system. Therefore, by minimizing expression (1.35), the γ_i that optimally describes the system at the 1D-3D crossover can be determined. For typical experimental parameters (N=1×10^4, $\omega_\parallel/2\pi = 10\,\mathrm{Hz}$, $\omega_\perp/2\pi = 2\,\mathrm{kHz}$), one finds $\gamma_\perp = 0,69$ and $\gamma_\parallel = 1,8 \times 10^{-4}$.

Once the optimized values for γ have been found, the physical quantities of the system can be derived in close analogy to the Thomas-Fermi approximation:

$$\mu = \sum_{i=1}^{3}\frac{\hbar\omega_i}{2}\sqrt{\gamma_i} + \tilde{\mu}_{\mathrm{TF}}, \tag{1.36}$$

and

$$n(\mathbf{r}) = \tilde{n}_{\mathrm{TF}}(\mathbf{r}) \tag{1.37}$$

where $\tilde{\mu}_{\mathrm{TF}}$ and $\tilde{n}_{\mathrm{TF}}$ are the results, obtained by the Thomas-Fermi approximation (see (1.25) and (1.26)) with modified oscillation frequencies $\tilde{\omega}_i = \omega_i\sqrt{1-\gamma_i}$. The density profile obtained by the Zubarev-Kim approach is therefore also of parabola shape.

Figure (1.4) compares the transverse shape of the condensate, obtained by a numerical integration of the Gross-Pittaevskii equation to different analytical models: it becomes obvious, that a single particle description (dotted line) fails to reproduce the wave function. The result of the Thomas-Fermi approximation (dashed line) describes well the peak density and the central region of the condensate, but underestimates its extension at the edges. The Zubarev-Kim approach reflects the width of the condensate more properly, but poorly describes the central region. In conclusion, Bose-Einstein condensates at the 1D-3D crossover are not sufficiently described by analytical expressions yet, systems that critically depend on the exact shape of the wave form (*e.g.* tunnel coupling experiments) have to be simulated numerically.

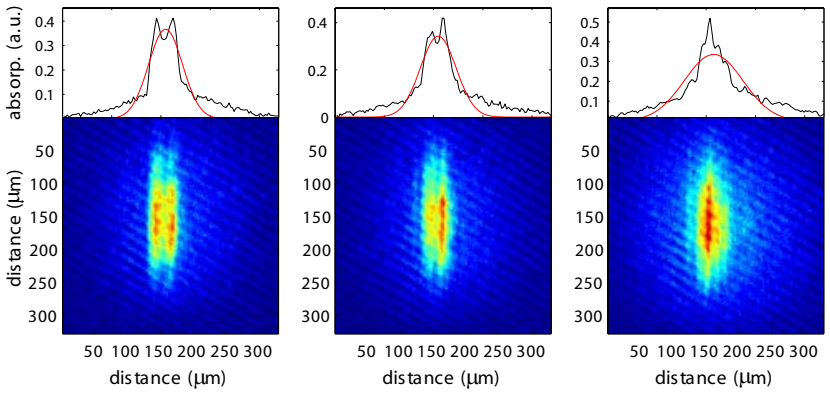

Figure 1.5: Longitudinal phase fluctuations in a quasi-condensate convert into (random) interference fringes in (20 ms) time-of-flight absorption imaging [25] (preliminary data from the Heidelberg experiment). Compare also section 9.2.1.

1.3.3 Longitudinal phase fluctuations

For interacting Bose condensates in elongated traps, not only the shape of the wave function is modified, but also the phase transition itself is affected by interactions and geometry. Where the ideal gas goes through a two-step-condensation when cooled down (see figure 1.2), the interacting gas establishes uniform longitudinal density and longitudinal uniform phase at two distinct temperatures $T_c \simeq T_{3D}$ (compare (1.13) and (1.31)) and T_ϕ with $T_c > T_\phi$. Although no phase transition in the strict sense of the word occurs in very elongated systems, cold atomic samples of temperature $T_\phi < T < T_c$ are referred to as *quasi-condensates*.

The suppression of density fluctuations close to T_c and the effect of interactions thereon has been studied very recently in the experiment in Orsay [REF, LINK TO OUTLOOK]. Longitudinal phase fluctuations have been observed in the Heidelberg experiments and have a direct impact on the interference experiments presented in this manuscript. Their theory will be therefore briefly resumed in the following.

The correlation function for quasi-condensates

Phase fluctuations are elementary excitations of the system and have been described by Bogoliubov theory in terms of quasi-particles u_ν and v_ν of wavelength ν and energy ϵ_ν [21]. They obey a set of coupled linear Schrödinger equations

$$\left(-\frac{\hbar^2}{m}\nabla^2 + V(\mathbf{r}) + gn_0 - \mu\right) f_\nu^+ = \epsilon_\nu f_\nu^-, \tag{1.38}$$

$$\left(-\frac{\hbar^2}{m}\nabla^2 + V(\mathbf{r}) + 3gn_0 - \mu\right) f_\nu^- = \epsilon_\nu f_\nu^+, \tag{1.39}$$

where $f_\nu^\pm = u_\nu \pm v_\nu$. For $\epsilon_\nu > \hbar\omega_\perp$ these excitations are 3D, for $\epsilon_\nu < \hbar\omega_\perp$ they are of 1D character. 3D excitations do usually not affect the overall coherence of the system as they damp out rapidly for temperatures below T_c. Low lying longitudinal modes with wavelength comparable to the spatial extension of the condensate in contrast can be easily populated, giving rise to excitations of 1D character even in elongated, but not strictly 1D systems [25, 26, 27, 28]. as they are considered in this manuscript.

To characterize longitudinal phase fluctuations, we will analyze the first order correlation

function for the phase state $\hat{\Psi} = \sqrt{n}e^{i\phi}$ [31]:

$$\rho(\mathbf{r}, \mathbf{r}') = \langle \hat{\Psi}^\dagger(\mathbf{r})\hat{\Psi}(\mathbf{r}')\rangle \tag{1.40}$$

$$= \sqrt{n(r_\perp, z)n(r'_\perp, z')}e^{\frac{-\Delta^2\phi(z,z')}{2}}, \tag{1.41}$$

where $\Delta^2\phi(z, z') = \langle[\phi(z) - \phi(z')]^2\rangle$ only depends on the longitudinal coordinates z and z', as the fluctuations are 1D. The spatial correlation function $C(\mathbf{s})$ is defined as the integrated single particle correlation function in coordinate space

$$C(s) = \int d^3r\rho(\mathbf{r} + \frac{s\mathbf{u}_z}{2}, \mathbf{r}' - \frac{s\mathbf{u}_z}{2}) \tag{1.42}$$

and with $\mathbf{q} = s\mathbf{u}_z$ as

$$P(\mathbf{p}) = \left(\frac{1}{2\pi\hbar}\right)^3 \int d^3qC(\mathbf{q})e^{-i\mathbf{p}\cdot\mathbf{q}/\hbar} \tag{1.43}$$

in momentum space. By integrating over the transverse momenta p_x and p_y, one obtains the longitudinal momentum distribution

$$P(p_z) = \frac{1}{2\pi\hbar}\int dsC(s)e^{ip_z s/\hbar}. \tag{1.44}$$

The longitudinal momentum distribution $P(p_z)$ is therefore the Fourier transform of the correlation function $C(s)$.

Up to now, no complete analytical expression for $C(s)$ or $P(p_z)$ has been found, describing the entire quasi-condensate in a trap. Still, it has been show that the system can be well described by a local density approach, considering separate regions of the condensate individually [32,26,33]. Consequently, the coherence properties only depend on the integrated ($n_{1\mathrm{D}}(z) = \int dx\,dy\,n(\mathbf{r})$) local density $n_{1\mathrm{D}}(z)$ and on temperature T. Following [27,33], we introduce the coherence length $L_\phi(z)$ as

$$L_\phi(z) = \frac{\hbar^2 n_{1\mathrm{D}}(z)}{mk_BT}. \tag{1.45}$$

By doing so, we directly obtain the transition temperature T_ϕ, for which the coherence length L_ϕ is equal to the extension of the quasi-condensate L and full longitudinal phase coherence is established:

$$k_BT_\phi = \frac{15}{32}\frac{N(\hbar\omega_\parallel)^2}{\mu}. \tag{1.46}$$

The coherence length (1.45) can be rewritten as $L_\phi = LT_\phi/T$. The phase fluctuations depend linearly on distance:

$$\Delta\phi^2(z, z') \simeq \frac{T}{T_\phi}\frac{|z - z'|}{L}. \tag{1.47}$$

For $T \gg T_\phi$ and applying the local density approach, the spatial correlation function can be written

$$C(s) = \int dz\, n_{1\mathrm{D}}(z)\exp\left(\frac{Tn_{1\mathrm{D}}(0)s}{2T_\phi n_{1\mathrm{D}}(z)L}\right) \tag{1.48}$$

in coordinate space and

$$P(p_z) \simeq \frac{n_{1\mathrm{D}}(0)}{2\pi p_\phi}\int dz\frac{\left(\frac{n_{1\mathrm{D}}(z)}{n_{1\mathrm{D}}(0)}\right)^2}{\left(\frac{n_{1\mathrm{D}}(z)}{n_{1\mathrm{D}}(0)}\right)^2\left(\frac{p_z}{p_\phi}\right)^2 + \frac{1}{4}}, \tag{1.49}$$

where $p_\phi = \hbar/L_\phi$. The momentum distribution is of Lorentzian shape of width $\Delta p_\phi = 0,64 p_\phi$. The width of the distribution in momentum space is therefore a direct measure for the coherence length in an elongated quasi-condensate, this has been probed by velocity selective Bragg spectroscopy in experiments in Orsay [28, 27].

In time-of-flight expansion, in-trap phase fluctuations transform into density modulations that can be directly observed in absorption imaging [25, 34]. These fluctuations can be understood as matter wave interference originating from an extended coherent source with (arbitrary) fluctuating spatial phase, in analogy to speckle patterns in coherent optics. Such interference fringes have first been observed in experiments in Hannover, where quasi-condesates were released from magnetic traps of aspect ratios $\Re = 25 - 50$. High contrast interference has also been observed in the Heidelberg experiment with high aspect ratio traps ($\Re > 200$) and are currently under investigation (see figure (1.5)).

1.4 Interference of two Bose-Einstein condensates

Dilute Bose-Einstein condensates behave in many aspects like coherent radiation fields; releasing mater waves from spatially separated sources gives rise to interference phenomena. Matter wave interference allows studies ranging from fundamental properties of (de-)coherence to the effects of many particle interactions on the quantum system. Due to their rest mass, coherent atomic systems are extremely sensitive to gravity, accelerations or rotations, qualifying the system for metrology based on matter wave interferometry.

In this section, we resume the theory describing interference of two spatially separated Bose-Einstein condensates of individual, but uniform phase. Multiple realizations as created in periodic optical lattices [35, 36] are not discussed.

Conceptually, there are two ways to realize a pair of spatially separated condensates: creation of distinct condensates from already separated thermal clouds or dynamic splitting of a single condensate into two. For the latter case, given an initial phase coherent source, one expects to observe interference with a fixed relative phase of the two condensates after the splitting. Surprisingly, interference was observed even for separately created sources, where no global phase was established [37].

The theory for phase locked sources as well as for independently created sources will be treated in the following. We close by a short description of the phase diffusion process, which describes the loss of "phase memory" of initially phase locked clouds due to number fluctuations, directly related to the uncertainty principle.

1.4.1 Phase locked sources

For a weakly interacting Bose condensate, the description can be carried out in close analogy to (phase-)coherent electromagnetic waves. We assume two spatially separated (not overlapping) wave packets described by the single particle wave function $\psi_1(\mathbf{r},t)$ and $\psi_2(\mathbf{r},t)$. We furthermore assume a *coherent state*:

$$\psi(\mathbf{r},t) = \sqrt{N_1}\psi_1(\mathbf{r},t) + \sqrt{N_2}\psi_2(\mathbf{r},t), \tag{1.50}$$

where N_1 and N_2 denote the expectation values for particle number of the two clouds. Analogous to intensity in electromagnetic radiation, the atomic density at any point is given by the square of the wave function:

$$\begin{aligned} n(\mathbf{r},t) &= |\psi(\mathbf{r},t)|^2 = |\sqrt{N_1}\psi_1(\mathbf{r},t) + \sqrt{N_2}\psi_2(\mathbf{r},t)|^2 &(1.51)\\ &= N_1|\psi_1(\mathbf{r},t)|^2 + N_2|\psi_2(\mathbf{r},t)|^2 + 2\sqrt{N_1N_2}\mathrm{Re}[\psi_1(\mathbf{r},t)\psi_2^*(\mathbf{r},t)], &(1.52)\end{aligned}$$

where Re[...] denotes the real part. The last term of this expression gives rise to interference due to the spatial dependence of the phases of the two wave functions of the individual clouds.

We assume the initial clouds to be of gaussian shape of width R_0 when released from their individual traps, centered at $\mathbf{r} = \pm\mathbf{d}/2$. The traps are switched of at $t = 0$, the effect of external potentials and interactions after switch-off are neglected:

$$\psi_1 = \frac{e^{i\phi_1}}{(\pi R_t^2)^{3/4}} \exp\left[-\frac{(\mathbf{r}-\mathbf{d}/2)^2(1+i\hbar t/mR_0^2)}{2R_t^2}\right] \tag{1.53}$$

and

$$\psi_1 = \frac{e^{i\phi_1}}{(\pi R_t^2)^{3/4}} \exp\left[-\frac{(\mathbf{r}-\mathbf{d}/2)^2(1+i\hbar t/mR_0^2)}{2R_t^2}\right]. \tag{1.54}$$

Here ϕ_1 and ϕ_2 are the initial phases of the two condensates, R_t the width of the wave packet at time t given by

$$R_t^2 = R_0^2 + \left(\frac{\hbar t}{mR_0}\right)^2. \tag{1.55}$$

The interference term in equation (1.51) thus varies as

$$2\sqrt{N_1 N_2}\mathrm{Re}[\psi_1(\mathbf{r},t)\psi_2^*(\mathbf{r},t)] \propto A\cos\left(\frac{\hbar}{m}\frac{\mathbf{r}\cdot\mathbf{d}}{R_0^2 R_t^2}t + \phi_1 - \phi_2\right). \tag{1.56}$$

Here, the prefactor A varies slowly with the spatial coordinates. Planes of constant phase are therefore perpendicular to the vector connecting the two centers of the clouds. The positions of fringe maxima and minima depend on ϕ_1 and ϕ_2 and directly allow a measurement of the differential phase $(\phi_1 - \phi_2)$. The fringe spacing is given by

$$\Delta z = 2\pi\frac{mR_t^2 R_0^2}{\hbar t d}. \tag{1.57}$$

For sufficiently large expansion times, the size of the initial cloud R_0 can be neglected against the size of the expanded cloud and the width is given by $R_t \simeq \hbar t/mR_0$. Therefore, the fringe spacing is given by

$$\Delta z \simeq \frac{ht}{md} \tag{1.58}$$

which is the the de Broglie wavelength associated with a particle that has travelled the distance d between the sources in the expansion time t.

As pointed out by [38], the observation of interference fringes does not provide evidence for phase coherence of the two clouds, since interference effects occur even if the two sources are completely decoupled (or created separately) before they overlap. This will be presented in the following section.

1.4.2 Independent sources

We now consider an initial state in which the number of particles N_1 and N_2 in each source cloud is fixed. The corresponding state vector is

$$|N_1, N_2\rangle = \frac{1}{\sqrt{N_1! N_2!}}(a_1^\dagger)^{N_2}(a_2^\dagger)^{N_2}|0\rangle, \tag{1.59}$$

which is referred to as a *Fock state*. As above, we calculate the particle density at a position $\mathbf{r}$:

$$n(\mathbf{r}) = N_1|\psi_1(\mathbf{r},t)|^2 + N_2|\psi_2(\mathbf{r},t)|^2. \tag{1.60}$$

A comparison with (1.51) clearly shows no "mixed term" and no obvious interference in this expression. This is due to the fact, that, according to the usual interpretation of quantum mechanics, the expectation value of an operator gives an *average* value for a physical quantity. However, a Fock state may show interference effects in a "one-shot" experiment, as the are usually performed in BEC experiments, based on destructive measurement techniques. Furthermore, many particles are involved in experiments with Bose-Einstein condensates, showing interference effects, where the single particle would not interfere. A famous example of this is the Hanbury Brown and Twiss experiment [39, 39] which has been performed with electromagnetic radiation and very recently with cold atomic samples and Bose condensates [Cite ORSAY He*].

In these systems, interferences often can be found by looking at the two-particle correlation function, which gives the amplitude for destroying particles at points $\mathbf{r}$ and $\mathbf{r}'$ and then creating them again at the same points:

$$\langle N_1, N_2, t|\hat{\psi}^\dagger(\mathbf{r})\hat{\psi}^\dagger(\mathbf{r}')\hat{\psi}(\mathbf{r}')\hat{\psi}(\mathbf{r})|N_1, N_2, t\rangle = \tag{1.61}$$

$$[N_1|\psi_1(\mathbf{r},t)|^2 + N_2|\psi_2(\mathbf{r},t)|^2][N_1|\psi_1(\mathbf{r}',t)|^2 + N_2|\psi_2(\mathbf{r}',t)|^2] \tag{1.62}$$

$$- N_1|\psi_1(\mathbf{r},t)|^2|\psi_1(\mathbf{r}',t)|^2 - N_2|\psi_2(\mathbf{r},t)|^2|\psi_2(\mathbf{r}',t)|^2 \tag{1.63}$$

$$+ 2N_1 N_2\mathrm{Re}[\psi_1^*(\mathbf{r}',t)\psi_1(\mathbf{r},t)\psi_2^*(\mathbf{r},t)\psi_2(\mathbf{r}',t)]. \tag{1.64}$$

The correlation found by Hanbury Brown and Twiss is expressed in the last term (1.64), demonstrating that coherence between sources is not imperative for interference effects. We assume two identical wave packets with different (arbitrary) phases $\phi_1(\mathbf{r},t)$ and $\phi_2(\mathbf{r},t)$:

$$\psi_1(\mathbf{r},t) = \psi_0 e^{i\phi_1(\mathbf{r},t)} \tag{1.65}$$

and

$$\psi_2(\mathbf{r},t) = \psi_0 e^{i\phi_2(\mathbf{r},t)}. \tag{1.66}$$

The two-particle correlation function (1.61) then becomes

$$\langle N_1, N_2, t|\hat{\psi}^\dagger(\mathbf{r})\hat{\psi}^\dagger(\mathbf{r}')\hat{\psi}(\mathbf{r}')\hat{\psi}(\mathbf{r})|N_1, N_2, t\rangle = \tag{1.67}$$

$$N(N-1)|\psi_0|^4 + 2N_1N_2|\psi_0|^4\cos[\Delta(\mathbf{r},t) - \Delta(\mathbf{r}',t)], \tag{1.68}$$

with $N = N_1 + N_2$ and $\Delta(\mathbf{r},t) = \phi_1(\mathbf{r},t) - \phi_2(\mathbf{r},t)$. This expression clearly gives rise to interference fringes, which can not be discriminated from the signature (1.56) of coherent sources in a single realization of the experiment. However, as the relative phase of independent sources is arbitrary in successive realizations of the same experiment, the measured differential phase $\Delta(\mathbf{r},t)$ will be randomly distributed between 0 and 2π for many repetitions of an interference experiment. In contrast, for two coherent sources originating from the same condensate, the differential phase $\phi_1 - \phi_2$ is fixed, giving rise to a constant differential phase in multiple repetitions of an interference experiment. Therefore, the width of the distribution of the relative phase is a measure for the coherence of the sources (for a more quantitative discussion, see section 2.2.3). The experimental challenge consists in splitting the condensate without destroying the phase relation between the two halves.

1.4.3 Phase diffusion

Even though two completely separate condensates can have a fixed relative phase if coherently split, this "phase memory" gets lost (and reappears in a revival) on a specific timescale t_D due to the fundamental process of phase diffusion: In a technically perfect experiment, the number of atoms in each well fluctuates due to the uncertainty principle [40]. Assuming Poissonian noise, these fluctuations are on the order of $\sqrt{N}$, where N is the total number of atoms. As interactions contribute to the total energy in each cloud, fluctuations in atom number lead to corresponding fluctuations in the evolution of the differential phase, washing out the phase in repeated realizations of the experiment [41,42]. The exact timescale of this process is an ongoing issue of discussion, for Poissonian number fluctuations in a completely decoupled 3D double well we find [41, 43]:

$$T_D \simeq \frac{5h\sqrt{N}}{2\mu} \tag{1.69}$$

where μ is the BEC chemical potential. As discussed in [44], fluctuations in atom number become sub-Poissonian for strongly interacting clouds; a non-negligible tunnel coupling between the wave packets leads to complex phase dynamics, possibly counteracting the phase diffusion [45]. The role of dimensionality of the system has not been considered so far.

All authors agree, that the timescale for phase diffusion is approximately two orders of magnitude above the oscillation period in a single well. Experimental observation of phase diffusion in Bose-Einstein condensates is therefore a major technological challenge, as not only the splitting has to be performed in a coherent fashion, but the coherence has to be "kept alive" for a long time, unaffected by technical fluctuations and noise. Due to high trap frequencies, chip-based magnetic double wells as presented in this manuscript are well suited to address this problem. Here, phase diffusion times may be reduced to a few tens of milliseconds, which may be within the reach of current experiments.

Chapter 2

Double well physics

This chapter resumes the theory of Bose-Einstein condensates in double well potentials. The strong (nonlinear) influence of interactions enriches the bosonic system compared to *e.g.* superconducting tunnel junctions. The macroscopic condensate wave function allows for direct observation of tunnel currents, the phase information is easily accessible through interference experiments. This topic has therefore attracted an enormous amount of attention in the recent literature, which is vast and partly controversial.

The chapter is divided into two sections, aiming to develop some theoretical background to the experimental implementations of double wells, described in part 2 and 3 of the manuscript.

Section 2.1 describes the static double well. A mean field two modes model is used to derive dynamics of the non-interacting and the interacting Bose gas for different regimes. Where it is relevant for the design and understanding of the experimental implementation, we go beyond the two modes model and briefly discuss instabilities and phase fluctuations due to nonlinear coupling to (additional) energetically low lying modes. Parameter constrains found in this analysis are closely related to the actual realization of a double well potential based on nano-fabricated wires presented in part 2.

Section 2.2 describes the Bose condensate in a dynamic double well and tries to understand the splitting process, as it will be experimentally demonstrated in part 3. Here, a quantum phase model is implied to describe the internal dynamics throughout the splitting process and the unavoidable breakdown of adiabaticity due to the (exponentially) vanishing tunnel coupling.

2.1 The static double well

2.1.1 The two modes model, tunnel coupling

We will first concentrate on the non-interacting Bose gas in a symmetric double well, as schematically illustrated in figure (2.1). For a very high potential barrier, the two wells are completely isolated, their equally spaced (single particle) eigenstates of energy $\hbar\Delta$ are these of an harmonic oscillator of trap frequency ω_0: $\hbar\Delta = \hbar\omega_0$ [46]. For a low potential barrier, the two lowest lying (symmetric and antisymmetric) states of the system are delocalized over both wells, their energy difference $\hbar\delta$ describes the tunnel coupling. We will restrict our analysis to the situation, where $\Delta \gg \delta$ and only the symmetric and the antisymmetric state are necessary to characterize the system. This *two modes model* has been widely discussed in the literature, as it allows for analytic expressions of the system dynamics [47, 44, 48, 49, 50, 51]. In general it is fairly realistic when the symmetric and the antisymmetric state are well separated from higher modes, it has limited validity in the case of a a very low potential barrier (when it is not allowed to neglect higher excitation modes) and in the case of strong atom-atom interactions. We introduce a

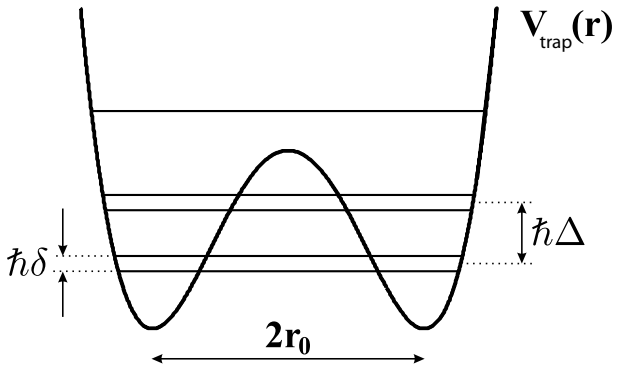

Figure 2.1: Schematic representation of the double well level structure: levels below the potential barrier are (almost) twofold degenerate, their energy difference characterizes the tunnel coupling. To avoid excitations due to tunnelling dynamics, it is favorable to design the double well such as $\hbar\Delta \simeq 10\hbar\delta$ (two modes tunnelling).

generic double well potential

$$V_{\mathrm{trap}}(r) = \frac{m\omega_0}{8r_0^2}\left(r^2 - r_0^2\right)^2 \tag{2.1}$$

where $\pm r_0$ denotes the positions of the potential minima, ω_0 is the single well oscillation frequency and $m\omega_0^2 r_0^2/8$ is the barrier height. Both double well schemes presented in part 2 and part 3 this manuscript can be well approximated by expression (2.1) within a few percent.

We now fix the on-well oscillation frequency ω_0 and thereby the extension of the single particle wave function $a_0 = \sqrt{\hbar/m\omega_0}$ and only vary the trap separation r_0 to modify the tunnel coupling. The Hamiltonian describing the non interacting system is $H_0 = p^2/(2m) + V_{\mathrm{trap}}(r)$. For bound states below the potential barrier, the obtained eigenenergies are doublets with vanishing energy difference for larger trap separations ($r_0 \gg a_0$). We will now focus on the two lowest lying states: the ground state $|\Phi_{\mathrm{sym.}}\rangle$ of the double well (2.1) is delocalized over both wells and symmetric, $|\Phi_{\mathrm{antis.}}\rangle$ is equally delocalized but antisymmetric. The completely left (right) localized state $|\Phi_{\mathrm{left}}\rangle$ ($|\Phi_{\mathrm{right}}\rangle$) can be constructed as

$$|\Phi_{\mathrm{left}}\rangle = \frac{1}{\sqrt{2}}\left(|\Phi_{\mathrm{sym.}}\rangle + |\Phi_{\mathrm{antis.}}\rangle\right) \tag{2.2}$$

$$|\Phi_{\mathrm{right}}\rangle = \frac{1}{\sqrt{2}}\left(|\Phi_{\mathrm{sym.}}\rangle - |\Phi_{\mathrm{antis.}}\rangle\right). \tag{2.3}$$

These states are no proper eigenstates of the hamiltonian: The system prepared in the (left) localized state $|\Phi_{\mathrm{left}}\rangle$ will evolve into the (right) localized state $|\Phi_{\mathrm{right}}\rangle$ and back with a frequency δ, defined by the energy difference $\hbar\delta$ between the eigenstates $|\Phi_{\mathrm{sym.}}\rangle$ and $|\Phi_{\mathrm{antis.}}\rangle$ (Rabi oscillations). The tunnel coupling can be easily calculated:

$$\hbar\delta = \langle\Phi_{\mathrm{antis.}}|H_0|\Phi_{\mathrm{antis.}}\rangle - \langle\Phi_{\mathrm{sym.}}|H_0|\Phi_{\mathrm{sym.}}\rangle = -2\langle\Phi_{\mathrm{left}}|H_0|\Phi_{\mathrm{right}}\rangle. \tag{2.4}$$

The simplest approach to this consists in identifying $|\psi_{\mathrm{left}}\rangle$ and $|\psi_{\mathrm{right}}\rangle$ with the single particle ground state of an harmonic oscillator potential with trap frequency ω_0, neglecting the tunnel coupling [47]. By doing so, one obtains

$$\delta \simeq \frac{r_0^2\omega_0^2}{a_0^2}\exp\left(-\frac{r_0^2}{a_0^2}\right). \tag{2.5}$$

A more complex variational approach [52] of WKB type based in the generic double well potential (2.1) gives

$$\delta \simeq \frac{4}{\sqrt{\pi}}\frac{r_0\omega_0}{a_0}\exp\left(-\frac{2r_0^2}{3a_0^2}\right). \tag{2.6}$$

For both expressions, we find an exponential decay of the tunnel coupling δ (for fixed ground state size a_0) with the double well separation r_0. To have a significant tunnel coupling, one has to prepare a double well spacing on the order of only a few times the wave function extension.

To avoid excitations in a tunnel experiment, one is aiming for a small tunnel coupling $\hbar\delta$ compared to the level separation $\hbar\Delta$ to the third lowest lying state. We will assume excitations sufficiently suppressed and the two modes model to be valid, when $\delta \simeq \omega_0/10$. Using expression (2.6) to describe the tunnel coupling, this fixes the ratio r_0/a_0 to 2,45.

2.1.2 The bosonic weak link Josephson junction

To take into account atom-atom interactions in the Bose condensate, the above Hamiltonian has to be extended to the Gross-Pittaevskii equation (1.21):

$$i\hbar\frac{\partial}{\partial t}\Psi(r,t) = \left(-\frac{\hbar^2\nabla^2}{2m} + V_{\mathrm{trap}}(r) + g|\Psi(r,t)|^2\right)\Psi(r,t). \tag{2.7}$$

where $V(r)_{\mathrm{trap}}$ is the (not necessarily symmetric) double well potential. We assume a weakly coupled system, leading to a low atomic density in the region of the potential barrier between the wells. The nonlinear interaction term can therefore be neglected in this region and we can make a product ansatz to separate spatial and temporal evolution (nonlinear two-mode approximation [50]):

$$\Psi(r,t) = \psi_{\mathrm{left}}(t)\Phi_{\mathrm{left}}(r) + \psi_{\mathrm{right}}(t)\Phi_{\mathrm{right}}(r) \tag{2.8}$$

where $\Phi_{\mathrm{left}}(r)$ and $\Phi_{\mathrm{right}}(r)$ are the left and right localized states as constructed in (2.2) and (2.3). The

$$\psi_{\mathrm{i}}(t) = \sqrt{N_{\mathrm{i}}}e^{i\theta_{\mathrm{i}}t}, \quad i = \{\mathrm{left,right}\} \tag{2.9}$$

describe the time development of the atom number distribution N_{left} and N_{right}, where $N_{\mathrm{left}} + N_{\mathrm{right}} = |\psi_{\mathrm{left}}|^2 + |\psi_{\mathrm{right}}|^2 = N$ is the total number of atoms. By injecting this ansatz into the Gross-Pittaevskii equation (2.7) we obtain a set of coupled differential equations [47, 50]:

$$i\hbar\frac{\partial}{\partial t}\psi_{\mathrm{left}} = \left(E^0_{\mathrm{left}} + U_{\mathrm{left}}N_{\mathrm{left}}\right)\psi_{\mathrm{left}} - K\psi_{\mathrm{right}} \tag{2.10}$$

$$i\hbar\frac{\partial}{\partial t}\psi_{\mathrm{right}} = \left(E^0_{\mathrm{right}} + U_{\mathrm{right}}N_{\mathrm{right}}\right)\psi_{\mathrm{right}} - K\psi_{\mathrm{left}}. \tag{2.11}$$

Effects of damping and finite temperature are ignored. E^0_i is the energy of the left (right) localized state in absence of interactions:

$$E^0_i = \int\left[\frac{\hbar^2}{2m}|\nabla\Phi_i|^2 + |\Phi_i|^2V\right]dr; \quad i = \{\mathrm{left,right}\}. \tag{2.12}$$

U_iN_i describes the nonlinear interaction energy:

$$U_i = g\int|\Phi_i|^4\,dr; \quad i = \{\mathrm{left,right}\}. \tag{2.13}$$

K is the coupling energy

$$K = -\int\left[\frac{\hbar^2}{2m}(\nabla\Phi_{\mathrm{left}}\nabla\Phi_{\mathrm{right}}) + \Phi_{\mathrm{left}}V\Phi_{\mathrm{right}}\right]dr; \quad i = \{\mathrm{left,right}\}. \tag{2.14}$$

We introduce the atom number population difference $z(t)$ as:

$$z(t) = \frac{N_{\mathrm{left}}(t) - N_{\mathrm{right}}(t)}{N} \equiv \frac{|\Phi_{\mathrm{left}}|^2 - |\Phi_{\mathrm{right}}|^2}{N}, \qquad z(t) \in [-1,1] \tag{2.15}$$

and the relative phase $\phi(t)$ as

$$\phi(t) = \theta_{\text{left}} - \theta_{\text{right}}, \qquad \phi(t) \in [0, 2\pi]. \tag{2.16}$$

After additionally rescaling the time $t \to \frac{2K}{\hbar}t$ to a dimensionless quantity, we can express equations (2.10) and (2.11) using (2.15) and (2.16):

$$\dot{z}(t) = -\sqrt{1 - z^2(t)}\sin\phi(t) \tag{2.17}$$

and

$$\dot{\phi}(t) = \Delta E + \Lambda z(t) + \frac{z(t)}{\sqrt{1 - z^2(t)}}\cos\phi(t). \tag{2.18}$$

These two equations completely describe the dynamics of the coupled system. The right hand side of (2.18) describes the chemical potential difference through $\Delta\mu = -\hbar\dot{\phi}$. Different regimes of stable solutions of (2.18) and (2.17) are identified by the dimensionless parameters ΔE and Λ and will be discussed in the following:

$$\Delta E = \frac{(E^0_{\text{left}} - E^0_{\text{right}})}{2K} + \frac{U_{\text{left}} - U_{\text{right}}}{4K}N \tag{2.19}$$

$$\Lambda = \frac{UN}{2K}, \quad \text{with} \quad U \equiv \frac{U_{\text{left}} + U_{\text{right}}}{2} \tag{2.20}$$

where ΔE takes into account a potential asymmetry of the double well and Λ describes the strength of the (nonlinear) interaction energy, both compared to the coupling energy. The total (rescaled) energy of the system can be expressed entirely with the new generalized coordinates $z(t)$, $\phi(t)$ and the parameters ΔE, Λ:

$$H = \frac{\Lambda z^2}{2} + \Delta E z - \sqrt{1 - z^2}\cos\phi. \tag{2.21}$$

The coordinates $z(t)$ and $\phi(t)$ can be identified with classical conjugated variables for momentum and position:

$$\dot{z} = -\frac{\partial H}{\partial \phi} \quad \text{and} \quad \dot{\phi} = \frac{\partial H}{\partial z}. \tag{2.22}$$

Starting from (2.18) and (2.17), the description of the bosonic weak link Josephson junction can be fully mapped to the mechanical analogon of a momentum shortened pendulum [53] in contrast to a rigid pendulum in the case of superconducting Josephson junctions [54].

To analyze different regimes for the bosonic weak link Josephson junction, we will concentrate in the symmetric double well where $E^0_{\text{left}} = E^0_{\text{right}}$ and $U_{\text{left}} = U_{\text{right}} \equiv U$. Consequently, $\Delta E = 0$ and we obtain the simplified equations of motion

$$\dot{z}(t) = -\sqrt{1 - z^2(t)}\sin\phi(t) \tag{2.23}$$

$$\dot{\phi}(t) = \Lambda z(t) + \frac{z(t)}{\sqrt{1 - z^2(t)}}\cos\phi(t). \tag{2.24}$$

Already the symmetric double well, in the absence of damping or finite temperature effects, gives rise to a rich scenery of stable modes: five different regimes are usually identified in the literature, characterized by the time averages $\langle z\rangle$ and $\langle\phi\rangle$ of the system coordinates [53]. Some of these modes do only exist due to the momentum dependence of the pendulum length, expressed in the $\sqrt{1 - z^2}$ term in (2.21). These modes do not occur in superconducting Josephson junctions, they have not yet been experimentally observed [55] in the bosonic system.

Here we will only discuss three main regimes, identified by the ratio Λ of interaction energy to coupling energy, a more refined analysis, taking into account damping and double well imbalances can be found in [53].

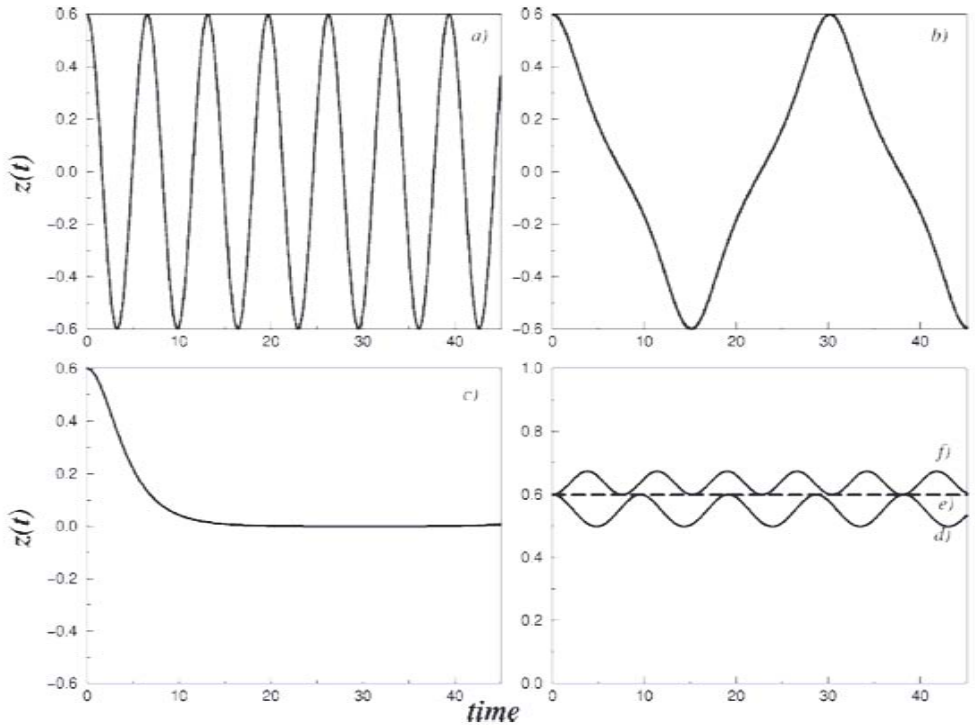

Figure 2.2: Double well population imbalance $z(t)$ as a function of dimensionless time $2Kt$ (in units of $\hbar$). The initial conditions are $z(0) = 0,6$ and $\phi(0) = \pi$. Λ takes the values (a) 0,1; (b) 1,1; (c) 1,111; (d) 1,2; (e) 1,25 and (f) 1,3. Further descriptions in the text. Figure from [50].

The Rabi regime

For $\Lambda < 1$ or, equivalently, $\delta > \mu$, the effect of interactions can be neglected in the description of the tunnel dynamics: the equations (2.23) and (2.24) describe sinusoidal Rabi oscillations between the two traps with a frequency $\omega_R = \delta = (2/\hbar)K$. These oscillations are equivalent to the single particle dynamics, their amplitude corresponds to the initially prepared population imbalance, that causes the evolution (see figure (2.2a)). The time average of the population imbalance vanishes ($\langle z \rangle = 0$), the time average $\langle \phi \rangle$ of the relative phase can be either $\langle \phi \rangle = 0$ (*zero-phase modes*) or $\langle \phi \rangle = \pi$ (π-*phase-modes*).

The Josephson regime

For $1 < \Lambda < \Lambda_c$, interactions become more important in the system dynamics. Small amplitude (plasma) oscillations mainly get shifted to higher oscillation frequencies [55]:

$$\omega_{\text{Josephson}} = \sqrt{2UNK/\hbar + \delta_{\text{Rabi}}^2} \tag{2.25}$$

independent of the initial conditions of the system. For large amplitude oscillations, higher harmonics mix to the sinusoidal oscillations (see figure (2.2b)). The period of such oscillations increases and undergoes a critical slowing down (see figure (2.2c)) with a logarithmic divergence at $z(0) = z_c$ or $\Lambda = \Lambda_c$ with

$$\Lambda_c = \frac{1 + \sqrt{1 - z(0)^2}\cos\phi(0)}{z(0)^2/2}, \tag{2.26}$$

$$z_c = \frac{2}{\Lambda}\sqrt{\Lambda - 1}. \tag{2.27}$$

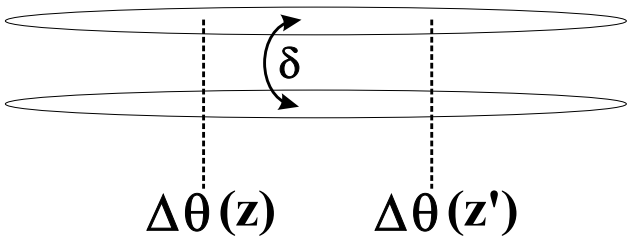

Figure 2.3: Elongated quasi 1D Bose-Einstein condensates are coupled via tunnel coupling δ along their entire length. Longitudinal phase fluctuations lead to combined phase dynamics in the transverse and the longitudinal direction.

These effects occur for both, zero-phase-modes and π-phase-modes.

Macroscopic quantum self trapping

For $\Lambda > \Lambda_c$ or $z(0) > z_c$, an initially prepared population imbalance becomes trapped, the system undergoes (small amplitude) number oscillations around this imbalance (see figure (2.2d)), which relaxes to equilibrium on a very long timescale [56]. Several versions of this macroscopic quantum self trapping exist, which are again characterized by the time average $\langle\phi\rangle$: *running-phase modes* of self trapped systems occur directly for $\Lambda > \Lambda_c$ [55], for even stronger interactions, the self trapped system makes a transition to a π-phase-mode (see figure (2.2f)).

2.1.3 Beyond the two modes model: phase fluctuations and instabilities

So far, the description of the two modes model and the tunnel dynamics has been completely one-dimensional. As this manuscript mainly deals with very elongated condensates transversally coupled along their entire length (see figure (2.3)), the coupling is essentially one dimensional: It has been verified numerically, that the two transverse degrees of freedom are well decoupled, the two modes model is not affected by the second transverse spatial dimension.

In contrast, taking into account the third, longitudinal direction necessarily violates the two modes assumption, as longitudinal modes are of low energy and can not be neglected in the dynamics ($\hbar\omega_\parallel \ll \hbar\delta \ll \hbar\omega_\perp$). We will briefly resume the influence of longitudinal modes on the tunnel dynamics.

Relative phase fluctuations in coupled elongated condensates

At non-zero temperature, thermally excited longitudinal phase fluctuations may be present in the elongated (quasi) condensates, as described in section 1.3. These fluctuations tend to reduce the phase coherence between the condensates, washing out the signal in an interference experiment as presented in part 3 of the manuscript. In contrast, a tunnel coupling between the condensates locally favors identical phase; interference may be observed, even when the phase fluctuates along the cloud. At thermal equilibrium, the correlation function of relative phase fluctuations for two coupled 1D gasses has been found as [57]

$$\langle\Delta\theta(z)\Delta\theta(z')\rangle = \frac{k_B T}{2n_{1\mathrm{D}}\hbar}\sqrt{\frac{m}{\hbar\delta}}\exp\left[\frac{-2\sqrt{m\hbar\delta}|z-z'|}{\hbar}\right] \tag{2.28}$$

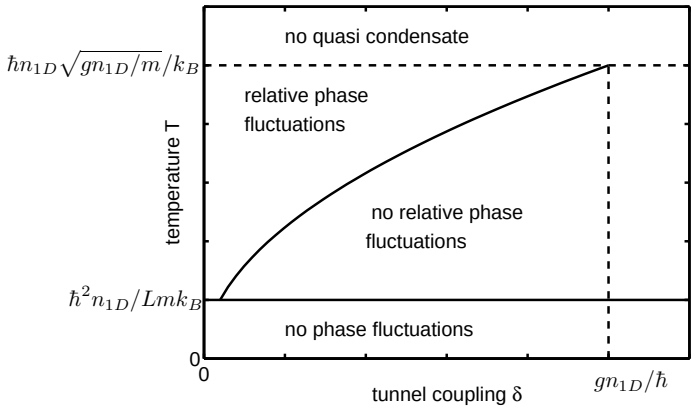

Figure 2.4: Phase diagram for the fluctuations of the relative phase between two condensates. Phase fluctuations are reduced by tunnel coupling for temperatures below $\hbar n_{1\mathrm{D}}\sqrt{\hbar\delta/m}/k_B$.

where $n_{1\mathrm{D}}$ is the 1D longitudinal density. Phase fluctuations are small when

$$k_B T \ll n_{1\mathrm{D}}\hbar\sqrt{\frac{\hbar\delta}{m}}. \tag{2.29}$$

As schematic phase diagram of the system is shown in figure (2.4): for temperatures above $\hbar n_{1\mathrm{D}}\sqrt{g_{1\mathrm{D}}n_{1\mathrm{D}}/m}/k_B$, no quasi condensate exists; below $\hbar^2 n_{1\mathrm{D}}/Lmk_B$ phase fluctuations are suppressed. Here, $g_{1\mathrm{D}} = 2\hbar\omega_\perp a$ is the one-dimensional coupling constant. For temperatures larger than $\hbar n_{1\mathrm{D}}\sqrt{\hbar\delta/m}/k_B$, each condensate has individual longitudinal phase fluctuations. The above description reflects a "steady state" picture, where phase dynamics are assumed to be slow. In the case of significant tunnel coupling (*e.g.* Rabi/Josephson oscillations) or a rapid variation thereof (*e.g.* dynamic splitting of a condensate), the time phase evolution in the longitudinal direction has to be compared to the transverse time scale. In the case of dynamic splitting, the longitudinal phase evolves independently in both condensates, once the tunnel coupling is negligible. For a fixed position z along the condensate, we find

$$\langle[\theta(0)-\theta(t)]^2\rangle = \frac{k_B T}{2\hbar^2}\sqrt{\frac{m g_{1\mathrm{D}}}{n_{1\mathrm{D}}}}t. \tag{2.30}$$

For experiments as presented in part 3 of this manuscript, the time to completely wash out a relative phase information along the split condensates is on the order of $1-3\,\mathrm{ms}$. A reduction of fringe contrast on this timescale has indeed been observed in interference experiments in Heidelberg (see section 9.2.4)

Modulational instabilities in coupled elongated condensates

Even at zero temperature, longitudinal modes get excited due to the nonlinearity in the tunnel coupling. It has been shown [58] that the uniform Josephson mode, where all atoms simultaneously oscillate between the two wells (independent of their longitudinal position), is unstable and decays to modes of non-zero longitudinal momentum. The timescale of this decay can be estimated by linearizing the equations of motion (2.23) and (2.24) in the weakly coupled Josephson regime where $\hbar\delta \ll n_{1\mathrm{D}}g_{1\mathrm{D}}$:

$$\Gamma = 0,122\,\Theta_{\mathrm{osc}}^2\sqrt{\hbar\delta n_{1\mathrm{D}}g_{1\mathrm{D}}}/\hbar = 0,122\,\Theta_{\mathrm{osc}}^2\,\omega_{\mathrm{Josephson}}/2. \tag{2.31}$$

Depending on their amplitude Θ_{osc}, only few uniform Josephson oscillations can be observed (see figure (2.5)) before energy is transferred to longitudinal modes of long wave vectors k. As

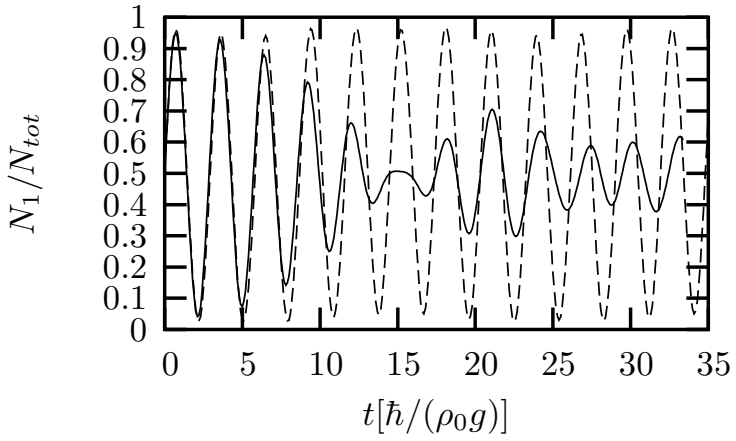

Figure 2.5: Amplitude of the uniform Josephson mode. Due to nonlinear coupling to longitudinal modes, the uniform Josephson mode decays and re-appears in a damped revival in a homogeneous 1D system (solid line). The mode can be stabilized by restricting the longitudinal size of the system (dashed line). Image from [58].

discussed in [58], the uniform mode reappears in a damped revival. The longitudinal mode, which will receive most of the energy is of wave vector

$$k_{\max} = 0.97 \frac{\sqrt{m\hbar\delta}}{\hbar}\Theta_{\rm osc}. \tag{2.32}$$

Excitation of longitudinal modes may therefore be suppressed by reducing the longitudinal size L of the system and thereby introducing a frequency cutoff at $2\pi/L$. For

$$L < \frac{h}{\sqrt{m\hbar\delta}\Theta_{\rm osc}} \tag{2.33}$$

stable Josephson oscillation can be observed (see figure (2.5)). In a harmonic trapping geometry, this corresponds to a longitudinal trap frequency of

$$\omega_{\parallel} > \alpha\Theta_{\rm osc}\sqrt{\hbar\delta n_{\rm 1D} g_{\rm 1D}}/\hbar = \alpha\Theta_{\rm osc}\omega_{\rm Josephson}/2, \tag{2.34}$$

where α is a numerical factor close to unity. This imposes strong constrains on the actual choice of parameters, when implementing an experiment aiming for the observation of the uniform Josephson mode, as will be discussed in part 2 of this manuscript.

2.2 The dynamic double well

We will now focus on the dynamics of a Bose-Einstein condensate trapped in a double well potential with a dynamically rising barrier. This Problem has caused some controversy in the recent literature [41, 42, 44]: in [41], Javanainan and Wilkens analyzed the condensate splitting in two steps: first, the potential barrier is raised slowly (adiabatic with respect to the Josephson plasma frequency) and then suddenly is increased to infinity (and then the system is probably left alone to evolve for an additional time). There has been a debate [42] on the timescale, on which the system looses its "phase memory" in the second stage (see section 1.4.3). The crucial point in the discussion are the number and phase fluctuations of the ground state of the system [44], which have been determined numerically. This two-step scheme circumvents the problem of the unavoidable breakdown of adiabaticity [59] when dynamically splitting a BEC by rising a potential barrier. In the following we will briefly describe a continuous splitting of the condensate.

2.2.1 The quantum phase model

As pointed out in [60], a two modes mean field theory as presented in section 2.1.2 is well suited to describe the "Josephson-related" effects in a static double well, it fails to describe the "number squeezing effects" necessary to understand the dynamic evolution of the quantum phase. The dynamic splitting of a condensate is therefore described in a more appropriate quantum phase two modes model in [59] and will be resumed in the following.

We assume a Bose-Einstein condensate of zero temperature in a symmetric, tunable double well potential $V_{\mathrm{trap}}(r,t)$. The second quantization Hamilton for bosons interacting with a δ pseudo potential (compare section 1.2.1) is given by

$$\hat{H}(t) = \int dr\, \hat{\Psi}^\dagger(r,t) \left(-\frac{\hbar^2}{2m}\frac{\partial^2}{\partial r^2} + V_{\mathrm{trap}}(r,t) \right) \hat{\Psi}(r,t) + \frac{g}{2} \int dr\, \hat{\Psi}^\dagger(r,t)\hat{\Psi}^\dagger(r,t)\hat{\Psi}(r,t)\hat{\Psi}(r,t), \tag{2.35}$$

where $\hat{\Psi}$ is the bosonic field operator and $g = 4\pi\hbar^2 a/m$ the interparticle interaction strength. The two modes ansatz reads

$$\hat{\Psi}(r,t) = \Phi_1(r,t)\hat{a}_1 + \Phi_2(r,t)\hat{a}_2 \tag{2.36}$$

where $\Phi_{1,2}(r,t) = \Phi_{\mathrm{left,right}}(r,t)$ as constructed in (2.2) and (2.3). The operator $\hat{a}^\dagger_{1,2}$ ($\hat{a}_{1,2}$) creates (destroys) a particle in the mode 1,2 respectively.

As shown by Menotti and Stringari in [29], the internal and external dynamics described by (2.35) can be decoupled [61]. The timescale of external dynamics τ_z is given by the trap oscillation frequency ω_0 as $\tau_z = 2\pi/\omega_z$. If the potential barrier is raised on a timescale $\Delta t \gg \tau_z$, the process is adiabatic which respect to the external dynamics and excitations are suppressed. The timescale of internal dynamics τ_r is given by the phase coherence revival time (1.69) and is beyond the reach of current experiments. We will therefore consider $\tau_z \ll \Delta t \ll \tau_r$ and concentrate on the breakdown of adiabaticity with respect to the internal phase dynamics.

Injecting the two modes ansatz (2.36) into (2.35), one obtains

$$\hat{H} = \frac{E_c}{4}(\hat{a}_1^\dagger\hat{a}_1^\dagger\hat{a}_1\hat{a}_1 + \hat{a}_2^\dagger\hat{a}_2^\dagger\hat{a}_2\hat{a}_2 - \frac{E_j}{N}(\hat{a}_1^\dagger\hat{a}_2 + \hat{a}_2^\dagger\hat{a}_1). \tag{2.37}$$

The operator $\hat{N} = \hat{n}_1 + \hat{n}_2 = \hat{a}_1^\dagger\hat{a}_2 + \hat{a}_2^\dagger\hat{a}_1$ describes the total number of atoms and commutes with $\hat{H}$. The quantity E_j is the *Josephson coupling energy* which can be identified with the coupling term NK used in the mean field description (compare (2.14)):

$$E_j = -N \int \left[\frac{\hbar^2}{2m}\frac{\partial\Phi_1^*(r,t)}{\partial r}\frac{\partial\Phi_2(r,t)}{\partial r} + \Phi_1^*(r,t)V_{\mathrm{trap}}(r,t)\Phi_2(r,t) \right] dr. \tag{2.38}$$

E_c describes the *one-site energy* (or *charge energy*) in analogy to the nonlinear interaction term U in (2.13):

$$E_c = 2g \int dr\, |\Phi_1(r,t)|^2 = 2g \int dr\, |\Phi_2(r,t)|^2. \tag{2.39}$$

We will use the Bargmann representation for phase states [48] to describe a general state of our two modes Hilbert space:

$$|\Phi\rangle = \int_{-\pi}^{+\pi} \frac{d\phi}{2\pi} \Psi(\phi,t)|\phi\rangle, \tag{2.40}$$

where ϕ is the relative phase between the two modes, and

$$|\phi\rangle = \sum_{n=-N/2}^{N/2} \frac{e^{in\phi}}{\sqrt{n!}}|n\rangle \tag{2.41}$$

are non-normalized vectors, written for the relative number of atoms n. In this representation, the action of any operator on $|\Phi\rangle$ can be represented in terms of differential operators acting on the associated phase amplitude $\Psi(\phi,t)$ [62].

For the Josephson regime, where $E_j \ll NE_c$, the dynamical equation for the 2π periodic phase amplitude $\Psi(\phi,t)$ is

$$i\hbar \frac{\partial \Psi(\phi,t)}{\partial t} = -\frac{E_c}{2} \frac{\partial^2 \Psi(\phi,t)}{\partial \phi^2} - E_j \cos(\phi) \Psi(\phi,t). \tag{2.42}$$

2.2.2 Breakdown of adiabaticity

Before making an ansatz for $\Psi(\phi,t)$, we will first discuss the relevant timescale in the dynamic splitting process. In experiments presented in part 3 of this manuscript (and also in [43]), the splitting is performed by moving the double well potential minima apart in space: $d(t) = d_{\rm start} + d_{\rm end} t/\Delta t$ where $d_{\rm start}$ and $d_{\rm end}$ are initial and final well separations and Δt the total ramp time. Following equation (2.6), it is reasonable to assume that the Josephson coupling E_j decays exponentially with time: $E_j(t) = E_j(0)e^{-t/\tau}$, where the effective ramping time $\tau = \Delta t\hbar/\sqrt{2m(V_0-\mu)d_{\rm end}^2}$ depends on the initial barrier height V_0 and the chemical potential μ. This of course holds only for well separated wells. In the two modes approximation, the one-site energy E_c remains approximately constant during the dynamics. During the beginning of the splitting, when the chemical potential is close to the potential barrier, the process remains adiabatic, as the strong tunnel coupling allows the system to adapt to the change of the double well potential rather rapidly. The adiabaticity will break down only at large separation of the two condensates, deep in the tunnelling regime.

In reference [59], a time dependent variational phase amplitude

$$\Psi(\phi,t) = \frac{1}{(2\pi\sigma_\phi(t))^{1/4}} \exp\left(-\frac{\phi^2}{4\sigma_\phi^2(t)} + i\frac{\delta(t)}{2}\phi^2\right), \tag{2.43}$$

of Gaussian shape and width $\sigma_\phi(t) \ll 2\pi$ is chosen. Injecting this ansatz into (2.42) one obtains an differential equation of motion for the width of the phase amplitude:

$$\ddot{\sigma}_\phi = \frac{E_c^2}{4\hbar^2}\frac{1}{\sigma_\phi^3} - \frac{E_c E_j(t)}{\hbar^2}\sigma_\phi e^{-\sigma_\phi^2/2}. \tag{2.44}$$

We now linearize and seek a solution for (2.44) of the form $\sigma_\phi(t) = \sigma_{\phi,\rm ad}(t) + \epsilon(t)$. If $\epsilon(t)$ starts to make a significant correction, we assume σ_ϕ to vary rapidly with time and adiabaticity to break down. This happens at a time $t_{\rm ad}$ for which

$$4\sqrt{E_c E_j(0)/\hbar^2}\tau e^{t_{\rm ad}/2\tau} \simeq 1. \tag{2.45}$$

With $E_j(t) = E_j(0)e^{-t/\tau}$ and the Josephson frequency $\omega_{\text{Josephson}}(t) = \sqrt{E_c E_j(t)}/\hbar$ one can rewrite (2.45) to

$$\frac{1}{\omega_{\text{Josephson}}(t_{\text{ad}})} \simeq 4\tau \tag{2.46}$$

or as explicit expression for t_{ad}:

$$t_{\text{ad}} \simeq 2\tau \ln\left(4\omega_{\text{Josephson}}(0)\tau\right). \tag{2.47}$$

Equation (2.46) has a straightforward physical meaning: Initially, the system is in the ground state, we assume $E_j(0) \gg E_c$; the phase dispersion is small: $\sigma_\phi^2(0) = 1/2\sqrt{E_c/E_j(0)} \ll 1$. By ramping the two wells, $E_j(t)$ decreases with a timescale τ. As long as $\omega_{\text{Josephson}}(t) \gg 1/\tau$, the system adjusts itself in such a way, that it stays in the ground state. After the time t_{ad}, the frequency $\omega_{\text{Josephson}}(t)$ is on the order if $1/\tau$ and it becomes impossible for the system to adjust to the ground state, the evolution becomes non-adiabatic.

2.2.3 Phase diffusion

After passing the point of non-adiabaticity in the splitting process, the phase dispersion σ_ϕ increases rapidly until it becomes of the order 1 at the dephasing time t_D. We recall, that in a single shot experiment, a well defined phase will still be measured. However, in multiple repetitions, the measured phases will differ, with a mean-square fluctuation of σ_ϕ. The width of phase dispersion can directly be measured as a reduction of contrast by a factor $e^{-\sigma_\phi/2}$ when summing up many interference images.

The dephasing time t_D is estimated in reference [59] and always found to be $t_D \gg t_{\text{ad}}$. This estimate is too complex to be discussed in this manuscript, the evolution of the phase dispersion depends delicately on the "history" of the splitting process. We find it interesting to note, that stopping the splitting process after having passed the point of non-adiabaticity "freezes" the actual relative phase and leads to a slow phase diffusion during the hold time. Stopping before adiabaticity breakdown leads to a rapid broadening of the phase distribution, comparable to an infinitely continuing splitting.

The estimated timescales for phase diffusion in recent literature [42,63,59] still presents large discrepancies, the issue of phase diffusion in a double well can not be considered closed.

Chapter 3

Magnetic micro traps

3.1 Magnetic trapping of neutral atoms

The interaction of an atomic spin $\mathbf{S}$ and an associated magnetic moment $\boldsymbol{\mu} = -g_F \mu_B \mathbf{S}/\hbar$ with an external magnetic field $\mathbf{B}$ is described by the well known Zeeman Hamiltonian [64]:

$$H_Z = -\boldsymbol{\mu} \cdot \mathbf{B} = \frac{g_F \mu_B}{\hbar} \mathbf{S} \cdot \mathbf{B}, \tag{3.1}$$

where g_F is the Landé g-factor of the atomic hyperfine state F (for ^{87}Rb $g_{F=1} = -1/2$ and $g_{F=2} = 1/2$) and μ_B the Bohr magneton. In an adiabatic system (see below) this Hamiltonian gives rise to magnetic quantum numbers $m_F = \{-F, ..., F\}$ with the corresponding eigenenergies

$$E_{m_F} = m_F g_F \mu_B |\mathbf{B}|. \tag{3.2}$$

In an inhomogeneous external magnetic field $\mathbf{B} = \mathbf{B}(\mathbf{r})$, atomic states that are aligned anti-parallel with the external field ($m_F g_F > 0$) get attracted by regions of weak local magnetic field (*low field seekers*). States that are aligned parallel to the external magnetic field get attracted by regions of strong magnetic field (*high field seekers*). States of $m_F = 0$ are not affected by (static) external magnetic fields. Neutral atoms can therefore be trapped in local (3D) maxima or minima of an appropriately designed magnetic field. According to the Maxwells equations, the creation of a 3D magnetic field maximum in free space is impossible [65]. In contrast, the creation of a 3D magnetic field minimum in free space is possible and forms the basis of almost any magnetic trapping geometry [66]. It is interesting to note, that trapped low field seeking states are usually not in the ground state of the system; the trapped state is therefore meta-stable and suffers from losses due to inelastic (spin-flipping) two- or three-body collisions.

3.1.1 Adiabaticity

For the above discussion to hold, we have to impose, that the atom moves sufficiently slowly in the external magnetic field, so that the atomic spin can adiabatically follow the direction of the external quantization axis. In a classical picture, the angle θ between the spin and the external field has to vary slowly with respect to the Lamor frequency $\omega_L = m_F g_F \mu_B |\mathbf{B}|/\hbar$:

$$\frac{d\theta}{dt} < \omega_L. \tag{3.3}$$

Adiabaticity can only be guaranteed, when there is always a well defined quantization axis, justifying the quantum number m_F. Regions of very small or vanishing field give rise to (Majorana) spin-flip transitions to different (possibly untrapped) states and have to be avoided in the design of stable atom traps [67, 68, 69].

3.1.2 Orders of magnitudes

To hold neutral atoms against gravity and to compensate the gravitational force, a magnetic field gradient

$$B'_{\text{grav}} = \frac{mg}{m_F g_F \mu_B} \tag{3.4}$$

is necessary. For ^{87}Rb in the double stretched $F = m_F = 2$ state, this gradient corresponds to 15,3 G/cm. The depth of the magnetic trap directly determines the temperature of atoms, that may be captured: again for ^{87}Rb, a trap depth of 1 G corresponds to a thermal energy of 67 μK. To directly trap rubidium atoms at room temperature, a magnetic field of 450 T would be necessary, which is beyond the reach of current experiments. In contrast, atoms that were pe-cooled by laser cooling (*e.g.* for ^{87}Rb to Doppler temperature $T = 143\,\mu$K) can easily be captured in magnetic traps of a few G depth.

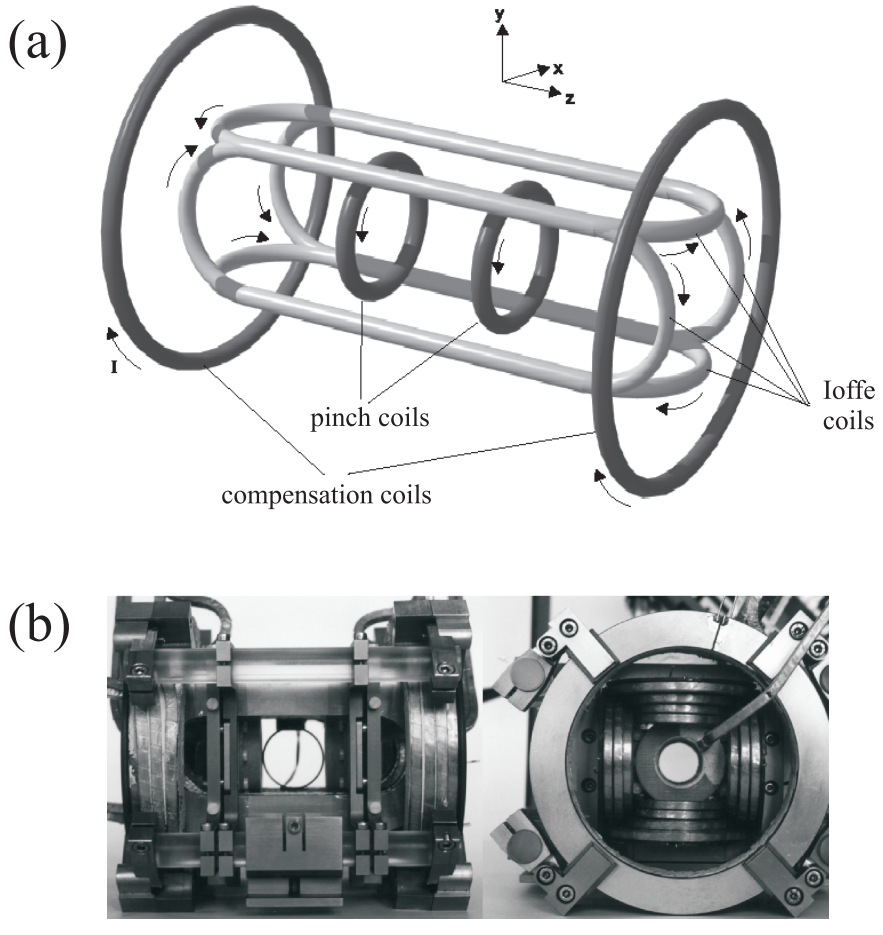

Figure 3.1: Ioffe-Pritchard trapping configuration (a) schematically and (b) picture of an implementation in Amsterdam [70].

3.2 The Ioffe-Pritchard trap

3.2.1 The magnetic field configuration

As mentioned above, for stable trapping of weak field seeking neutral atoms, a three dimensional, but non-zero magnetic field minimum has to designed. Such a magnetic field geometry is today referred to as the *Ioffe-Pritchard trap*, following a proposal of Pritchard from 1983. In [66] a linear (2D) magnetic quadrupole field to confine atoms in two (transverse) direction is combined with a homogeneous longitudinal field which has a slight superimposed trapping curvature ("magnetic bottle"). A similar configuration has already been used in 1962 by Ioffe and coworkers to magnetically confine plasmas [71]. Today, a huge zoology of trapping configurations, all based on the same principle, are in use (see [72] for a review).

The most common realization of the Ioffe-Pritchard trap is schematically depicted in figure (3.1a): the transverse confinement is provided by currents running through so-called *Ioffe-bars*, creating a linear quadrupole field in the transverse plane:

$$\mathbf{B}_{\text{bars}} = \begin{pmatrix} B'x \\ -B'y \\ 0 \end{pmatrix}, \tag{3.5}$$

where B' is the gradient in the transverse direction. The longitudinal confinement is provided by two *pinch coils* which carry equal current in the same sense and are separated by more than their diameter. This gives rise to a magnetic field minimum $\mathbf{B}_{\text{offset}}$ on the symmetry axis (between the coils), the field created writes

$$\mathbf{B}_{\text{pinch}} = \frac{1}{2} \begin{pmatrix} -B''xz \\ -B''yz \\ 2B_{\text{offset}} + B''(z^2 - \frac{1}{2}(x^2+y^2)) \end{pmatrix}, \tag{3.6}$$

where B'' is the curvature of the longitudinal trapping field. The longitudinal offset field in the center of the trap is rather large, unnecessarily reducing the trap depth. To reduce the offset field to the so-called *Ioffe field* B_0 (see next section), two *compensation coils* in Helmholtz configuration create a homogeneous field in opposite direction. The total magnetic field of the Ioffe-Pritchard trap is

$$\mathbf{B}_{\text{I.P.}}(\mathbf{r}) = B_0 \begin{pmatrix} 0 \\ 0 \\ 1 \end{pmatrix} + B' \begin{pmatrix} x \\ -y \\ 0 \end{pmatrix} + \frac{B''}{2} \begin{pmatrix} -xz \\ -yz \\ z^2 - \frac{1}{2}(x^2+y^2) \end{pmatrix}. \tag{3.7}$$

The movement of an atom is this trapping field is characterized by the transverse and the longitudinal (harmonic) oscillation frequencies $\omega_\perp$ and $\omega_\parallel$:

$$\omega_\perp = \sqrt{\frac{m_F g_F \mu_B B'^2}{m B_0}} \quad \text{and} \quad \omega_\parallel = \sqrt{\frac{m_F g_F \mu_B B''}{m}}. \tag{3.8}$$

In most cases, $\omega_\perp \gg \omega_\parallel$. The harmonic approximation is very good in the longitudinal direction, in the transverse direction, hot atoms experience the linear region of the trapping potential, once $r = \sqrt{x^2+y^2} > B_0/B'$.

3.2.2 Majorana losses in a trap

As described above, the movement of the trapped atom in the external potential has to be slow with respect to the Lamor frequency, in order to suppress non adiabatic spin flips. We define

the adiabaticity parameter α as:

$$\alpha \equiv \frac{\omega_L}{\omega_\perp} = \frac{m_F g_F \mu_B B_0}{\hbar \omega_\perp}. \tag{3.9}$$

The rate for non-adiabatic spin flips γ has been estimated [69] to

$$\gamma = 4\pi\omega_\perp e^{-2\alpha}. \tag{3.10}$$

To obtain a desired lifetime $\tau = 1/\gamma$ in a specific trap of frequency $\omega_\perp$, a minimum Ioffe field B_0 of

$$B_0 \geq \frac{\hbar\omega_\perp}{2m_F g_F \mu_B} \ln(4\pi\omega_\perp \tau) \tag{3.11}$$

has to be chosen. For a trap of $\omega_\perp = 2\pi \times 1\,\mathrm{kHz}$ and a (e.g. background gas limited) lifetime of 100 s, the necessary Ioffe field to suppress spin flips is of the order milligauss. In practice, as technical noise of frequencies up to 500 kHz drives unwanted transitions, a Ioffe field of $B_0 \simeq 1\,\mathrm{G}$ (effectuating a frequency cutoff at 700 kHz) is often used in experiments.

3.2.3 Orders of magnitudes

To efficiently cool atoms to quantum degeneracy, a high elastic collision rate and therefore a high atomic density is necessary. Therefore, the magnetic trap has to provide strong confinement. A figure of merit is the mean harmonic oscillator trap frequency $\omega_{\mathrm{ho}} = (\omega_\perp^2 \omega_\parallel)^{1/3}$, which has to be on the order of $2\pi \times 100\,\mathrm{Hz}$. To realize this in a Ioffe-Pritchard trap, based on (macroscopic) coils and rods, high currents are necessary. As an example, figure (3.1b) shows a Ioffe-Pritchard trap realized in Amsterdam [70]. Using coils carrying 400 A this setup reaches $\omega_{\mathrm{ho}} = 2\pi \times 170\,\mathrm{Hz}$ ($\omega_\perp = 2\pi \times 485\,\mathrm{Hz}$ and $\omega_\parallel = 2\pi \times 22\,\mathrm{Hz}$). The total power dissipated in the coils is 5,4 kW. The next chapter will show, how much stronger confinement can be reached using wire traps, carrying only a few Amperes current and dissipating around 1 W of power.

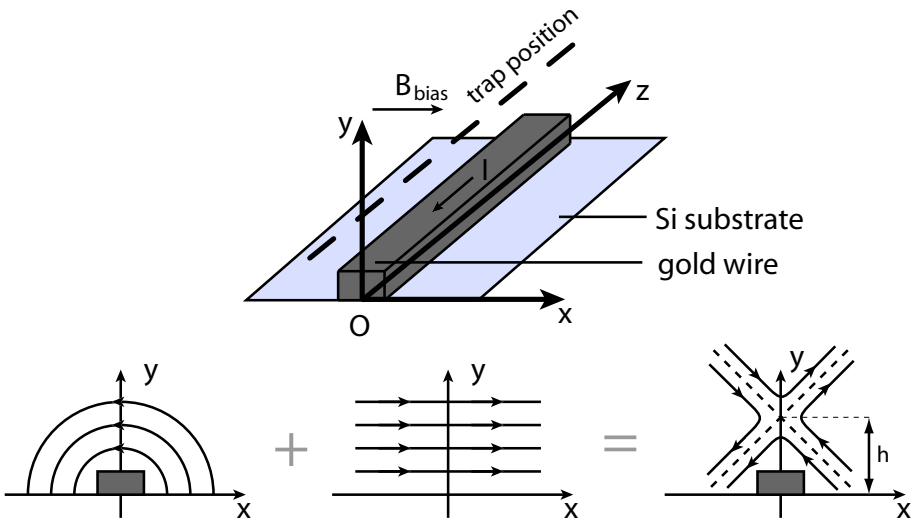

Figure 3.2: Schematic operation principle of the side wire guide. A circular magnetic field created by a current carrying wire is superimposed to a homogeneous (external) bias field. The two fields chancel on a line of distance h from the wire (picture from [73])

3.3 Wire traps

In 1995 it has been proposed [74, 75] to use magnetic field created by current carrying wires directly under vacuum to create strongly confining magnetic traps and complex trapping geometries. Soon afterwards, first experiments were carried out using freestanding macroscopic wire structures [76, 77, 78, 79]. These wire structures were miniaturized and integrated to complex patterns using techniques from microelectronics and chip fabrication. It was shown, that Bose-Einstein condensates can be created very efficiently on such *atom chips* [80, 81, 82].

In the following section, we will mainly concentrate on the most basic element of atom chip based wire traps, the so called *side wire guide*.

3.3.1 The side wire guide

Consider an infinitely thin, infinitely long straight wire, carrying a current I (see figure (3.3.1)). This current creates a circular magnetic field $\mathbf{B}_{\text{wire}}$ with $|\mathbf{B}_{\text{wire}}| = \mu_0 I/(2\pi r)$ at a distance r around the wire. To this circular field we now superimpose a homogeneous magnetic *bias field* $\mathbf{B}_{\text{bias}}$ (*e.g.* created by large, external coils) perpendicular to the wire. The two fields will cancel at a distance

$$h = \frac{\mu_0}{2\pi}\frac{I}{|\mathbf{B}_{\text{bias}}|} \tag{3.12}$$

from the wire, creating a two dimensional magnetic minimum of vanishing magnetic field in the plane transverse to the wire; trapped atoms are confined on a line (guide) along the wire (see figure (3.2)). Around the zero, the magnetic field can be well approximated by a linear quadrupole:

$$B_x = B'(y-h) \quad \text{and} \quad B_y = B'x \tag{3.13}$$

with a gradient

$$B' = \frac{|\mathbf{B}_{\text{bias}}|}{h} = \frac{2\pi}{\mu_0}\frac{B_{\text{bias}}^2}{I}. \tag{3.14}$$

This field is identical (to first order) to the corresponding field (3.5) created by the Ioffe bars in a standard Ioffe-Pritchard trap. We will see in the following, that the gradients created by wire traps can be orders of magnitiudes lager than in conventional macroscopic setups.

Finite size effects

As can be easily seen from (3.14), the gradient (and thus the confinement of the atoms) can be increased by reducing the distance h to the wire. Any physical implementation of this scheme involves wires of finite (non-zero) dimensions. When the distance of the atoms to the wire becomes on the order of the wire dimensions, these have to be taken into account, when calculating the magnetic fields.

We assume a wire of rectangular cross section (see figure (3.4)) of width W and height U. We will calculate the field on the (O, y)-axis, where the magnetic field created by the wire only has a component in the perpendicular x direction. By integrating the Biot-Savart law over the spatial extension of the wire one obtains:

$$B_x = \frac{\mu_0}{2\pi}\frac{I}{WU}\left[(U+2y)\arctan\left(\frac{W}{U+2y}\right) - (U-2y)\arctan\left(\frac{W}{U-2y}\right) + \frac{W}{2}\left(1+\frac{8Uy}{W^2+(U-2y)^2}\right)\right]. \tag{3.15}$$

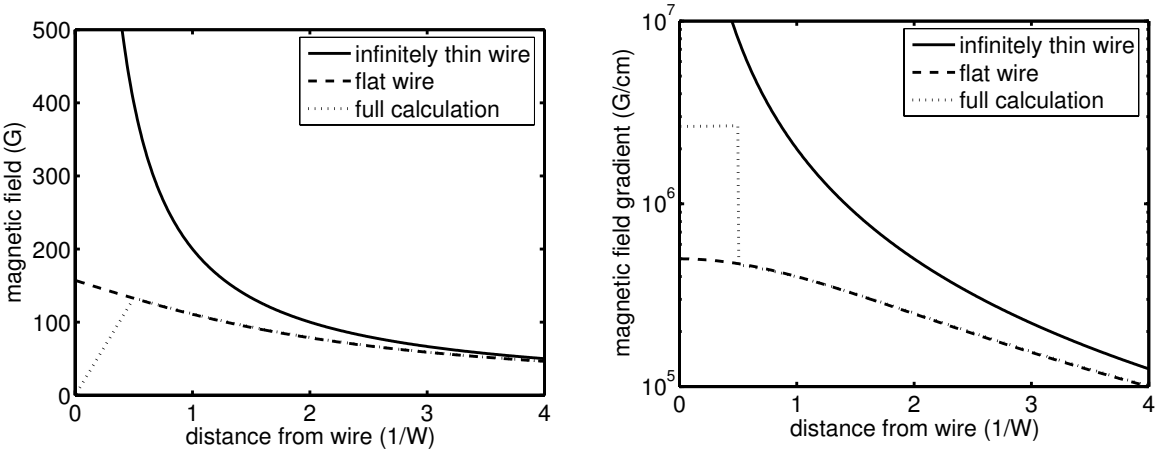

Figure 3.3: Effect of finite wire dimensions on magnetic field (left) and field gradient (right) in a wire trap. A wire of $W = 2\,\mu$m width and $U = 1\,\mu$m height carries a current of $I = 100\,$mA. The solid line indicates the result for an infinitely thin wire, the dotted line is the complete finite size result. The dashed line indicates the approximation of a flat wire.

In the case of a flat wire ($W \gg U$), this expression can be developed to first order in W/y:

$$B_x = \frac{\mu_0 I}{\pi W} \arctan\left(\frac{W}{2y}\right). \tag{3.16}$$

Figure (3.3) compares the magnetic field calculated for an infinitely thin wire to the exact expression (3.15) and the simplified expression for a flat wire (3.16). As can be seen in the figure, the flat wire approximation is already very good for $W = 2U$. Finite size effects have to be taken into account, once the distance between wire and atoms is about 2-3 times the wire width: while the field of an infinitely thin wire diverges at small distances, the field of a finite size wire saturates and reaches a value of

$$B_{\mathrm{sat}} = \frac{\mu_0}{2\pi}\frac{I}{WU}\left[2U \arctan\left(\frac{W}{2U}\right) + W \log\left(1 + \frac{4U^2}{W}\right)\right] \simeq \frac{\mu_0 I}{2W} \tag{3.17}$$

at the surface of the wire, the last expression is for a flat wire. As can be seen in figure (3.3), also the magnetic field gradient saturates, when $h \simeq W$. The maximum gradient that can be created with a (flat) wire carrying a current I is therefore

$$B'_{\mathrm{max}} \simeq \frac{\mu_0}{2\pi}\frac{I}{W^2}. \tag{3.18}$$

We will now analyze, how the wire dimensions determine the maximum current I that can be send through the wire.

Critical wire currents

The maximum current in a wire is determined by the dissipation of ohmic heat generated in the conductor. It may vary significantly, depending on the actual realization of the wire trap. In the following, we will describe a model which is valid for both the Heidelberg and the Orsay atom chip experiment presented in this manuscript. Figure (3.4) schematically shows the physical system: a gold wire of rectangular cross section (width W and heigth U) is fabricated on an atom chip carrier substrate (Si). To electrically isolate the wire from the (semiconducting) silicon, the substrate is covered by a thin (200-500 nm) insolation layer of silicon oxide (SiO_2).

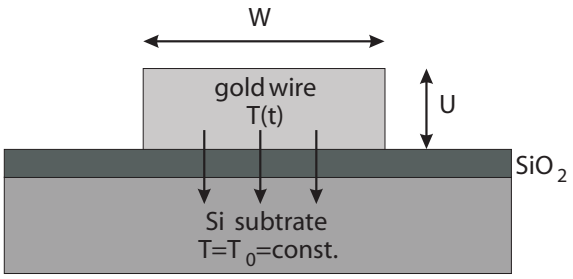

Figure 3.4: Schematic representation of heat transport from the gold wire to the Si chip substrate at fixed temperature.

The substrate is in good thermal contact with a heat sink, we can assume it at constant (room) temperature $T_0 = 293\,\mathrm{K}$. At all times $t > 0$, the wire is in thermal equilibrium with the heat sink: $T(t < 0) = T_0$. At $t = 0$ we turn on a current I. Due to the non-zero resistance ρ of the wire, its temperature increases as

$$T(t) = T_0 + \frac{j^2 \rho_0 U}{\kappa - \alpha \rho_0 j^2 U} \left(1 - e^{-t/\tau}\right) \quad \text{with} \quad \tau = \frac{UC}{\kappa - \alpha \rho_0 j^2 U}, \tag{3.19}$$

where j is the current density, $\rho = \rho_0(1 + \alpha(T - T_0))$ the wire resistance and C the gold heat capacity. κ describes the heat conductance from the gold through the insolation layer into the heat sink. It has been measured for the Heidelberg setup [83] to $\kappa = 3,5 \times 10^6\,\mathrm{W/Km^2}$ [84].

If $\tau < 0$ the wire temperature diverges with time, which leads to the destruction of the wire. The condition $\tau > 0$ directly leads to a definition of the critical current density $j_{\mathrm{crit}} = \sqrt{\kappa/(\alpha \rho_0 U)}$ or the total critical current

$$I_{\mathrm{crit}} = \sqrt{\frac{\kappa U W^2}{\alpha \rho_0}}. \tag{3.20}$$

For $\rho_0 = 2,2 \times 10^{-8}\,\Omega\mathrm{m}$, $\alpha = 3,8 \times 10^{-3}\,\mathrm{K}^{-1}$ and $C = 2,5 \times 10^6\,\mathrm{J/Km^3}$ and a $U = W = 1\,\mu\mathrm{m}$ square cross section wire, the critical current is $I_{\mathrm{crit}} \simeq 200\,\mathrm{mA}$.

Scaling laws

As seen in the last section, the maximum current is determined exclusively by material parameters and the wire dimensions. Combining equation (3.20) and (3.18), we obtain the maximum gradient for a wire trap located at a distance $h = W$

$$B'_{\mathrm{max}} = \frac{\mu_0}{\pi} \sqrt{\frac{\kappa}{\alpha \rho_0}} \frac{U^{1/2}}{W}. \tag{3.21}$$

For a square cross section wire ($W = U$) the gradient scales as $B' \propto 1/\sqrt{W}$. This indicates, that by reducing the structure size and using smaller wires, simultaneously reducing the wire current, the confinement of the atoms can be increased. This motivates ongoing efforts on miniaturizing trapping structures on atom chips.

The $1\,\mu\mathrm{m}$ square cross section wire carrying 200 mA current will produce a gradient of $\sim 10^7\,\mathrm{G/cm}$, which is orders of magnitudes higher than what can be obtained with macroscopic systems (*e.g.* a transverse gradient of $350\,\mathrm{G/cm}$ in the setup shown in figure (3.1)).

It is interesting to note, that in principle also the transverse oscillation frequency is fixed by the wire geometry: as can be seen in equation (3.8), $\omega_\perp \propto B'/\sqrt{B_0}$. As the Ioffe field B_0 has to

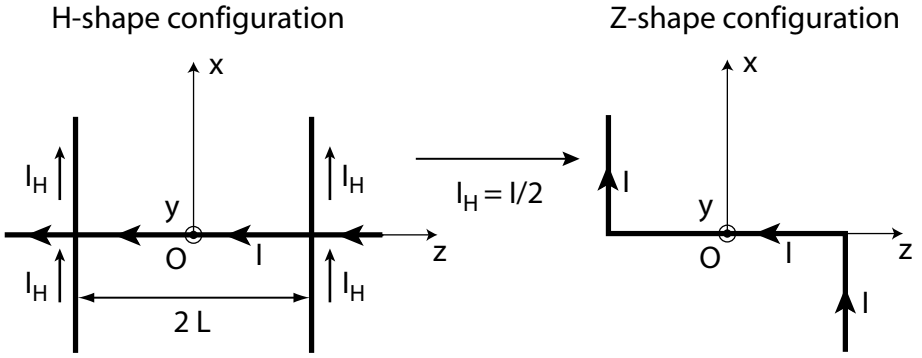

Figure 3.5: Schematic representation of the H shape wire structure used in the Orsay setup and the Z shape structure used in the Heidelberg experiments. The description carried out for the H structure can be applied to the Z shaped system by replacing $I_H \rightarrow I/2$.

be chosen according to equation (3.11) in order to suppress spin flip losses, only depending on the trap frequency and the desired lifetime in the trap, the wire geometry fixes the maximum trap frequency. The 1 μm at maximum current and minimal Ioffe field (to hold the atoms for 1 h) will create trap frequencies on the order MHz. As we will see in section 3.4, technical and fundamental effects will prevent such high trap frequencies, as surface effects perturb the magnetic trap, when brought very close to the wire.

3.3.2 A Ioffe-Pritchard trap with wires

To provide trapping in all three spatial dimensions and avoid spin flip losses due to vanishing magnetic field at the trap minimum, an appropriate longitudinal trapping field has to be designed for the side wire guide. Analogous to the Ioffe-Pritchard configuration, this could be done by additional pinch and compensation coils. It is also possible and more convenient to use magnetic fields created by additional wired to create the longitudinal confinement. The most simple and most commonly used technique is to bend the trapping wire to a Z-shape, as indicated in figure (3.5). Here, the longitudinal confinement is provided by the same current, that (together with the external bias field B_{bias}) also realized the trapping in the transverse plane [85].

In experiments presented in this manuscript, the Z-shaped configuration will be used as well as an H-shaped wire structure, which allows for independent control of the transverse and the longitudinal confinement. The following description will focus on the latter H-shape structure, expressions for trapping position and trap frequencies can be transferred to the Z-shape case by replacing the current I_H in the "input leads" of the H by $I_Z = I_H/2$ (see figure (3.5)).

We assume the input leads of the H-structure carrying identical current I_H in the same direction, as indicated in figure (3.5). We will concentrate on the additional magnetic fields created by these currents on the line of vanishing field of the side guide ($x = 0, y = h$). Around the origin ($|z| \ll L$) and for $h \ll L$, the two lead wires create a field along z with a non-zero minimum at $z = 0$, replacing the pinch coils in a standard Ioffe-Prichard configuration. In contrast to the macroscopic setup, the field created at the minimum is rather small. Usually, external coils producing an homogeneous magnetic field $B_{0.z}$ along z are used to increase the field at the minimum position to B_0.

The field produced by the currents in the input leads of the H-structure is (to first order) a linear quadrupole field in the (O, y, z) plane, with primary axes turned by $\pi/4$:

$$\left.\begin{array}{l} B_y = B'_H z \\ B_z = B'_H y \end{array}\right\} \quad \text{where} \quad B'_H = \frac{\mu_0}{\pi}\frac{I_H}{L^2}. \tag{3.22}$$

Usually, the gradient B'_H is much smaller than the transverse gradient B', we define $B'_H/B' = h^2/L^2 \equiv \alpha$. The combined (linearized) fields created by the wire currents I and I_H and the homogeneous external fields B_{bias} and $B_{0,z}$ writes:

$$\begin{aligned} B_x &= B'(y-h) \\ B_y &= B'x + B'_H z \\ B_z &= B'_H y + B_{0,z}. \end{aligned} \tag{3.23}$$

By symmetry, the minimum of the combined magnetic field is located on the $(x = z = 0)$ line, where the quadratic field norm writes

$$|\mathbf{B}|^2 = B'^2(y-h)^2 + (B'_H y + B_{0,z})^2. \tag{3.24}$$

The trap distance from the wire gets slightly reduced under the influence of the additional longitudinal fields:

$$y_{\min} = h - \frac{B'^2_H h + B'_H B_{0,z}}{B'^2 + B'^2_H}. \tag{3.25}$$

The additional fields do also slightly turn the principal axes of the new 3D trap with respect to $\{\mathbf{e}_x, \mathbf{e}_z\}$ [86]: by calculating the Hesse matrix to determine the trap frequencies, we find off-diagonal elements. Diagonalizing this matrix gives new principal axes $\{\mathbf{e}'_x, \mathbf{e}'_z\}$, obtained by rotating $\{\mathbf{e}_x, \mathbf{e}_z\}$ by the angle $\alpha = B'_H/B' = h^2/L^2$, as defined introduced. The trap frequencies, defined as

$$\omega_i = \sqrt{\frac{m_F g_F \mu_B}{m} \frac{\partial^2 B}{\partial i^2}} \quad \text{with} \quad i = \{x', y, z'\} \tag{3.26}$$

can be determined from the magnetic field curvatures along the new principal axes. In the transverse direction, we recover the result of the side wire guide (zero order term):

$$\frac{\partial^2 B}{\partial x'^2} = \frac{\partial^2 B}{\partial y^2} = \frac{B'^2}{B_{0,z}} = \frac{4\pi^2 B^4_{\text{bias}}}{\mu_0^2 I^2 B_{0,z}} \tag{3.27}$$

In the longitudinal direction we find

$$\frac{\partial^2 B}{\partial z'^2} = 6\frac{B'^2_H}{B_{\text{bias}}} = \frac{3\mu_0^2 I_H^2}{2\pi^2 B_{\text{bias}} L^4} \tag{3.28}$$

The longitudinal trap frequency is usually much below the transverse frequencies giving rise to highly anisotropic traps. The trap aspect ratio is found to $\Re = \omega_\perp/\omega_\parallel = \sqrt{B_{\text{bias}}/(6B_{0,z}\alpha^2)}$. In experiments presented in this manuscript, aspect rations between 10 and 400 were realized.

The above discussion draws a simplified picture of the properties of a magnetic trap created by a current carrying H-shape structure; often, only first order dependencies are carried out, valid in the restricted region close to the trap minimum. A more thorough description of the magnetic field configuration discussed here can be found in [73, 87].

3.3.3 Complex geometries

The freedom to design almost arbitrary wire patterns using lithographical techniques from micro electronics allows for the construction of increasingly complex magnetic trapping potentials, far beyond what can be realized with conventional macroscopic trapping schemes. Miniaturizing these structure leads to potential variations on the size of the trapped wave function and is therefore especially suited for the realization of atom optical elements. Consequently, there exists a vast numbers of proposals for wire geometries in the context of coherent manipulation

of Bose-Einstein, see for recent reviews. In the following, we will briefly mention some of the concepts and refer to the dedicated literature.

Already the building block of magnetic micro traps, the side wire guide, offers many possibilities: by modifying or discarding the longitudinal confinement, ultra cold atoms can be released into a magnetic guide in a controlled fashion [88]. In the simple scheme presented in section 3.3.1 (a straight wire and an external magnetic bias field) the necessity of an external field reduces the flexibility of the setup. This can be overcome by using schemes involving two wires and a vertical bias field [89, 90], or completely integrated patterns where also the "external" bias field is (now locally) produced by neighboring wires [91, 92]. The transport of ultra cold atoms along curved guides has been experimentally demonstrated in [93, 89].

The need for a more controlled transport of coherent ensembles along guides has led to the development of conveyor belt structures [94, 95] which allow to separate the region where the Bose condensate is created from the region where the experiment is performed or from a detection facility.

Many schemes for the implementation of matter wave beam splitters and interferometers have been suggested [96, 97, 92]. Due to technical and fundamental problems (loss channels, surface effects, lack of adiabaticity), none of its implementations has so far succeeded to coherently manipulate a Bose-Einstein condensate.

Magnetic micro traps provides by atom chips are well suited for the integration and combination with other than magnetic potentials acting on the atoms: static electric fields have been used to implement a conveyor belt transport scheme. A Mach-Zehnder interferometer of the Bragg type has been performed in a magnetic side wire guide, the mirrors directly mounted on the chip [98]. Standing wave optical potentials using the chip as a mirror have been successfully loaded with Bose condensates in the Heidelberg group.

In part 3 of this manuscript we will demonstrate how atom optical elements can be created by a combination of static (trapping) fields and oscillating magnetic fields [99, 100]. The arising adiabatic potentials have numerous advantages [Schneewittchen] over the purely static configuration and allowed for the coherent splitting of a Bose-Einstein condensate on an atom chip [101].

In addition to creation and manipulation of matter waves, there is an ongoing effort to also integrate the detection on the atom chip. Especially high finesse cavity seem promising candidates for even single atom detection and a possible achievement of the strong coupling regime.

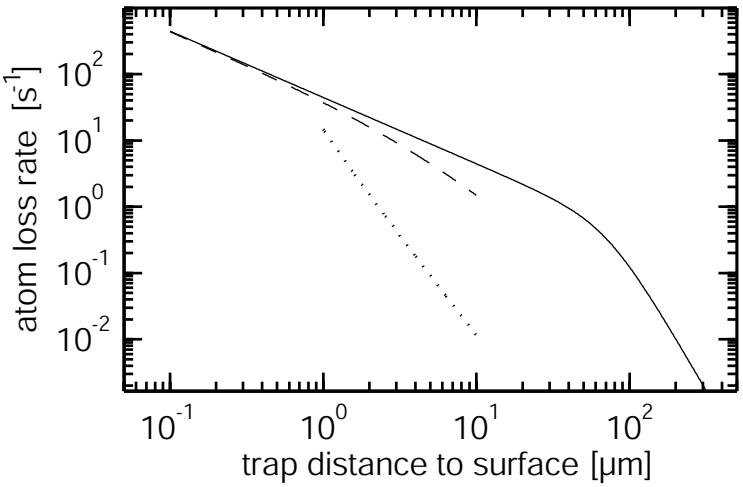

Figure 3.6: Atom loss rate due to thermally excited current in the atom chip. The solid line indicates the loss rate for a gold half space. The dotted line corresponds to a thin gold layer of 5 μm, the dotted line is for a square cross section gold wire of 700 nm width. The atoms are assumed at rest at the bottom of a magnetic trap of $B_0 = 1$ G.

3.4 Surface effects

In section 3.3.1 we described, how the magnetic field gradient and hence the confinement of atoms in a magnetic wire trap can be increased by using smaller wires and bringing the trap closer to the trapping structure. This miniaturization is limited by malicious surface effects, which will be briefly discussed in the following.

3.4.1 Johnson Noise

We recall, that the atom chip and the trapping wire itself are assumed to be at room temperature $T \simeq 300$ K. Conducting materials at non-zero temperature radiate an electromagnetic field, created by the Brownian motion of the electrons (Johnson noise). As at least the trapping wire itself consists of conducting material, this electromagnetic field can drive spin-flip transitions to untrapped states and hence cause atom loss in wire traps in the vicinity of the surface. Additional malicious effects as parametric heating of the atoms or surface induced decoherence may also be present. They are described in detail in the work of Henkel and coworkers [102,103,104,105,106]; here we will exclusively consider loss processes.

The rate, at which an initially trapped atom in the state $|m_t\rangle$ undergoes a transition to an untrapped state $|m_u\rangle$ can be found [103] as:

$$\Gamma_{t\to u} = \frac{1}{\hbar^2} \sum_{\alpha,\beta} \langle m_t|\mu_\alpha|m_u\rangle\langle m_u|\mu_\beta|m_t\rangle S_{\alpha,\beta}(\omega_{t,u}), \tag{3.29}$$

where α, β are elements of the Zeeman subspace, $S_{\alpha,\beta}(\omega_{t,u})$ the power spectral density of electromagnetic noise at the frequency $\omega_{t,u}$, which denotes the difference in Lamor frequency between the states $|m_t\rangle$ and $|m_u\rangle$. The calculation of the power spectral density is complex and strongly depends on the actual experimental implementation. For a metallic half space [103] finds:

$$S_{\alpha,\beta} = \frac{\mu_0^2}{(16\pi)^2} \frac{k_B T}{\rho h} \left(1 + \frac{2h^3}{3\delta^3}\right)^{-1} s_{\alpha,\beta}, \tag{3.30}$$

where ρ is the metals resistance, T its temperature and δ the skin depth, defined as $\delta = \sqrt{2\rho/(\mu_0\omega_{t,u})}$. Figure 3.6 shows the atom loss rate in a trap at different distances from a

metallic half space. This prediction has been verified experimentally in [107] using metallic bulks of different materials. In chip experiments, the atom chip is composed of several (conducting and nonconducting) materials, multiple layers may introduce shielding effects [106], finite wire dimensions have to be considered [104]. Also the extended theory has been well verified experimentally in [108, 106]. Figure 3.6 also shows the atomic loss rate above a thin gold film of $5\,\mu$m heights, which is a typical height for wires in chip experiments, and for square cross section gold wires of 700 nm width, as used in experiments presented in part 2 of the manuscript. It becomes obvious, that for large atom-wire separations ($h > 1\,\mu$m), the half space assumption overestimates the loss rate compared to realistic systems. Once, the distance becomes comparable to the structure size, the atoms "see" more and more conducting material, around $1\,\mu$m distance, the loss rate is comparable to a bulk model and presents a significant obstacle for the miniaturization of wire structures [105].

3.4.2 Technical noise

The expressions (3.29) and (3.30) and more refined considerations in the above literature allow us to calculate the trap losses for a given spectral density of noise. The origin of this noise may by fundamental, as the Johnson noise due to thermally excited currents in the conducting materials; it may as well be technical, *e.g.* noise on the current sources providing the currents in the trapping wires. The power spectral density of noise on a current S_I directly translates into magnetic field noise of power spectrum S_B with

$$S_B(\omega) = \left(\frac{\mu_0}{2\pi h}\right)^2 S_I(\omega). \tag{3.31}$$

Reference [73] shows, that for a shot-noise limited current supply, the technical noise exceeds the fundamental effect for atom-wire distances above $100\,\mu$m. For smaller distances, fundamental surface effects are dominant. Still it is a significant technical effort to reduce the technical fluctuations to a limit, where fundamental effects become observable [108].

3.5 Random magnetic potentials

In essentially all realizations of magnetic wire traps that achieved Bose-Einstein condensation (or atom clouds of sufficiently low temperatures), an unexpected phenomenon occurred: cold atomic clouds break up into pieces when brought close to the trapping structure [109, 88, 110, 111, 73]. Extensive experimental studies could attribute this effect (also referred to as *fragmentation*) to a random static magnetic field component B_z along the direction of the wire, introducing a certain potential roughness and causing the atom cloud to fragment, once $k_B T < m_F g_F \mu_B B_z$ ($\mu < m_F g_F \mu_B B_z$ for Bose condensates).

It was suspected, that corrugation of the trapping wire edges [112] (surface) or bulk impurities might lead to a slight deviation of the current flow within the wire, creating additional magnetic field components in the trapping potential.

The experimental proof of this theory for at least one specific realization of a magnetic wire trap represents a major result of this manuscript and will be described in detail in part 2 [113]. Here, we will resume the theory, that allows to link geometrical deformations of the wire, characterized by a spectrum of edge (surface) noise, to the resulting magnetic trapping potential and the roughness therein. The following sections are resumed excerpts of the articles [92, 114] which can be found in completeness in annexe 1.

3.5.1 Magnetic field roughness due to distorted current flow

In this section, we present a general calculation of the additional magnetic field created by distortions in the current flow creating the trapping potential. By $\mathbf{j}$ we denote the current density that characterizes the distortion in the current flow. The total current density $\mathbf{J}$ is equal to the sum of $\mathbf{j}$ and the undisturbed flow $j_0\,\mathbf{e}_z$ (axes defined in figure (3.7)). As the longitudinal potential experienced by the atoms is proportional to the z component of the magnetic field, we restrict our calculation to this component. We thus have to determine the x and y components of the vector potential $\mathbf{A}$ from which the magnetic field derives. In the following, we consider the Fourier transform of all the quantities of interest along the z axis which we define by

$$A_{l,k}(x,y) = \frac{1}{\sqrt{2\,\pi\,L}} \int A_l(x,y,z)\, e^{-i\,k\,z}\; dz \;, \tag{3.32}$$

where l stands for x or y and L is the length of the wire.

The vector potential satisfies a Poisson equation with a source term proportional to the current density in the wire. Thus the Fourier component $A_{l,k}$ satisfies:

$$\left(\frac{\partial}{\partial x^2} + \frac{\partial}{\partial y^2}\right) A_{l,k} - k^2\, A_{l,k} = -\mu_0\, j_{l,k} \;. \tag{3.33}$$

where j_l is one component of the current density $\mathbf{j}$. In the following, we use cylindrical coordinates defined by $x = r\,\cos(\varphi)$ and $y = r\,\sin(\varphi)$. Outside the wire, the right hand side of equation (3.33) is zero. The solution of this 2D heat equation without source term can be expanded in a basis of functions with a given "angular momentum" n. The radial dependence of the solution is therefore a linear combination of modified Bessel functions of the first kind I_n and of the second kind K_n. Thus expanding $A_{l,k}$ on this basis, we obtain the following linear combination for the vector potential

$$A_{l,k}(r,\varphi) = \sum_{n=-\infty}^{n=\infty} c_{l_n}(k)\; e^{i\,n\,\varphi}\; K_n(k\,r) \;. \tag{3.34}$$

The $c_{l_n}(k)$ coefficients are imposed by equation (3.33), and can be determined using the Green function of the 2D heat equation [115]. We obtain

$$c_{l_n}(k) = -\frac{\mu_0}{2\pi} \iint I_n(k\,r)\; e^{-i\,n\,\varphi}\; j_{l,k}(\varphi, r)\; r\,dr\,d\varphi \;. \tag{3.35}$$

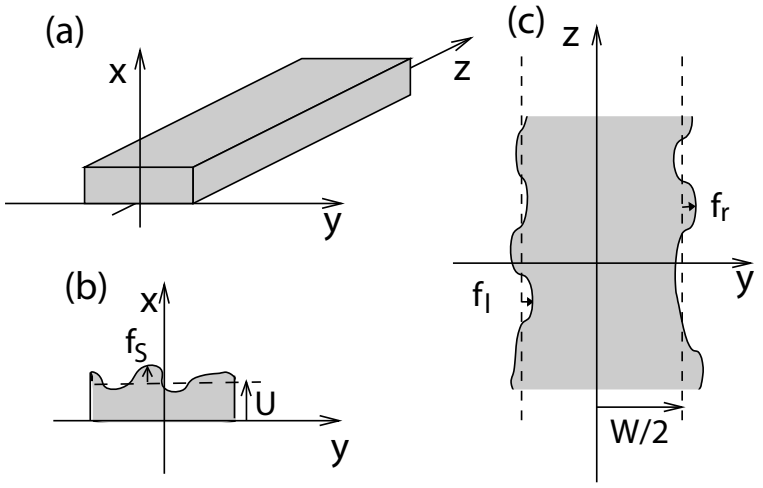

Figure 3.7: Schematic representation of wire corrugation. (a) Definition of axes. (b) Deviations of the wire height from the nominal value U are denoted by f_S. (c) Fluctuations of the left (right) wire edge are denoted by f_l (f_r) and considered to be independent of x.

Taking the curl of the vector potential and using the relations $K_n' = -(K_{n-1} + K_{n+1})/2$ and $2\,n\,K_n(u)/u = -K_{n-1} + K_{n+1}$, we obtain the z component of the magnetic field from equation (3.34)

$$\begin{aligned} B_{z,k} = \; & -\frac{k}{2} \sum_{n=-\infty}^{\infty} [c_{y_{n-1}}(k) + c_{y_{n+1}}(k)] K_n(k\,r) e^{i\,n\,\varphi} \\ & -i\,\frac{k}{2} \sum_{n=-\infty}^{\infty} [c_{x_{n-1}}(k) - c_{x_{n+1}}(k)] K_n(k\,r) e^{i\,n\,\varphi} \; . \end{aligned} \tag{3.36}$$

This expression is valid only for r larger than r_0, the radius of the cylinder that just encloses the wire. At a given distance x from the wire, we expect that only fluctuations with wavelengths larger or comparable to x contribute to the magnetic field, since fluctuations with shorter wavelengths average to zero. Therefore we can simplify expression (3.36) assuming we calculate the magnetic field above the center of the wire ($y = 0$) for x much larger than r_0. The argument of I_n in equation (3.35) is very small in the domain of integration and we can make the approximation $I_n(k\,r) \simeq (k\,r)^n/(2^n\,n!)$. This shows that the c_{l_n} coefficients decrease rapidly with n. Keeping only the dominant term of the series in equation (3.36), we obtain

$$B_{z,k}(x) \simeq -\frac{c_{y_0}(k)}{k} \times \left[k^2\,K_1(k\,x)\right] \; . \tag{3.37}$$

We will see in the next section that the first factor of this expression, characterizing the distortion flow, is proportional to the power spectral density of the wire corrugation. The second factor peaks at $k \simeq 1.3/x$ justifying the expansion. Fluctuations with a wavelength much smaller or much larger than $1/x$ are filtered out and do not contribute. As we approach the wire, more and more terms have to be added in the series of equation (3.36) to compute the magnetic field. We emphasize that the expressions derived in equations (3.36) and (3.37) are general for any distorted current flow that may arise from bulk inhomogeneities or edge and surface corrugations.

3.5.2 Current flow in a corrugated wire

We will now analyze the distortion of the current flow due to wire edge and surface corrugations in order to determine the associated c_{l_n} coefficients of equation (3.37). The wire is assumed to

have a rectangular cross section of width W and height U as shown in figure (3.7).

We will first concentrate on the effect of corrugations of the wire edges, *i.e.* the borders perpendicular to the substrate (model equivalent to [112]). The function $f_{r/l}$ that describes the deviation of the right (respectively left) wire edge from $\pm W/2$ is assumed to depend only on z [116].

Conservation of charge and Ohm's law give $\nabla \mathbf{J} = 0$ and $\mathbf{J} = -\chi \nabla V$ where χ is the electrical conductivity and V the electrostatic potential. We will make the approximation that χ is uniform inside the wire (and thereby exclude the effect of bulk impurities from the analysis). In this case, V satisfies the Laplace equation $\nabla^2 V = 0$. As we are interested in deviations from the mean current density $j_0 = I/(U\,W)$, we introduce the electric potential $v = V - j_0\, z/\chi$ which is equal to zero in the absence of deviations. From what we have said above, v only depends on y and z and satisfies the 2D Laplace equation. The boundary conditions for the current density on the wire edge require the current to be parallel to the wire edge. Thus v satisfies

$$\frac{df_{r/l}}{dz}(z) \times \left[j_0 - \chi \frac{\partial v}{\partial z}(y = \pm W/2 + f_{r/l}, z) \right] = -\chi \frac{\partial v}{\partial y}(y = \pm W/2 + f_{r/l}, z). \tag{3.38}$$

In the following we assume the amplitude of $f_{r/l}$ to be small enough so we can make an expansion to first order in $f_{r/l}$ of both terms. We then obtain a linear relation between $v(\pm W/2, z)$ and $f_{r/l}(z)$ which in Fourier space can be written as

$$i\,k\,j_0\,f_{r/l,k} = -\chi \frac{\partial v_k}{\partial y}(y = \pm W/2)\ . \tag{3.39}$$

The potential v satisfies the 2D Laplace equation, so the k component $v_k(y)$ is a linear combination of $e^{+k\,y}$ and $e^{-k\,y}$. The two coefficients are imposed by the two boundary conditions of equation (3.39). To complete the calculation of these two coefficients, we introduce the symmetric component $f^+ = (f_r + f_l)/2$ and antisymmetric component $f^- = (f_r - f_l)/2$ of the wire edge fluctuations. Going back to the current density, we obtain

$$j_{y,k} = i\,k\,j_0 \left(\frac{\cosh(k\,y)}{\cosh(k\,W/2)} f_k^+ + \frac{\sinh(k\,y)}{\sinh(k\,W/2)} f_k^- \right). \tag{3.40}$$

We note that the symmetric part (first term) of the current deviation is maximal near the wire edges for components with a wave vector large compared to $1/W$. On the other hand, the components with a small wave vector are constant over the width of the wire.

A similar analysis may be performed to calculate the effect of surface corrugation on the current distribution in the trapping wire. Here, f_S denotes the fluctuations of the height of the wire from its mean value U (see figure (3.7)). This calculation is slightly more complex, as it involves a 3D Laplace equation and a 2D fourier decomposition ($f_S \to f_{S_{k,m}}$) into wave vectors k and m along the directions z and y. The calculation is carried out in [114] in annexe 1, here we just give the result:

$$j_{x_{k,m}}(x,y) = 2ikf_{S_{k,m}} j_0 \sqrt{\frac{\pi}{W}} \sum_{p=0}^{\infty} \left(\gamma_{m,p} \frac{\sinh(\nu_p x)}{\sinh(\nu_p U)} \sin((2p+1)\pi y/W) \right) \tag{3.41}$$

$$j_{y_{k,m}}(x,y) = 2ikf_{S_{k,m}} j_0 \sqrt{\frac{\pi}{W}} \sum_{p=0}^{\infty} \left(\gamma_{m,p} \frac{\cosh(\nu_p x)}{\sinh(\nu_p U)} \frac{(2p+1)\pi}{\nu_p W} \cos((2p+1)\pi y/W) \right). \tag{3.42}$$

The Fourier components j_{l_k}, which allow for the calculation of the disturbed magnetic field following equations (3.35) and (3.36), are obtained by summing equation (3.41) and (3.42) for $m = 1, \ldots, \infty$.

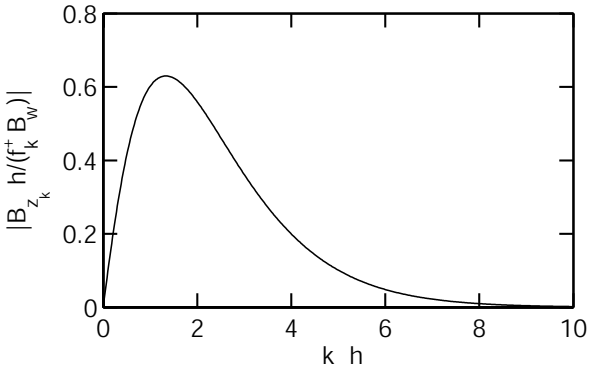

Figure 3.8: Response function relating the (left/right) wire edge fluctuations f_k^+ to the magnetic field roughness component B_{z_k}, $k = \{l, r\}$. The magnetic field created by the nominal (unperturbed) current in the wire is expressed by B_W, h describes the distance between atoms and wire.

3.5.3 Consequences for magnetic wire traps

In this section, we combine the results of the two previous sections to compute the z component of the rough magnetic field in the specific case of a flat rectangular wire ($U \ll W$). This simplification enables us to obtain analytical results for a system that is widely used in experiments [117, 111, 118, 80, 119, 81].

We perform the calculation on the x axis for $x > W/2$ (and $y = 0$). Since the wire is considered flat, we replace the volume current density $\mathbf{j}$ by a surface current density $\sigma = \int \mathbf{j}\, dx$. Then we can rewrite the c_{l_n} coefficients of equation (3.35) as

$$c_{l_n}(k) = -\frac{\mu_0}{2\pi}(-i)^n \int_0^{W/2} dy I_n(ky)[\sigma_{l,k}(y) + (-1)^n \sigma_{l,k}(-y)] \ . \tag{3.43}$$

Effect of wire edge corrugation

In the case of a flat wire, the distorted current has no component along x. The associated magnetic field is thus given by the first sum in equation (3.36). For $\varphi = 0$ and using $K_n(kr) = K_{-n}(kr)$ and $c_{y_{-n}} = (-1)^n c_{y_n}$ (see equation (3.43)), we obtain:

$$B_{z,k} = -k \sum_{n=0}^{\infty} (c_{y_{2n}}(k) + c_{y_{2n+2}}(k)) K_{2n+1}(kr). \tag{3.44}$$

Since only coefficients c_{y_n} with even n contribute, we see from equation (3.43) that only the symmetric part of the current density contributes to the magnetic field fluctuations. This is expected from simple symmetry arguments. For the $c_{y_{2n}}$ coefficients we find:

$$c_{y_{2n}} = (-1)^{n+1} \frac{\mu_0 I}{\pi W}\, i\, k\, f_k^+ \int_0^{W/2} I_{2n}(k\, y) \frac{\cosh(k\, y)}{\cosh(k\, W/2)}\, dy. \tag{3.45}$$

The sum over the angular momenta n in equation (3.44) converges rapidly with n if $x \gg W$. More precisely, the dominant term proportional to $K_1(k\, x)$ gives the correct result within 10 % as soon as $x > 1.5\, W$. As x approaches $x = W/2$, more and more terms contribute.

We now derive the response function of the magnetic field to the wire edge fluctuation for $x > W/2$ which we define as $R(k, x) = |B_{z,k}/f_k^+|^2$. It is shown in figure (3.8). As already mentioned in the previous section, far away from the wire ($x \gg W$), only wave vectors $k \ll 1/W$

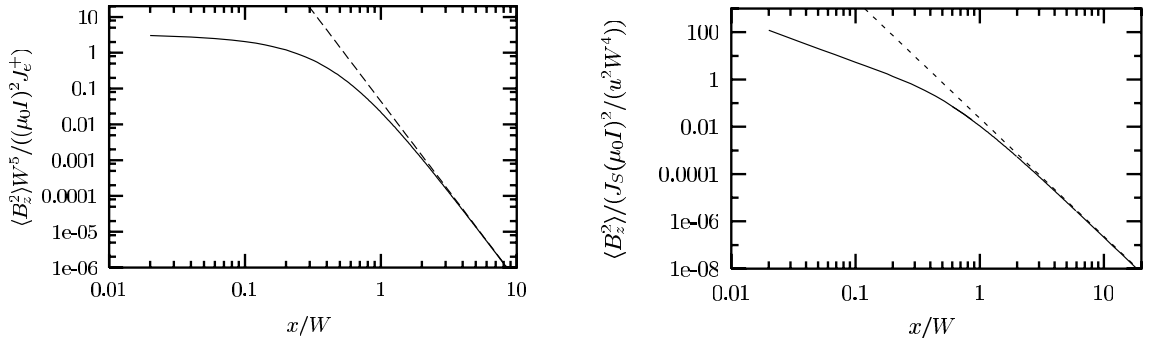

Figure 3.9: Magnetic field fluctuations $\langle B_z^2\rangle$ as a function of the (normalized) distance to the wire. (left) The effect of edge corrugation saturates for small distances, as the distance to the edges saturates very close to the wire surface. (right) The effect of wire surface roughness becomes dominant for $x \simeq 0,1\,W$ and increases for smaller distances. (both) The solid line indicates the analytical result for $x > W$ and a numerical calculation for $x < W$. The dotted lines are the $1/x^5$ scaling laws (3.47) and (3.48).

are relevant. We then can approximate the integral in equation (3.45) by expanding the integrand to zeroth order in $k\,y$. Keeping the dominant term in the series that defines the magnetic field, we obtain the following expression for the response function

$$R(k,x) \simeq \frac{(\mu_0 I)^2}{4\pi^2 x^4}(k\,x)^4 K_1^2(k\,x)\ . \tag{3.46}$$

For a given height x, as k increases, this function increases from zero as k^2, peaks at $k = 1.3/x$ and then decays exponentially. This behavior can be understood as follows: at low wave vectors, the angle between the direction of the distorted current flow and the z axis tends to zero, thus the contribution of these components becomes negligible. At high wave vectors, fluctuations with a wave length much shorter than the distance to the wire will average out.

Assuming a white power spectrum of the wire edge corrugations with a spectral density J_e^+, we can integrate the equation (3.46) over the entire spectral range [120]. We then find the following scaling law for the rms fluctuations of B_z with the atom-wire distance x:

$$\langle B_z^2\rangle = J_e^+ \frac{(\mu_0 I)^2}{x^5} \times 0.044\ . \tag{3.47}$$

The numerical factor has been found by a numerical integration of equation (3.46). Figure (3.9) shows that this expression is valid within 10 % as soon as $x > 2W$. For smaller distances x, the fluctuations of magnetic field increase more slowly and tend to a constant [121].

Effect of wire surface corrugation

A comparable analysis is carried out in [114] to take into account the contribution of top surface corrugation f_S to the trapping potential roughness. We find a comparable scaling law:

$$\langle B_z^2\rangle = J_s \frac{W}{U^2}\frac{\pi}{6}\frac{(\mu_0 I)^2}{x^5} \times 0.044, \tag{3.48}$$

where J_s is the 2-dimensional spectral density of f_S. Figure (3.9) compares this expression with a numerical calculation [114].

Orders of magnitudes, scaling laws

Comparing edge and surface corrugation, we see that for large distances, both effects scale in the same way (see equations (3.47) and (3.48)). However, at small distances from the wire, the amplitude of the magnetic field roughness produced by surface corrugation does not saturate. Thus, we expect surface roughness to become the dominant source of magnetic field fluctuations at small distances from the wire [122].

The scaling laws (3.47) and (3.48) are of major importance as they impose strong constrains in the use of micro traps. As mentioned in section 3.3.1, high magnetic field gradients are achieved with small wires and small atom wire separations. However, as the distance to the wire decreases, the roughness in the magnetic trapping potential increases according to the above scaling laws. Imposing a maximum potential roughness $\Delta B_{\max}$ tolerable in an experiment therefore directly determines the maximal transverse gradient accessible with a specific realization of a micro wire.

More precisely, as mentioned in section 3.3.1, the maximum current in a micro wire is limited by heat dissipation: $I_{\max} = \xi W U^{1/2}$ [83]. To analyze the scaling of the system, we consider the trap center at a distance comparable to the wire width $x \simeq W$ and a wire height U small and constant. For a given fabrication technology, we expect the wire roughness to be independent of the wire dimensions W and U and we assume white noise spectral densities J_e and J_S for the edge and top surface corrugations [120]. Using the above expressions for x and I and equations (3.47) and (3.48), we obtain the following scaling laws:

$$\langle B^2_{\text{edge}} \rangle = \frac{J_e \mu_0^2 \xi^2 U}{W^3} \tag{3.49}$$

$$\langle B^2_{\text{surf}} \rangle = \frac{\pi}{6} \frac{J_S \mu_0^2 \xi^2}{W^2 U} \tag{3.50}$$

for the magnetic field fluctuations induced by the edge and the surface roughness respectively.

Imposing magnetic field fluctuations smaller than $\Delta B_{\max}$ determines a minimal wire width $W_{\min}$ and the maximal transverse gradient $B'_{\max}$. If the potential roughness is dominated by effects due to wire edge corrugation, we find:

$$W_{\min} = \left(\frac{J_e \mu_0^2 \xi^2 U \times 0.044}{\Delta B^2_{\max}} \right)^{1/3} \tag{3.51}$$

$$B'_{\max} = \frac{1}{2\pi} \left(\frac{\mu_0 \xi \sqrt{U} \Delta B^2_{\max}}{J_e \times 0.044} \right)^{1/3} . \tag{3.52}$$

For a potential roughness dominated by effects due to wire top surface corrugation, we find:

$$W_{\min} = \left(\frac{\pi}{6} \frac{J_S \mu_0^2 \xi^2 \times 0.044}{\Delta B^2_{\max} U} \right)^{1/2} \tag{3.53}$$

$$B'_{\max} = \frac{1}{2\pi} \left(\frac{U \Delta B_{\max}}{J_S \frac{\pi}{6} \times 0.044} \right)^{1/2} . \tag{3.54}$$

As will be described in part 2 of the manuscript, a micro wire fabricated by electroplating presents an edge roughness of $J_e \simeq 0.1\,\mu\text{m}^3$. Neglecting top surface roughness, for a wire of $U = 5\,\mu$m height, a typical $\xi = 3 \times 10^7\,\text{A.m}^{-3/2}$ and imposing a maximal potential roughness of $\Delta B_{\max} = 1\,$mG, the wire width is limited to $W_{\min} \simeq 700\,\mu$m, the maximal gradient will be limited to $B'_{\max} \simeq 2000\,\text{G/cm}$.

To draw full benefit from magnetic micro traps and the miniaturization approach, the problem of potential roughness has to be overcome; the fabrication quality of micro wires becomes

a key point for the feasibility of many experiments (see part 2). A reduction of wire edge corrugation by two orders of magnitudes (compared to the above example) has been achieved in the Orsay setup by using state-of-the-art direct electron beam lithography, as will be described in part 2 of the manuscript. Even smaller wire roughness has been reported by the Heidelberg group [122].

Part II

A double well created by nanofabricated wires

Contents

Introduction

The second part of this thesis...

Chapter 4

Static magnetic double well potentials

4.1 Realizing the two modes model

In this section we briefly review some basic constrains on the design of the double well potential. As outlined in section 2.1.1, one is aiming to realize the two modes model, where the tunnel dynamics is governed by the two lowest lying (symmetric and antisymmetric) delocalized states, separated by the energy $\hbar\delta$ (see figure (2.1)). To avoid excitations of higher modes, we impose $\hbar\delta \ll \hbar\omega_0$ where ω_0 denotes the trap frequency for one individual well and $\hbar\omega_0$ approximately is the energy distance to the third level of the double well (see section 4.2 for a more complete analysis of the two modes model in the presented system). Excitations are assumed to be suppressed for $\delta \simeq \omega_0/10$.

In a physical implementation of the system, the timescales of the tunnel dynamics have to match the technical constrains imposed by the experimental setup. For an order of magnitudes estimation, we assume a Bose-Einstein condensate to have a limited lifetime of 100 ms. To observe several oscillations of a tunnel dynamic, we need a tunnel coupling on the order $\delta/(2\pi) \simeq 10\,\text{ms}$. As the two modes model imposes $\delta \simeq \omega_0/10$, it immediately becomes apparent, that trapping frequencies of the order $\omega_0/(2\pi) \simeq 1\,\text{kHz}$ will be necessary. Using the expression (2.6), we find $r_0/a_0 \simeq 2,45$, where $2r_0$ describes the double well separation and a_0 is the extension of the (single particle) wave function $a_0 = \sqrt{\hbar/(m\omega_0)}$ in a harmonic trap of frequency ω_0. As in a trap of $\omega_0/(2\pi) \simeq 1\,\text{kHz}$ this extension is $a_0 \simeq 350\,\text{nm}$, the required double well separation is on the order microns.

In conclusion, a realistic approach to realize tunnelling in a double well potential necessitates high trapping frequencies (order kHz) and potential variations on small spatial length scales (order microns). These may be provided by optical traps in standing wave [55] or tightly focussed [43] geometries, or by using magnetic wire traps. As will be presented in the following, in static magnetic traps based on current carrying wires, the size of the wires has to be on the order of the double well separation. Therefore we have chosen to use nanofabricated wires (700 nm width) on an atom chip to implement a magnetic double well potential in order to study tunnelling dynamics in the Rabi and in the Josephson regime.

4.1.1 Accessing the Rabi regime

As outlined in sections 2.1.1 and 2.1.2, the Rabi regime describes the single particle tunnelling dynamics, when the influence of atom-atom interactions can be neglected. This regime is of particular interest, as it enables the construction of atom-optical elements as beam splitters and interferometers based on tunnel coupling: we assume a double well system, in which the

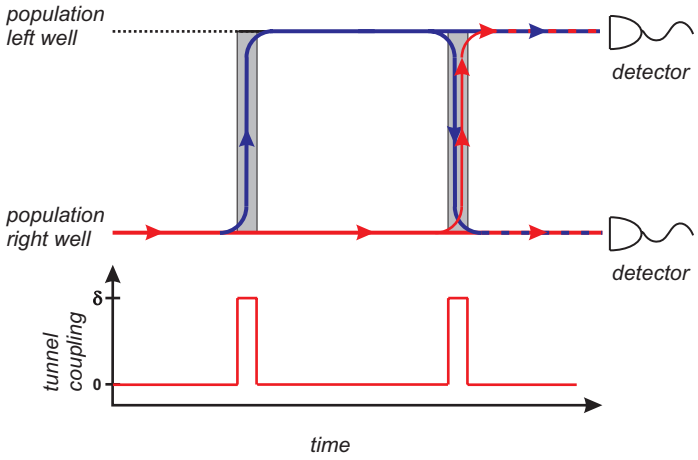

Figure 4.1: Schematic representation of a Michelson-type interferometer based or Rabi tunnelling. Two $\pi/2$ pulses are implemented by controlling the tunnel coupling, the phase accumulated in the sequence can be read out as a population difference in the two wells.

height of the potential barrier can be modified at will, in particular, the tunnel coupling can be switched between zero and $\hbar\delta$. In the absence of tunnel coupling, we prepare a wave packet $|\Phi_{\text{left}}\rangle$ localized *e.g.* in the left well. Turning on the coupling for a time $\tau_{\pi/2} = \pi/(2\delta)$ realizes a $\pi/2$ pulse (beam splitter pulse), preparing the wave packet in a (coherent) superposition $\alpha|\Phi_{\text{left}}\rangle + \alpha^*|\Phi_{\text{right}}\rangle$ with $\alpha = (1-i)/2$. A second $\pi/2$ pulse implements an interferometer of the Michelson type (see figure (4.1)) and allows for a precise measurement of the phase of the wave functions, accumulated throughout the sequence.

The Rabi regime in 3D

To obtain tunnelling in the Rabi regime, the interaction energy has to be small compared to all other energy scales, *e.g.* the kinetic energy of the harmonic oscillator ground state. Following equation 1.24, we find the condition to neglect interactions writes

$$a_{\text{ho}} \gg Na, \tag{4.1}$$

where a_{ho} is the extension of the wave function associated with the geometric mean of the trapping frequencies $\omega_{\text{ho}} = (\omega_x\omega_y\omega_z)^{1/3}$ and a the s-wave scattering length. Assuming a ^{87}Rb Bose-Einstein condensate with a very small number of atoms $N = 1000$, we obtain a maximum mean trapping frequency $\omega_{\text{ho}}/(2\pi) \simeq 5\,\text{Hz}$. A Rabi tunnelling in the two modes model would have a tunnelling period of 2 s. We therefore believe it to be impossible to reach the Rabi regime in a 3D geometry with today accessible experimental setups.

The Rabi regime in 1D

In contrast, the influence of interactions on the tunnelling dynamics can be massively reduced when going to reduced dimensions. In a 1D configuration, where tunnelling takes place in one of the transverse directions, the interaction energy ng has to be small compared only to the kinetic energy $\hbar\omega_0$ of the transverse harmonic oscillator ground state, where ω_0 can be very high. With $g = 4\pi\hbar^2 a/m$ and $n \simeq n_{1D}/a_\perp^2$, the condition to be in the 1D Rabi regime writes $n_{1D}a \ll 1/(4\pi)$, the axial distance between the atoms has to be large compared to the s-wave scattering length. For ^{87}Rb atoms this translates to the condition $n_{1D} \ll 10\,\mu\text{m}^{-1}$. In an

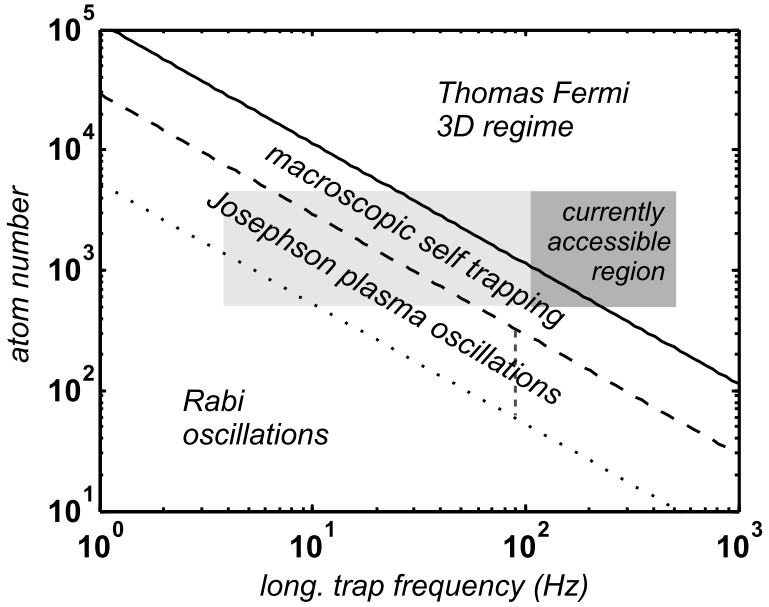

Figure 4.2: Different regimes of tunnelling dynamics in an elongated double well of $\omega_0/(2\pi) = 3\,\mathrm{kHz}$ as presented in this manuscript. The solid line indicates the condition $N\Re a/a_0 \ll 1$ which identifies the Thomas-Fermi 1D regime [29]. The dotted line corresponds to $\Lambda = 1$ and separates the Rabi and The Josephson tunnelling regime. Within the Josephson regime, number oscillations of reduced amplitude can be observed for $1 < \Lambda < \Lambda_c$. The dashed line indicated $\Lambda_c = 5,5$ corresponding to $z(0) = 0,6$ and $\phi(0) = \pi$. These oscillations are unstable for too high trap anisotropy (left of the dotted vertical line). The light shaded area indicates the parameter space that should in principle be accessible with our device. Random magnetic potentials currently restrict the system to the dark shaded area.

experiment with 3000 atoms confined in a (boxlike) potential, the tunnel coupling has to be constant to a few percent over a distance of more than $300\,\mu$m. This seems feasible but still represents a significant technical challenge as will be described in the following.

As outlined in section 4.1, a transverse trapping frequency of $\omega_0/(2\pi) \simeq 1\,\mathrm{kHz}$ is desirable. Using the condition $\chi = N\Re a/a_\perp \ll 1$ to identify the 1D regime [29], we find a high trap aspect ratio $\Re \gg 50$, which imposes a maximum longitudinal trapping frequency of $\omega_\parallel \ll 20\,\mathrm{Hz}$.

4.1.2 Accessing the Josephson regime

If we relax the condition on the influence of interactions to $\mu \gg \hbar\omega_0 \gg \hbar\delta$, the system enters the Josephson regime. Experimentally, this is much easier to realize, as less anisotropic condensates can be used and stable tunnelling has to be realized over a smaller spatial region. However, as $\mu \gg \hbar\delta$, $\Lambda > 1$ (compare section 2.1.2) large amplitude oscillations in double well population are rapidly suppressed (macroscopic quantum self trapping). Oscillations of small amplitude may be observed for a narrow parameter regime $1 < \Lambda < \Lambda_c$ with Λ_c defined as in (2.26) [55].

Different regimes of phase dynamics may be realized even in the "locked" system [55,50]. They may be read out by analyzing matter wave interference fringes or by Bragg spectroscopy [123].

Figure (4.2) shows different regimes for a trap of $\omega_0/(2\pi) = 3\,\mathrm{kHz}$, as experimentally realized with the wire pattern presented in section XYZ. We have assumed an initial population imbalance of $z(0) = 0,6$ ($\phi(0) = \pi$) which leads to $\Lambda_c = 5,5$. The light shaded parameter area may in principle be investigated with our device. However, random magnetic potentials as described in 3.5 do cause the atom cloud to fragment, leading to high local longitudinal trapping frequencies

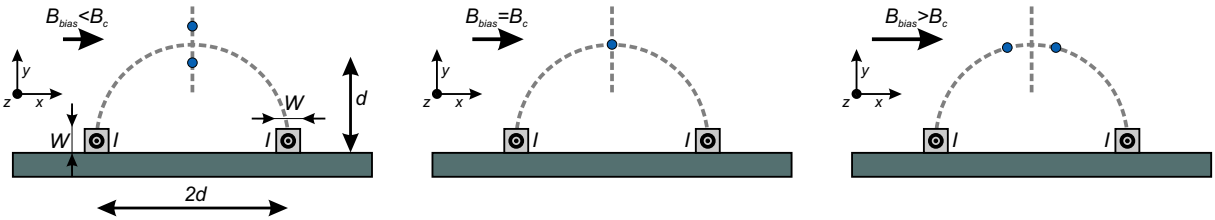

Figure 4.3: Schematic representation of the two wire beamsplitter/double well scheme proposed by [96]: for a small external bias field, two trap minima form an a vertical line (left). They merge at the coalescence point located at a distance d from the surface for $B_{\mathrm{bias}} = B_c$ (center) and horizontally split for larger bias field (right).

and a reduction of the parameter region as indicated by the dark shaded region.

Avoiding dynamic instabilities

In very elongated geometries, the uniform Josephson mode is unstable and decays to modes of non-zero longitudinal momentum as outlined in section 2.1.3 [58]. This can be partially suppressed by reducing the longitudinal size of the system and thereby the number of accessible modes. Almost total suppression is possible when choosing

$$\omega_{\parallel} \simeq \frac{z(0)}{2}\omega_{\mathrm{Josephson}}, \tag{4.2}$$

where $z(0)$ is the initial population imbalance. As $\delta \simeq \omega_0/10 < \omega_{\mathrm{Josephson}} < \omega_0$, it becomes obvious, that low aspect ratio traps are favorable for the suppression of dynamic instabilities. This is in conflict to the above discussion, where high aspect ratios where found to enable observation of number oscillations in the Rabi and Josephson regime. An experimental implementation aiming to observe both regimes in an elongated geometry will therefore comprise a compromise between both effects, dynamical instabilities will always be present.

The vertical dotted line in figure (4.2) indicates the longitudinal trapping frequency, from which on instabilities are suppressed (right of the line) in a trap of $\omega_0/(2\pi) = 3\,\mathrm{kHz}$ and $z(0) = 0,6$. For simplicity, we have assumed $\omega_{\mathrm{Josephson}} \simeq \omega_0/10$.

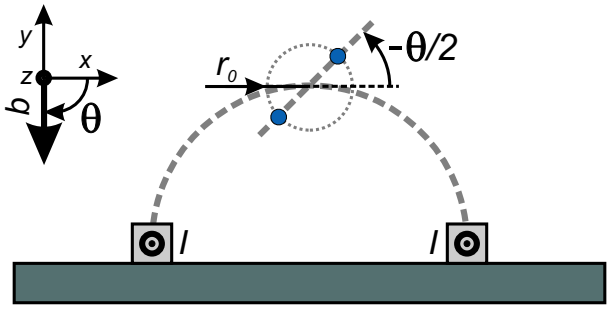

Figure 4.4: Tilting the double well: a small magnetic field **b** splits the double to a radius $r_0 = \sqrt{A/b}$, rotating this field by θ rotates the double well by $-\theta/2$. A field **b** orthogonal to the chip surface rotates the double well to 45° which allows for horizontal splitting, when the chip is mounted under the same angle as in the Orsay setup.

4.2 A 1D double well based on magnetic micro traps

Starting from the side wire guide (compare section 3.3.1), the most simple configuration to create a double well is to use two parallel wires [96]. Indeed, it has been shown, that in a planar wire configuration, the number of necessary wires is equal to or larger than the number of potential minima [124].

4.2.1 A two wire geometry

We assume two parallel wires separated by $2d$, carrying an equal current I as indicated in figure (4.3). For an external bias field $B_{\text{bias}} < B_c$ two quadrupole traps are formed on a vertical line between the two wires. For $B_{\text{bias}} = B_c$, the two quadrupoles coalesce to form a field of hexapole shape with a single potential minimum at a distance d from the wire surface. For $B_{\text{bias}} > B_c$ the hexapole again splits vertically into two quadrupole traps. As in most atom chip experiments the chip surface is mounted horizontally, the horizontal splitting is favorable, as both wells are equally effected by gravity.

For the theoretical description of the system, it is convenient to consider the situation $B_{\text{bias}} = B_c$ and add a small additional homogeneous field **b** to describe the splitting of the hexapole. Around the hexapole minimum, the magnetic field writes

$$B_x = A(y^2 - x^2) \quad \text{and} \quad B_y = 2Axy \tag{4.3}$$

where we have positioned the reference system at the coalescence point and

$$A = \frac{\mu_0 I}{2\pi d^3} \tag{4.4}$$

describes the strength of the hexapole field in analogy to the gradient describing the strength of a quadrupole field. The critical bias field B_c to superimpose both quadrupole traps at the coalescence point is

$$B_c = \frac{\mu_0 I}{2\pi d} = Ad^2. \tag{4.5}$$

Adding a small homogeneous field **b** to B_c will split the hexapole into two quadrupole traps separated (to first order) by

$$r_0 = \sqrt{\frac{b}{A}}. \tag{4.6}$$

If the field **b** makes an angle θ with the horizontal x axis, the two trap minima will be located on a line which makes an angle $-\theta/2$ with the x axis. By rotating the external field **b**, the

minima of the double well can be rotated on a circle of radius r_0 (see figure (4.4)). Applying *e.g.* a field orthogonal to the chip surface will create a double well tilted by 45°, which is especially convenient in the Orsay experiment, where the atom chip is mounted under an angle of 45° (compare section XYZ). In the following we assume a reference system rotated by the angle $-\theta/2$, so that the new x' axis contains both trap minima.

To prevent Majorana spin flip losses at the potential minima, we superimpose a homogeneous longitudinal ("Ioffe") field B_0. In the harmonic approximation and using the new defined axes $\{x', y'\}$ the 2D double well potential writes

$$V(x', y') = \frac{m\omega_0^2}{4} y'^2 + \frac{m\omega_0^2}{4x_0'^2} x'^2 y'^2 + \frac{m\omega_0^2}{8x_0'^2} \left(x'^2 - x_0'^2\right)^2, \tag{4.7}$$

where $x_0' = r_0 = \sqrt{b/A}$ is the position of the trap minima and

$$\omega_0 = \sqrt{\frac{4m_F g_F \mu_B A b}{m B_0}} \tag{4.8}$$

the trap frequency at the individual wells. On the x' axis ($y' = 0$) we recover the generic double well potential (2.1).

To verify for the two modes model, we have numerically calculated the single particle tunnel coupling $\hbar\delta$ for the potential (4.7) and compared to the energy separation to the next lowest lying state for different ratios r_0/a_0 where $a_0 = \sqrt{\hbar/(m\omega_0)}$ denotes the size of the single particle ground state. As indicated in figure (4.5), we find a ratio of $r_0/a_0 = 2,65$ to verify $\omega_{2,0} = 10\delta$ and therefore guarantees for tunnelling in the two mode approximation.

The two wire configuration therefore seems in principle well suited for the realization of a tunnelling experiment in an elongated geometry. In practice, this setup is very sensitive to noise in the currents and magnetic fields: as an example we will analyze fluctuations in the trap distance due to instabilities in the external field b effectuating the splitting. From (4.6), (4.7) and (4.8) we derive

$$\frac{\delta r_0}{r_0} = \frac{1}{2}\frac{\delta b}{b} = \frac{1}{2}\frac{d^2}{r_0^2}\frac{\delta b}{B_c}. \tag{4.9}$$

This illustrates, that stability can be increased using small wire separations (comparable to the desired double well separation) and large external fields B_c. The smallest wires we could create within our collaboration with the LPN were of 500 nm square cross section, separated by 2.5 μm. To obtain a tunnel frequency of $\delta/(2\pi) = 100$ Hz within the two modes model, a trap separation of $2r_0 = 520$ nm has to be realized. To create the hexapole trap, an external field of 16 G is necessary, a small field of 183 mG will split the trap to the desired separation. A magnetic field fluctuation of 2 mG causes a change of the tunnelling frequency of 10 %. This means, that a total external magnetic field of about 16 G will have to be controlled on the level of 2 mG (neglecting possible fluctuations of the wire current). We believe a magnetic field homogeneity and stability of 10^{-4} over the entire coupling region (200-500 μm) to be out of reach for our experimental setup, even using passive or active magnetic shielding.

4.2.2 A five wire geometry

To circumvent these stability problems, we decided to use a system, where the magnetic fields forming the hexapole trap are entirely generated by current carrying chip wires. The final splitting into the double well potential is still performed by adding a small homogeneous external field b, which now only has to be stable on the percent level.

In analogy to the self-sustaining three wire traps [91], consisting of a main side guide wire and two parallel wires, replacing the external bias field, we developed a five wire geometry to

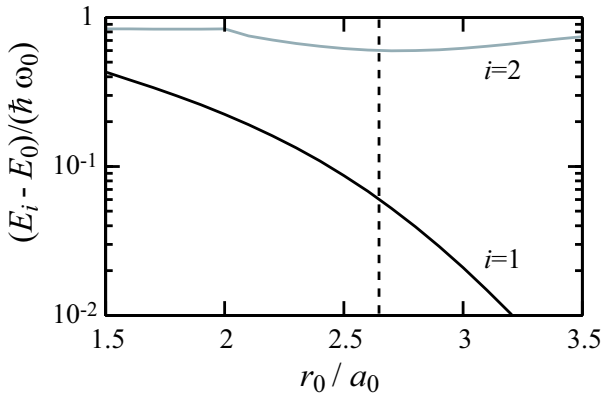

Figure 4.5: Bohr frequency between the (symmetric) single particle ground state of the double well and the first two nearest lying states. The dashed vertical line indicates $r_0/a_0 = 2,65$, where $\omega_{2,0} = 10\,\omega_{1,0} = 10\,\delta$.

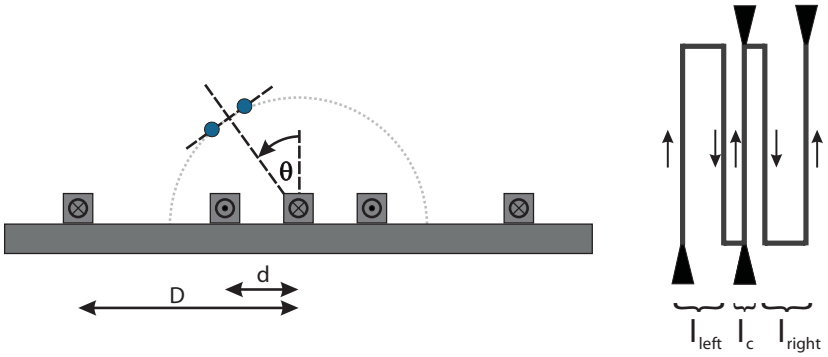

Figure 4.6: Five wire configuration to realize a stable hexapole magnetic field (left). Equal current in all wires create a single trap directly above the central wire. Additional contacts on the wires in series allows for individual control of the currents in outer two branches and the central wire (right). By des-equilibrating these currents, the hexapole can be moved on a circle of radius $\sqrt{3}d$ (left). The splitting can be either performed by an additional external field **b** or by increasing the central wire current.

create a stable hexapole field. As the same current will be used in all five wires, a high level of noise rejection can be obtained. By using sufficiently long wires, this stability can be realized along the entire coupling region, only limited by the precision of the lithographic fabrication process.

The five wire structure can be understood as two close-by three wire traps, where the two central wires were merged into one in order to approach the two wells. We find it interesting to note, that a hexapole magnetic field can not we created by less than five wires in a planar geometry [124]. As the wire system will be symmetric, only two distances d and D completely determine the pattern, as indicated in figure (4.6). We are now interested to find the distances, where the same current I in all wires creates a single trap of hexapole shape. For symmetry reasons, this trap will be located on the y axis, along this axis the magnetic field writes

$$B_x = \frac{\mu_0 I}{2\pi}\left(\frac{2y}{D^2+y^2} - \frac{2y}{d^2+y^2} + \frac{1}{y}\right). \tag{4.10}$$

This field has a double zero, which indicates the hexapole configuration for $D = 3d$. The height of the hexapole trap above the central wire will be $y_0 = \sqrt{3}d$. The position of this coalescence point is exclusively fixed by the wire pattern, it does not depend on the current in the wires.

A development of the magnetic field around the hexapole position gives

$$B_x = A'(x^2 - y^2) \tag{4.11}$$

$$B_y = -2A'xy \tag{4.12}$$

where $A' = (1/2\sqrt{3})\,A$ and A defined as in (4.4). Apart from the factor $1/2\sqrt{3}$, the five wire configuration with wire separations d ($2d$ for the wires of equal current) and $3d$ creates an identical magnetic field as two wires separated by $2d$ together with an external magnetic field $B_{\text{bias}} = B_c$. The potential around the hexapole configurations is well described by (4.7), the two modes model is equally valid for $r_0/a_0 = 2.65$. However, the problem of magnetic field fluctuations is transferred to stability constrains on the wire current and the precision of the lithographic process. Using actively stabilized current drivers, it is relatively easy to obtain a current stability of $\delta I/I < 10^{-4}$. The quality of the micro fabricated wires still represents an issue as already outlined in section 3.5.

The splitting of the magnetic hexapole into a double well is realized analogous to the two wire system by adding a small homogeneous field $\mathbf{b}$. As the above example illustrates, a field stability of 1 % over the coupling region is sufficient to allow for stable tunnelling, which we believe to be feasible in our experimental setup.

In our experimental realization of the five wire scheme, it is possible to also individually control the currents in the wires, as indicated in figure (4.6). By I_{left} (I_{right}) we denote the current in the left (right) outer two wires, I_{center} is the current in the central wire. By desequilibrating the currents in the outer wires, it is possible to move the coalescence point on a circle of radius $\sqrt{3}d$:

$$\sin\theta = -\frac{2}{\sqrt{3}}\frac{I_{\text{right}} - I_{\text{left}}}{I_{\text{right}} + I_{\text{left}}}. \tag{4.13}$$

The current in the central wire has to be adapted accordingly, to realize the hexapole configuration at $I_{\text{center}} = I_c$. For $I_{\text{center}} > I_c$, the two wells will be located on a line tangential to the circle of radius $\sqrt{3}d$ as depicted in figure (4.6). Consequently, by controlling the currents in the wires individually, the double well can be realized under an arbitrary angle without the need of any external fields. Of course, using different currents in the wires reduces the noise rejection of the setup. Whether an external field $\mathbf{b}$ or three separate currents are easier to stabilize, will have to be decided experimentally.

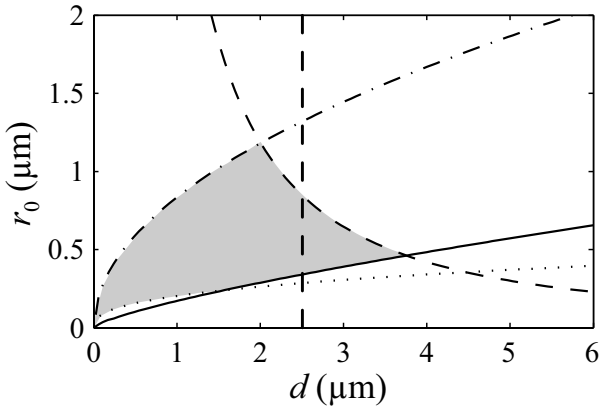

Figure 4.7: Stability diagram for the magnetic double well based on a five wire geometry. The shaded area represents the parameter sets for wire separation d and double well separation r_0 for which stable tunnelling is possible, assuming random ambient magnetic field fluctuations of 1 mG. Details on the different delimiting processes are given in the text. The dashed vertical line indicates our device at $d = 2,5\,\mu$m.

4.3 Stability of the double well

We will now perform a stability analysis of the five wire double well configuration, in order to determine the appropriate size of the setup. The system is characterized by the wire separation d, the wire current I, a small homogeneous field $\mathbf{b}$ effectuating the double well splitting $2r_0$ and the longitudinal ("Ioffe") field B_0 which suppresses Majorana spin flip losses at the trap minima.

We assume equal and noise-free current I in all five wires, creating a non-fluctuating magnetic hexapole field at a distance $\sqrt{3}d$ from the chip surface. To analyze the scaling of the system, we will relate the wire current to the wire separation: as the trap distance from the wires is on the order of the wire separation, we will use square cross section wires of width (and heights) W, where $W = (1/5)\,d$, to be able to neglect finite size effects. These wires can carry a maximum current $I_{\mathrm{crit}} = \sqrt{\kappa/(\alpha\rho_0)}W^{3/2} = \xi d^{3/2}$ limited by heat dissipation to the chip substrate (compare equation (3.20)). Based on test measurements we choose $\xi = 1,8 \cdot 10^6\,\mathrm{Am}^{-3/2}$, which is in agreement with the value measured by the Heidelberg group [83]. The strength of the hexapole field created by the five wire geometry is thus only determined by the wire separation: $A = (\mu_0\xi)/(2\sqrt{3}\pi d^{3/2})$.

The splitting of the hexapole into the double well trap is performed by a small homogeneous magnetic field $\mathbf{b}$ in arbitrary direction, realizing a well separation of $2r_0 = 2\sqrt{b/A}$. To guarantee tunnelling dynamics in the two modes approximation, we will add a longitudinal field B_0, so that $r_0/a_0 = 2.65$. This longitudinal field is therefore related to the double well separation. For technical reasons, we will limit this field to 100 G.

Consequently, the system is totally determined by the wire separation d and the double well separation $2r_0$. We will now analyze the effects of fluctuations in the fields B_0 and $\mathbf{b}$ on the tunnel coupling. The wire current is assumed to be stable at the 10^{-4} level.

Two major effects might degrade the measured signal in a tunnel experiment:

- Fluctuations in tunnel coupling: Noise on the additional external magnetic fields B_0 and $\mathbf{b}$ or random magnetic field components might alter the tunnel coupling (*e.g.* modify the trap separation). This effect will degrade the signal of an experiment, which reads out relative population in the two wells (*e.g.* Rabi or Josephson oscillations). As criterion for the feasibility of a tunnel experiment, we will tolerate a modification of the tunnel coupling up to 10 %.

- Tilting of the double well: Noise on the additional external magnetic field **b** or random magnetic field components will modify the position of the static trap and in result tilt the double well. A height difference h of the two wells induces a potential energy difference mgh, which leads to a corresponding (arbitrary) evolution of the differential phase. This effect will degrade the signal of an experiment, which reads out the relative phase of the two condensates. As criterion for the feasibility of a tunnel experiment, we will tolerate differential energy shift of 10 % of the tunnel coupling ($mgh = 0.1\,\delta$).

We will first concentrate on variations of the tunnel coupling $\Delta\delta$ due to fluctuations in the longitudinal (B_0) or transverse (b) field. From the numerical calculations performed to check for the two modes assumption (figure (4.5)), we obtain the dependencies:

$$\frac{\Delta\delta}{\delta} = -2,40\frac{\Delta r_0}{r_0} - 2,18\frac{\Delta\omega_0}{\omega_0} \tag{4.14}$$

$$= -4,27\frac{\Delta b}{b} + 1,09\frac{\Delta B_0}{B_0}. \tag{4.15}$$

If we impose $\Delta\delta/\delta = 0.1$ on the stability on the tunnel coupling, the stability of $\Delta b/b$ and $\Delta B_0/B_0$ has to be on the same level which is easy to achieve with an experimental setup designed for he creation of Bose-Einstein condensates. Still, random additional magnetic fields due to an electromagnetic environment may be problematic. We assume, that some experimental effort has been employed (*e.g.* passive or active shielding) to reduce these fluctuations to approximately 1 mG. As can be seen from equation (4.15), mainly noise Δb in the transverse direction has an influence on the tunnel coupling, as usually $B_0 \gg b$. Only considering this leading term, we obtain

$$\frac{\Delta\delta}{\delta} \simeq -4,27\frac{\sqrt{3}\pi}{\mu_0\xi}\frac{d^{3/2}}{r_0^2}\Delta b. \tag{4.16}$$

Thus imposing $\Delta\delta/\delta = 0.1$ and $\Delta b = 1\,\mathrm{mG}$ restricts the double well separation r_0 to the domain above the solid line in figure (4.7).

We now focus on the calculation of the fluctuations of the gravitational energy shift between the two wells. Transverse magnetic field fluctuations Δb lead to fluctuations $\Delta h = \Delta b/(Ar_0)$ of the height difference between the wells. The associated fluctuations of the gravitational energy difference have to be small compared to the tunnel coupling so that the phase difference between the wells is not significantly modified throughout one oscillation in the double well. The ratio of these two energies is

$$\frac{mg\Delta h}{\hbar\delta} \simeq 2,37\frac{\sqrt{3}\pi m^2}{\mu_0\xi\hbar^2}r_0 d^{3/2}\Delta b. \tag{4.17}$$

Again, fixing this ratio to 0,1 and assuming $\Delta b = 1\,\mathrm{mG}$ restricts the accessible double well splittings to the parameter region below the dashed line in figure (4.7).

For each double well separation $2r_0$, the longitudinal field B_0 has to be adapted to ensure $r_0/a_0 = 2,65$. As for small wire structures the trap frequencies increase, the longitudinal field has to increase accordingly. For technical reasons, we limit this field to 100 G, which restricts the domain of accessible parameter sets for d and r_0 to the region below the dash-dotted line in figure (4.7). In contrast, for very small double well separations, the trap frequencies are low and therefore also the longitudinal field is reduced. The condition to suppress Majorana losses ($m_F g_F \mu_B B_0 > 10\hbar\omega_0$) restricts the double well separations to the region above the dotted line.

As can be directly seen from figure (4.7), the wire separation d has to be below 5 μm to ensure stable tunnelling in the two modes approximation, even with a noise rejecting five wire configuration.

Chapter 5

Experimental setup

Intro, read Jerome, Christine, Collaboration, Dominique , Gian-Carlo

5.1 A single layer atom chip for Bose-Einstein condensation

The first chip generation, as it will be described in the following, was designed to create a Bose-Einstein condensate in a simple, single chamber experimental setup. With this chip, we obtained condensation in March 2003 and performed an in-depth study on random magnetic potentials created by current deviations in the chip wires, as will be presented in chapter 6 of this manuscript. We will start by resuming the design considerations for a single layer atom chip and describe the different fabrication steps.

5.1.1 Design considerations

In a simple single chamber setup, as employed in the Orsay experiment, the atom chip fulfills many purposes throughout the creation of a Bose-Einstein condensate:

- The surface of the atom chip serves as a mirror in a reflection magneto optical trap (MOT) for the atoms in the first stage of optical cooling. Furthermore, the imaging beam is reflected on the chip surface. This surface therefore has to be of optical quality for light of a wavelength of 780 nm. Large wavelength corrugation has to be avoided in order not to deform the image of the atomic cloud. As coherent light is used for the imaging, scattering on edges or relief on the chip structure will lead to interference effects and therefore regions of vanishing probe beam intensity.

- In the surface magneto optical trap, the atoms are located about 10 mm from the chip surface. In order to approach the atoms in a controlled fashion, the MOT is transferred to a distance of about 2 mm with the help of a U shaped wire structure [125] on the atom chip. As this structure has to create important magnetic field gradients (10-20 G/cm) far from the wire, a significant current has to be employed ($\approx 5\,A$). The size of the structure has to match the capturing area of the MOT and is therefore of several millimeters.

- The optically pre-cooled atoms are recaptured in a magnetic wire trap based on a Z shaped wire, as described in 3.3.1. The position of this trap has to be matched to the position of the atoms after the pre-cooling, additionally, this trap has to be sufficiently deep to capture the atoms at around $T \simeq 100\,\mu$K. This again necessitates high currents in the Z shaped structure (≈ 2 A). However, in a phase of compression, the atoms will be brought

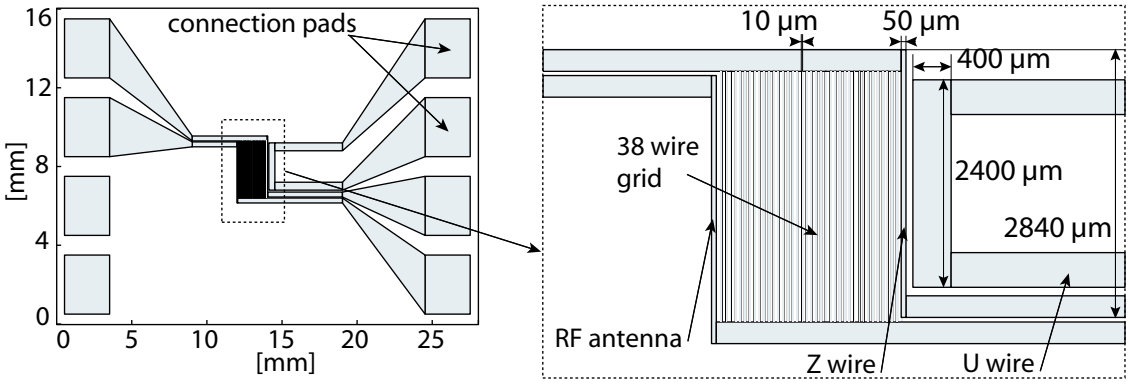

Figure 5.1: Design layout of the first generation atom chip. Note that all wires are connected among each other.

closer to the wire, in order to increase the atomic density and the elastic collision rate. As outlined in 3.3.1, the confinement of a magnetic trap is limited by the finite size of the wire. Therefore, a small wire structure is preferable.

- In a highly integrated setup, a limited number of vacuum connections to contact the atom chip is available. In our setup, all necessary wire currents have to be created using 8 contacts.

In conclusion, the first atom chip generation was designed to allow for high wire currents in comparably large structures. Still, a low wire aspect ratio (ideally square cross section) would be preferable in order to reduce finite size effects and allow for highly compressed traps. We therefore decided to use electroplating as basic fabrication technique, as it enables the creation of rather high wires ($\approx 10\,\mu$m, compared to $\approx 1\,\mu$m for evaporation).

The choice for the employed materials was motivated by the need of high wire currents. As outlined in section 3.3.1, the maximum current in a wire is determined by the dissipation of ohmic heat to the chip support.

For the chip carrier substrate we chose a single crystal silicon wafer of $250\,\mu$m thickness. Silicon is an excellent thermal conductor (K=1,46$\times 10^4\,$WK^{-1}m^{-2}) and a standard material in microchip fabrication. As silicon is a semiconductor, the substrate has to be covered with an insulation layer before the chip wires can be fabricated. This is usually done by oxidizing the substrate at high temperature and thereby creating a layer of insulating SiO_2. As silicon oxide is a bad thermal conductor (K=6,5$\times 10^8\,$WK^{-1}m^{-2}), this layer has to be kept as thin as possible. We found a layer of 200 nm sufficient to suppress current leaks to the substrate. The chip wires are fabricated in gold, which has low ohmic resistance ($\rho_0 = 2,2\times 10^{-8}\,\Omega$m) and can conveniently be used in thermal evaporation as in electroplating.

5.1.2 Wire pattern

Figure 5.1 shows the wire pattern of the first generation of atom chips used in our setup. It contains a large U shaped wire of $400\,\mu$m width and a central region of $2400\,\mu$m length. With a height of $\approx 5\,\mu$m it should be able to carry up to 25 A continuous current. In experiments, we used up to 5 A without observing any heating or degradation of the wire.

Close-by, we fabricated a Z shaped wire of $50\,\mu$m width and $2840\,\mu$m length in the central region, the current is brought to this wire by connection leads of $200\,\mu$m thickness. This wire can theoretically carry 4 A continuous current and was used up to 3 A in the experiment. The

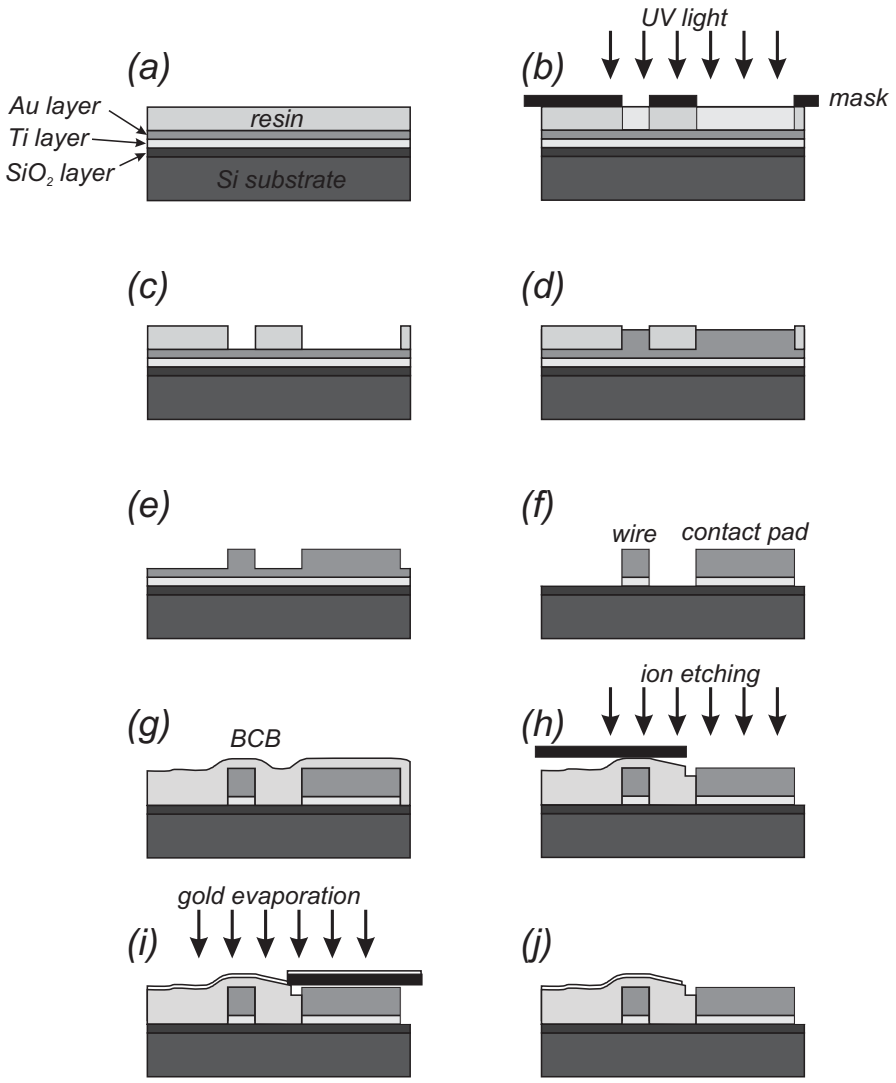

Figure 5.2: Fabrication steps of the first generation single layer atom chip. The different processes are explained in the text.

first Bose-Einstein condensate achieved with the setup was created in a magnetic trap provided by this wire. This magnetic trap and the wire itself have been investigated in great detail in order to understand the origins of random potential roughness, as will be presented in chapter 6 of this manuscript. A second Z shaped wire with the same dimensions was used as a radio frequency (RF) antenna in evaporative cooling.

Between the two Z wires, a grid of 38 parallel wires of 10 μm width, separated by 50 μm was fabricated to create an array of parallel traps. These wires were never used in an experiment.

All the wires in the central region of the atom chip are connected to contact pads of 3 mm$\times$ 3 mm size at the side of the chip. A ribbon of copper wires of the same size will be mechanically clamped on the pads to link the chip wires to the vacuum feedthrough as will be described in 5.3.

5.1.3 Fabrication

The basic techniques used for the fabrication of the atom chip are optical lithography and electroplating. Optical lithography allows for the creation of structure sizes of $\approx 2\,\mu$m over a

large spatial surface (several cm^2). The resolution is limited by the wavelength of the (UV) light used for the process ($\approx 400\,nm$). Electroplating allows for the creation of high wire structures ($\approx 10\,\mu m$) in reasonable time.

Mask preparation

A mask for optical lithography consists of a thin glass plate carrying a chrome layer which absorbs the UV light in the exposure of the photoresist. The chrome layer is patterned to carry a negative image of the design to be fabricated. This first "parent" lithography is performed in dedicated electron beam writers. Electron beam writes obtain a very high spatial resolution ($\approx 10\,nm$) over a reduced field of view ($20\,\mu m \times 20\,\mu m$ for the JEOL), to cover larger spatial regions, the sample is displaced mechanically with interferometric precision. In this way, the high resolution of the electron beam can be transferred to a total area of up to $10\,cm \times 10\,cm$. Depending on the surface of the pattern negative, the fabrication of a mask takes up to 20 h. The mask for the first atom chip generation was generated by a JEOL JBX 5D2U with a resolution of 20 nm.

Substrate preparation

As a chip carrier substrate we chose single crystal silicon wafers, which are semiconductors. Therefore, currents might leak from the wires into the substrate, if the wires were directly fabricated on the silicon. To ensure electrical insulation, we thermally oxidize the waver to create a layer of (non-conducting) SiO_2. The wafer is heated to 950° C under continuous flux of H_2 and O_2 in a dedicated oven. Within 1 h, a layer of 200 nm is created, which is sufficient to ensure electrical insulation.

Before starting the actual lithographic process, we create a thin gold layer on the entire substrate, which serves as a "seed" for the electroplating (see figure (5.2a)): a thin Ti layer (200) is evaporated on the entire substrate, followed by a 200 nm layer of Au. The Ti layer is necessary, as the gold does not stick very well on the SiO_2 and tends to peel off in the absence of a Ti contact layer. As Ti and Au have comparable thermal properties, this layer does not affect the heat dissipation from the wire. Both layers are deposited by thermal evaporation under vacuum.

Optical lithography

In the process of optical lithography, the prepared wafer is covered with a photoresist (AZ4562), spinned to the substrate (4000 rpm) and cured for 3 min at 120° C. These values are optimized to obtain a maximum thickness of the resist (limiting the height of the wires) of $6{,}2\,\mu m$. The wire pattern is transferred to the photoresist by illuminating it through the mask for 120 s with UV light (see figure (5.2b)). The resist is developed (AZ400K, diluted 1:3, 60 s), washing away the exposed regions and allowing direct excess to the seed gold layer (figure (5.2c)).

Electroplating

The electroplating is performed in a bath of gold-cyanide solution (PurAGold 402), which is temperature stabilized to 40° C and kept under constant circulation. The chip is mechanically fixed to a non-conducting mount and contacted with a single, capton-isolated wire. The part of the seed layer, which has become accessible in the lithographic process defines the chip wires and acts as a cathode in the electroplating. For convenience, the pattern has been designed to provide a single closed circuit, all wires are connected among each other.

The thickness of the deposited gold layer calculates to $h = 1,05\,j\,t$ using Faradys law, where j is the current density and t the time of deposition. As the surface of the wire pattern is

$\approx$1,5 cm^2, we chose a current of 4 mA to fill the gaps in the photoresist up to 6 μm within 40 min (see figure (5.2c)). The speed of deposition depends delicately on the concentration of dissolved gold, the deposition process has to be monitored carefully to avoid the wire height to exceed the photoresist thickness (figure (5.2d)). Lower currents lead to a more uniform growth of wires over the region of the chip.

After the deposition of gold is finished, the photoresist is washed away by the help of ultrasound in a acetone bath. At this point, all wires are still connected by he seed layers of Au and Ti (figure (5.2e)). The gold seed layer is dissolved in a solution of potassium iodide-iodine for about 60 s which also reduced the gold wires by $\approx$ 200 nm. To finish, the Ti contact layer is etched away by dry reactive ion etching (DRIE) (figure (5.2f)).

The chip mirror

To fabricate a mirror of sufficient optical quality on the atom chip, we use a planarizing resin (BCB, Cyclotene 3022) to level the wire relief of $\approx 6\,\mu$m. When cured in the absence of oxygen (400° C for 2 h under continuous flux of N_2 and Ar), the resin is UHV compatible. The BCB manages to planarize small scale variations ($\approx 1\,\mu$m) of the underlying chip structure and locally creates a smooth surface of good optical quality (figure (5.2g)). However, large surface structures (*e.g.* connection pads, the 400 μm U shape structure), create plateaus, that can not be levelled entirely by the resin. Consequently, the surface reproduced the underlying pattern in a washed out fashion, as indicated in figure (5.2g)).

To allow for electrical contact, the connection pads are uncovered from BCB by reactive ion etching, the central region of the chip being shielded from the (directional) ions by a silicon plate of appropriate size (figure (5.2h)). A thin layer (200) of gold is evaporated onto the BCB in the central chip region to realize the mirror for 780 nm (figure (5.2i)).

The waviness of the chip mirror significantly perturbs the wave front of the MOT beams, creating regions of low intensity close to the surface and hence a reduced capturing of atoms from background gas. The quality if the images taken with a reflected probe beam is less affected, as the imaged object is small compared to the wavelength of corrugations in the mirror.

5.2 A double layer atom chip for realizing a magnetic double well

The second generation of atom chip was designed to realize a magnetic double well potential for Bose-Einstein condensates, as described in chapter 4 of the manuscript. The fabrication started in November 2004 and took about 5 month. This chip is currently under vacuum and first measurements performed are outlined in section 6.3.

5.2.1 Design considerations

The design of the second chip generation was in many respects influenced by the experiences made with its precursor: the transfer of optically pre-cooled atoms from a reflection MOT to the atom chip with the help of a U shaped wire structure worked satisfactory with the chosen currents and dimensions. Efficient loading of the magnetic trap created by a Z shaped wire structure could be performed, a significant compression of the magnetic trap allowed for efficient evaporative cooling within only 4 s [87].

However, some severe disadvantages showed up in the first design. The central part of the Z shaped wire was designed rather long to capture a large number of atoms far from the surface. When the magnetic trap was compressed and brought close to the trapping wire, the longitudinal trap frequency was reduced to a few Hz, imposing a limit on the elastic collision rate and creating difficulties concerning adiabaticity. We therefore decided to replace the Z shape structure by an H geometry as shown in figure XYZ and described in section 3.3.2. By the use of three independent, floating power supplies, the currents in the central part of the H structure and in the connection leads can be controlled individually, allowing for independent control of the transverse and the longitudinal trapping frequency. The payoff for this flexibility is the consumption of 4 (out of 8) connections on the atom chip.

Cold atom clouds were observed to fragment in the vicinity of the trapping wire. We attributed this to disturbed currents, meandering within the wire [126] and creating random additional magnetic field components. Within this assumption, reducing the dimensions of the wire would reduce the amplitude of the current fluctuations and consequently create a smoother potential. We therefore decided to fabricate square cross section wires for the next chip generation.

The low quality of the gold mirror on the atom chip created regions of reduced light intensity within the intersection area of the MOT beams and strongly reduced the number of pre-cooled atoms. To increase the surface quality and especially level large wavelength corrugation still present in the BCB layer, we learned how to mechanically polish the hardened BCB to sub-lambda quality.

As described in section 4.3, the creation of a stable magnetic double well potential based on a five wire structure necessitates the fabrication of sub-micron chip wires ($\approx 500\,\mathrm{nm}$). In such a double well, the atoms will be located a few microns above the trapping wires and will be extremely sensitive to random magnetic potentials. Consequently, the wire quality has to be improved by several orders of magnitudes compared to the first generation atom chip. These strong constrains are impossible to meet with fabrication techniques based on optical lithography and electroplating. We therefore decided to use direct electron beam lithography and gold evaporation to create the small wire structures. As this technique resembles in many aspects the procedure for the creation of optical masks, it should be possible to obtain a comparable resolution ($\approx 10\,\mathrm{nm}$) over a sufficiently large area.

In a first attempt, we tried to use a fabrication similar to the first chip generation to create the large wire structures and additionally fabricate the small wires directly in the planarizing BCB layer. This approach was not successful for two reasons: in the first place, BCB turned out to

be a very bad thermal conductor (K=3,24×10^{10} $WK^{-1}m^{-2}$). As the thickness of the BCB layer could not be controlled entirely in the mechanical polishing, we usually ended up with several microns of BCB, entirely isolating the small wires from the chip substrate. Due to lack of heat dissipation, the necessary continuous currents (20 mA) could not be send without destroying the structure. Secondly, as will be described in the following, the fabrication of a complete atom chip involves more than 30 different steps. Some of these procedures are extremely delicate and depend on the performance of the employed machines, the purity of involved materials and demand certain skills in handling and manipulation. The probability to successfully complete all steps diminishes with their number and in our case lead to a loss rate of over 80 %.

To circumvent these problems, we decided to realize the two different spatial scales by two different techniques of fabrication on separate chips. As in this approach, the small wires were directly implemented on separate, thin (90 μm) Si wafers, the problem of heat dissipation could be easily overcome. By separating the two main fabrication processed, many samples could be produced in parallel and only the successful ones were assembled to a double layer atom chip.

In the following, we describe the fabrication of the two individual chip layers and how they are joined. As the decision for separate fabrication was taken in the middle of the process, some inconsistencies will show up in the design, *e.g.* the interconnection of the two layers is somehow improvised.

5.2.2 Fabrication of the large structure carrier chip

As mentioned above, one of the aims in the second atom chip generation was to fabricate real square cross section wires with comparable total cross section (15 μm×15 μm instead of 50 μm×5 μm). As even higher wires would create an even more wavy optical mirror, we decided to integrate the wires into the silicon wafer by fabricating them into especially etched groves.

Substrate preparation

To etch groves of a designed pattern into the silicon wafer, a first lithographical process becomes necessary. We therefore oxide the Si wafer at 950° C under O_2-H_2 flux over night (10 h), to create a thick layer of SiO_2, which will be used as an effective mask in the Si etching process. To pattern the SiO_2, we apply a negative photoresist (AZ5214) to the sample (spinning 4000 rpm for 30 s, cure for 60 s at 125° C) (figure (5.3a)). The design is transferred to the resist by illuminating it by UV light through a negative mask (6 s) (figure (5.3b)). The photoresist is cures again at 125° C for 45 s and then is entirely exposed (without mask) to UV light for another 20 s ("flood"). The development is done in AZ726Nif (30 s), washing away the resist, where it has NOT been exposed to UV light. This slightly more complex procedure allows for "negative" lithography, where the mask carries a pattern identical to the one produced in the pattern (not inverted). As usually the surface of the structure to be produced is much smaller than the untouched surface, this saves a lot of time in the fabrication of the mask. Secondly, it allows for an alignment of successive lithographic processes by the help of alignment marks, as necessary in the current example.

After the optical lithography, the SiO_2 layer has become accessible on the regions of the wire pattern as indicated in figure (5.3c). Using the photoresist as a mask, we locally remove the SiO_2 by directive ion etching ($\approx$ 4 min) (figure (5.3d)). Afterwards, the resist is removed in an acetone bath with the help of ultrasound. We thereby have created a mask of SiO_2, carrying the wire pattern, directly on the Si for the following wet etching process (figure (5.3e)).

The etching of the silicone is performed in a temperature stabilized (80° C) bath of TMAH, which is held under rapid rotation by a magnetic beater to avoid the accumulation of bubbles on the sample, which lead to inhomogeneous etching. The Si etching follows the (1,1,0) and (1,0,0) surfaces of the crystalline structure, thus creating groves under an angle of 55 ° as depicted in

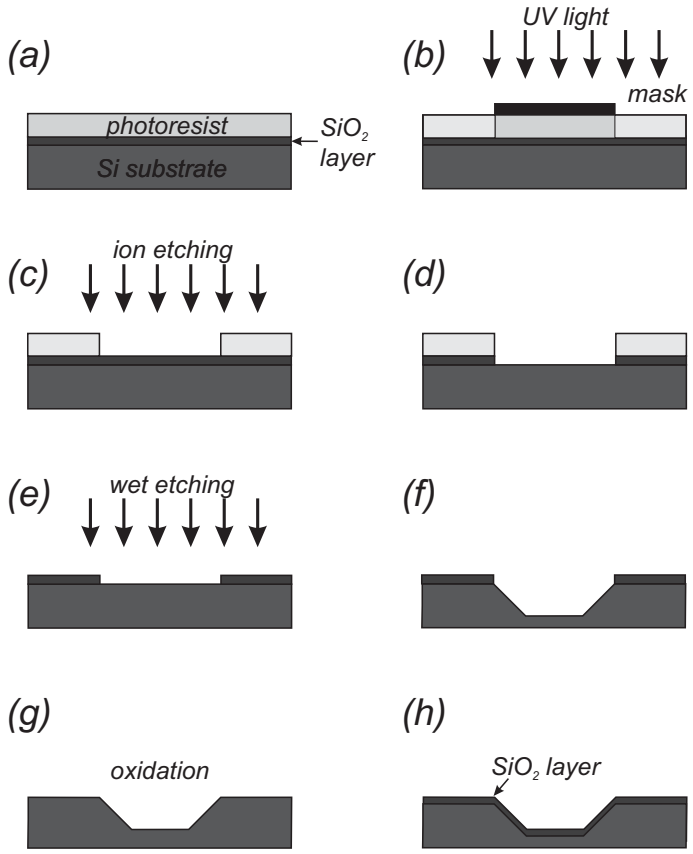

Figure 5.3: Fabrication steps to etch the wire pattern into the Si carrier substrate. Details can be found in the text.

figure (5.3f). The process is rather rapid (1,4 μm/10 min), depending on TMAH concentration and purity, and has to be monitored carefully.

After the desired depth of 15 μm has been achieved, the SiO_2 mask is removed in a HF solution (20 s) and one ends up with a pure, now patterned Si wafer (figure (5.3g)). This wafer is oxided again at 950° C (2 h) to create a closed layer of SiO_2 for electrical insulation of the wires (figure (5.3h)), which will now be fabricated in the groves in a second step of optical lithography.

Optical lithography

For the second step optical lithography, we apply a negative photoresist (AZnLof 2070) to the sample (spin at 4000 rpm for 20 s, cure at 100° C for 60 s) [127]. We use a special mask positioner to align the pattern for the second lithography with the pattern already present in the substrate to a precision of $\pm 2\,\mu$m (figure (5.4a)). Alignment crosses in the patterns can be seen in figure XYZ. The pattern is transferred to the photoresist by a 34 s pulse of UV light. After development, the SiO_2 insulation layer has become accessible at the surface of the wire pattern (figure (5.4b)).

From here on, the fabrication process proceeds as in the first generation atom chip: a contact layer of Ti (200) followed by a gold seed layer (200 nm) is evaporated to the substrate, unwanted Ti/Au is removed by lift-off in an acetone bath (figure (5.4c,d)).

In the second generation wire design, not all wire structures are connected among each other (see figure XYZ), *e.g.* the connection leads to the small wires have no contact to the H/U shaped structure. To generate a single cathode for the electroplating process, all wires are connected in the region of the contact pads by wire bonding (25 μm gold wire).

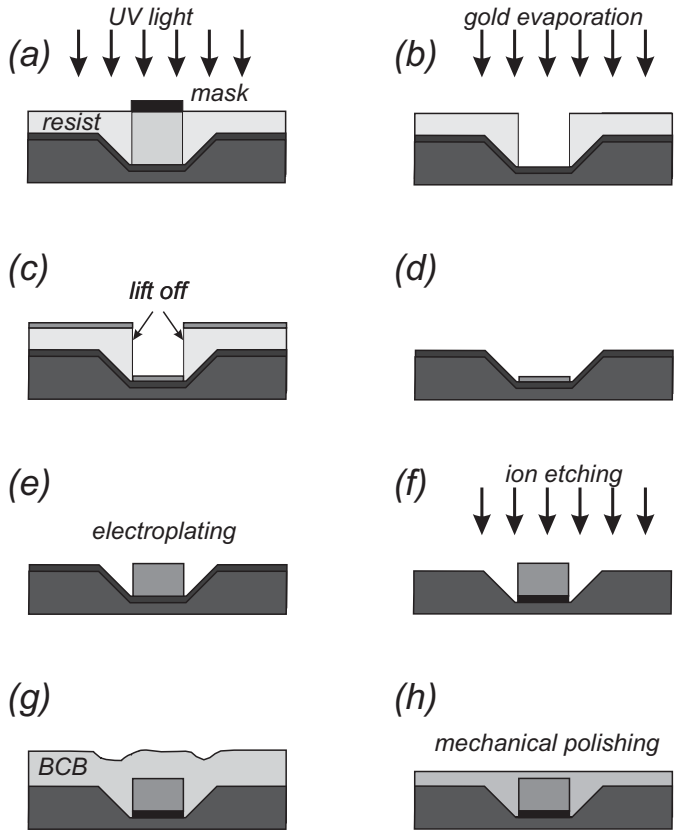

Figure 5.4: Fabrication steps for the large wire structures, based on optical lithography and electroplating. A closed surface is created by a mechanically polished polymer resin. Details can be found in the text.

Electroplating

The electroplating is carried out in the same bath of gold-cyanide as described in 5.1. As no photoresist of a thickness above 6 μm cold be found, the gold is allowed to grow freely starting from the seed layer (compare figures (5.2d) and (5.4d)). Even for wires of 15 μm height, the gold was found to grow sufficiently straight to create almost quadratic wire cross sections. However, the "free" electroplating process appears to be more sensitive to inhomogeneities in the electric field lines of the cathode, the gold preferably deposits at the wire edges, giving rise to slightly "hollow" wire profiles. This could be partially avoided by a very slow deposition process (2 mA deposition current, 2 h 30 deposition time).

After the groves in the Si substrate have been filled up with gold wires of appropriate height, the bonding wires were removed mechanically under a binocular microscope(figure (5.4e)).

The planarization layer

To create a closed, flat surface for further fabrication steps, we applied a layer of BCB planarizing resin. As in the first atom chip generation, the hard cured resin reproduced large features of the underlying structure. To remove this waviness, we decided to mechanically polish the BCB layer. In first attempts it showed, that the resin adheres only weakly to the SiO_2 layer of the chip substrate and easily comes off, when exposed to mechanical stress. This can be overcome by removing the SiO_2 layer by reactive ion etching before applying the BCB (figure (5.4f)).

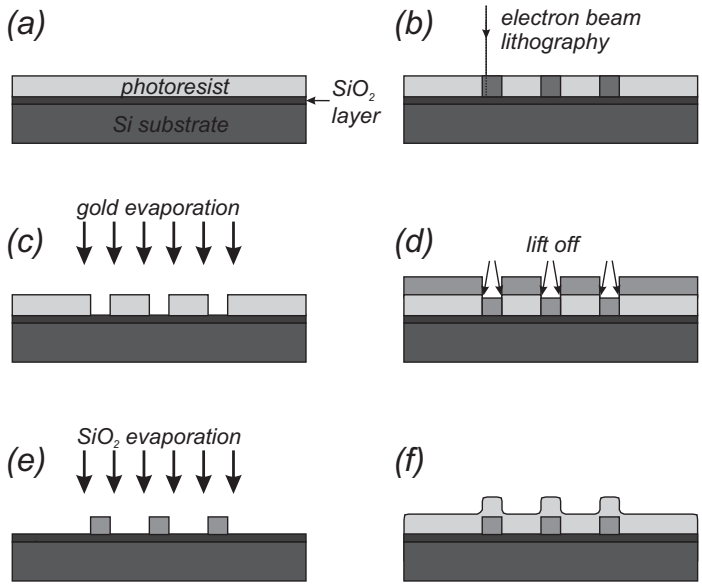

Figure 5.5: Fabrication steps of the five wire structure, based on direct electron beam lithography and gold evaporation. Details can be found in the text.

The polishing was performed using a semi-automatic machine (PRESI P123), applying successive steps using different abrasive materials (*e.g.* AlO_3 spheres of 2 μm, 0,7 μm and 0,3 μm diameter). In this way, several microns of BCB were removed, creating a surface of optical quality, with no corrugation caused by the underlying structure (figure (5.4h)). However, the thickness of the remaining BCB layer was hard to control, the final surface had a slight curvature due to uneven transport of abrasive material to the central region of the atom chip. Although improved, the adherence to the Si substrate was not perfect, the sample loss rate in the polishing procedure was about 50 %.

After polishing the BCB, it was removed from the chip contact pads using reactive ion etching as described in section 5.1.3 (see also figure (5.2h)).

5.2.3 Fabrication of the five wire chip

After several futile attempts to fabricate the five wire structure directly on the BCB layer (insufficient heat dissipation, insufficient flatness, BCB deforms under the influence of the electron beam in lithography), we decided to build a double layer chip and fabricate the sub-micron structures on a separate waver.

Substrate preparation

As described in section 3.3.1, the confinement (namely the gradient) of a magnetic trap is inversely proportional to its distance from the wire (see equation (3.14)). As placing a second substrate on top of the large wire structures necessarily imposes a lower limit on this distance, we chose a very thin (80 μm-100 μm) Si wafer (1 inch diameter) as carrier for the second chip layer. As described above, this substrate was oxidized to create a 200 nm insulation layer of SiO_2. We spin a layer of PMMA (50 g/L), a resist that is developed when exposed to an electron beam, to the substrate (2000 rpm for 33 s, cure at 150° C for 10 min). The so prepared sample (see figure (5.5a)) is then inserted into the beam writer for electron beam lithography. For the

following precesses (namely the cleaving of the wafer) it is necessary to align the wire pattern with the crystal axis of the Si, indicated on the waver by a small notch.

Electron beam lithography

As a beam writer, we used a LEICA EBFG5000 series, which was installed in a prototype version at the LPN. Due to improved control of the electron beam (higher energy, self alignment, active electromagnetic shielding of the whole beam writer lab), this machine can write a $200\,\mu\text{m}\times200\,\mu\text{m}$ field of view with a resolution of 2 nm (figure (5.5b)). The sample is mechanically displaced under interferometric control to the same precision, in total, wafers up to 15 cm diameter can be treated. The LEICA uses auto focussing to optimize the size of the electron beam, whenever starting a new writing field. This auto focus can compensate for $2\,\mu$m difference of level over the whole surface of the sample. That means, that height variations (*e.g.* due to edge effects when depositing the photoresist have to be below this value. As we are using the thickest possible layer of resist (800 nm) this turned out to be problematic, creating a sample loss rate of 40 %.

Gold evaporation

After successfully writing the pattern (25 min), the resin is developed (MIKB, 75 s) and cleaned in isopropanol. The SiO_2 has now become accessible, where the wire pattern has been written (figure (5.5c)). The wires themselves are now fabricated by (gold) evaporation.

The sample is therefore placed in a multi evaporation vacuum vessel. To improve adherence to the SiO_2 and remove remaining bits of resist, the substrate was exposed for 20 s to a beam of accelerated ions (a short step of reactive ion etching (20 s) has the same effect). Then, a mediating layer of Ti (50) was evaporated to the substrate, followed by a gold layer of 700 nm thickness, monitored by a quartz oscillating crystal (4 /s). The temperature of the electrofused gold had to be controlled by hand to avoid boiling and bubbles in the gaseous jet to the substrate. The gold deposition turned out a very delicate step in the fabrication, the loss rate was 50 %.

The redundant gold layers are washed away by lift off in heated (80° C) trichlor ethylen, leaving behind the gold five wire structure (figure (5.5d,e)).

The chip mirror

To electrically isolate the five wire structure from the gold mirror, the substrate is entirely covered with a 800 nm layer of SiO_2, deposited by plasma enhanced chemical vapor deposition (PECVD) (figure (5.5f) and (5.6a)). To regain access to the contact pads, a Si wafer of appropriate size is positioned to cover the central region of the chip, the accessible SiO_2 is removed by reactive ion etching (15 min) (figure (5.6b,c)).

To protect the contact pads during the evaporation of the gold mirror, we employ another step of optical lithography: photoresist (AZ5214) is applied to the substrate (spin at 4000 rpm for 33 s, cure at 125° C for 60 s), the contact pads are covered by small pieces of Si, the uncovered surface is exposed to UV light for 15 s, the photoresist is developed (MIF726, 30 s). The contact pads are now covered with photoresist (figure (5.6d-f)).

The gold mirror is fabricated identical to the gold wires: an adherence layer of Ti (50) is evaporated under vacuum, followed by 200 nm of gold (figure (5.6g)). The gold deposited on the photoresist is removed by lift off in an acetone bath, allowing access to the gold contact pads of the five wire structure below the mirror (figure (5.6h)).

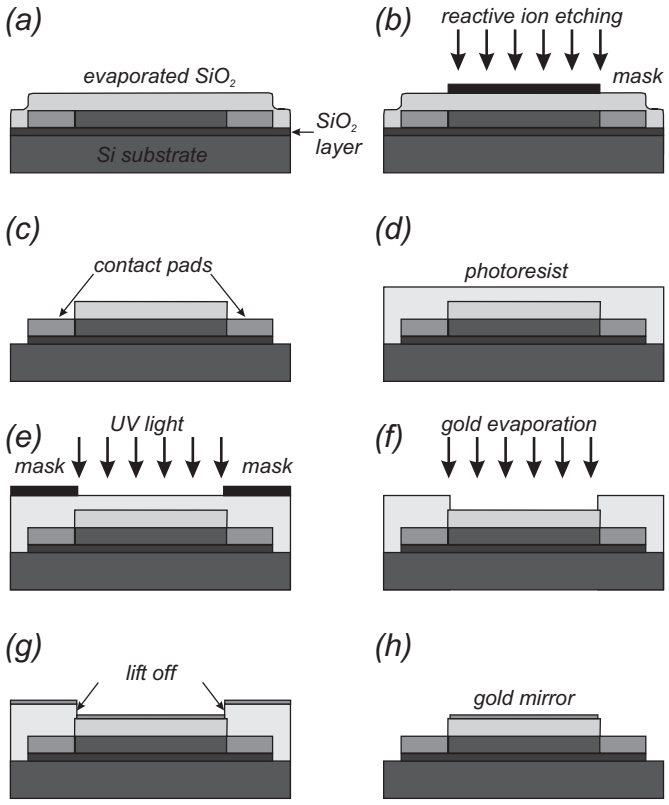

Figure 5.6: Fabrication steps for the gold mirror on the five wire structure. Details can be found in the text.

5.2.4 Merging the two chip layers

For the substrate, carrying the five wire structure, to fit onto the large structures chip, it has to be cut to the correct size. As the pattern of the small wires has been aligned with the crystal axes of the Si, this can be done by cleaving. We therefore scratch the surface of the wafer along the contact pads with a sapphire needle in a dedicated machine ("scriber"). The chip is than cleaved along this line with the help of two glass plates, which help to avoid local stress (loss rate 33 %) (figure (5.7a)).

During the fabrication of the large structure chip, alignment crosses where necessary to correctly superimpose the patterns in successive steps of lithography. Identical crosses were fabricated on the five wire chip, to help in the alignment of the two chip layers: the large structure carrier chip was fixed to a microscope with a digitally controlled $x - y$ translation stage, the position of the alignment crosses was determined with the help of the microscope reticle. The small structures chip was manually positioned to align with the stored coordinates. An alignment accuracy better than 50 μm in both directions could be obtained (figure (5.7b)).

To connect the two chip layers, small drops of UHV compatible glue (Epotek H77, 15 %) are applied to the side of the smaller substrate. Positioning the glue between the layers had shown to create mechanical stress during the curing (60 min at 150° C), resulting in a deformation of the thin wafer.

The electrical contact between both chips is realized by gold wire bonding (25 μm), the connection pads of the five wire structure were designed to face the contact pads of the carrier structure (figure (5.7c)). Several bonding wires (up to 5) are used to reduce the resistance of the interconnection. Figure (5.8) shows a photograph of the final, assembled double layer atom

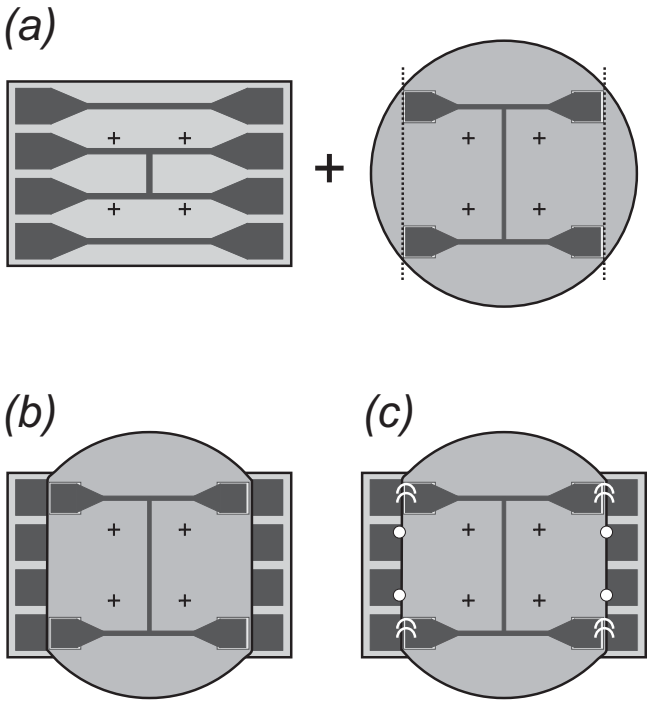

Figure 5.7: Merging of the large structure carrier chip and the small five wire structure chip, which is cleaved to size. The positioning is performed by the help of alignment crosses on both layers, small drops of UHV compatible glue hold the small chip in position. The electric interconnection of both layers is realized by bonding the small structure chip to the connection pads of the carrier substrate.

chip, which is currently in use.

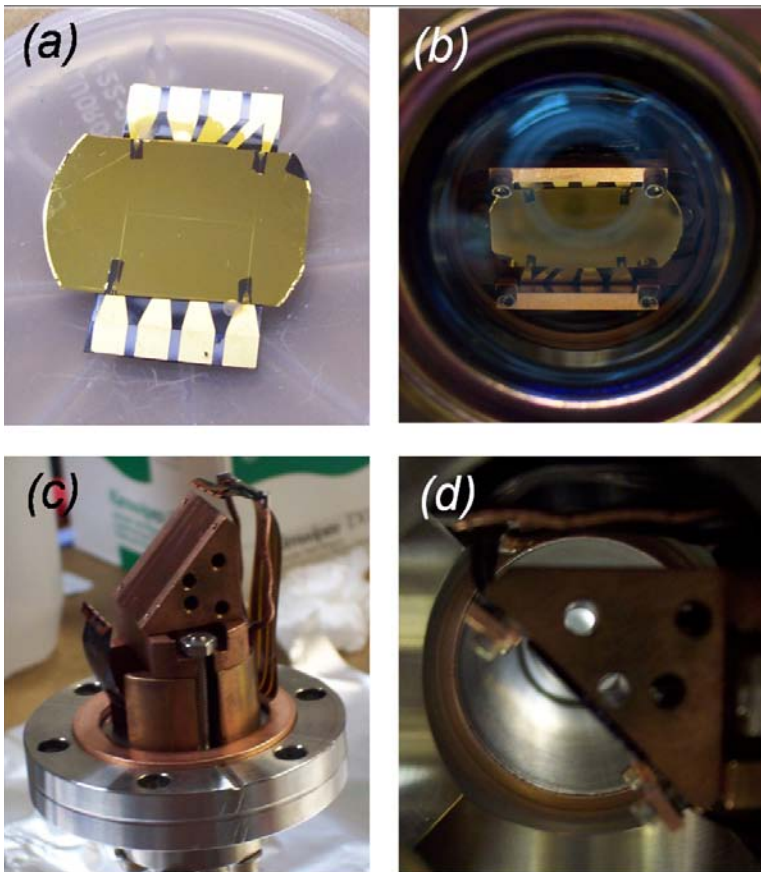

Figure 5.8: (a) photograph of the assembled double layer atom chip. One identifies the 8 large connection pads in the carrier structure as well as the smaller interconnection pads on the five wire chip. On the chip (mirror) surface, a faint H shape structure, which realizes the connections to the five wires in the central region. Alignment crosses, used to superpose both layers, can also be seen. (b) and (d) front and side view photographs of the atom chip under vacuum, mounted upside down under 45 °, to allow atoms to fall freely under the influence of gravity. (c) atom chip mount without chip. One identifies the massive copper heat sink triangle, the two connection ribbons and the single dispenser Rb source.

5.3 Experimental setup

ALL DESCRIBED IN DETAIL::: SO SIMPLE wegen toller atom chips

5.3.1 Chip mount

To hold the atom chip in position within the vacuum system and to provide the electrical contacts, a dedicated mount has to be fabricated. The employed materials have to be compatible with 10^{-11} mBar pressures, UHV compatibility has to be anticipated in the mechanical design (*e.g.* avoiding cavities and hard to evacuate areas). As no active cooling is foreseen in our setup, heat dissipation becomes a major design constrain. The mount has to fit into a (relatively small) stainless steel standard vacuum cube of 7 cm side length, which provides six CF-35 connection flanges.

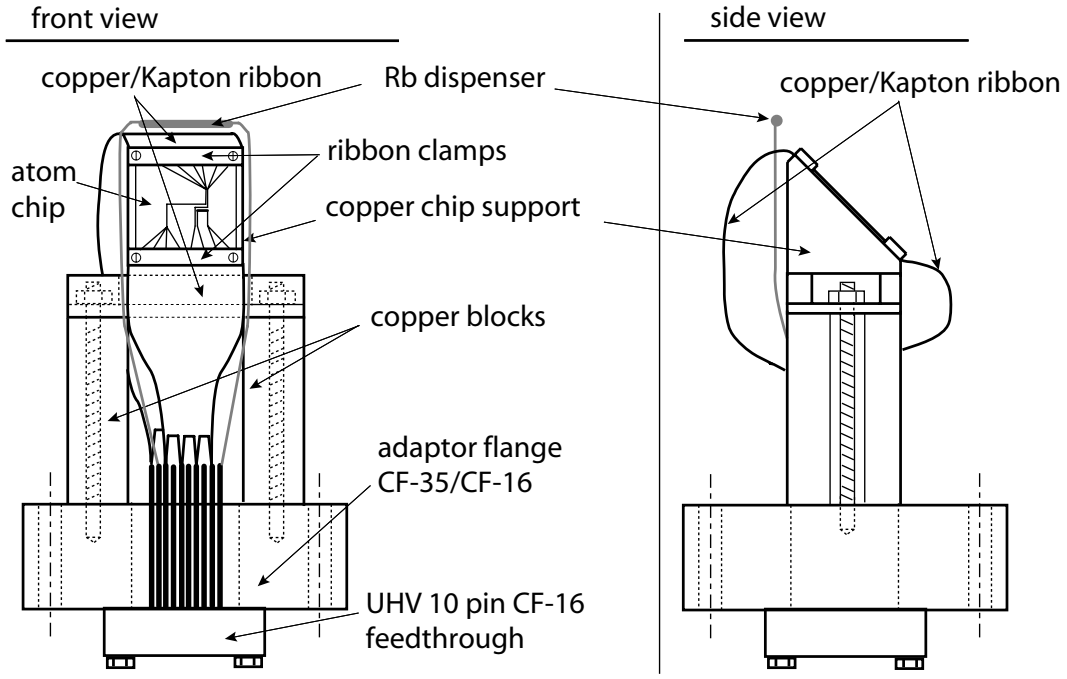

Figure 5.9: Schematic drawing of the atom chip mount, holding the chip upside down under 45 ° in the vacuum chamber. A stainless steel CF-35-CF-16 adaptor flange forms the basis, all other mechanical parts are fabricated out of copper to optimize heat dissipation from the chip. Electrical contact is realized by lithographically patterned copper ribbons, clamped to the chip and connected to a UHV 10 pin vacuum feedthrough. A single dispenser serves as a pulsed source for thermal Rb atoms.

Mechanical mount

The chip mount is constructed on a CF-35-CF-16 adaptor flange, where the CF-16 side carries a standard 10 pin UHV current feedthrough. The mount itself consists of a massive copper triangle, which holds the atom chip under 45 ° in the vacuum vessel as schematically depicted in figure XYZ. Copper was chosen for its adventurous properties such as excellent heat dissipation, UHV compatibility and easy machinability. In a worst case scenario, a total heat of 20 W was assumed to be produced by the atom chip. The mount was designed sufficiently massive to enable a thermal conductivity of 1 W/K to the vacuum vessel, acting as a heat sink. We therefore expect the temperature of the mount not to increase by more than 20° C during constant operation. In practice, the dissipated heat is much below 20 W, additionally, the setup is never in constant operation, the duty cycle is about 33 %. Consequently, no degradation of vacuum due to the operation of the atom chip could ever be observed.

Electrical contacts

The electrical connection between the UHV feedthrough pins and the atom chip is provided by a copper ribbon, which was fabricated onto a Kapton band using standard techniques for the creation of flexible electrical circuits. The dimensions of the copper wires were matched the dimensions of the contact pads of the atom chip. The connection between the feedthrough pins and the copper wires were realized using commercially available UHV luster terminals. To contact the chip, the ribbon was bent to a zigzag shape, which creates a spring-like behavior. The ribbon is then mechanically clamped to the contact pads by two horizontal copper bars (see figure CXYX), realizing an electrical contact of $R < 100\,\mathrm{m}\Omega$.

Rb Dispenser

As indicated in figure CXYZ, the atom chip mount also carries the Rb dispenser, which acts a the only (pulsed) source of thermal Rb atoms in our setup. The dispenser is held in position by two 3 mm copper wires, electrical contact is provided by clamping the dispenser into a corresponding slit in the wires. As for the copper-ribbon, the copper wires are fixed to the feedtrough pins using luster terminals. To avoid a degradation of the chip surface, the dispenser is mounted slightly below the level of the atom chip, so that the connecting copper bar shadows the chip mirror from atoms directly cast by the dispenser.

The dispenser itself is a commercially available model (SAES Getters), containing absorbed Rb, which is desorbed when exceeding a threshold temperature of 450° C. To activate the dispenser, it is heated by ohmic heat when sending a current, the threshold value is 2,4 A [128,129]. In the experiment, the dispenser is contiguously held at a temperature slightly below threshold by a continues current of 2 A, a pulse of Rb atoms is created by increasing the dispenser current to 8 A for about 3 s. After operation, the dispenser quickly cools down to below threshold within ≈ 100 ms.

5.3.2 Vacuum system

As described above, the extreme confinement that can be realized with magnetic micro traps allows for efficient evaporative cooling and to reach the BEC quantum phase transition within only a few seconds. This implicates a relaxation of lifetime constrains for trapped cold atom, consequently Bose condensates can be created in much simpler systems [80]. Following this approach, our apparatus consists of a single chamber vacuum vessel, based on a standard UHV stainless steel cube of 7 cm side length. This cube provides six CF-35 connection ports on the cube surfaces.

Three of these six ports carry UHV optical view ports, anti-reflection coated for 780 nm light. A fourth port carries the above described chip mount. The two remaining openings are connected to vacuum pumps: a CF-35-CF-150 adaptor flange allows the connection to a Ti sublimation pump (Varian TSP cartridge filament source with cryopanel, 500 L/s (N_2), reduced to $\approx$ 80 L/s by the adaptor flange). A second output port is connected to a standard CF-35 4-way cross, which carries another optical view port and connects to a 40 L/s ion pump (Varian VacIon Plus 40 Diode, pump speed (N_2) reduced to $\approx$ 20 L/s by the cross). An additional T-piece connects a cold cathode vacuum gauge and allows for the docking of an additional pre-pump station (roughing pump and turbo molecular pump) for the first evacuation stage after breaking of vacuum.

Operating only with an ion pump and a Ti sublimation pump, the setup presents a "closed system," where vacuum will only degrade very slowly in case of power failure. No moving parts are present, avoiding vibrations during the experimental cycle.

The vacuum quality in this setup without operating the Rb dispenser is $\approx 2 \times 10^{-11}$ mbar, which is also the lower limit of the vacuum gauge. A 3 s pulse of the Rb dispenser degrades the vacuum by one order of magnitude. As the total volume of the vessel is approximately 1 L and the overall pump speed is about 100 L/s, the vacuum recovers to the 10^{-11} mbar level within less than 2 s.

5.3.3 External Magnetic fields

The homogeneous bias field

As described in section 3.3.1, the basic magnetic wire trap is based on the combination of a circular magnetic field created by the atom chip wire and an external, homogeneous bias field,

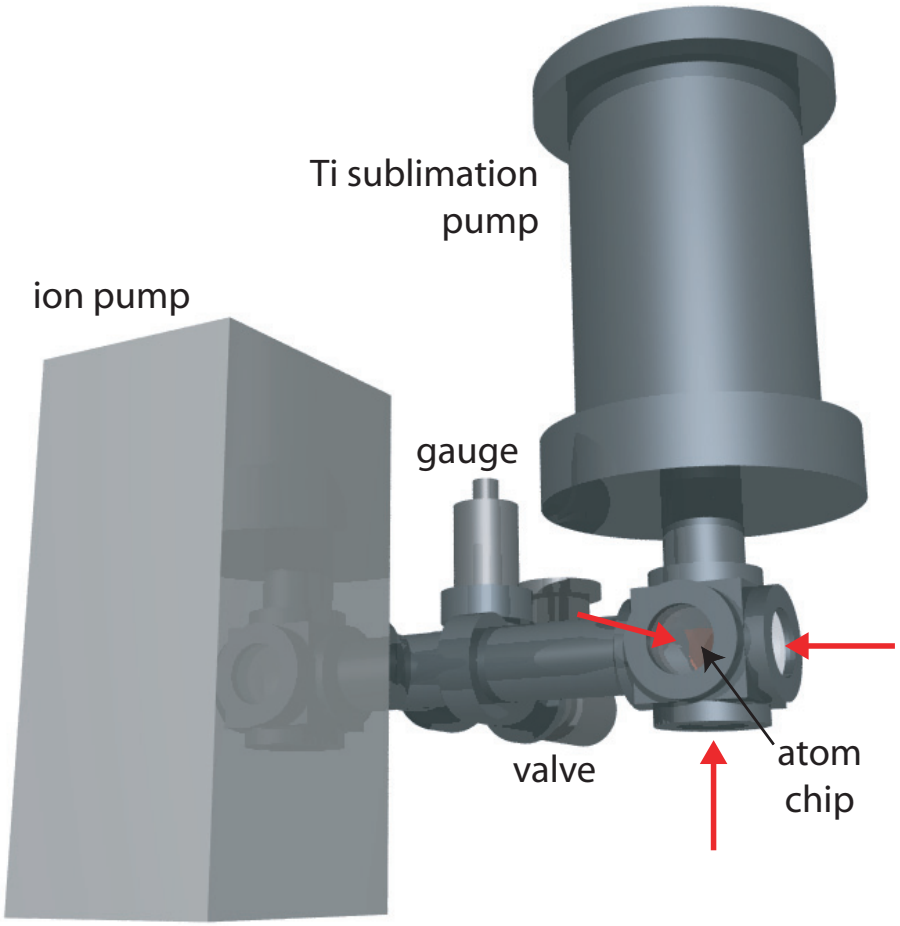

Figure 5.10: Design drawing (to scale) of the vacuum system. A stainless steel cube of 7 cm side length holds the atom chip, it is pumped by a Ti sublimation pump and a ion getter pump. A cold cathode ion gauge allows to monitor the vacuum pressure, which is on the 10^{-11} mbar level.

usually orientated orthogonal to the wire and parallel to the chip surface (compare figure (3.2)). An additional longitudinal "Ioffe" field is necessary to suppress Majorana spin flip losses.

As in our setup, the atom chip is mounted under 45 °, the external bias field has to be tilted accordingly. As a single pair of coils under this angle would be difficult to combine with the four laser beams entering the vacuum chamber, the bias field is created by two orthogonal pair of coils ("horizontal" and "vertical") in Helmholtz configuration. These coils are rectangular and of pyramidal shape, their internal diameter is 7 cm, corresponding to the side length of the stainless steel cube, their external diameter is 10,2 cm. The pyramidal shape enables us to accommodate three pairs of coils in a cube of less than 11 cm around the experimental chamber (see figure XYZ). There pairs of coils are made of Kapton isolated 1 mm copper wire, each has 136 windings. which allows the creation of 12 G/A homogeneous field at the position of the atoms. The total field is limited to 48 G due to the limitation to 3 A of the used power supplies (HighFinesse BCS 12 V/3 A, response time 100 μs). Each coil has a resistance of about 1 Ω, so the total dissipated power is below 10 W, which makes active cooling unnecessary. The inductance of each coil is around 1 mH, it should therefore be possible to turn of the magnetic field within 100 μs. However, Eddy currents in the stainless steel chamber lead to a decay of the magnetic field in $\approx$ 3 ms. In most experiments, the external fields are therefore not switched,

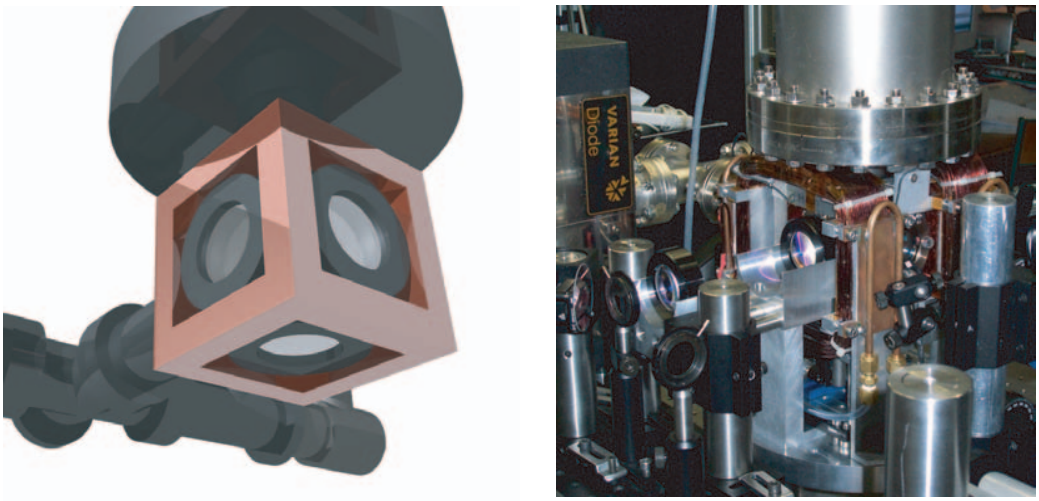

Figure 5.11: Left: design drawing of the coil system surrounding the stainless steel cube. Three pairs of orthogonal, pyramidally shaped Helmholtz coils can be used to create a homogeneous magnetic field in arbitrary spatial direction. Right: photograph of the experimental setup (without magnetic field shielding). One identifies the Ti sublimation pump (upper edge) and the ion getter pump (left edge). Two massive, water cooled MOT coils surround the central cube. The two achromatic doublets, transporting the image of the atomic cloud in a confocal telescope configuration can be identified in the center of the picture.

imaging is performed in presence of the homogeneous external field.

The longitudinal Ioffe field

Whereas the coils creating the external bias field are connected in series, the third pair of coils ("longitudinal") allows for independent control of the currents in each coil with the help of two individual power supplies (home-built current stabilized 2 A sources). These coils can therefore create a homogeneous longitudinal field as well as a superimposed magnetic field gradient, which can be used to translate the magnetic trap along the wire. As lower fields are necessary in this direction, the equally pyramidally shaped coils have slightly less windings (55), which allows for 5 G/A homogeneous magnetic field.

The MOT quadrupole field

For the operation of a magneto optical trap, a quadrupole field with a typical gradient of 15 G/cm has to be generated. This may be provided by a pair of coils in anti-Helmholtz configuration. To reduce the necessary currents, we have approached this pair of coils as close as possible to the stainless steel cube, the outer dimensions of the rectangular MOT coils are $\approx 12,5$ cm. These coils consist of 200 windings of 2 mm isolated copper wire, 9 A are employed, provided by a switching power supply (Delta electronics ES-15-010, 15 V/10 A). The total power dissipated in these coils is ≈ 90 W. To evacuate the generated heat, massive water cooled copper blocks were clamped to the coils, which reduced the overall heating of the system to less than 10° C.

5.3.4 Laser System

In a simple single chamber setup as employed in our setup, the requirements regarding the optical laser system are relaxed: as the capturing area in a reflection MOT is reduced in the

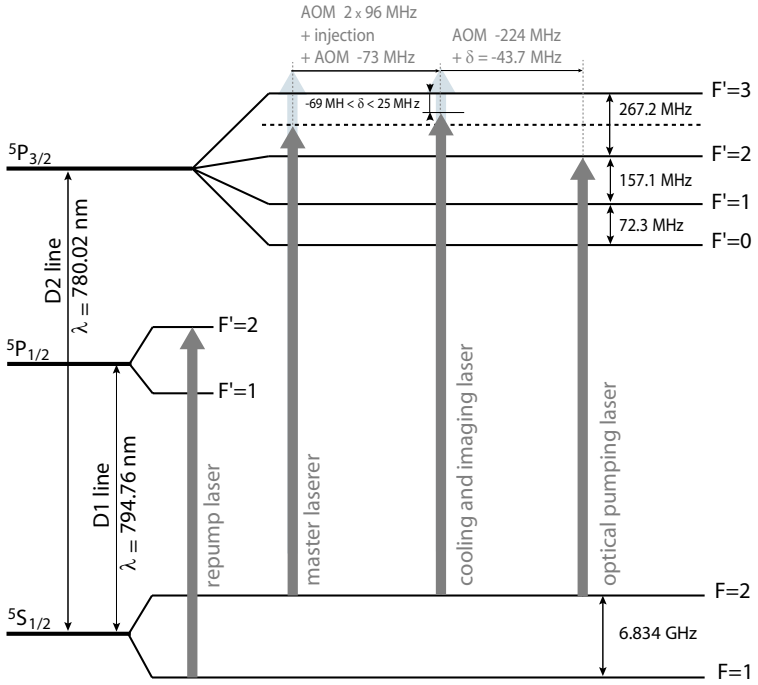

Figure 5.12: ^{87}Rb levels used for laser cooling, optical pumping and absorption detection in the Orsay setup. The individual components are described in the text.

presence of the surface, rather small beam diameters can be used, necessitating only small laser power. We were able to work with a simple optical setup, based on only two main lasers (one of which in an master-slave configuration), which occupies about 1 m^2 on an optical table. The laser system has been described in detail in [87] and [73], only its main features will be briefly resumed in the following.

The master-slave cooling laser

As a master laser we use a Sanyo DL-7140-201 (70 mW) diode, centered at 781 nm and with a spectral width of ≈ 10 MHz. As this width is too large to efficiently laser cool ^{87}Rb atoms, the laser diode is employed in a Littrow extended cavity setup, narrowing it to $\approx 1,5$ MHz [130,131]. The laser is frequency stabilized to the 2-3 crossover of the $F = 2 \leftrightarrow F' = 2/F' = 3$ transition of the D2 line of ^{87}Rb in Doppler free absorption spectroscopy (780,02 nm). The feedback is based on FM spectroscopy, modulating the atomic transition via Zeemann effect with the help of a small coil around the absorption cell. This technique avoids frequency sidebands, that arise when directly modulating the laser frequency.

Stabilized in this way, the master laser implements a frequency standard, detuned by -133 MHz with respect to the $F = 2 \leftrightarrow F' = 3$ cooling transition. This laser light is injected into an acusto optical modulator (AOM) in double pass configuration, which allows the shift the optical frequency between +138 MHz and +232 MHz without moving the beam in space. This light is now injected into a slave laser, based on the same Sanyo diode but without external cavity. The hence amplified laser light passes another AOM at -73 MHz, which serves as a rapid switch and shifts the total laser detuning to between -69 MHz and +25 MHz with respect to the $F = 2 \leftrightarrow F' = 3$ transition. After the AOM, the laser power is ≈ 50 mW, this light is divided as follows to serve different purposes in the experiment:

Optical cooling For laser cooling the atoms, 45 mW are extracted, the beam size is enlarged to

16 mm diameter. With the help of polarizing beam splitter cubes, the light is distributed among four branches, which are prepared to the correct circular polarization and injected into the vacuum chamber to realize the magneto optical trap. The laser detuning in this stage is typically ≈ 15 MHz.

Imaging About 1 mW is extracted from the slave laser beam, which is enlarged to 1 cm diameter and attenuated to $1/10\, I_{sat}$, where I_{sat} is the saturation intensity of the atomic transition (1,6 mW/cm^2). The beam is superimposed with a MOT beam and reflected on the atom chip mirror before reaching the camera, creating a double image of the atomic cloud (see next section). As the frequency of the light emitted by the slave laser can be adjusted over a large range (-65 MHz to +25 MHz), we are able to compensate for an occasional Zeeman shift of the atomic resonance in the presence of magnetic fields. This is especially convenient in magnetic micro trap experiments: as the trap is formed by a combination of an inhomogeneous magnetic field created by the current carrying wire and an homogeneous external bias field, the trap can be extinguished by simply switching off the wire current. As such a chip wire has negligible inductance, this can be done very rapidly (50 μs in our case, limited by the Highfinesse power supplies). By imaging in the presence of the homogeneous external field, problems due to coil inductances and Eddy currents can be overcome.

Optical pumping The remaining power if the slave laser light (3 mW) is injected into another AOM, which shifts the light frequency to be resonant with the $F = 2 \leftrightarrow F' = 2$ transition. Provided the correct polarization, a short light pulse on this transition allows to polarize the atomic sample by optical pumping and thereby enhance the capturing efficiency of the magnetic trap.

All three beam path are controlled by individual mechanical shutters.

The repump laser

To close the optical cooling cycle we have to re-inject atoms that decay to the $F = 1$ hyperfine state. In our setup this is implementing by shining in light at the $F = 1 \leftrightarrow F' = 2$ transition of the D1 line (794,76 nm). For this we use a Mitsubishi MI641140N laser diode (30 mW) of ≈ 10 MHz spectral width. The advantage of the D1 $F = 1 \leftrightarrow F' = 2$ transition over the corresponding D2 line is the enhanced level spacing (≈ 800 MHz compared to ≈ 80 MHz), which can be easily resolved even with a spectrally broad laser diode, avoiding the need for an extended cavity solution. The laser is stabilized to the atomic line by FM spectroscopy, identical to the cooling master laser. The repumping light is superimposed to a MOT beam (anti-parallel to the optical pumping beam) and is only controlled by a mechanical shutter.

5.3.5 Atom detection

We used standard (destructive) absorption imaging to detect trapped atoms *in situ* or after being released in time of flight expansion [132]. As the region around the central stainless steel vacuum cube is hard to access, we transport the image of the atom cloud with the help of a confocal telescope. This telescope consists of two achromatic doublets of a focal length of 63 mm and 38 mm diameter, it works at the diffraction limit, the numerical aperture is 0,3, allowing for a resolution of 3 μm.

A third simple plano convex lens of 60 mm focal length is used to focus the image of the atomic cloud onto the surface of a CCD camera chip. By varying the distances between the telescope and this lens as well as between the lens and the camera, we can adjust the magnification of our optical system, we usually work with a magnification $\times 3$.

The camera is a Princeton Instruments ST138 with a Kodak chip of 512×768 pixels, each of which is 9 μm×9 μm in size. The quantum efficiency at 780 nm is 45 %, each pixel can bin up to 850000 electrons, the electronic noise of the 12 bit a/d converter is 10 electrons. We have removed the glass vacuum window of the (initially evacuated) camera to avoid fringes due to multiple reflections between window and the CCD chip.

5.3.6 Experimental Control

Up to now, almost any cold atom or BEC experiment relies on a destructive read-out technique; extracting information about the state of the system destroys the specific sample. An experiment therefore has to be repeated many times in order to accumulate statistics or investigate dependencies on experimental parameters. A major experimental task in design of such a setup is to verify the repeatability of the cycle, in order to realize the same conditions in every run.

The creation of a Bose-Einstein condensate is a complex procedure and involves many steps taking place on different timescales: very short optical pulses have to be controlled on the μs level, magnetic fields have to be switched in ms, the loading of a magneto optical trap can take tens of seconds. To pilot all stages of the cycle with the required precision and ensure repeatability, a sophisticated, computer based electronic control system becomes necessary.

In our setup, we employ a home-built "sequencer", realized by the group electronics engineer A. Villing. This sequencer consists of a motherboard, which implements an independent, external 8 MHz clock and manages the dialog with the control computer. Up to eight signal output cards, carrying TTL, analog level or analog ramp channels can be added to the motherboard, synchronizing to the same clock and using individual on-board memory. The jitter between different cards is below 5 μs.

The experimental sequence is programmed on the control computer using a script language, developed by J. Esteve and D. Stevens, a more detailed description can be found in [73]. Often used experimental parameters can be easily manipulated in a graphical interface, the readout (namely the camera signals) is processed immediately after a successful cycle, directly providing a low level analysis of the run.

In each experimental cycle, the sequence is written from the control computer to the motherboard and from there distributed to the different cards. Once the programming finished, the main board awaits a start trigger, once the trigger received, the sequence is written out to the different channels, completely independent of the control computer. This independence from the (uncontrolled) real-time behavior of the computer (which e.g. shows up in ±10 ms fluctuations in the programming time) allows us to obtain a synchronized signal precision of 10 μs over the entire experimental cycle of $\approx$ 25 s.

Chapter 6

Experimental results

6.1 Bose-Einstein condensation

Since the first realizations in 1995 [8,133,10], Bose-Einstein condensates have attracted enormous interest in the physics community; today more than 80 research groups have realized BEC all over the world. The exceptional properties (*e.g.* phase coherence) of Bose condensates have lead to numerous proposals to (among many others) employ this "state of matter" as coherent source in the field of *atom optics*, in close analogy to coherent optics with photons. Due to their hight flexibility in the design of trapping and manipulation geometries, atom chips seem promising candidates for the implementation of atom optical elements [134, 135, 85]. In consequence, the standard procedures for the creation of Bose-Einstein condensates have been adapted and combined with the atom chip approach.

The first realization of BEC on atom chips has been achieved by groups by J. Reichel [80] and C. Zimmermann [81] in 2001. Their approach showed, that taking benefit from the strong confinement of magnetic wire traps, the experimental setups could be significantly simplified, remedying the need for double MOT systems or Zeeman slowers. Other groups have since than realized Bose condensates on atom chips, either following the simplified scheme or combining atom chips with conventional BEC technology [108, 82, 98, 88, 118, 136, 137].

Our group achieved Bose-Einstein condensation in 2003 following the scheme of [80]. A detailed description of the setup as well as the experimental sequence can be found in the theses of C. Aussibal [87] and J. Estève [73].

The procedure for the creation of a Bose condensate on an atom chip mainly follows the well travelled path of conventional setups (based on magnetic traps): pre-cooling of atoms in a magneto optical trap, additional cooling through optical molasses, spin polarization of the atomic sample by optical pumping, transfer to a non-dissipative magnetic trap, evaporative cooling. However, some stages have to be modified to comply with the atom chip approach: the presence of the atom chip is usually hard to combine with the extensive optical access needed for a conventional 6-beam MOT. This problem has been overcome by the so-called *surface reflection MOT*, where two incoming beams are replaced by beams that were reflected on the chip surface, acting as a mirror. This enables the creation of a MOT of reduced capturing area in the vicinity of the chip wire structures. The transfer of atoms captured in a magneto optical trap to the magnetic micro traps (of extremely small capturing area) is a crucial phase of the experiment and is often done with the help of an intermediate MOT stage, where magnetic fields are created by large wire structures on the chip, which are by construction well aligned with the magnetic trapping fields.

Once transferred to the magnetic trap, the atoms can be efficiently (and rapidly) cooled to quantum degeneracy. Due to the reduced capturing capacities of the reflection MOT and the magnetic micro trap, atom chip experiments usually work with comparably low atom numbers

in the condensate (10^3-10^5) but allow for high experimental repetition rates ($\approx 10\,\mathrm{s}$/cycle).

In the following, we will briefly resume the experimental sequence for the creation of a Bose-Einstein condensate in our setup, more detailed descriptions can be found in [87, 73].

6.1.1 Magneto optical surface traps

The pulsed atom source

As described in section 5.3.1, we use a single, pulsed dispenser as a source for thermal Rb atoms. The dispenser is operated by ohmic heat, it is activated, once the threshold current of 2,4 A is exceeded. The filament is held at a temperature near threshold by running a continuous current of 2 A, it is pulsed by increasing the current to 8 A for a time of 3,6 s. The pulse creates a Rb vapor which loads a magneto optical trap but degrades the vacuum quality by at least one order of magnitude. As the lifetime of atom trapped in a magnetic trap depends on the quality of the background pressure, vacuum has to recover before the atoms can be transferred. We therefore hold the atoms in the MOT for 12 s before the transfer. As during this hold time, the number of atoms in the MOT decays, a compromise between transferred atom number (favoring a short hold time) and magnetic trap lifetime (favoring a long hold time) has to be found. A dispenser pulse time of 3,6 s and a hold time of 12 s allow for the transfer of 3×10^6 atoms to the magnetic trap, which then has a lifetime of $\tau > 10\,\mathrm{s}$. Both values are optimized to reach Bose condensation of 1×10^4 atoms within 4 s of evaporative cooling.

When running the experiment continuously, the average vacuum pressure is slightly above the value which is obtained without operating the dispenser. To guarantee for stable experimental conditions, we have implemented an experimental background cycle, which continuously simulates an experiment, involving the dispenser pulse and all operations on elements, that experience temperature changes (coils, wire currents). A self-adjusting dead time at the end of the experimental sequence guarantees constant total duration of the cycle, even when changing timings within the sequence. In this way, stable experimental conditions can be obtained, the system takes about 10-20 cycles to reach the stationary regime concerning vacuum pressure and temperatures when turned on.

Reflection MOT with external quadrupole field

As described above, the technique of laser cooling [ZITATE], relying on the combination of a quadrupole magnetic field and six orthogonally intersecting laser beams, can be combined with atom chips, when using the chip surface as a mirror in a reflection surface MOT. Here, two of the originally six beams are replaced by reflections on the chip surface, which makes a 45 ° angle with the two incoming and the two reflected beams. Although having become a standard technology, the surface MOT still crucially depends on the quality of the chip mirror. We managed to largely improve the flatness of the gold mirror in the second atom chip generation, which immediately increased the performance and stability of the surface MOT. Still the capturing efficiency is reduced compared to conventional setups due to inhomogeneities in the reflected beam intensity and a reduced capturing area owing to the presence of the atom chip.

In most atom chip experiments, the substrate is mounted upside-down to allow the atoms to fall freely under the influence of gravity, when released from a trap. To allow for the use of standard UHV vacuum components and horizontal and vertical laser beams (with respect to the surface of the optical table), the chip is mounted upside-down under 45 ° in our setup, as can be seen in figure (5.8). The four MOT beams necessary for the surface MOT are simply injected into the vacuum cube by standard anti-reflection coated view ports.

The magnetic quadrupole field in the first 12 s phase of laser cooling is produced by massive, water cooled coils in anti-Helmholtz configuration, positioned close to the stainless steel cube, as

can be seen in figure (5.11). By mechanical alignment, the position of the quadrupole minimum can be adjusted to to the intersection of the laser beams to a precision of ±3 mm. For fine tuning (and to compensate the earth magnetic field), the center of the quadrupole is shifted by adding a homogeneous external field, created by three orthogonal pairs of pyramidally shaped coils in Helmholtz configuration (see figure (5.11)).

The first magneto optical trap, based on an external quadrupole field, contains about 5×10^5 atoms at a temperature of 150 μK at the end of the 12 s hold time after the dispenser pulse.

Reflection MOT based on a U shaped wire

The magneto optical trap based on an external quadrupole magnetic field is located 1-2 mm above the atom chip surface, the position with respect to the chip wires is not very well defined. The magnetic trap created by such a wire has a small capturing area and limited to small distances from the surface (<800 μm). Direct loading of atoms from the surface MOT to the magnetic trap is therefore extremely difficult and inefficient.

To overcome this problem, we follow a proposal of [80] which employs a second surface MOT phase, where the magnetic quadrupole field is directly created by atom chip wires. The position of such a trap can be controlled to high accuracy, it is by construction aligned with chip traps created by different wires.

As described in [87] and [73], a quadrupole magnetic field can be created by the combined fields of a U shaped current carrying chip wire and an external homogeneous bias field. The so-called *U-MOT* will be centered between the wire connection leads, the trap height follows equation (3.12).

Atoms can be transferred adiabatically from the magneto optical trap created by an external quadrupole field to the U-MOT by simultaneously ramping the quadrupole field, the external homogeneous field and the wire current.

However, the U-MOT turned out to be rather unstable, transferred atoms are lost within 100 ms. We attribute the effect to geometric deformations of the magnetic field created by the wire structure, which is of quadrupole shape only in the close vicinity of the minimum ($d < 2$ mm) and thus suffers from a reduced capturing area. The weak performance of the U-MOT justifies the use of external coils and the first MOT phase to collect a large number of atoms. The deficiencies of the U-MOT can be overcome by using an optimized (macroscopic U wire geometry). It has been shown [125]. That a large number of atoms can be captured in such a trap without the need for external quadrupole coils. However, this scheme employs rather bulky structures carrying high currents (60 A) and necessitate active cooling of the chip mounting.

Despite the deficiencies in holding atoms trapped, the U-MOT has turned out to be efficient to rapidly transport atoms close to the chip surface. After accumulating atoms in the "external" MOT during the 12 s hold time, we transfer to the U-MOT by simultaneously ramping down the external quadrupole field and ramping up the U wire current (4A) and the homogeneous bias field (1,8 G) within 40 ms. The atoms are approached to the surface by decreasing the current (2,6 A) and increasing (and rotating) the bias field (3,2 G) within 5 ms, the frequency of the cooling laser is detuned to -20 MHz. The external field is turned

We end up with $\approx 2 \times 10^7$ atoms of a temperature of 140 μK in the U-MOT at a distance of 700 μm from the surface.

6.1.2 Optical molasses and optical pumping

To further reduce the temperature of the atomic sample before transfer to the magnetic trap, we employ a phase of optical molasses [138,139,140,141]. In theory, efficient sub-Doppler cooling is obtained in the absence of magnetic field and with strongly detuned, intensity attenuated lasers.

As no rapid switching off of the homogeneous field (below 3 ms) is possible in our experiment, we ramp down the the U-Wire current and the bias field within 3,8 mx. Simultaneously detuning the laser to -65 MHz already cools the atoms to 40 μK, no further cooling could be obtained in the absence of magnetic fields [87].

As described in section 3.1, we aim to magnetically trap atoms in the double stretched $|F = 2, m_F = 2\rangle$ state, which provides strongest confinement. To spin polarize the atomic sample, we establish a homogeneous magnetic guiding field (in the same direction as the bias field of the U-MOT) to define a magnetic quantization axis. We then shine in a short (50 μs) optical pumping pulse of σ^+ polarized light, resonant with the $F = 2 \leftrightarrow F' = 2$ transition, which successively drives the atoms into the $|F = 2, m_F = 2\rangle$ dark state. In principle, this technique allows to perfectly polarize the atomic cloud and we would expect to gain a factor of 5 in the transferred (to the magnetic trap) atom number [142]. However, as atoms expand freely during the time needed to establish the guiding field ($\approx$ 2 ms), a reduced fraction of atoms is recaptured, scattered photons during the optical pumping additionally heat up the sample. We therefore only could increase the number of transferred atoms by a factor of 2,5 by applying optical pumping, the optimization of the procedure is described in detail in [87].

6.1.3 Magnetic trapping

To efficiently load atoms to a magnetic trap based on a Z shaped wire structure (compare section 3.3.2), the position of the trap has to match the position of the atoms after the optical pumping pulse. Additionally, the trap has to be sufficiently deep to hold the atoms of a specific temperature T. Furthermore, the confinement has to math the spatial extension of the atom cloud. Formally, perfect mode matching is achieved when the transfer to the magnetic trap optimizes phase space density [132].

The potential depth is given by the external bias field as $\Delta V_{\text{trap}} = m_F g_F \mu_B |\mathbf{B}_{\text{bias}}|$. We denote by η the ratio $\eta = \Delta V_{\text{trap}}/(k_B T)$. A $\eta \approx 10$ is sufficient to suppress thermal evaporation from the trap [143]. This of course refers to the temperature of the atoms after loading to the magnetic trap, which might have increased due to the gain of potential energy in presence of the trapping potential and due to exitations/heating caused by imperfect mode matching.

The need for a deep magnetic trap far from the surface forces us to work at maximum current in the Z shape structure; for a fixed trap distance, the potential depth is directly proportional to the wire current (compare equation (3.12). In the second generation atom chip, the wire current is limited to 3 A by thermal heating, the wire temperature increases by $\approx 40°$ C within 5 s under maximum charge.

The wire current being fixed, we experimentally optimize the external bias field (orientation and magnitude) to load a maximum number of atoms to the magnetic trap. In fact, the iterative optimization process incudes also the parameters of the compressed U-MOT, which affect the position of the atom cloud to be transferred, details can be found in [87, 73]. It has turned out advantageous to load with a rather shallow trap ($\Delta V_{\text{trap}} \simeq k_B \times 520\,\mu$K), far away from the surface (550 μm [144]), the parameter are 3 A wire current, 9 G bias field and 1 G longitudinal Ioffe field.

Due to the limited depth, hot atoms get lost from the magnetic trap during the first 200 ms after the transfer, which leads to a cooling of the trapped cloud (plain evaporation). After these 200 ms, the gas comes to a (quasi) equilibrium, plain evaporation breaks down exponentially [143], accidentally excited vibrational modes are damped out. We end up with 5×10^6 atoms at a temperature of 50 μK, which corresponds to 25 % transfer efficiency from the U-MOT and 10 % from the initial external quadrupole MOT.

In order to increase the elastical collision rate and allow for efficient evaporative cooling, we adiabatically (1100 ms) compress the magnetic trap by increasing the external bias field to 35 G,

which brings the atomic cloud to a distance of $50\,\mu$m from the chip surface. This compressed trap has a transverse oscillation frequency of $\omega_\perp \simeq 2\pi \times 1,5\,\text{kHz}$ and a longitudinal oscillation frequency of $\omega_\perp \simeq 2\pi \times 17\,\text{Hz}$. During the compression, the temperature of the trapped atom cloud increases to $T \simeq 250\,\mu$K.

6.1.4 Evaporative cooling

A rather serious problem was encountered in the compression phase of the magnetic trap: as the atom temperature increases during compression, the thermal cloud has a typical radius of $\approx 75\,\mu$m, which exceeds the distance of the trap center from the surface of $50\,\mu$m. Hot atoms therefore collide with the atom chip during the compression and are expelled from the trap. A small "surface induced" cooling [107] was observed, still this cooling was not efficient, backscattered atoms from the surface are suspected to heat the remaining sample and create additional losses. Reducing the compression resulted in an increased trap-surface separation but did not provide sufficient elastical collision rate for the following phase of evaporative cooling.

This problem could be overcome by a more effective cooling of the atoms already during the compression phase: we expose the atoms to a weak oscillating (RF) magnetic field, radiated by the U shaped wire, which is used as an antenna. This RF field of frequency ω drives spin flip transition to untrapped states, where the condition $\hbar\omega = g_F \mu_B |\mathbf{B}_{\text{trap}}(\mathbf{r})|$, effectively truncating the potential depth [145]. We set the RF frequency to 5,5 MHz, fixing the trap depth to $\Delta V_{\text{trap}} \simeq k_B \times 500\,\mu$K during the entire compression. As the compression is performed relatively slow (1100 ms), the temperature of the atomic cloud is held constant at $\approx 50\,\mu$K by plain evaporation without loosing too many atoms (1×10^6 in the final compressed trap). The corresponding thermal radius of the compressed cloud is only $\approx 30\,\mu$m, which is compatible with the surface distance of $50\,\mu$m.

To further cool the atomic cloud and increase phase space density, we employ forced evaporative cooling, based on continuous lowering of the effective trapping potential depth by lowering the frequency of the magnetic RF field, ideally keeping η constant. This is a standard technique in Bose-Einstein condensation and is used identically in atom chip experiments as in conventional setups. The ratio of final (N_f) to initial (N_i) atom number in such an evaporative cooling ramp, which reduces the temperature from T_i to T_f writes

$$\frac{N_f}{N_i} = \left(\frac{T_f}{T_i}\right)^{(\eta-2)/3} \tag{6.1}$$

Once $\eta > 3$, one obtains a gain in phase space density [143]. For $\eta \simeq 7$, the elastical collision rate increases rapidly troughout the evaporation ramp, the cooling accelerates and becomes increasingly efficient. This regime is referred to as runaway regime (or runaway cooling). Although Bose-Einstein condensation can be reached outside this regime, it is strongly favorable as it potentiates faster cooling and higher atom numbers.

To realize a constant truncation parameter η, the frequency of the magnetic RF frequency has to be lowered exponentially with time. In the experiment, we approximate the decay function by 12 segments of linear frequency ramps. The duration of each segment is optimized by an iterative procedure [146] which is described in detail in [87]. The final ramp has a total duration of 3700 ms, it is deficted in figure XYZ.

6.1.5 Bose-Einstein condensation

Once the temperature of the atomic cloud falls below the critical temperature discussed in section 1.1.1 and 1.31, the phenomenon of Bose-Einstein condensation occurs. As discussed in section 1.1, it can be identified as a sharp parabolic peak (assuming the Thomas-Fermi regime) in

the atomic density distribution in time-of-flight expansion [147], corresponding to a macroscopic population of the vibrational ground state of the trapping potential. The theoretical value for the critical temperature in the compressed trap is 290 nK, which can not be verified experimentally: the strong homogeneous external magnetic bias field, present after switching off the wire trap, introduces a large Zeemann shift of the atomic resonance, which is beyond the reachable detuning for our imaging system [73,87]. To be able to perform absorption imaging of the atomic cloud, we therefore decompress the magnetic trap be reducing the external bias field to 12 G (which can be imaged with a 17 MHz laser detuning, compare figure (5.12)) before releasing the atoms from the trap. Figure XYZ shows the onset of Bose-Einstein condensation in our system when reducing the atomic temperature by lowering the frequency of the RF magnetic field. The properties of the BEC have been studies in detail in the theses of C. Aussibal [87] and J. Estève [73], in situ measurements of density fluctuations were published in [148], which can be found in the annexe.

6.2 Study of random magnetic potentials

6.3 Experiments in a magnetic double well

Part III

A double well realized by adiabatic dressed potentials

Contents

Introduction

The third part of this manuscript presents a novel and simple scheme to realize double well potentials starting from elongated magnetic micro traps on atom chips. This scheme is based on adiabatic dressed potentials (ADP) and has been introduced by [99, 100] in order to realize two-dimensional traps; Atoms confined in a static (DC) magnetic trap are *dressed* by means of a strong, rapidly oscillating (AC) magnetic field in the radio frequency (RF) domain, which couples the atomic Zeeman sub-states. For strong coupling, the resulting adiabatic potential presents avoided crossings, forming new potential minima for the initially trapped Zeeman states and thereby considerably altering the geometry of the static magnetic trap [149, 150].

Depending on the shape of the initial magnetic trap and on the orientation, amplitude and frequency of the alternating magnetic field, a rich scenery of trapping geometries can be realized, including 1D and 2D traps and multiple versions thereof, aligned along their weakly or strongly confining axis.

As the initial static trapping potential can be adiabatically deformed to the dressed potential, this kind of trap can be loaded by simply adjusting the parameters of the magnetic RF field. The transfer of Bose condensed atoms into the ADP with almost no loss or heating is experimentally demonstrated for the first time in the experimental section of this manuscript.

Combining adiabatic dressed potentials with magnetic micro potentials formed on atom chips has several major advantages: The strong confinement and resulting elevated trap frequencies provided by these traps are maintained (and possibly enhanced) throughout the transfer to the ADP. This is of interest for realizing reduced dimensions and experiments aiming for coherent splitting and tunnelling, where timescales and adiabaticity are important issues. Twofold benefit is drawn when integrating the source of the RF magnetic field on the atom chip itself: By designing the wire pattern for static trap and RF source, precise control over relative position, strength and direction of the static and oscillating magnetic fields is obtained. Furthermore, the strong local magnetic near field created by the chip wires allows for large, unperturbed RF amplitudes, which are difficult to realize with external sources.

Chapter X briefly reviews the theory of dressed states and adiabatic potentials. A more refined analysis of the initial proposal [99] allows for a variety of trap configurations, among which we will focus on the elongated double well. Its scaling and characteristic properties will be examined for different parameter regimes. Stability requirements for tunnel experiments will be discussed. It will be especially pointed out, that a stable double well based on this scheme may be realized with almost any structure size on an atom chip.

II. Second list item Corresponding second text.

Chapter 7

Adiabatic dressed double well potentials

Add a short intro here?

7.1 Atoms in rapidly oscillating magnetic fields

7.1.1 The Hamiltonian for a dynamic magnetic field

We consider atoms trapped in a static magnetic field $\mathbf{B}_{\mathrm{trap}}(\mathbf{r})$ as described in chapter (???). We superimpose an oscillating magnetic field $\mathbf{B}_{\mathrm{RF}}(\mathbf{r})\cos(\omega t)$ in the radio frequency domain. For simplicity we will assume the RF field to be linearly polarized and homogenous over the size of the magnetic static trap [151] ($\mathbf{B}_{\mathrm{RF}}(\mathbf{r}) = \mathbf{B}_{\mathrm{RF}}$). The Hamiltonian describing the interaction of the atomic magnetic moment $\mathbf{S}$ with the total magnetic field $\mathbf{B}(\mathbf{r},t)$ can be written:

$$\begin{aligned} H(\mathbf{r},t) &= \frac{g_F\mu_B}{\hbar}\mathbf{S}\cdot\mathbf{B}(\mathbf{r},t) \\ &= \frac{g_F\mu_B}{\hbar}\mathbf{S}\cdot[\mathbf{B}_{\mathrm{trap}}(\mathbf{r}) + \mathbf{B}_{\mathrm{RF}}\cos(\omega t)] \\ &= \frac{g_F\mu_B}{\hbar}S_Z\left[B_{\mathrm{trap}}(\mathbf{r}) + B_{\mathrm{RF},Z}(\mathbf{r})\cos(\omega t)\right] + \frac{g_F\mu_B}{\hbar}S_X B_{\mathrm{RF},X}(\mathbf{r})\cos(\omega t). \end{aligned} \tag{7.1}$$

The axis Z is determined by the local orientation of the static trapping field $\mathbf{B}_{\mathrm{trap}}(\mathbf{r})$ at the position $\mathbf{r}$, X is a perpendicular axis so that $\mathbf{B}_{\mathrm{RF}}$ is in the $X-Z$ plane ($\mathbf{B}_{\mathrm{RF}} = B_{\mathrm{RF,X}}\mathbf{e}_X + B_{\mathrm{RF},Z}\mathbf{e}_Z$). S_Z and S_X are the projections of the total magnetic moment $\mathbf{F}$ on these axes. We assume the static trapping field $\mathbf{B}_{\mathrm{trap}}(\mathbf{r})$ to always be sufficiently strong to fully determine the quantization axis Z and the magnetic moment of the atom to adiabatically follow the direction imposed by the trapping field (see adiabaticity, chapter XYZ).

The RF field component $B_{\mathrm{RF},Z}(\mathbf{r})$ does not couple Zeeman states of the same hyperfine level, as there are no π transitions with $\Delta m_F = 0$. The coupling is effectuated by the RF component $B_{\mathrm{RF},X}(\mathbf{r})$ which is orientated perpendicular to the static magnetic trapping field. This field can be decomposed to equal parts into σ^+ and σ^- circular polarized component, one of which couples $\Delta m_F = \pm 1$ transitions. For a positive (negative) Landé factor g_F, the σ^+ (σ^-) polarized component couples the magnetic sub-states. It is pointed out, that strong coupling is obtained, where the oscillating magnetic RF field is orientated perpendicular to the direction of the static trapping field (therefore, the explicit spatial dependence of $B_{\mathrm{RF},Z}(\mathbf{r})$ and $B_{\mathrm{RF},X}(\mathbf{r})$ reappears in the last line of (7.1)):

$$B_{\mathrm{RF},X}(\mathbf{r}) = \frac{|\mathbf{B}_{\mathrm{trap}}(\mathbf{r})\times\mathbf{B}_{\mathrm{RF}}(\mathbf{r})|}{|\mathbf{B}_{\mathrm{trap}}(\mathbf{r})|}. \tag{7.2}$$

As $B_{\mathrm{RF},Z}(\mathbf{r})$ does not introduce any coupling, it can be neglected in the following:

$$H(\mathbf{r},t) = \Omega_{\mathrm{trap}} S_Z + 2\Omega_{\mathrm{RF}} S_X \cos(\omega t), \tag{7.3}$$

where Ω_{trap} and Ω_{RF} are the Rabi frequencies associated with the static trapping field $|\mathbf{B}_{\mathrm{trap}}(\mathbf{r})|$ and the oscillating magnetic field $B_{\mathrm{RF},X}(\mathbf{r})$ respectively:

$$\hbar\Omega_{\mathrm{trap}} = g_F \mu_B |\mathbf{B}_{\mathrm{trap}}(\mathbf{r})|, \qquad \hbar\Omega_{\mathrm{RF}} = \frac{1}{2} g_F \mu_B B_{\mathrm{RF},Z}. \tag{7.4}$$

The factor 1/2 in the definition of Ω_{RF} takes into account the reduced coupling due to the fact, that only the σ^+ (σ^-) circular component of $B_{\mathrm{RF},Z}$ is resonant.

7.1.2 The rotating wave approximation and dressed states

The Hamiltonian (7.3) can be well described in a rotating frame which turns around the quantization axis Z with the angular frequency ω of the oscillating magnetic field [152]. It is convenient to define the operator

$$R_Z(-\omega t) = \exp(i\omega t S_Z/\hbar) \tag{7.5}$$

which implements a rotation by an angle $-\omega t$ around the Z axis. Be $\Psi(t)$ a spinor in the coordinate subspace of $\psi_m(t)$ ($-F \le m \le F$), a solution of the Hamiltonian (7.3) $i\hbar\,\partial\Psi/\partial t = H(t)\Psi$. Be also $\Phi(t)$ the spinor obtained by rotating $\Psi(t)$ around Z by an angle $-\omega t$:

$$\Phi(t) = R_Z(-\omega t)\Psi(t). \tag{7.6}$$

Φ then follows $i\hbar\,\partial\Phi/\partial t = H'(t)\Phi$, the Hamiltonian $H'(t)$ in the rotating frame can be calculated

$$\begin{aligned} H'(t) &= R_Z(-\omega t)H(t)R_Z^\dagger(-\omega t) + i\hbar\frac{\partial R_Z}{\partial t}(-\omega t)R_Z^\dagger(-\omega t) \\ &= R_Z(-\omega t)H(t)R_Z^\dagger(-\omega t) - \omega S_Z \\ &= -\delta S_Z + 2\Omega\cos(\omega t)R_Z(-\omega t)S_X R_Z^\dagger(-\omega t) \\ &= -\delta S_Z + 2\Omega\cos(\omega t)\left[S_X\cos(\omega t) - S_Y\sin(\omega t)\right] \\ &= -\delta S_Z + \Omega S_X + \Omega S_X\cos(2\omega t) - \Omega S_Y\sin(2\omega t). \end{aligned} \tag{7.7}$$

We introduce δ the detuning between the RF frequency ω and the Rabi frequency Ω_{trap} at a specific position $\mathbf{r}$:

$$\delta \equiv \omega - \Omega_{\mathrm{trap}}. \tag{7.8}$$

The last line of (7.7) contains two terms which are constant in the rotating frame and two terms which oscillate with twice the resonance frequency. The rotating frame approximation now consists in neglecting these far off resonance terms, which have almost no effect on the spinor. In the case of a positive (negative) g factor, this corresponds to neglecting the non-resonant σ^- (σ^+) polarization of the magnetic RF field. In the rotating frame we thereby obtain the stationary Hamiltonian

$$H_{\mathrm{eff}} = -\delta S_Z + \Omega_{\mathrm{RF}} S_X. \tag{7.9}$$

The eigenstates of this Hamiltonian are called *dressed states* as the energy of the resonant photon is included in the term δS_Z. The term $\Omega_{\mathrm{RF}} S_X$ describes the strength of the coupling. The effective Hamiltonian can also be written as:

$$H_{\mathrm{eff}} = \sqrt{\delta^2 + \Omega_{\mathrm{RF}}^2}\, S_\theta \tag{7.10}$$

$$S_\theta = S_Z\cos\theta + S_X\sin\theta = R_Y(\theta)S_Z R_Y^\dagger(\theta) \tag{7.11}$$

$$\tan\theta = -\Omega_{\mathrm{RF}}/\delta, \qquad 0 \le \theta \le \pi, \tag{7.12}$$

which is the Hamiltonian of the atomic magnetic moment in an effective static magnetic field

$$\mathbf{B}_{\text{eff}} = \frac{\hbar}{g_F \mu_B} \sqrt{\delta^2 + \Omega_{\text{RF}}^2} \left(\cos\theta \mathbf{e}_Z + \sin\theta \mathbf{e}_X\right). \tag{7.13}$$

This effective magnetic field is in the plane spanned by $\mathbf{B}_{\text{trap}}(\mathbf{r})$ and $\mathbf{B}_{\text{RF}}$, it is tilted away from the Z axis by the angle θ.

For a large (compared to Ω_{RF}) negative detuning δ, the angle θ tends to zero and the effective potential coincides with the static trapping potential. On resonance ($\delta = 0$), the effective magnetic field is aligned with the X axis ($\theta = \pi/2$). For large positive detuning δ, the angle θ equals π and the effective magnetic field is again aligned with the Z axis.

The dressed eigenstates $|m'\rangle$ in the rotating frame (r.f.) are simply obtained by rotations of the unperturbed states $|m\rangle$ in the rest frame:

$$|m'\rangle_{\text{r.f.}} = R_Y(\theta)|m\rangle \tag{7.14}$$

with the corresponding eigenenergies [153]

$$\varepsilon_{m'} = m'\hbar\sqrt{\delta^2 + \Omega_{\text{RF}}^2}. \tag{7.15}$$

In line with the effective magnetic potential, the dressed eigenstates coincide with their *undressed* counterpart for large negative detunings. For large positive detunings, the dressed states are the reversed undressed states.

7.1.3 Adiabaticity and Landau-Zener losses

The considerations above describe the effect of static and oscillating magnetic fields on an atom located at a specific position $\mathbf{r}$. An atom moving in the combined field configuration experiences the effective field (7.13) which varies in space. In section (7.1.1) we have imposed adiabaticity of the atomic magnetic moment with respect to the static trapping field $\mathbf{B}_{\text{trap}}(\mathbf{r})$. We will now verify adiabaticity with respect to the effective magnetic field $\mathbf{B}_{\text{eff}}(\mathbf{r})$ in the rotating frame. For this, the projection of $\partial|m'\rangle/\partial t$ on the other dressed states $|n'\rangle$ has to be negligible compared to the corresponding energy difference:

$$\left|\langle n'|\frac{\partial}{\partial t}|m'\rangle\right| \ll \sqrt{\delta^2 + \Omega_{\text{RF}}^2}, \qquad \forall\ n \neq m. \tag{7.16}$$

Using (7.14), the dressed state $|m'\rangle$ can be rewritten:

$$\frac{\partial}{\partial t}|m'\rangle_{r.f.} = \frac{\partial}{\partial t}\left(\exp(i\theta S_Y/\hbar)|m\rangle\right) \tag{7.17}$$

$$= \dot{\theta}\left(-i\frac{S_Y}{\hbar}\right)|m'\rangle_{r.f.} \tag{7.18}$$

$$= \dot{\theta}\frac{S_- - S_+}{2\hbar}|m'\rangle_{r.f.} \tag{7.19}$$

The derivative $\partial|m'\rangle/\partial t$ can be expressed by the neighboring states $|m' \pm 1\rangle_{r.f.}$. As $|\langle n|m' \pm 1\rangle_{r.f.} \leq 1$ for $n \neq m$, the adiabaticity condition (7.16) can be written

$$|\dot{\theta}| \ll \sqrt{\delta^2 + \Omega_{\text{RF}}^2}. \tag{7.20}$$

This condition is identical to the adiabaticity criterium for an atomic spin in a inhomogeneous magnetic field (see XYZ), which can be transferred to the effective magnetic field $\mathbf{B}_{\text{eff}}(\mathbf{r})$ in the

rotating frame. If the above condition in not fulfilled, an atom in a specific dressed state might undergo non-adiabatic transitions to other (possibly untrapped) dressed states. This will mainly take place at the position of the avoided crossing, where the directional change of the effective magnetic field is maximal. This situation is formally equivalent to the system described by Landau [154] and Zener [155] for avoided crossings in adiabatic molecular potentials, apart the fact, that in the RF system, all Zeeman sub-levels have to be considered. Still, as all Zeeman states are energetically equidistant (see (7.15)), the problem can be reduced to a two-level system [156]. The probability for a spin-flip Landau-Zener transition is

$$P_{\mathrm{L.Z.}} \simeq 4 \exp\left(-\frac{\pi}{2}\frac{\Omega_{\mathrm{trap}}}{|\dot{\delta}|}\right), \tag{7.21}$$

which is analogous to the expression for Majorana losses in a static magnetic trap (HIER MUSS EIN VERWEIS HIN!!!). The adiabaticity criterion as well as the spin-flip loss mechanism in the adiabatic dressed potential can be mapped to the case of a static magnetic potential. We will therefore use the more common language of static traps wherever possible.

7.1.4 The effective adiabatic potential

If the adiabaticity criterion (7.20) is fulfilled, the local eigenenergies (7.15) of the dressed states give rise to an effective adiabatic potential:

$$V_{m'}(\mathbf{r}) = m'\hbar\sqrt{\delta^2 + \Omega_{\mathrm{RF}}^2} \tag{7.22}$$

$$= m' \sqrt{\underbrace{\left[\hbar\omega - g_F\mu_B|\mathbf{B}_{\mathrm{trap}}(\mathbf{r})|\right]^2}_{\text{resonance term}} + \underbrace{\left[\frac{1}{2}g_F\mu_B B_{\mathrm{RF},\perp}(\mathbf{r})\right]^2}_{\text{coupling term}}} \tag{7.23}$$

where $B_{\mathrm{RF},\perp}(\mathbf{r})$ is the component of the RF field perpendicular to the local static trapping field:

$$B_{\mathrm{RF},\perp}(\mathbf{r}) = \frac{|\mathbf{B}_{\mathrm{trap}}(\mathbf{r}) \times \mathbf{B}_{\mathrm{RF}}(\mathbf{r})|}{|\mathbf{B}_{\mathrm{trap}}(\mathbf{r})|}. \tag{7.24}$$

The first term below the square root in (7.23) contains the energy shift of the dressed system due to the energy of the RF photon $\hbar\omega$. This term will be referred to as *resonance term*, as in many realizations of adiabatic potentials, new minima form where the RF resonantly couples the undressed states of the static trapping potential: $\hbar\omega = g_F\mu_B|\mathbf{B}_{\mathrm{trap}}(\mathbf{r}_{\mathrm{min}})|$. The resonance term only depends on the frequency ω of the oscillating magnetic field.

The second term in (7.23) describes the strength of the coupling of the RF field to the atom in the initial static potential and will therefore be referred to as *coupling term*. In the case of strong coupling, it causes level repulsion at the avoided crossings of the adiabatic potential. The *coupling term* plays the role of a effective Ioffe field, as it suppresses spin-flip losses at the resonance points and therefore allows for long lifetimes in the adiabatic potential.

The spatial dependence of the coupling term has been ignored so far in the literature [99,100]. In the following we will show that this is not permitted and that this spacial dependence allows for the formation of a variety of trapping geometries, *e.g.* double wells.

7.2 Realizing a double well geometry

In this section, basic trapping geometries that may be formed in adiabatic dressed potentials are discussed on a general level. We will then concentrate on adiabatic potentials based on highly elongated static magnetic traps formed on atom chips and how this system can be used to form a double well potential. Where possible, analytic expressions for the relevant physical parameters of the double well are derived. Based on these expressions, we investigate the feasibility of a tunnel experiment in this system under realistic conditions. In contrast to the purely static magnetic system analyzed in SecXYZ, such an experiments is found to be possible with almost any structure size, using adiabatic dressed potentials.

7.2.1 Adiabatic potentials based on a Ioffe trap

To examine the general geometrical features of adiabatic potentials, we will analyze the effect of an oscillating magnetic field on atoms in a magnetic trap of the Ioffe-Pritchard type:

$$\mathbf{B}_{\mathrm{trap}}(\mathbf{r}) = B_0 \begin{pmatrix} 0 \\ 0 \\ 1 \end{pmatrix} + B' \begin{pmatrix} x \\ -y \\ 0 \end{pmatrix} + \frac{B''}{2} \begin{pmatrix} -xz \\ -yz \\ z^2 - \frac{1}{2}(x^2+y^2) \end{pmatrix}. \tag{7.25}$$

A possible anisotropy of the magnetic trap does not affect the following considerations; without loss of generality one can set $(B')^2/B_0 = B''$. This describes an isotropic trap ($\omega_x = \omega_y = \omega_z$) with the trap frequencies $\omega_{x,y,z}/2\pi = \sqrt{m_F g_F \mu_B / m}\sqrt{B''}$. The Ioffe field is aligned with the z axis (see figure 7.1), it's magnitude at the trap bottom is B_0. It is convenient to redefine the detuning δ of the RF magnetic field with respect to the Rabi frequency at the trap bottom:

$$\delta = \omega - \frac{g_F \mu_B B_0}{\hbar}. \tag{7.26}$$

The effect of gravity will be neglect in the following. As in section (7.1.1), the oscillating magnetic field is supposed to be linear polarized and homogeneous over the size of the trap [151].

It will turn out, that the orientation of the RF field with respect to the magnetic field vectors of the static magnetic trap is crucial for the geometry of the effective adiabatic potential. We will thus analyze two limiting cases which allow to overview the range of possible topologies, intermediated configurations can be easily derived afterwards.

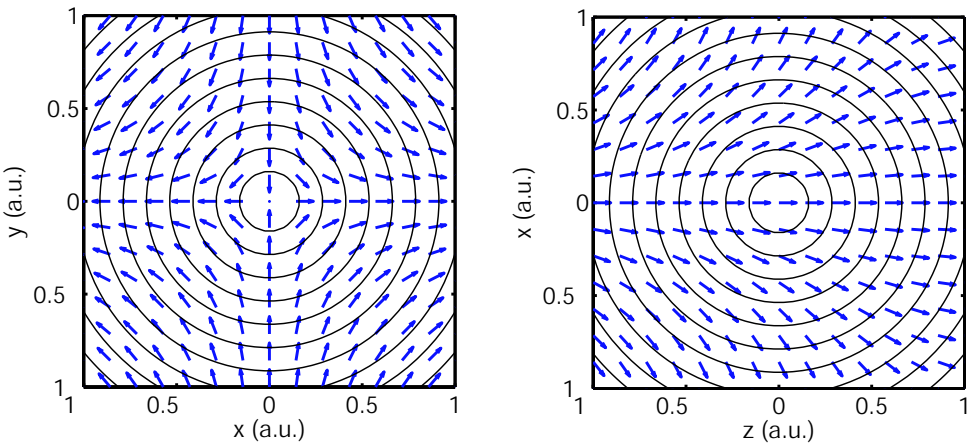

Figure 7.1: Normalized field vectors and equipotential lines of an isotropic Ioffe-Pritchard trap in the $(x, y, 0)$ plane (left) and the $(x, 0, z)$ plane (right).

An RF field aligned with the Ioffe field

Here we will analyze a configuration, where the linear polarized RF magnetic field is aligned with the z axis ($\mathbf{B}_{\mathrm{RF}} = B_{\mathrm{RF}}\mathbf{e}_z$) and thereby is parallel to the Ioffe field at the trap center (see figure (7.1, right). We will first concentrate on the case of positive detuning ($\hbar\omega > g_F\mu_B B_0$), which is easiest to understand.

The effective adiabatic potential (7.23) is the geometric mean of the resonance term and the coupling term, which will now be analyzed separately.

The effect of the resonance term on the static magnetic potential can be seen schematically in figure (7.2). Where the resonance condition $\hbar\omega = g_F\mu_B|\mathbf{B}_{\mathrm{trap}}(\mathbf{r})|$ is fulfilled, a new potential minimum of zero magnetic field is formed. In the case of an isotropic static magnetic trap, this means forcing the atoms into an iso-$|\mathbf{B}_{\mathrm{trap}}|$ sphere of radius r. The steepness of the potential at the minimum position corresponds to the gradient $\partial|\mathbf{B}_{\mathrm{trap}}|/\partial r$ of the original static potential at the resonance position. For small positive RF detunings, the harmonic region of the initial trap is sampled; for high positive detuning, the linear region of the static potential is explored.

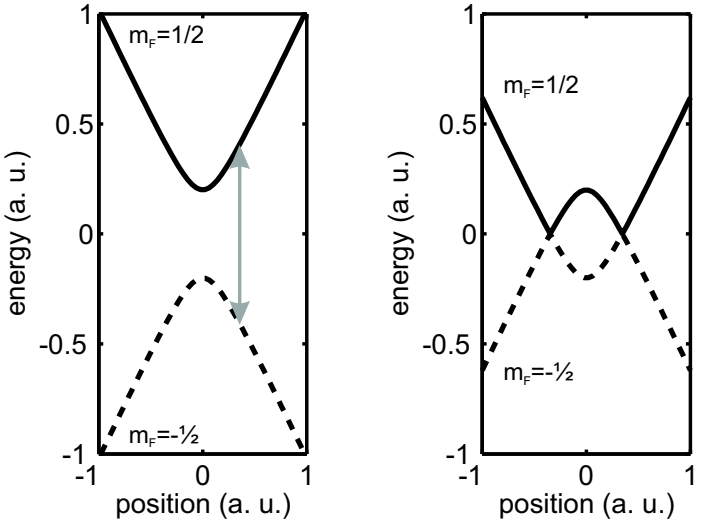

Figure 7.2: Schematic illustration of the resonance behavior of the adiabatic potential, neglecting the coupling term. Left: two Zeeman sub-states in a semi-linear trap are coupled by a locally resonant RF field. Right: new potential minima are formed at the resonance position by shifting the initial potentials by the RF photon energy.

The coupling term $\frac{1}{2}g_F\mu_B B_{\mathrm{RF},\perp}(\mathbf{r})$ vanishes, where $\mathbf{B}_{\mathrm{RF}}$ is parallel to $\mathbf{B}_{\mathrm{trap}}(\mathbf{r})$ and has its maximal value $\frac{1}{2}g_F\mu_B B_{\mathrm{RF}}$ where both fields are orthogonal. In the (x, y) plane the coupling is zero at the trap center $(0, 0)$ and then quickly increases to its maximal value as an atom moves away from the center; the influence of the Ioffe field along z diminishes rapidly for increasing r and the trapping field vectors are mainly in the (x, y) plane and thus perpendicular to the RF field along z (see figure (7.1, left)). The RF coupling follows the rotational symmetry of the Ioffe-Pritchard trap in the (x, y) plane (see figure (7.3, left)).

In the (x, z) or (y, z) plane, the rotational symmetry is of the static trapping field is broken by the Ioffe field (see figure (7.3, right)), the coupling vanishes on the entire z axis and rapidly increases to its maximal value for atoms moving away from $x = y = 0$.

As mentioned above, the overall adiabatic potential is the geometric mean of resonance and coupling term and can be easiest described in the regime of large positive detuning. In this regime, the position of the newly formed minima is almost completely determined by the resonance condition, which will create a 3D trapping surface (sphere topology). The absolute

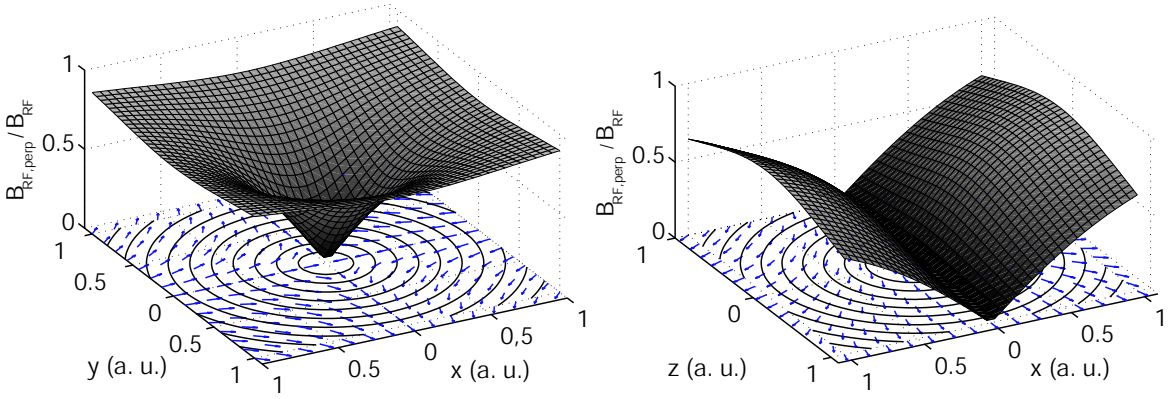

Figure 7.3: Effect of an RF field parallel to the Ioffe field at the trap center (along z). Left: The coupling in the (x, y) plane is zero at the trap center and tends to a constant elsewhere. Right: The coupling in the (x, z) plane vanishes on the entire z axis.

value at the minimum position in contrast is determined by the coupling term at the specific position, which varies in space from zero to its maximum value. Where the z axis intersects the sphere of radius r, two overall minima of zero field [157] are formed, giving rise to a double well configuration in 3D. As spin-flip losses are not suppressed at these minima, this trapping configuration is not stable.

For small positive detuning, the system becomes slightly more complex: still the resonance condition is forcing the atoms onto a sphere, which is now closer to the center of the initial static trap. In this region, the coupling term varies strongly on the region of the newly formed minima, counteracting the effect of the resonance condition and deforming the sphere. Still, two spatially separated overall minima of vanishing field will form in the adiabatic potential. The configuration $\mathbf{B}_{\mathrm{RF}}$ parallel to the direction of the Ioffe field is unstable once $\hbar\omega \geq B_0$.

For negative detuning, the topology of the initial static trap is not changed fundamentally, for RF frequencies close to resonance, the initially isotropic trap becomes slightly elongated along the z direction.

An RF field perpendicular to the Ioffe field

We will now analyze a configuration, where the RF magnetic field is oriented perpendicular to the Ioffe field at the trap center. Without loss of generality, we can assume the RF field aligned with the x axis: $\mathbf{B}_{\mathrm{RF}} = B_{\mathrm{RF}}\mathbf{e}_x$. Again, first the most intuitive case of large positive detuning will be described.

The effect of the resonance term in the effective adiabatic potential (7.23) is the same as in the configuration described above, as only scalar properties of the static trapping potential come into play. Again the resonance condition is forcing the atoms onto a closed sphere of radius r, where $\hbar\omega = g_F\mu_B|\mathbf{B}_{\mathrm{trap}}(\mathbf{r})|$.

In contrast, the contribution of the coupling term is fundamentally changed for an RF field aligned perpendicular to the Ioffe field: It is maximal (and constant) in the entire (y, z) plane. Consequently, the coupling is also maximal at the trap center in the (x, y) plane and vanishes for $x \to \pm\infty$, where the trapping field vector is parallel to the RF field. For realistic experimental settings, the coupling term never completely vanishes, although care has to be taken to avoid spin-flip losses.

As in the former scenario, the spherical symmetry imposed by the resonance condition,

is broken by the coupling term, giving rise to a double well trapping geometry in 3D. The two minima will be located on the x axis and are of non-zero field. Stable long term trapping of atoms in this configuration is therefore possible. The precise effect of the RF amplitude and frequency on the effective adiabatic double well potential will be discussed in detail in section (7.2.2).

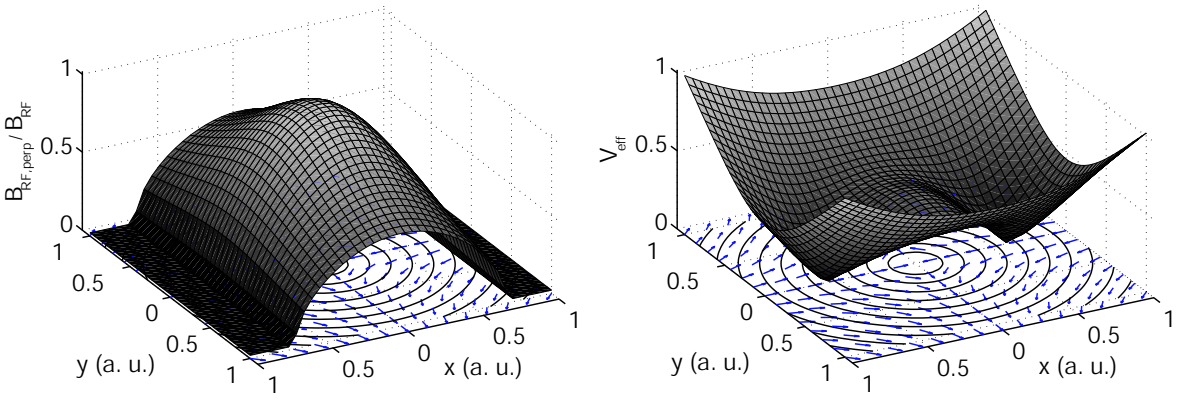

Figure 7.4: Effect of an RF field perpendicular to the Ioffe field at the trap center (along x). Left: Spatially inhomogeneous coupling in the (x, y) plane (constant in the orthogonal (y, z) plane). Right: The resulting effective adiabatic potential presents two minima of finite magnetic field.

General remarks on topology

The two scenarios described above present limiting cases, both giving rise to a double well trapping structure in 3D. The general behavior can be qualitatively described as follows.

As only the scalar potential of an atom in an external magnetic field appears in the resonance condition, this term acts on the iso-$|\mathbf{B}_{\text{trap}}|$ lines of the static trap, which are closed 3D surfaces, reflecting the symmetries of the initial trap.

The coupling however depends on the relative orientation of the field vectors. For any configuration of a Ioffe-Pritchard trap (provided three orthogonal principal axes), this creates regions of minimal or zero coupling, usually located on the axis of the RF field. In combination with the resonance condition, this always leads to a double well configuration for positive RF detuning. This configuration is unstable in the special case of an RF field exactly aligned with the Ioffe field at the trap center.

This description is in contrast to the original proposal of [99, 100], where the spatial dependence of the coupling term has been neglected. This has lead to to the impression, that trapping of atoms on the entire iso-$|\mathbf{B}_{\text{trap}}|$ surface would lead to the formation of large "matter wave bubbles". We believe this to be impossible without considerable further effort to compensate the spatial inhomogeneity of the coupling term.

Auxiliary forces acting on the atoms, like gravity, static or oscillating electric fields may additionally modify the effective adiabatic potential, giving rise to a rich scenery of trapping geometries: trapping on a 2D iso-$|\mathbf{B}_{\text{trap}}|$ surface under the influence of gravity has been demonstrated in [149, 150]. Several RF sources with different spatial orientation can be used to form complex trapping structures, depending on the relative phase, which may be additionally adjusted in time.

So far, the RF field has been considered as homogeneous over the trapping region. A well designed spatial variation of the RF amplitude results in a corresponding variation of coupling

strength and also allows for the design of complex trapping structures. A design for a guided atom interferometer on a chip based on this concept will be presented in chapter [????]

7.2.2 Properties of the adiabatic potential double well

This section focuses on a more quantitative analysis of the stable double well configuration introduced above, where the RF field is orientated perpendicular to the Ioffe field at the trap bottom. The initial static magnetic trap shall be a very elongated chip trap orientated along the z axis with a Ioffe field aligned along the same axis, as it is created by Z-shaped wire traps. We assume a small number of Bose-condensed atoms, sampling the very bottom of the trap. Numerical calculations and explicit experimental values are given for ^{87}Rubidium in the $F = m_F = 2$ state.

As an atomic cloud trapped in a magnetic wire trap usually is of cigar shape, cylindrical coordinates will be used:

$$\mathbf{B}_{\mathrm{trap}}(\mathbf{r}) = \mathbf{B}_{\mathrm{trap}}(r\phi, z) = \begin{pmatrix} B'r\cos\phi \\ -B'r\sin\phi \\ B_0 + \frac{1}{2}B''z^2 \end{pmatrix}. \tag{7.27}$$

For elongated traps with longitudinal trap frequencies of a few Hertz, the change in longitudinal field $\Delta B_z = 1/2\, B''z^2$ is on the order milligauss over the size of the cloud [158]. We will neglect this term and consider the trap as invariant under translation along z, reducing the system to the 2D transverse plane. The trapped atoms are assumed to be non interacting and in the transverse single particle ground state (ideal 1D trap). Numerical results are obtained by searching for stationary solutions of the 2D Schrödinger equation. The RF field is aligned along the x axis: $\mathbf{B}_{\mathrm{RF}} = B_{\mathrm{RF}}\mathbf{e}_x$. The effective adiabatic potential writes [153]:

$$V_{\mathrm{eff}}(r,\phi) = m'_F\sqrt{\left[\hbar\omega - g_F\mu_B\sqrt{B_0^2 + (B'r)^2}\right]^2 + \left[\frac{1}{2}g_F\mu_B B_{\mathrm{RF}}\sqrt{\frac{B_0^2 + (B'r\sin\phi)^2}{B_0^2 + (B'r)^2}}\right]^2}. \tag{7.28}$$

The following analysis takes interest in the two primary physical quantities describing a double well: the double well separation $2r_0$ and the oscillation frequency $\omega_0/2\pi$ at the minimum position. Analytical expressions for these quantities can not be derived directly from (7.28). Depending on parameter regimes, useful approximations have to be made. We will explicitly treat two different regimes, identified by the region of the initial static trap, which will be explored by the adiabatic potential. These regimes allow for the realization of large trap separations (hundreds of ground state sizes) and therefore completely isolated sites as well as for small separations (on the order of the ground state size) where tunnel coupling can be important. For these two regimes, simple analytic expressions for the physical quantities of interest could be found, allowing for an analysis of the scaling and the robustness of the splitting and a comparison with other schemes to realize a double well potential. However, these regimes do not entirely cover the parameter space of the system and some realizations of the RF double well can only be described numerically.

The linear regime: large positive RF detuning

We will first focus on the regime of large positive detuning $\hbar\omega \gg g_F\mu_B B_0$, as it has been described qualitatively in the section above. In this case, the resonance condition forces the atoms to a region far out of the initial semi-linear trap, mainly sampling its linear region. The trapping potential can therefore be approximated as purely linear: $|\mathbf{B}_{\mathrm{trap}}(\mathbf{r})| \simeq B'r$. This approximation is precise to better than 10 %, once $r \geq 2,2B_0/B'$ (*e.g.* 22 μm for a trap of

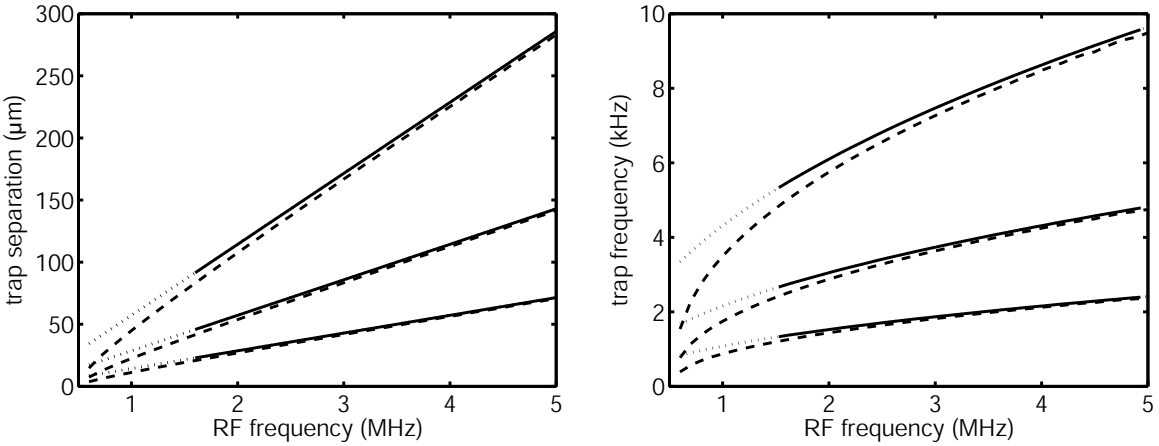

Figure 7.5: Trap separation and oscillation frequency for the dressed adiabatic potential in the linear regime for initial static traps of different gradient. Left: trap separation $2r_0$ for $B_0 = B_{\mathrm{RF}} = 1\,\mathrm{G}$, $B' = 500\ (1000, 2000)\,\mathrm{G/cm}$ (top to bottom). The dotted/solid line indicates the analytical result of (7.29), the graph is solid from $r_0 > 2,2B_0/B'$ on. The dashed lines are numerical results obtained directly from equation (7.28). Right: oscillation frequencies $\omega_0/2\pi$ for the same initial traps, analytic result of equation (7.32) and numerical calculation. Trap frequencies of the initial static trap are $\omega_{\mathrm{trap}}/2\pi = 2550\ (1280,\ 640)\,\mathrm{Hz}$ (top to bottom).

$B_0 = 1\,\mathrm{G}$, $B' = 1000\,\mathrm{G/cm}$). In this regime, the position of the minimum in the adiabatic potential is completely determined be the coupling term:

$$r_0 = \frac{\hbar\omega}{g_F\mu_B B'}. \tag{7.29}$$

The trap separation increases linear with the RF frequency, the slope being determined by the gradient of the static trap (see figure (7.5, left)). The effective magnetic field $B_{0,\mathrm{eff}}$ at the minimum position is given by the coupling term at $r = r_0$, $\phi = 0$ (using $B'r_0 \gg B_0$):

$$B_{0,\mathrm{eff}} = \frac{1}{2}B_{\mathrm{RF}}\sqrt{\frac{B_0^2}{B_0^2 + (B'r_0)^2}} \tag{7.30}$$

$$\simeq \frac{1}{2}B_{\mathrm{RF}}\frac{B_0}{B'r_0}. \tag{7.31}$$

The effective minimum trapping frequency is therefore:

$$\omega_0 = \sqrt{\frac{m_F g_F \mu_B B'^2}{m B_{0,\mathrm{eff}}}} \tag{7.32}$$

$$= \sqrt{\frac{2\hbar\omega}{g_F\mu_B B_{\mathrm{RF}}}}\omega_{\mathrm{trap}} \tag{7.33}$$

Depending on the ratio $2\hbar\omega/g_F\mu_B B_{\mathrm{RF}}$, the trap frequency ω_{trap} of the initial trap can be maintained or even increased during the transfer to the adiabatic potential (see figure (7.5, right)). As the trapping gradient stays constant, the effective magnetic field at the trap minimum is the equivalent of the Ioffe field of the initial static trap. Though in principle, this Ioffe field could be reduced at will in order to increase the oscillation frequency, this is often hindered by technical problems: static traps with low Ioffe fields (*e.g.* below 0,5 G) are very sensitive to AC magnetic

noise in the frequency domain of some some hundred MHz which induces spin flip losses. In the case of an adiabatic potential, the system is insensitive to noise of frequencies below the RF frequency, which can be several MHz. Therefore, adiabatic potentials in the linear regime may be used to further increase the trapping frequency of the initial static trap.

The harmonic regime: RF frequency on resonance

If the RF frequency is close to resonance ($\hbar\omega \approx g_F\mu_B B_0$), the harmonic region of the initial static potential close to the trap bottom is explored by the atoms. Therefore, a harmonic approximation can be applied for the trapping potential:

$$|\mathbf{B}_{\mathrm{trap}}(\mathbf{r})| \simeq B_0 + \frac{(B'r)^2}{2B_0}. \tag{7.34}$$

This approximation is precise to better than 10 %, once $r_0 \leq 1,14B_0/B'$ (*e.g.* 11 μm for a trap of $B_0 = 1\,\mathrm{G}$, $B' = 1000\,\mathrm{G/cm}$). In the following, much stronger constrains will be imposed on r_0, so we can consider (7.34) a very good approximation. The effective adiabatic potential along the $\phi = 0$ axis then writes:

$$V_{\mathrm{eff}}(r,\phi) = m'_F\sqrt{\left[\hbar\omega - g_F\mu_B\left(B_0 + \frac{(B'r)^2}{2B_0}\right)\right]^2 + \left[\frac{1}{2}g_F\mu_B B_{\mathrm{RF}}\frac{B_0}{B_0 + \frac{(B'r)^2}{2B_0}}\right]^2}. \tag{7.35}$$

The minimum position and local trap frequency of this effective potential are harder to find, as in the linear regime, as the spatial dependence of the coupling term has a strong influence on the overall potential at the center of the initial static trap (see figure (7.4)). Analytic expressions for the quantities of interest can in principle be derived from (7.35), but are too complex to allow insight into the physical processes. The coupling term of (7.35) has the shape of a Lorenz curve

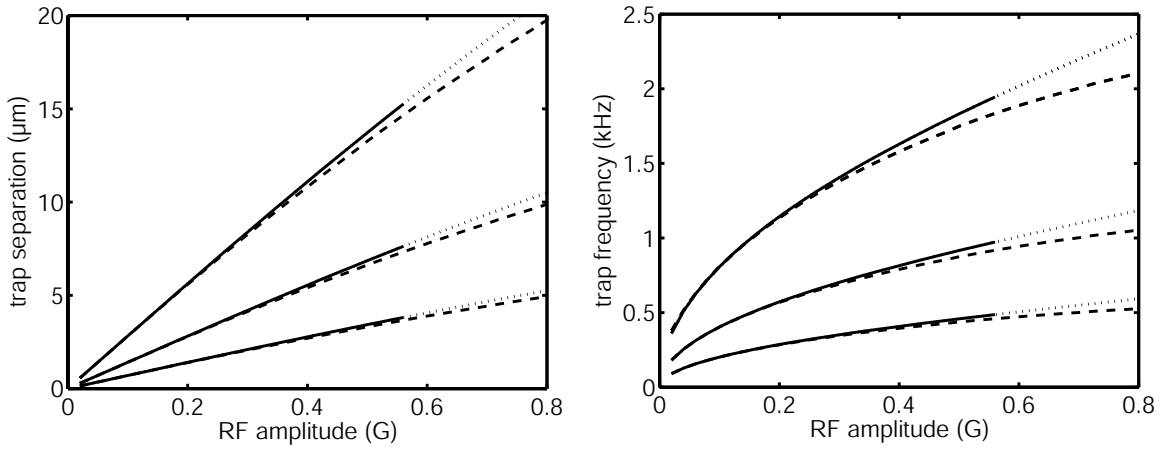

Figure 7.6: Trap separation and oscillation frequency for the dressed adiabatic potential in the harmonic regime for initial static traps of different gradient. Left: trap separation $2r_0$ for $B_0 = B_{\mathrm{RF}} = 1\,\mathrm{G}$, $B' = 500\ (1000, 2000)\,\mathrm{G/cm}$ (top to bottom). The dotted/solid line indicates the analytical result of (7.40), the graph is solid from $r_0 > 0,77B_0/B'$ on. The dashed lines are numerical results obtained directly from equation (7.28). Right: oscillation frequencies $\omega_0/2\pi$ for the same initial traps, analytic result of equation (7.42) and numerical calculation.

and is badly approximated by a finite polynomial. Still, we will apply a harmonic approximation

and take care to well stay within the validity region of this approximation:

$$V_{\text{eff}}(r,\phi) = m'_F \sqrt{\left[\hbar\omega - g_F\mu_B\left(B_0 + \frac{(B'r)^2}{2B_0}\right)\right]^2 + \left[\frac{1}{2}g_F\mu_B B_{\text{RF}}\left(1 - \frac{(B'r)^2}{2B_0^2}\right)\right]^2}. \tag{7.36}$$

This approximation is precise to better than 10 %, once $r_0 \leq 0,77 B_0/B'$ (*e.g.* 7,7 μm for a trap of $B_0 = 1\,\text{G}$, $B' = 1000\,\text{G/cm}$). From (7.36), reasonably simple expressions for the minimum position of the adiabatic potential can be derived:

$$r_0 = \pm\sqrt{2}\frac{B_0}{B'}\sqrt{\frac{\frac{4\hbar\omega_{RF}B_0}{g_F\mu_B} + B_{RF}^2 - 4B_0^2}{B_{RF}^2 + 4B_0^2}}. \tag{7.37}$$

To obtain a splitting configuration, the numerator below the square root has to be positive:

$$1 < \frac{\hbar\omega_{RF}}{g_F\mu_B B_0} + \frac{B_{RF}^2}{4B_0^2}. \tag{7.38}$$

To be well within the limits of the harmonic approximation for the coupling term, we furthermore impose

$$\frac{1}{2} \leq \sqrt{\frac{4\frac{\hbar\omega_{RF}B_0}{g_F\mu_B} + B_{RF}^2 - 4B_0^2}{B_{RF}^2 + 4B_0^2}}. \tag{7.39}$$

To satisfy the conditions (7.38) and (7.39), it is convenient to fix $\hbar\omega_{RF} \equiv g_F\mu_B B_0$ and $B_{RF} < B_0$. This corresponds to an RF frequency on resonance. By doing so, the richness of the system is significantly reduced to make it accessible to analytic description. For technical reasons, it may be advantageous not to work within these limits. Nevertheless, describing the system on resonance has the advantage of allowing for simple expressions for the physical properties of interest. Furthermore, the splitting process starts at $B_{\text{RF}} = 0$, making the RF amplitude a control parameter, which can be directly identified with $\mathbf{b}$ in the purely magnetic double well system presented in chapter 2.

With the above conditions, the minimum position is

$$r_0 = \pm\sqrt{2}\frac{B_0}{B'}\sqrt{\frac{B_{RF}^2}{B_{RF}^2 + 4B_0^2}} \tag{7.40}$$

$$\simeq \pm\frac{1}{\sqrt{2}}\frac{B_{RF}}{B'} \quad \left[\mp\frac{1}{8\sqrt{2}}\frac{B_{RF}^3}{B_0^2 B'} \pm ...\right]. \tag{7.41}$$

Especially for small RF amplitudes ($B_{\text{RF}} \ll B_0$), the linear approximation (7.41) is very accurate. This shows, that the trap separation in the RF adiabatic double well increases linear with the control parameter at the beginning of the splitting, in strong contrast to the square root dependence (ZITE!) in the purely magnetic scheme.

The oscillation frequency ω_0 at the minimum position is

$$\omega_0 = \frac{1}{\sqrt{2}}\frac{B'}{B_0}\sqrt{\frac{m_F g_F\mu_B B_{RF}}{mB_0}}\sqrt{B_{RF}^2 + 4B_0^2} \tag{7.42}$$

$$\simeq \frac{B'}{B_0}\sqrt{\frac{m_F g_F\mu_B}{m}}\sqrt{B_{RF}} \quad \left[+\frac{1}{16}\frac{B'}{B_0^3}\sqrt{\frac{m_F g_F\mu_B}{m}}B_{RF}^{5/2} + ...\right] \tag{7.43}$$

$$\simeq \sqrt{\frac{B_{\text{RF}}}{B_0}}\omega_{\text{trap}}. \tag{7.44}$$

Again, the leading term of the development (7.43) is already very precise for small RF amplitudes, showing a square root dependence for the oscillation frequency on the control parameter, as it is the case in the purely magnetic system (CITE!).

7.2.3 Realizing the two-modes model

In this section, the feasibility of a tunnel experiment in a double well formed by adiabatic potentials is examined. The following calculations are carried out for the ^{87}Rubidium atom in the $F = m_F = 2$ state, we assume the RF frequency on resonance as described above. Based on (7.41) and (7.43), the adiabatic potential in the direction of the double well ($\phi = 0$) can be approximated by the universal expression

$$V(r) = \frac{m\omega_0^2}{8r_0^2}(r^2 - r_0^2)^2 \tag{7.45}$$

$$\simeq \frac{1}{4}\mu_B B_{\mathrm{RF}} \frac{B'^4}{B_0^2 B_{\mathrm{RF}}^2}\left(r^2 - \frac{1}{2}\frac{B_{\mathrm{RF}}^2}{B'^2}\right)^2. \tag{7.46}$$

The approximation (7.46) is excellent for small RF amplitudes (small double well separations) and close to the inner region of the double well. It fails in the linear region, far out of the trap center, which is usually not explored by cold or Bose condensed atoms. The tunnel coupling

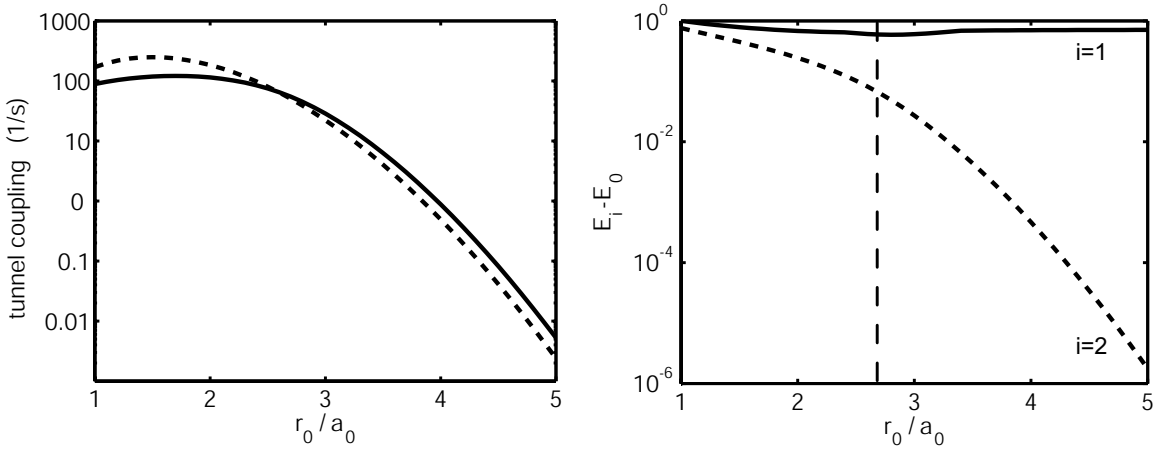

Figure 7.7: Left: Tunnel coupling of the double well for different ratios of well separation $2r_0$ and ground state size a_0 based on an initial static trap of B_0=1G, B'=1000 G/cm. The analytic expression (**??**) (dottes line) is compared to an numerical calculation (solid line). Right: Bohr frequency between the ground state ($i = 0$) and the first two excited states of the double well potential. For $r_0/a_0 = 2.74$, the Bohr frequency $\omega_{2,0}$ is ten times the tunnelling rate $\delta = \omega_{1,0}$.

δ for a double well potential of the form (7.45) is given by (REF INSTANTON) (see chapter XYZ). Figure (7.7, left) compares the analytic expression to a numerical 2D calculation of the coupling for varying ratio r_0/a_0 of the trap separation to the size of the single particle ground state. The analytical expression describes the tunnel coupling well within a factor of two. The absolute values depend on gradient and trap separation, the relative behavior is universal. The two curves cross at $r_0/a_0 = 2,6$, within a region from $r_0/a_0 = 2,5 - 2,8$ the description is precise to better than 10 %.

As described in chapter XYZ, for tunnel experiments, one is interested to work in a regime, where the two-modes approximation can be applied, in order to avoid excitations due to the tunnel coupling. Numerical calculations show, that in the RF adiabatic system, a ratio $r_0/a_0 = 2,74$ guaranties $\omega_0 = 10\delta$, as can be seen in figure (7.7, right). This ratio is completely universal, independent of gradient or double well separation [159]. A tunnelling configuration can therefore always be realized in the RF adiabatic system, only limited by technical constrains, as will be discussed in the following section.

7.3 Stability of the double well

The former considerations where based on a generic static trap of the Ioffe-Pritchard type. We will now concentrate on a concrete realization of a double well for tunnel experiments based on a wire trap on an atom chip. As above, we consider the system to be invariant to translation along the z axis, which is the axis along the trapping wire as well as the direction of the Ioffe field B_0 at the trap bottom. If the RF frequency is set on resonance, as described above, the

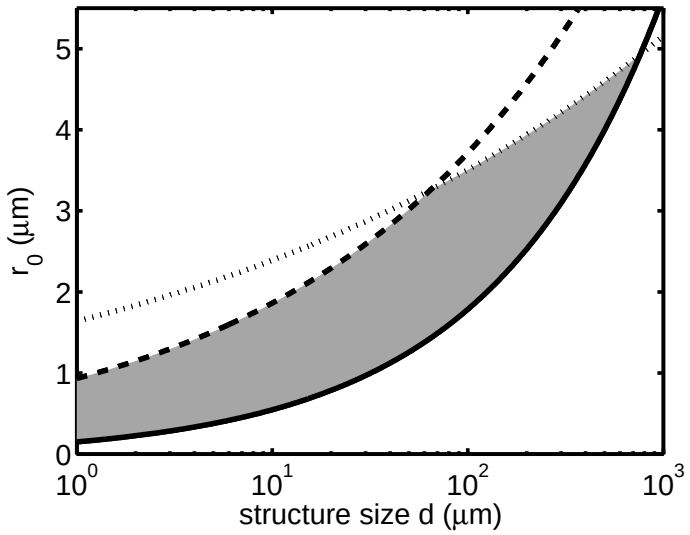

Figure 7.8: Stability diagram for double wells of trap separation $2r_0$, created by a wire structure of size d. The gray area represents the parameter region, in which noise and fluctuations do not significantly affect the tunnelling dynamics. The region is limited from below (solid line) by the effect of fluctuating RF amplitude (10 mG) and limited from above by external field noise (1 mG) tilting the double well (dotted line) and the constraint $B_0 < 100G$ (dashed line).

system is determined by three parameters: the gradient B' of the initial static trap, the Ioffe field B_0 and the RF amplitude B_{RF}. To analyze the scaling of the system, we introduce a structure size d, give by the distance of the atomic cloud to the trapping wire. Furthermore, we assume the trapping wire to also have a maximal width of d. As it has been shown in Part 1, section XYZ, for a separation between atoms and wire equal to the wire width, the approximation of an indefinitely thin wire can still be applied and finite size effects can be neglected. For simplification, we will assume square cross section wires, in practice, it is favorable to use flat wires of identical cross section for reasons of heat dissipation (see XYZ). The structure size imposes a maximum current I_c in the trapping wire following the scaling law $I_c = \xi d^{3/2}$ [83]. With d being the distance of the cloud from the wire, also the homogeneous field constituting the trap is determined, thereby fixing the static trap gradient: $B' = \mu_0 I_c/(2\pi d^2)$. For the following analysis we chose $\xi = 1,8 \cdot 10^6\,\mathrm{Am}^{-3/2}$. This allows for a direct comparison to the purely magnetic double well scheme based on 5 wires, presented in part 2, chapter XYZ [92].

We are now free to choose a double well separation $2r_0$. As to first order, the splitting distance is independent of the Ioffe field (see (7.41)), the trap separation fixes the RF amplitude B_{RF}. The Ioffe field B_0 is then adapted to satisfy $r_0 = 2,74\,a_0$, in order to guaranty tunnelling in the two modes approximation. For technical reasons, we limit the maximal Ioffe field to 100 G (dotted line in figure (7.8)).

Choosing a structure size d and a trap separation $2r_0$ completely determines the system. We will now analyze the influence of fluctuations and noise on the system. Two major effects might

degrade the measured signal in a tunnel experiment:

- Fluctuations in tunnel coupling: Noise on the physical quantities determining the system or random additional external magnetic field fluctuations might alter the tunnel coupling (*e.g.* modify the trap separation). This effect will degrade the signal of an experiment, which reads out relative population in the two wells (*e.g.* Rabi or Josephson oscillations). As criterion for the feasibility of a tunnel experiment, we will tolerate a modification of the tunnel coupling up to 10 % due to noise or fluctuations

- Tilting of the double well: Noise on the physical quantities determining the system or random additional external magnetic field fluctuations will modify the position of the static trap and in result tilt the double well. A height difference h of the two wells induces a potential energy difference mgh, which leads to a corresponding (arbitrary) evolution of the differential phase. This effect will degrade the signal of an experiment, which reads out the relative phase of the two condensates. As criterion for the feasibility of a tunnel experiment, we will tolerate differential energy shift of 10 % of the tunnel coupling ($mgh = 0.1\,\delta$) due to noise or fluctuations

We will first analyze the effect of noise on the physical quantities constituting the system: the wire current, the external homogeneous magnetic field, the Ioffe field and the RF frequency and amplitude. For a chosen set of structure size d and trap separation $2r_0$, the tunnel coupling is derived from a 2D numerical simulation, as described above. This coupling is compared to the one obtained, when one of the above quantities is modified.

We find the double well structure astonishingly stable against this kind of noise: a relative stability of 1 % in all quantities is sufficient to allow stable tunnelling (in the limits described above) for the entire parameter space depicted in figure (7.8). The most critical parameter is the RF amplitude, a relative fluctuation of 1 % causes a fluctuation in tunnel coupling that saturates at 8 % for large trap separations.

A relative stability of 1 % in the parameters generating the initial static trap can be easily implemented in a BEC experiment; the achievement of a Bose condensate with a less stable system seems not realistic. The stability of the static magnetic trap can be further improved by using noise reducing wire geometries, where external fields and wire fields are generated by the same current, as proposed in part 2 of this manuscript (see XYZ). RF frequencies can controlled to the 10^{-6} level using standard laboratory equipment. The stability of RF amplitude rests an issue: the control of low RF amplitudes has turned out to be non-trivial. We take this into account by assuming an absolute noise of $\Delta B_{\mathrm{RF}} = 10\,\mathrm{mG}$ on the RF amplitude. For small RF amplitudes (and consequently small trap separations) this fluctuation causes variations in the tunnel coupling that exceed the 10 %. The solid line in figure (7.8) indicates the trap separations, that are excluded from the parameter space because of this effect.

Under real experimental conditions, random magnetic field fluctuations independent of deliberately generated fields are present. We assume, that some experimental effort has been undertaken to reduce these fluctuations (*e.g.* passive shielding). To analyze their effect, a homogeneous magnetic field of 1 mG in an arbitrary spatial direction is added to the static field configuration. It turns out, that field fluctuations along the direction of the Ioffe field or along the direction of the homogeneous magnetic field (direction of the double well splitting) do not affect the configuration significantly, as they are small compared to the fields deliberately produced in these directions. In contrast, a field orientated transversally to the direction of the double well splitting causes a rotation of the double well. As initially, there is no magnetic field in this direction, even a small fluctuation of 1 mG creates a significant tilt, resulting in a shift of the relative phase of the condensates, as described above. The effect is stronger for larger

trap separations, excluding the region above the dotted curve in figure (7.8) from the parameter space.

A stability diagram resuming the above analysis is shown in figure (7.8). The gray area indicates the parameter region, in which a tunnel experiment can be performed. This area is limited from above by the condition $B_0 < 100\,\mathrm{G}$ (dashed line) and the effect of a tilted double well due to an auxiliary magnetic field noise of 1 mG perpendicular to the splitting direction (dotted line). It is limited from below by the effect of fluctuations in tunnel coupling due to instabilities in the RF amplitude (solid line).

As can be easily concludes from this analysis, a tunnel experiment based on dressed adiabatic potentials can be performed using structure sized from below $1\,\mu$m up to $740\,\mu$m. This is in strong contrast to the result of the corresponding analysis of the purely magnetic double well created by 5 wires, presented in chapter XYZ of part 2 of this manuscript. Here a tunnel experiment could only be performed with structures around $5\,\mu$m, applying the same constrains on stability, the same scaling law for maximum wire current and the same level of ambient noise.

The enhanced noise resistance of the RF adiabatic double well can be attributed to fundamental differences in scaling of the physical properties of the double well (*e.g.* trap separation and frequency) with structure size, which will be discussed in comparison in [CONCLUSION/OUTLOOK].

It is pointed out, that the structure size d indicates the distance of the trapped atoms from the trapping structure. Therefore tunnel experiments in adiabatic dressed potentials can be performed far from the chip surface, avoiding deleterious effect like heating and fragmentation described in part 1, chapter XYZ.

Chapter 8

Experimental setup

This chapter reviews the experimental setup employed by the Heidelberg group. We will focus on the description of the atom chip concept, which differs in many respects from the Orsay approach: it involves macroscopic (mechanically machined) structures as well as (lithographically fabricated) microscopic wire patterns. The wires itself act as a mirror for the (optimized and entirely chip-based) surface magneto optical trap.

The remaining setup is conceptually identical to the Orsay apparatus: a single chamber vacuum system holds the atom chip, ^{87}Rb atoms are loaded from a background gas created by pulsed dispensers, the laser system is based on extended cavity diode lasers.

The setup has been thoroughly characterized and described in great detail in the PhD and diploma theses [160, 161, 162, 163] and publications [79, 125, 82, 164] whereto we refer for further information.

8.1 A hybrid macroscopic-microscopic atom chip

8.1.1 The Micro fabricated atom chip

The atom chips used in the Heidelberg setups are realized by S. Groht, a detailed description of the procedure can be found in [165]. The fabrication is carried out at the Weizmann Institute of Science, Israel (department of condensed matter physics) in collaboration with the group of I. Bar-Joseph.

The Heidelberg atom chips follows a different approach in combining micro fabricated wires for magnetic trapping with a reflecting (mirror) surface used in a surface magneto optical trap: here, the (reflecting) top surface of the wires themselves is used to create the mirror. The wires are defined by small (1-10 μm) micro fabricated groves, the pattern is designed to cover the entire chip surface with wires or grounded surfaces to minimize non-reflecting areas (see figure (8.2a)).

The fabrication process is based on optical lithography and direct gold evaporation, almost analogous to the process for the design of the seed gold layer in the second generation atom chip in Orsay (compare section 5.2.2): a 20 mm$\times$25 mm Si wafer is thermally oxidized to create a 100 nm insulation layer of SiO_2. A photoresist (AZ5214E) is applied to the wafer and the wire pattern is transferred to the resist by shining UV light through a lithographic mask (created in a dedicated beam writer as described in 5.1.3). After development, the photoresist only remains on the small stripes, separating the wires. By thermal evaporation, a 50 nm Ti adhesion layer, followed by a 1-2 μm gold layer is deposited on the substrate. The gold evaporated onto the photoresist is removed by lift off in an acetone bath, realizing the separations between the wires.

Gold evaporation creates a surface of excellent optical quality. As the wires are directly fabricated on the (λ/100) flat single crystal wafer and by construction are of equal height, the atom chip mirror does not suffer from large wavelength waviness as encountered in the Orsay

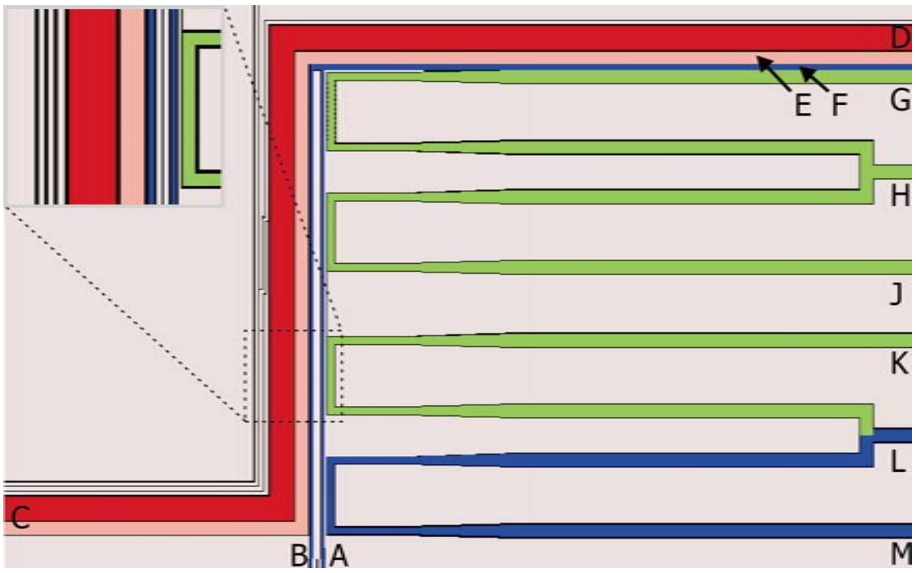

Figure 8.1: Design drawing of the central region of the atom chip wire pattern. All structures are 2 μm high and created by gold evaporation. The grey areas indicate grounded gold surfaces, current carrying structures are visualized by color. A detailed description and dimensions can be found in the text.

experiment. Small shadows in the reflected beams due to non-reflecting gaps between the wires were found to not disturb the functioning of the surface MOT significantly. However, light scattered at wire edges degrades the quality of absorption images when using the chip surface as a mirror.

Figure (8.1) shows the wire design in the central region of the atom chip. The magnetic traps used in experiments described in chapter 9 are created be the 100 μm (50 μm) Z shape wire depicted in dark (light) red. This wire is 2 μm high, has a central length of 1850 μm and can carry up to 2 A (1,2 A) continuously. A parallel L shaped 10 μm wire (blue, connections B-F) is used as an antenna for the RF induced double well potential. Four 20 μm U shape wire structures at the side of the RF antenna can be used to increase the longitudinal confinement or create additional potentials based on electric fields [166].

The use of gold evaporation limits the height of the structures to 1-2 μm (limited by the thickness of the photoresist and the non-directive nature of the evaporation process) and consequently limits the currents that can be employed. It is therefore hard to realize a magneto optical trap based on a U shaped wire using this technique, capturing atoms in a magnetic wire trap far from the chip surface is complicated. Therefore, to realize a U-MOT, simplify the transfer of atoms towards the surface and perform a first stage of magnetic trapping and evaporative cooling, macroscopic (copper) wire structures below the atom chip are employed.

8.1.2 Macroscopic wire structures

The underlying macroscopic wire structure has significantly evolved and improved throughout different generations of atom chip experiments in Heidelberg, starting with simple bend silver wires and ending up with optimized multi layer copper structures machined to 50 μm precision. This evolution is characterized in the theses [160, 161, 162, 163] and publications [79, 125, 82, 164]. Here we will briefly describe the system used in the actual experiments, depicted in figure (8.2b+d).

Optimized U shape structure The U shape wire structure has been thoroughly optimized

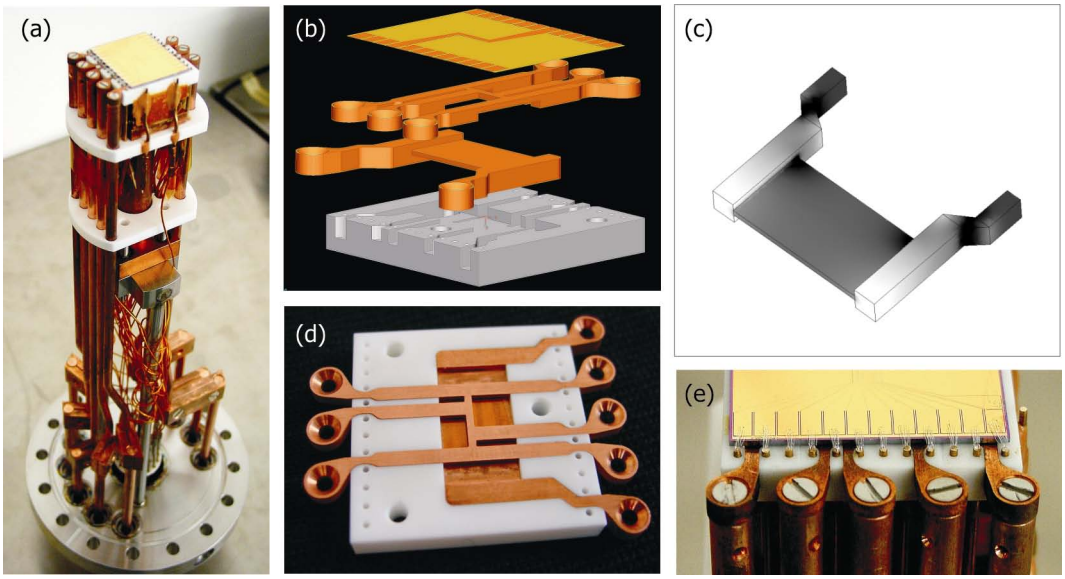

Figure 8.2: Photographs and design drawings of the macroscopic wire structures and the assembled chip mounting. (a) chip mounting as described in 8.2.1. (b) design drawing of the copper structures, the atom chip and the marcor carrier ceramic. (d) photograph of the elements without chip. (c) computer simulation to optimize for homogeneous current flow in the central bar of the U shape structure [167]. (e) photograph of the assembled system. One identifies the wire bondings connecting the atom chip to gold-copper terminals as well as massive 5 mm copper rods, connecting the underlying macroscopic structures.

to create an unperturbed magnetic quadrupole field over a large spatial region (compare section 6.1.1). The central U wire has therefore been extended to a bar of 21 mm length, 10 mm width and 0,7 mm height. To realize homogeneous current flow through the bar, the connection leads are fabricated significantly thicker (3 mm×3 mm), so that resistances become negligible (see figure (8.2c)). The structure can carry up to 60 A (power supply: HP 6011A) continuously and together with an external bias field realizes a quadrupole field of sufficient gradient at a distance of 6-8 mm from the chip surface. The shape of the magnetic field is only weakly deformed (over the size of the MOT beams $d \simeq 24$ mm) compared to an "ideal" quadrupole field created by coils in anti Helmholtz configuration.

Extended H shape structure Above the U shape copper structure (isolated by a 50 μm kapton foil), an "extended H shape" structure is inserted (see figure (8.2b+d)). It consists of an H structure with a central wire of 7 mm (compare section 3.3.2 for a discussion of the created magnetic fields), two additional connection leads allow to realize a magnetic Z wire trap with a central wire length of 3 mm. This structure can equally carry 60 A (power supply: HP 6551A) continuously and the created magnetic trap can be used to capture atoms released from the the surface MOT after a phase of approach. When compressed, magnetic traps created by the extended H structure provide sufficient confinement to apply efficient evaporative cooling. The first Bose-Einstein condensates realized in the Heidelberg group were achieved in wire traps based on such macroscopic structures [82, 164].

To electrically isolate the U shape structure and the H shape structure from the (metallic) atom chip mounting, both structures are embedded in an accordingly machined glass ceramic (marcor) carrier (see figure (8.2b+d)), which provides sufficient thermal conductivity (1.5 $\mathrm{WK^{-1}m^{-1}}$). To obtain good thermal contact and heat dissipation, the mechanical contact between the copper structures and the marcor ceramic were optimized, resulting in machining tolerances below

50 μm, which can be obtained with modern erosion machines and CNC lathes. The copper elements where electrically contacted by bolting them to massive 5 mm copper rods, on their part connected to high power UHV feedthroughs in the CF-100 carrier flange of the chip mounting. Again, mechanical contact was optimized to reduce contact resistances and to optimize heat dissipation (see figure (8.2a+e)).

Additional holes in the marcor carrier hold gold-covered copper pins, which provide connection terminals for isolated wires connecting to a standard 35 pin UHV feedthrough. Electrical connection to the chip is realized by bonding the chip contact pads to the gold-copper pins (see figure (8.2e)).

8.2 Experimental setup

8.2.1 Chip mount

The mechanical mounting of the atom chip setup is based on a CF-100 blind flange. A standard 35 pin feedthrough (2 A per pin) has been welded into the flange together with six high power copper feedthroughs (150 A, both Caburn MDC). A support bridge based on hollow stainless steel tubes is equally welded to the flange, holding the copper head of the chip and providing active water cooling of the entire mounting (see figure (8.2a)).

Onto the cooled bridge, an I shaped copper column is bolted. Two marcor spacers can move along the central part of the column and hold long, straight 5 mm copper bars that connect to the macroscopic wire structures. Contact to the high power feedthrough pins is realized by massive copper clamps to reduce contact resistances.

The head of the mounting carries the U shaped and the H shaped wire structures as described above. The atom chip itself is glued in place using UHV compatible epoxy (EpoTech 920). Macroscopic structures and atom chip are mounted horizontally and upside down to allow atoms to fall freely under the influence of gravity when released from the trap. The total length of the mounting is 31 cm, all materials were checked for UHV compatibility in a separate test chamber. Detailed engineering drawings and assembly guidelines can be found in [167].

8.2.2 Vacuum system

The vacuum system employed in the Heidelberg experiments is conceptually identical to the one used in the Orsay setup (compare section 5.3): a single stainless steel chamber is pumped by an Ti sublimation pump (Varian TSP cartridge filament source) and an ion getter pump (Varian Starcell 500 L/s), commercially available Rb dispensers are used as a pulsed atom source (see figure (8.3a)). The spatial dimensions are chosen slightly larger, optimizing for optical access (*e.g.* allowing for absorption imaging along all three axes) at the cost of pumping speed, consequently prolonging the experimental cycle to 45 s.

The central element of the vacuum system is a stainless steel (low magnetization 316LN steel) octagon of 7 cm height and 20 cm diameter (see figure (8.3c)). It is connected to a standard CF-100 5-way cross, leading to the pumps, a vacuum gauge and an inlet port to connect a turbo molecular pump needed in bake out after breaking the vacuum. Optical access is provided by anti reflection coated view ports, sealed to the chamber by HelicoFlex gaskets.

The pulsed Rb source is directly mounted to the main chamber: four high power copper UHV feedthroughs are welded into a CF-35 blind flange. Two of these hold three RB dispensers (SAES Getters) in parallel inside the vacuum. Outside the chamber, the feedthrough rods are connected to water cooling to rapidly reduce the temperature of the dispensers after the loading pulse. The two remaining feedthrough rods are connected by a copper bar on the vacuum side. The current operating the dispensers is led through this bar, running in opposite direction to compensate the created magnetic fields.

Without running the dispensers, a background pressure of $\approx 3 \times 10^{-11}$ mbar is obtained. In operation, the dispensers are pulsed by sending up to 32 A in a multi step procedure [163] for 27 s, which loads a magneto optical trap and allows vacuum to recover before transferring atoms to a magnetic trap. After this time, the measured lifetime of atoms in a magnetic trap is ≈ 45 s, which is sufficient to obtain a Bose-Einstein condensate and perform experiments.

8.2.3 External magnetic fields

As the magnetic quadrupole field necessary for the operation of a magneto optical surface trap is provided by the macroscopic U shape wire structure (in combination with a homogeneous

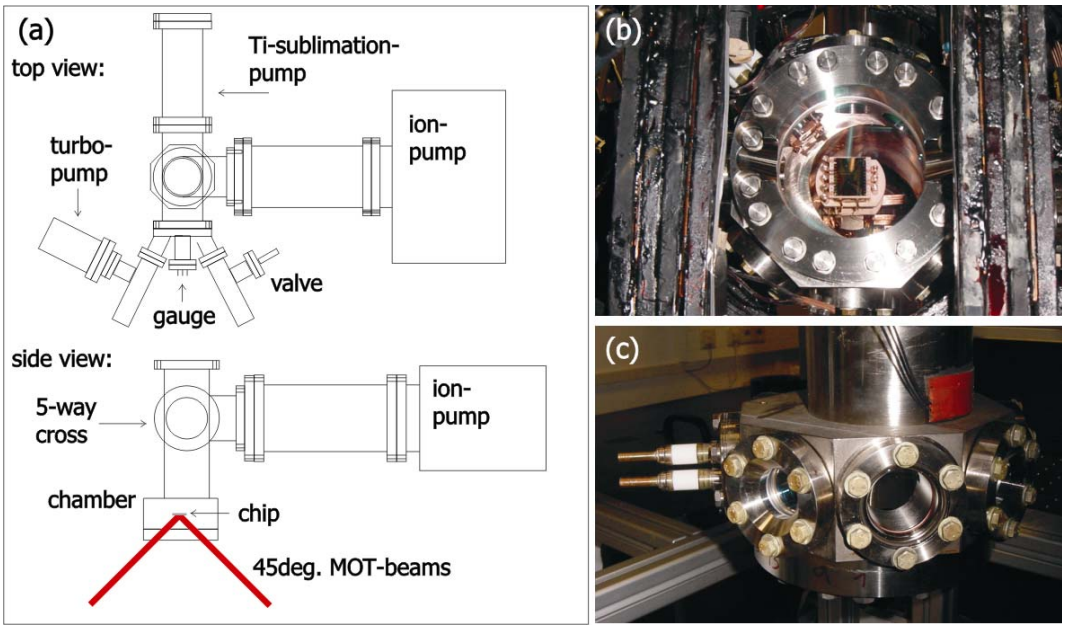

Figure 8.3: Design drawing and photographs of the vacuum system. (a) top and side view of the entire system. (b) photograph taken from below the setup in operation conditions. One identifies the coils creating the homogeneous external bias field, the central vacuum octagon with chip mounting and the Rb dispensers (top left in the chamber). (c) photograph of the vacuum octagon after bakeout. One identifies the high power feedthroughs (left) connecting to the Rb dispensers.

external bias field), no dedicated anti Helmholtz coils are required. The setup is equipped with three orthogonal pairs of rectangular coils (side length $\approx$ 34 cm) in Helmholtz configuration, providing a homogeneous magnetic field (over the size of the atomic cloud) in each spatial direction. There coils are wound (88 turns) of a massive 2 mm$\times$10 mm copper wire, held together by a special epoxy resin (Stycast 2850) with advantageous thermal properties (see figure (8.3b)). These coils can carry up to 60 A continuously, creating a magnetic field of 120 G. As the used power supplies (HP 6651A) can not switch off the coils sufficiently fast, dedicated switches are utilized, which are matched to the coil impedances and extinguish the magnetic field within 100 μs.

Three additional pairs of rectangular coils (side length 60 cm, 100 windings of a 1 mm cylindrical wire, power supplies HP 66312A) are used to continuously compensate the earth magnetic field.

8.2.4 Laser System

The optimized optical access and the larger (reflecting) atom chip surface in the Heidelberg experiment enables the use of larger beam diameters ($d \simeq 24$ mm) and consequently an enlarged capturing area in the magneto optical trap. This however necessitates high laser power and a more complex laser system compared to the Orsay setup: the two main frequencies of the optical cooling cycle are amplified, either using a master-slave configuration as discussed in section 5.3.4 (repump transition), or using a commercial MOPA (master oscillator power amplifier) laser system (cooling transition). The employed laser system has been studied and described in detail in [167].

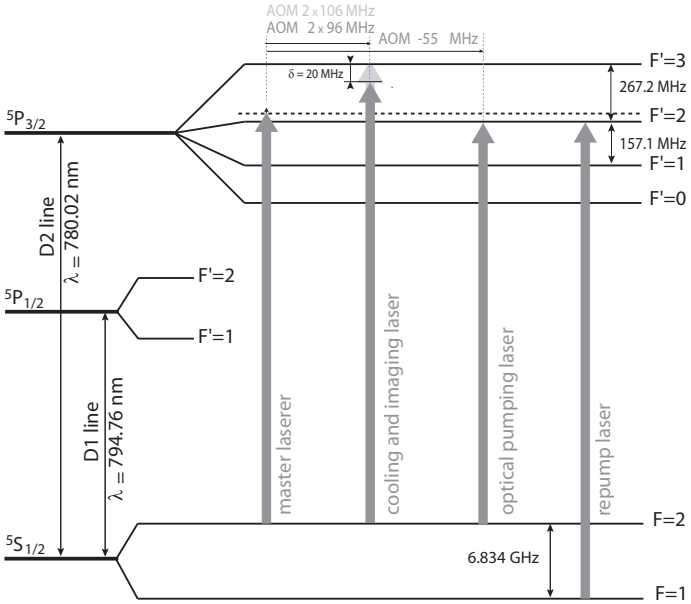

Figure 8.4: ^{87}Rb levels used for laser cooling, optical pumping and absorption detection in the Heidelberg setup. The preparation of the individual frequencies is described in the text.

The MOPA laser system

A commercial laser system (Topica TA 100) is used to produce up to 450 mW usable laser power for the D-2 cooling transition of ^{87}Rb ($\lambda \simeq 780,02\,\text{nm}$) with a spectral width of $\approx 1,2\,\text{MHz}$. A small fraction of the master laser light is extracted to a Doppler-free absorption spectroscopy setup. The laser frequency is feedback stabilized to the 1-3 spectroscopy crossover of the $F = 2 \leftrightarrow F' = 1/F' = 3$ transition using FM spectroscopy [168]. We thereby establish a frequency standard which is detuned by -213 MHz with respect to the $F = 2 \leftrightarrow F' = 3$ cooling transition. The so stabilized laser frequency is injected into the tapered amplifier crystal and intensified to 450 mW. It is distributed as follows:

Optical cooling About 90 % of the beam power are extracted and injected into an AOM in double-pass configuration (2×96 MHz) to prepare the cooling light, -20 MHz detuned with respect to the $F = 2 \leftrightarrow F' = 3$ transition. The beam is enlarged to $d \simeq 24\,\text{mm}$ and split into four to be injected into the vacuum chamber.

Imaging Five per cent of the remaining beam power are injected into an AOM in double-pass configuration (2×106 MHz) to be used in resonant absorption imaging. The beam is spatially filtered using an optical fiber and directly applied to the atoms using an beam expander. Three different expanders allow for the connection of imaging systems on all three axes.

Optical pumping The remaining 5 % if light intensity are injected into an AOM in single-pass configuration, detuned to additional -55 MHz, to prepare light resonant with the $F = 2 \leftrightarrow F' = 2$ transition, used for optical pumping (compare section 6.1.2).

In addition to fast switching performed by the AOMs, each beam is individually controlled by mechanical shutters.

The repump laser

Atoms that decay to the $F = 1$ ground state have to be re-injected into the cooling cycle. A repump laser is therefore applied to the atoms, resonant with the $F = 1 \leftrightarrow F' = 2$ transition. This optical frequency is provided by a home-built extended cavity laser in Littrow configuration, stabilized to the 1-2 crossover ($F = 1 \leftrightarrow F' = 1/F' = 2$) in a Doppler-free absorption spectroscopy, detuned by -79 MHz from resonance. This light is injected into a slave laser diode (compare 5.3.4) and thereby amplified to ≈ 50 mW. An AOM in single-pass configuration tuned to 79 MHz compensates the detuning and serves as a fast switch. The beam is enlarged to ≈ 24 mm, split into two and overlapped with two MOT beams, entering the vecuum chamber under 45 °.

8.2.5 Atom detection

Absorption imaging [132] is performed to detect trapped atoms in situ or in time of flight expansion when released from the trap. Two different optical systems are employed to record data presented in this manuscript:

Transverse imaging The first imaging system allows to take images orthogonal to the long axis of the usually elongated atomic cloud in a wire trap, parallel to the chip surface. Two monochromatic doublets ($f_1 = 100$ mm and $f_2 = 400$ mm) transport the image to the camera and realize a magnification $\times$ 3,9, the measured resolution is 3,4 μm [169]. The camera is a background illuminated MicroMAX 1024BFT with a quantum efficiency of 70 % at 780 nm, the pixel size is 13 μm$\times$13 μm. The camera is mounted on a motorized, computer controlled translation stage, which allows for focussing with micron precision.

Longitudinal imaging To detect interference phenomena as presented in chapter 9 of this manuscript, a new imaging system was constucted, allowing for absorption imaging along the elongated axis of the atomic cloud. As initially no imaging system was foreseen in this direction, the optical access is restricted, resulting in a rather long distance between the atom cloud and the first lens (monochromatic doublet, f =150 mm). A second lens (monochromatic doublet, f =1200 mm) projects the picture onto the CCD camera chip and realizes a magnification of $\times$ 9,3, according to the large pixel size of 20 μm$\times$20 μm. The obtained resolution is 5,7 μm [170]. As a camera, we employ a Roper Scientific NTE/CCD-1340/400 with 65 % quantum efficiency at 780 nm. The electronic readout of the camera is relatively slow, limiting the time between the two pictures to 200-400 ms. This makes the setup vulnerable to mechanical vibrations and drifts, great care has been taken to reduce these effects (reduction of optical elements in the imaging beam path, rigid mechanical support structure, pulsed operation of the CCD chip cooling fan).

8.2.6 Experimental control

As described in section 5.3.6, a sophisticated computer based electronic control system is necessary to perform an experimental sequence of over 40 s with a temporal resolution on the microsecond level in a reproducible fashion. The Heidelberg setup utilizes a commercial control system (ADwin-Pro-System) which is conceptually identical to the sequencer employed in Orsay (compare section 5.3.6): a stand-alone unit carries a motherboard which provides an independent clock (50 kHz) and receives the experimental procedure via an opto-coupled local area network (LAN) interface. This decouples the experimental control from the noisy computer environment. The sequence is distributed to several input-output cards, 24 analog output, 32 digital output and 8 analog input channels are available in total. The signals are written out simultaneously

by all cards synchronized to the same clock, after the start trigger is received (which allows for a synchronization with the 50 Hz frequency of the ac power net).

The user interface is programmed in MatLab and is fully graphical, allowing to see and manipulate the entire sequence at once. A small local network gathers information from the control computer and the various camera computers to provide a first real time analysis of the experimental run. Parameters can be varied automatically, also multi dimensional parameter scans are possible. The stability of the experimental setup (especially the laser system) allows for uncontrolled operation over night, several days/nights of continuous data taking were performed to obtain results presented in chapter 9 of this manuscript. A detailed description of the programming as well as a characterization of the noise level of the experimental control system can be found in [171].

Chapter 9

Experimental results

This chapter presents experiments performed in double wells potentials based on dressed adiabatic potentials as introduced in chapter 7. All experiments are carried out with (pure) Bose-Einstein condensates, for the first time accessing the coherence properties of this quantum state in the context of magnetic micro traps on atom chips.

The creation of pre-cooled atomic samples in magnetic traps created by current carrying macroscopic wire structures is outlined in section 9.1, more detailed descriptions can be found in [163, 162, 172].

Section 9.2 describes the transfer of the cold atomic cloud to magnetic traps formed directly on the atom chip and the achievement of Bose-Einstein condensation herein. By applying an oscillating magnetic field in the radio frequency (RF) domain, Zeeman sub-states of the trapped atoms are strongly coupled. The spatial dependence of this coupling creates new potential minima in the "dressed" potential. Depending on frequency and amplitude of the RF magnetic field, these minima form in the harmonic or the linear region of the initial static magnetic wire trap (of Ioffe-Pritchard type) as described analytically and numerically in section 7.2.2. Both regimes are investigated experimentally: in the linear regime, large double well trap separations (up to $80\,\mu$m) can be directly observed in absorption imaging. For small distances in the harmonic regime, information about the double well is inferred from matter wave interference patterns, exploiting the property of the split condensates to posses a collective quantum phase.

We find, that atom-atom interactions significantly modify the interference patterns compared to an ideal gas model and have to be included to correctly interpret the measurements. For both splitting regimes we find excellent agreement between measurement and the theoretical models for the dressed adiabatic double well potential.

Combining dressed adiabatic potentials with the atom chip approach draws direct benefit from the high trap frequencies provided by wire traps and transfers adventurous properties to the RF induced double well. As a consequence, the (adiabatic) splitting of a condensate can be performed rapidly and on small spatial scales, rendering the process less vulnerable to technical fluctuations.

Coherent splitting of a Bose-Einstein condensate is experimentally demonstrated using this technique in a very simple wire geometry. We analyze the distribution of the measured relative phase throughout the splitting process: a broadening of the phase distribution and a coinciding loss of contrast on a timescale of $\approx 2,5\,$ms is observed, which remains to be understood. A deterministic evolution of the relative phase due to a residual imbalance in the double well potential is observed. By adjusting this imbalance, the phase evolution can be accelerated or reversed in direction.

The presented experiments aim to introduce dressed adiabatic potentials as a new tool for micro chip based atom optics. Quite naturally, they raise many new questions, some of which will be listed as an outlook in section 9.3.

9.1 Bose-Einstein condensation

This section briefly outlines the experimental sequence which is employed to create a cloud of ultra cold atoms or a Bose-Einstein condensate in a wire trap based on a macroscopic Z shape structure below the atom chip. This procedure is independent of the actual design of the atom chip wire patterns and has become a standard routine, which is used (in adapted versions) in all four atom chip experiments in Heidelberg [164, 82]. More detailed descriptions and a discussion of the optimized parameters can be found in [163,162,172,167]. The loading of atoms to magnetic wire traps formed on the atom chip and experiments therein are subject of section 9.2.

9.1.1 Magneto optical surface trap

The integrated magneto optical surface trap based on a macroscopic U shape wire structure (compare section 8.1.2) is loaded from a Rb background gas, created by pulsed dispensers. This loading stage takes 22 s in total an can be divided into three steps: during the first 10 s, a current of 35 A is send through the dispensers heating them up and causing the desorption of Rb atoms. The current is then reduced to 25 A for 7 s, where the U-MOT continues to load atoms but the dispensers cool down to below threshold. They are completely turned off for another 5 s to allow the vacuum quality to recover. During this time, the laser power is reduced by a factor of two (30 mW to 15 mW per beam) to suppress losses from the MOT due to exited-state collisions [163]. More than 95 % of the atoms remain trapped during these 5 s pumping time. The detuning of the cooling laser is permanently set to -20 MHz with respect to the $F = 2 \leftrightarrow F' = 3$ ^{87}Rb transition (compare figure 8.4), the distance of the atoms from the surface is about 5 mm.

The atoms are approached to the surface (2 mm) by increasing the external homogeneous bias field (compare equation (3.12)), which simultaneously increases the gradient (equation (3.14)), leading to a compression of the atomic cloud. Note, that the longitudinal (parallel to the U wire central bar) gradient is by a factor 1/4 lower than in the transverse directions, leading to an elongated shape of the MOT, well matched to the equally elongated shape of the magnetic trap. The homogeneous magnetic fields in all three spacial directions are employed to adjust the final position of the MOT and "mode-match" to the magnetic trap (compare section 6.1.3). The phase of approach takes 100 ms and can be performed without significant loss of atoms [173].

9.1.2 Optical molasses and optical pumping

After approaching and compressing the MOT, all magnetic fields are turned off (except the ones permanently compensating the earth magnetic field) within 100 μs (1 μs for the U shape wire). To perform sub-Doppler cooling in an optical molasses, the cooling laser is detuned to -50 MHz in the same time [138, 139, 140, 141]. The atoms are allowed to expand for 10 ms in this configuration, reducing the temperature to 20 μK, well below the Doppler temperature of 140 μK.

To polarize the atomic sample to the $|F = 2, m_F = 2\rangle$ trapping state, optical pumping is performed: to establish a well defined magnetic quantization axis, the homogeneous external bias field is ramped to 0,5 G, the atoms are illuminated by a 200 μs pulse of sigma polarized light resonant on the $F = 2 \leftrightarrow F' = 2$ transition (with repumper light on continuously) transferring the atoms to the desired double stretched dark state. By employing optical pumping, the number of atoms captured in the magnetic trap could be increased by a factor of ≈ 4 (compare section 6.1.2), close to the theoretically expected value of 5 [142] .

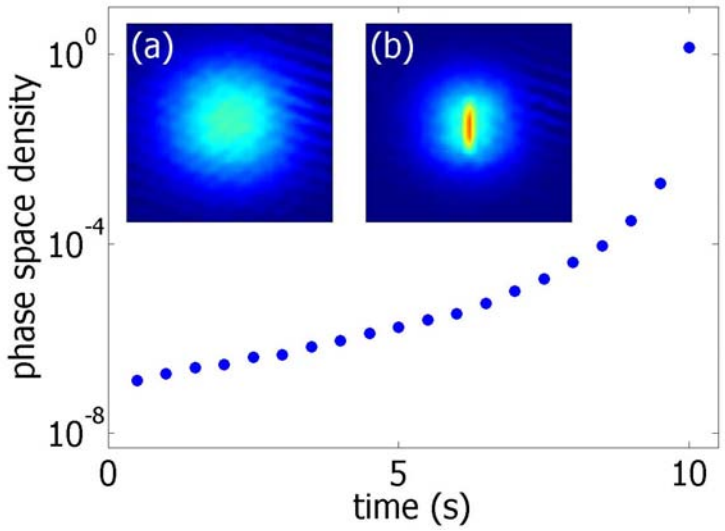

Figure 9.1: Phase space density throughout the first 10 s evaporative cooling phase in a magnetic trap based on a macroscopic Z shape wire. The insets show atomic density distributions after 14 ms free expansion: the onset of Bose-Einstein condensation can be identified by the appearance of a (anisotropic) density peak (b) in the isotropically expanding thermal gas component (a).

9.1.3 BEC in a macroscopic Z wire trap

After cooling and optical pumping, the atoms are re-trapped in a shallow magnetic trap based on the combined fields of a current carrying Z shape macroscopic copper wire and an homogeneous external bias field. A current of 60 A in the structure and an external field of 28 G creates a trap located 1,6 mm from the chip surface with trap frequencies $\omega_\perp = 2\pi \times 69$ Hz and $\omega_\parallel = 2\pi \times 24$ Hz, the longitudinal ("Ioffe") field at the trap bottom is 8,7 G. Up to 2×10^8 atoms are recaptured in this trap, mode matching imperfections lead to an increase of temperature to 350 μK.

The magnetic trap is compressed by linearly increasing the external bias field to 41 G and simultaneously lowering the longitudinal field to ≈ 1 G within 1 s. The compressed trap provides trapping frequencies of $\omega_\perp = 2\pi \times 380$ Hz and $\omega_\parallel = 2\pi \times 32$ Hz which is enough to apply radio frequency evaporative cooling (compare section 6.1.4)

The oscillating RF magnetic field driving spin flip transitions to untrapped states is generated by superimposing an oscillating current to the DC current in the macroscopic Z wire structure with the help of a bias tee. The frequency of the RF field is lowered linearly starting from 20 MHz down to ≈ 1 MHz in 10 s, pre-cooling the sample and increasing phase space density (see figure (9.1)). We typically obtain 3×10^6 atoms at a temperature of 10 μK after the pre-cooling phase.

These atoms are now either transferred to different magnetic traps, created by current carrying micro wires on the atom chip (see next section) or directly cooled to quantum degeneracy in the Z wire structure by a second RF cooling ramp. This ramp is generated by a different function generator, which allows for precise control of the final frequency to a precision better than 500 Hz. Starting at 2 MHz, the RF frequency is linearly reduced to a value a few kHz above the resonance frequency at the trap bottom within 2 s. By carefully adjusting the final ramp frequency, a Bose-Einstein condensate of 5×10^4 atoms can be obtained. Slightly higher numbers can be reached in magnetic traps created on the atom chip, which provide significantly higher trap frequencies and allow for more efficient evaporative cooling (compare next section).

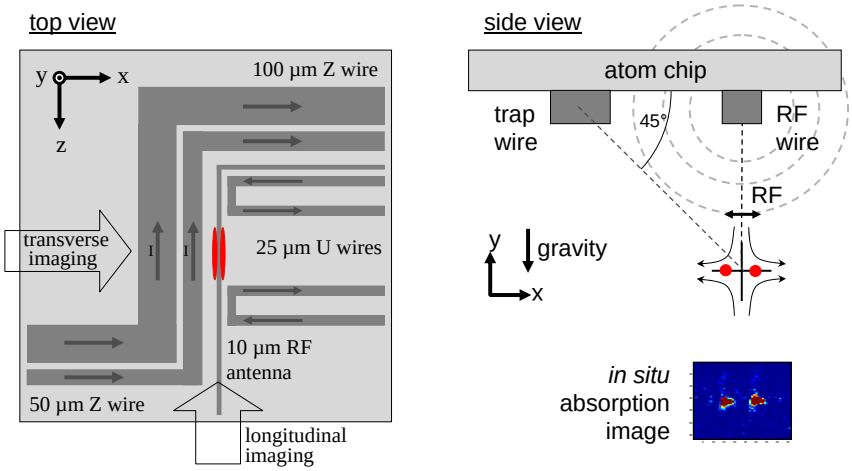

Figure 9.2: Schematic illustration of the atom chip wire pattern used in the dressed adiabatic double well experiments. Two orthogonal optical systems allow for absorption imaging in the transverse and in the longitudinal direction of the elongated atomic cloud (top view). The position of the static magnetic trap can be adjusted to allow for a balanced double well potential by rotating the external magnetic bias field (45 ° shown as an example) and by changing the trapping wire (dc) current.

9.2 Dynamic splitting of a BEC in an RF induced double well potential

9.2.1 BEC on the atom chip

To perform experiments in RF induced adiabatic double well potentials, a Bose-Einstein condensate is created directly on the atom chip: 3×10^6 pre-cooled atoms of a temperature of $10\,\mu$K are prepared by evaporative cooling in the magnetic trap based on a current carrying macroscopic Z wire structure below the chip, as described in the previous section. To simplify the following transfer to the atom chip trap, a continuous current of 1 A can be send through a $100\,\mu$m Z shape wire on the atom chip throughout the 10 s pre-cooling phase. The atoms are loaded to the chip trap by linearly increasing this current to 2 A within 1 s and simultaneously turning off the current in the Z wire copper structure. The external homogeneous bias field is lowered to 18,4 G, the longitudinal field is adjusted to maintain a trap bottom of ≈ 1 G in the same time. This creates an elongated magnetic trap ($\Re = 25$) of trapping frequencies $\omega_\perp = 2\pi \times 430$ Hz and $\omega_\parallel = 2\pi \times 17$ Hz, almost similar to the trap created by the macroscopic Z wire structure. A second stage of evaporative cooling, consisting of a 2 s linear frequency ramp from 3 MHz down to $600 - 800$ kHz, cools the atoms to below the critical temperature, pure Bose-Einstein condensates of up to 3×10^4 atoms were used in the following experiments.

The above procedure can be easily modified to create BECs in different magnetic traps (more or less confining, different aspect ratio) at different positions (*e.g.* by changing the wire current or the external magnetic field in angle and magnitude) or based on different wires. On-chip Bose condensates are routinely produced using wires of $100\,\mu$m, $50\,\mu$m and $10\,\mu$m width, at distances between $5\,\mu$m and $400\,\mu$m and aspect ratios between 10 and 500 have been realized [163, 172].

To characterize the BEC, atom clouds are analyzed in time of flight absorption images, taken along the transverse direction (see figure (9.2)). The onset of condensation can be easily identified by the characteristic elongated density peak within the isotropically expanding thermal background (compare inset in figure (9.1)). However, fluctuations of the longitudinal condensate

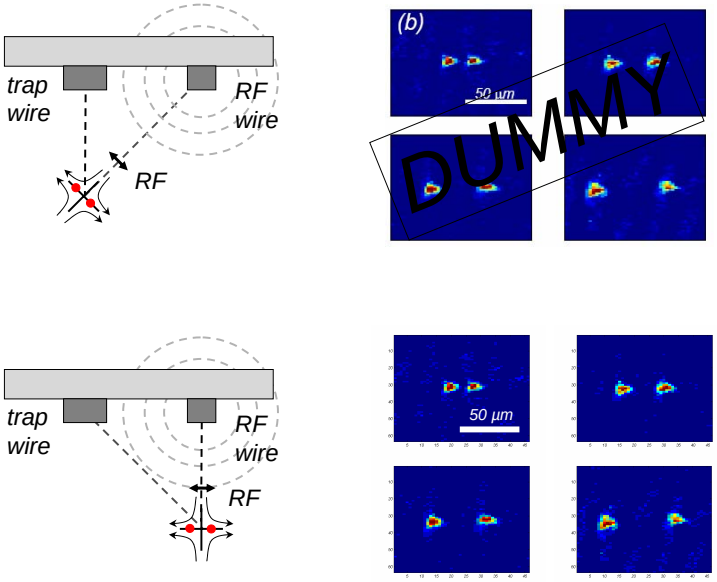

Figure 9.3: The spatial orientation of the RF induced double well is determined by the relative orientation of the static magnetic trapping field (of Ioffe-Pritchard type) and the oscillating magnetic RF field; potential minima form where both fields are parallel, which results in vanishing coupling of the atomic Zeeman states. A balanced double well potential, allowing for equal splitting of the condensate, can be realized for several static trap positions between the trapping wire and the RF antenna (see text for details).

phase lead to interference phenomena in expansion (compare section 1.3.3) and a (random) modulation of the longitudinal BEC density profile (see figure (1.5)), slightly complicating the analysis. On the other hand, the appearance of longitudinal interference fringes is an indicator for a common (though fluctuating) phase and can be used to identify the phase transition. At the atom-wire distances considered in the described experiments ($\geq 80\,\mu$m), magnetic potential roughness due to wire corrugation (compare section 3.5) is completely negligible [122, 163] and can not explain a (random) modulation of the BEC longitudinal density profile.

As a fluctuating longitudinal phase complicates an experiment aiming to study coherence in a transversally split condensate, we tried to create less elongated condensates by increasing the axial confinement. Additional currents (up to 700 mA) were send through 10 μm U shape wire structures on the atom chip (schematically depicted in figure (9.2)), increasing the longitudinal confinement to 35 Hz. In some experiments (see next sections), the magnetic trap was additionally approached to the U wires by rotating the external bias field (see figure (9.2)), increasing the effect. Qualitatively, a reduction of longitudinal interference fringes could be observed, indicating a more homogeneous condensate phase. However, fluctuations could not be completely suppressed and we believe them to be present in all experiments presented in the following. A dedicated study on how aspect ratio and atom temperature affect the longitudinal phase is underway and will be subject of the thesis of S. Hofferberth.

9.2.2 Exploring the linear splitting regime

The radio frequency source

To deform a single magnetic micro trap to a double well potential, the trapped atoms are "dressed" by means of a strong, near resonant oscillating magnetic (RF) field as described in

chapter 7. This RF field is applied using a 10 μm chip wire, parallel and close to the 100 μm and 50 μm Z shaped trapping wires, as an antenna (see figure (9.2)). The necessary RF signal is produced by a standard programmable frequency generator (stanford research systems SRS345), which provides linear (triggered) frequency ramps without phase discontinuities over the desired frequency range between 100 kHz and 10 MHz. The amplitude can be computer controlled via an analog input channel of the frequency generator [174]. For fast switching of the RF and to suppress RF noise close to resonance during the preparation of the Bose condensate, we employ an RF switch (MiniCircuits XYZ) with XYT dBm subbression. The signal is amplified using a simple XYW W solid state amplifier (Motorola XYZ) which can provide of to 100 mA oscillating current in the antenna wire. To avoid grounding problems, an 1:1 isolation transformer is used to decouple the chip wire from the RF source.

To determine the RF intensity radiated by the 10 μm antenna wire, the closed circuit (wire in parallel with the transformer) has been characterized in the frequency range from 350 kHz to 4 MHz using a network analyzer. Although the circuit consists mainly of straight wires (the inductance of the transformer is negligible in the frequency range of interest), the Smith diagram reveals an (with frequency) increasing inductive behavior in addition to the pure ohmic dc resistance. The impedance increases approximately linearly from 11,8 Ω (for 350 kHz) to 88,6 Ω (for 4 MHz), allowing for a maximum oscillating current of 100 mA at the highest frequency, realizing 1 G of oscillating magnetic field at a distance of 200 μm from the wire.

The splitting procedure

Double well potentials with large trap separations, sampling the linear regime of the initial static magnetic trap, are created using (final) RF frequencies of positive detuning, well above the Lamor frequency of the atoms at the trap bottom as described in section 7.2.2. To adiabatically transfer Bose-Einstein condensates into these traps, a static magnetic single well trap is deformed using a two step RF amplitude-frequency ramp: we start with a fixed RF frequency of 500 kHz, realizing a negative detuning of $\omega - g_F \mu_B |\mathbf{B}_0|/\hbar = -2\pi \times 250\,\text{kHz}$ and linearly increase the RF amplitude to an intermediate value ($\approx$ 50 mA oscillating current) within 5 ms. A numerical simulation of the dressed adiabatic potential (taking into account finite sizes of the chip wires) shows, that the single well trapping potential is not significantly deformed during this first amplitude ramp. A small heating of the atomic cloud could be observed for ramps much faster than 5 ms, from this value on, heating was suppressed.

In a second step, we increase the RF frequency by triggering a pre-programmed linear 20 ms ramp to a variable final frequency between 1 MHz and 3,5 MHz, effectuating the splitting to rather large trap separations. Again, a much faster ramp speed resulted in heating of the atomic sample (*e.g.* reduction of the condensate fraction), no significant heating is observed from 20 ms on. Unfortunately, the SRS345 signal generator does not allow for a constant final RF frequency after the triggered ramp, inhibiting hold time experiments, which would reveal heating mechanisms in the dressed double well potential in the linear regime (see next section for a lifetime heating/lifetime estimate in the harmonic regime).

Balancing the double well potential

As outlined in section 7.2.1, the spatial orientation of the RF induced double well crucially depends in the relative orientation of the magnetic field vectors constituting the static magnetic trap and the direction of the oscillating magnetic field (compare also section 7.3). Placing the static magnetic trap directly below the trapping wire results in a tilt of the resulting double well with respect to the (horizontal) chip surface, as indicated in figure (9.3). For gravity alone, cold atoms would consequently accumulate in the lower well during the (adiabatic) splitting process. However, two other processes affect the balancing of the double well potential: the

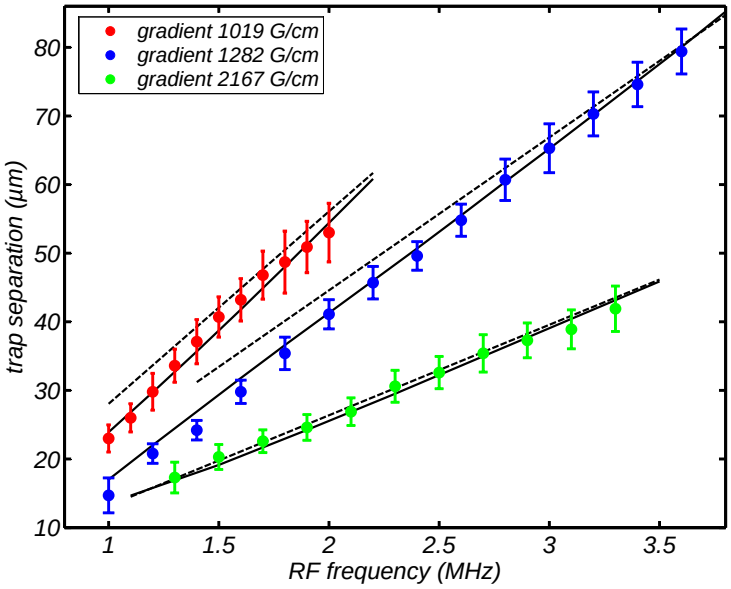

Figure 9.4: Double well trap separations for different RF frequencies, exploring the linear regime of three different static magnetic traps of different gradient (1019 G/cm, 1282 G/cm and 2167 G/cm). The distances are directly obtained from in situ absorption images as shown in figure (9.3). The error bars contain the statistical variance and a 6 % uncertainty in the camera calibration. The dotted lines represent the expected behavior for a purely linear magnetic trap (based on equation (7.29). The solid lines are results of a numerical simulation of the adiabatic double well potential, based on the magnetic fields of the actual wire geometry and the external calibration of the RF amplitude.

quadrupole magnetic field created in a wire trap is not completely rotational symmetric around the minimum, the gradient increases slightly in the direction towards the trapping wire. In a double well, this results in a corresponding increase in trap frequency for the well closer to the trapping wire. Additionally, the RF magnetic field is not fully homogeneous over the spatial extension of the double well potential, resulting in an increased coupling for the well facing the RF antenna, increasing the effective trap bottom.

By carefully adjusting the position of the static magnetic trap between the trapping wire and the RF antenna (*e.g.* tilting the external magnetic bias field or varying the trapping wire current) these three effects can be brought to cancel to zero, realizing a balanced double well (which may be nevertheless tilted in space, see figure (9.3)).

To directly observe the transversally split elongated clouds, a new longitudinal imaging system was installed (compare section 8.2.5). As it has to be combined with a pair of MOT beams along this axis, several optical elements (*e.g.* beam splitter cubes) have to be employed, degrading the optical resolution to $\approx 12\,\mu$m compared to the theoretical diffraction limit of the isolated optical system of $5{,}7\,\mu$m. Therefore, double well splittings from $15\,\mu$m on could be directly resolved in in situ absorption images, as depicted in figure (9.4). By varying the final frequency of the RF ramp, different double well trap separations can be obtained (compare equation (7.29) and figure (7.5)). Experimentally, splittings up to $80\,\mu$m could be realized. For even larger separations, the static field vector of the wire trap becomes more and more parallel to the orientation of the RF field vector (vanishing influence of the longitudinal "Ioffe" field $\mathbf{B}_0$), resulting in a reduced RF coupling at the trap minimum. Such a reduction of coupling strength leads to a reduction of level repulsion and enables spin flip transitions to different dressed Zeeman

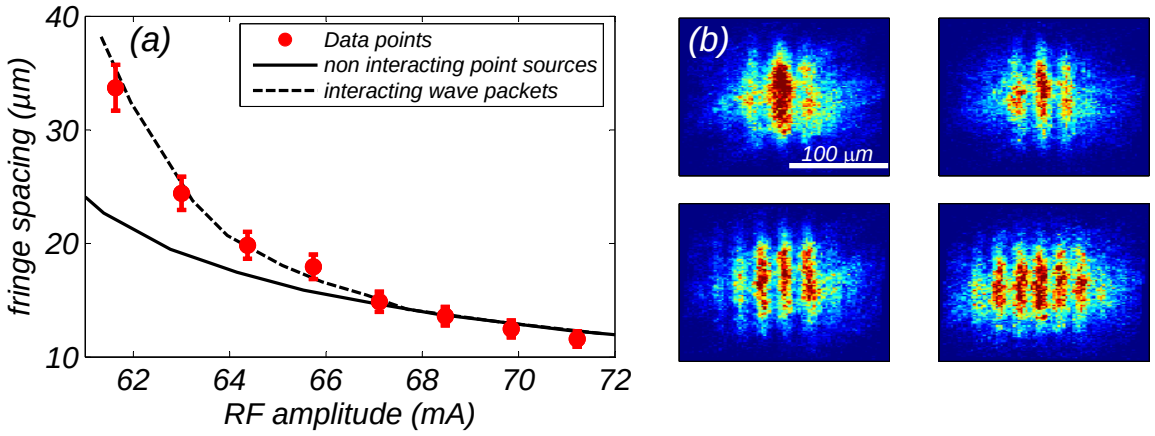

Figure 9.5: Bose-Einstein condensates released from double well potentials created in the harmonic regime of the static magnetic trap give rise to matter wave interference patterns (b). The interference fringe spacing contains information on the initial separation of the sources. (a) shows measured fringe spacings for different amplitudes of the RF oscillating magnetic field (realizing different double well separations). The error bars indicate the statistical variance of the mean value and a 6 % calibration uncertainty. The solid line indicates the fringe spacing expected for non-interacting point sources located at the bottoms of the individual wells (the double well separation being calculated numerically based on our experimental parameters). The dashed line takes into account the effect of interactions on the wave function in the double well and during the free expansion.

levels.

We find it interesting to note, that atoms undergoing spin flip transitions at the avoided crossings are partially re-trapped in lower lying dressed states, which present a potential minimum at the position of the initial static trap, centered between the double well (compare figure (7.2)).

To verify our theoretical models and the calibration of the RF amplitude, the double well separation for different RF frequencies was investigated for three different realizations of a static wire trap, providing three different gradients (1019 G/cm, 1282 G/cm and 2167 G/cm) at different balancing positions. Figure (9.4) compares the measured double well separations to the model for the linear regime (equation (7.29), dashed line) and to a full numerical simulation bases on our wire geometry (solid line). The excellent agreement to the complete model validates our RF amplitude calibration, all other quantities entering the model (wire currents and magnetic fields) are known to the percent level from independent calibrations [163].

9.2.3 Exploring the harmonic splitting regime

Measuring trap separations

For the creation of a double well in the harmonic regime of the static magnetic trap, it is convenient to work with on-resonant RF frequencies or small negative detunings and high RF amplitudes. As outlined in section 7.2.2, the harmonic approximation for the static trapping potential is valid up to double well separations $r_0 \leq 1,14 B_0/B'$. For typical wire traps realized in our experiments ($B_0 \simeq 1\,\mathrm{G}$, $B' \simeq 1000\,\mathrm{G/cm}$) this distance is below $10\,\mu$m and can therefore not be resolved directly in our longitudinal imaging system; an indirect measurement of the double well splitting has to be performed.

As the Bose-Einstein condensate remains in its degenerate quantum state (*e.g.* possesses a

defined phase) throughout the splitting, releasing both clouds from the trap gives rise to matter wave interference effects, as described in section 1.4 (see figure 9.5b). Neglecting atom-atom interactions and the shape and spatial extension of the initial wave packets, the fringe spacing Δz is characterized by

$$\Delta z \simeq \frac{ht}{md} \tag{9.1}$$

where t is the free expansion time and d the initial separation of the sources. Analyzing interference patterns therefore provides information on the initial double well splitting.

Balancing the double well potential

To realize RF induced double well potentials in the harmonic regime of the static magnetic trap, a simple 15 ms linear RF amplitude ramp to variable final value is performed at a fixed frequency of 500 kHz (detuning adjusted to $-2\pi \times 200$ kHz). To achieve high (local) RF power, the static magnetic trap, based on the 50 μm Z shape wire (compare figure (9.2)) is positioned directly below (80 μm distance) the RF antenna wire, by rotating the external magnetic bias field to 45 °, giving rise to a almost perfect horizontal splitting.

The balancing of the so prepared double well poses a problem, as the two clouds can not be directly resolved in the imaging system. An uneven balancing would in theory result in a reduction of fringe contrast in the interference signal. However, technical problems (e.g. a small tilt of the elongated atomic cloud with respect to the imaging probe beam, insufficient depth of field) already reduce the contrast to $\approx 30\,\%$, making this signal little reliable. The following procedure is employed to nevertheless directly monitor the balancing of the double well potential: the RF amplitude ramp is performed as described above to realize rather large trap separations. The oscillating magnetic field is then rapidly ramped down to zero within 100 μs. This ramp is sufficiently fast with respect to the Lamor frequency ($\approx 2\pi \times 1$ MHz), so that the atoms adiabatically return to the "undressed" double stretched $|F = 2, m_F = 2\rangle$ Zeeman trapping state. However, this turnoff is fast compared to the external dynamics timescale, namely the trap oscillation frequency of the atoms ($\approx 2\pi \times 1$ kHz). Not having moved significantly in space within 100 μs, the two clouds find themselves at the positions of the (largely split) double well minima, but experiencing the single well static magnetic trapping potential. They hence get accelerated towards the trap center. After $300 - 400\,\mu$s also the static trapping potential is suddenly switched of (wire current and external fields). The clouds ballistically cross each other and move apart with increasing expansion time, where they finally can be resolved individually in longitudinal absorption imaging. Although this rather violent method destroys the Bose condensate, counting atoms in both (now thermal) clouds allows for a fine tuning of the position of the static magnetic trap and therefore a balancing of the double well potential, as described in the previous section.

The splitting procedure

Once the balancing point is found, the experiment is carried out in the way described above: the RF frequency is set to a continuous value of 500 kHz. Using the analog amplitude control of the signal generator, the RF power is linearly increased to a variable final value within 15 ms, realizing a double well in the harmonic regime of the static magnetic trap. After the ramp, atoms are released from the trap by simultaneously turning off the oscillating magnetic field, all static magnetic fields and the trapping wire current [175].

As the splitting is performed horizontally, both clouds are projected on top of each other in transverse imaging (see figure (9.2)). Qualitative information about heating due to the splitting process can be obtained by looking at longitudinal density profiles (here, the condensate fraction is in the Thomas-Fermi regime and can be easily distinguished from the thermal background,

which is hard in the longitudinal imaging). Amplitude ramps have been performed in a range from 1 ms to 100 ms. From 3 ms on, no significant heating can be observed in the transverse imaging. By holding the RF amplitude at a constant value after the ramp, the clouds are maintained in the double well configuration. We observe a reduction of the (initially pure) condensate fraction by 50 % within 500 ms, which is equivalent to the heating rate in our static magnetic traps, which we attribute to inelastic three body processes and parametric heating induced by technical noise. Note that no RF shielding is employed in these experiments.

Measuring trap separations

As the split atom clouds are strongly confined in the transverse direction, the elongated shape converts to a pancake shape in expansion (inversion of elipticity), leading to low atomic densities in the longitudinal imaging (projecting transverse to the pancake surface), consequently restricting the maximum expansion time to 14 ms. Given the imaging resolution of $\approx 12\,\mu$m and applying equation (9.1), a maximum double well separation of $5{,}4\,\mu$m can be detected by looking at interference fringes. To realize a full splitting (with negligible tunnel coupling) of a BEC at this distance, a high transverse confinement if the initial static trap ($2\pi \times 2,1$ kHz, measured by parametric heating) at the balancing position was necessary, obtained by operating the $50\,\mu$m wire at its maximum current of 1,2 A.

Figure (9.5) compares the experimentally measured interference fringe spacings for different RF amplitudes to the theoretical expectation (solid line) based on equation (9.1) and a numerical simulation of the double well trap separation. As can be clearly seen, te simple model (neglecting interactions and spatial shape of the wave packets) well describes the experimental results for large RF amplitudes (small fringe spacings, large double well separations) but fails for small RF amplitudes (larger fringe spacings, small double well separations.

A similar effect has been reported in the MIT experiments, where a Bose-Einstein condensate was (incoherently) split by means of a blue detuned focussed laser beam and brought to interference for the first time [37]. A detailed study based on a numerical integration of the Gross-Pittaevskii equation identified this mismatch as an effect of atom-atom interactions, affecting the wave packets shape in the double well as well as during the first phase of expansion [176]. This influence becomes increasingly important for small trap separations and not entirely split condensates.

In the same spirit, we performed a numerical simulation of our system. Based on the theoretical model for the effective double well potential, the entire experimental sequence was numerically simulated using the split step Fourier method [177]. To reduce the computational effort, the simulation is performed in the 2D transverse plane, the (constant) longitudinal confinement is taken into account by adjusting the ground state energy in each computational step. Figure (9.6) shows a typical result of the simulation for a double well separation of $3{,}42\,\mu$m. In this calculation, the double well is held constant for 1 ms for a possible mismatch of the initial wave function to damp out and than is abruptly extinguished, allowing for a free expansion of the atoms (3 ms).

Two effects alter the numerically obtained fringe spacings compared to the simple model assuming non-interacting point sources localized at the double well potential minima: for small trap separations and even more for still connected wave packets, the barycenters of the wave functions are shifted inwards, resulting in a reduced "effective" trap separation ($3{,}10\,\mu$m instead of $3{,}42\,\mu$m in the shown example), giving rise to an increased fringe spacing. Additionally, repulsive interactions lead to a broadening of the modulated wave packet in the "collision" phase ($1 - 2$ ms) after releasing the clouds. Both effects contribute about equally to the effective interference pattern (leading to a fringe separation of $5{,}24\,\mu$m in the example instead of $4{,}03\,\mu$m expected from the simple model).

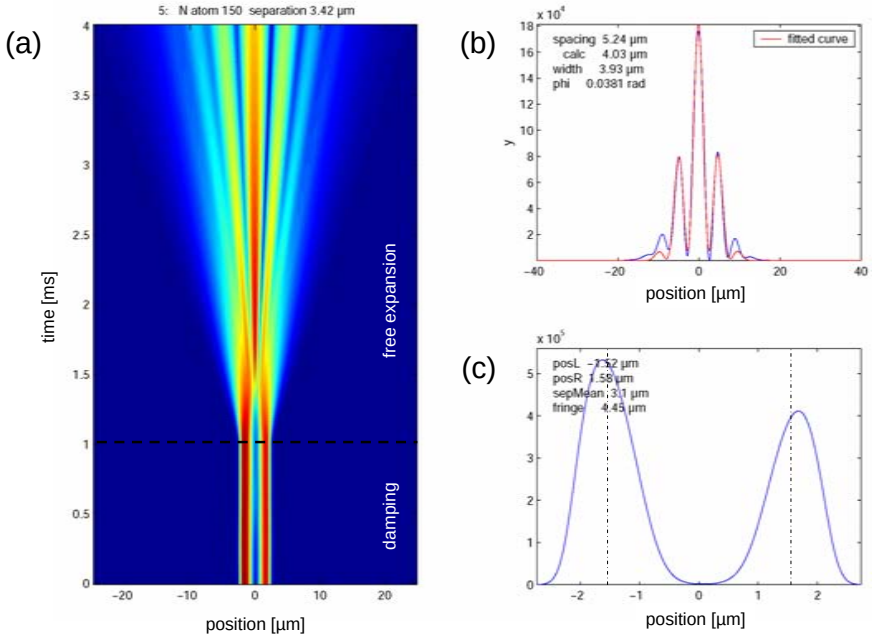

Figure 9.6: Numerical simulation to investigate the influence of interactions on the interference pattern (*e.g.* the fringe spacing). The in-trap ground state (after a 1 ms relaxation phase to damp out a potential initial wave function mismatch) shows a slight asymmetry (c), the barycenters slightly shifted inwards (indicated by dotted vertical lines) with respect to the minima of the double well potential (at the peak positions of the wave function), leading to a reduced "effective" double well splitting (and enlarged fringe spacing). The wave function is allowed to propagate freely for 3 ms (a). Repulsive interactions in the "collision" phase do additionally affect the interference pattern in the case of small double well distances (and consequently high densities). The fringe spacing is determined by fitting a cosine function with a gaussian envelope (see text) to the obtained probability distribution (b).

As the influence of interactions quickly breaks down in the expansion (as the atomic density reduces), the fringe spacing can be linearly extrapolated from 3 ms to the 14 ms, relevant for the interpretation of experimental data (instead of performing the entire time consuming propagation, which was done once to validated the linear extrapolation).

For large trap separations, where the wave packets are well centered around the individual trap minima and the atomic density is already significantly reduced in the (delayed) "collision" phase, the numerical calculation reproduces the results obtained using equation (9.1) (compare figure (9.5)).

The interference fringe spacings expected from the above numerical calculation, based on our experimental parameters (wire current, magnetic fields, atom number) are depicted in figure (9.5). The extended model is in excellent agreement with the measured fringe spacings, allowing us to infer the double well separation from the matter wave interference signal in the following experiments.

We would like to point out, that the elongated Bose condensates used in these experiments are at the 1D-3D crossover, where the chemical potential μ varies between $2,5-6\times\hbar\omega_\perp$ throughout the splitting process (initial static trap parameters: 2×10^4 atoms, $\omega_\parallel = 2\pi\times35\,\mathrm{Hz}$, $\omega_\perp = 2\pi\times2,1\,\mathrm{kHz}$). In the transverse direction, the Thomas-Fermi approximation is no longer valid

and the shape of the wave function approaches the (single particle) gaussian form of the ideal gas in a harmonic trap (compare section 1.3.2). However, neglecting atom-atom interactions leads to an underestimate of the matter wave fringe spacing and a corresponding overestimate of double well trap separation by almost a factor of two.

9.2.4 Coherent splitting of a Bose-Einstein condensate

As described in section 1.4, recombining two separate Bose-Einstein condensates gives rise to interference phenomena for (phase coherent) sources originating from a single BEC as well as for independently created sources (of arbitrary relative phase). For an adiabatic splitting as performed in the above experiments, one would expect a well defined, reproducible relative phase for each experimental realization. However, it has been shown to be extremely delicate to maintain the phase coherence throughout the splitting process in various experimental approaches [37,178]. The transition from a single condensate to two entirely separated (but phase coherent) clouds has been achieved recently, using optical potentials based on focussed red detuned laser beams [43]. A coupled (coherent) system in a double well with adjustable barrier height has been realized in [55] using combined optical potentials based on focussed lasers and standing waves. The demonstration of coherent splitting in a purely magnetic scheme on an atom chip represents a main result of this thesis [101].

Phase coherence

To test for phase coherence in the dynamic splitting of a Bose condensate in the RF induced double well, we repeat the above experimental sequence many times: we perform the RF amplitude ramp to a fixed finite value within 15 ms, the trap is immediately switched off after the ramp and the split clouds are allowed to expand freely for 14 ms time of flight. Atomic density profiles obtained from images taken in longitudinal absorption imaging (see figure (9.7 left, insets)) are integrated along the direction of the fringes and fitted by a generic function $f(z) = G(z)[1 + C\cos(\Delta\phi + 2\pi z/\Delta z)]$, where $G(z)$ describes a gaussian envelope, C the fringe contrast, $\Delta\phi$ the relative phase and Δz the fringe spacing as analyzed above. Figure (9.7 right) shows relative phase and contrast in a polar plot (inset) and a histogram of the measured relative phase for 40 realizations of the same experiment for two different final double well trap separations (3,45 μm and 3,85 μm).

We clearly find a narrow distribution of the measured relative phase, indicating a coherent splitting of the Bose condensate. The phase distributions is broadened for the larger splitting (using the same duration of the RF ramp) to 28 ° compared to the small splitting (13 °) but is still clearly non-random. Both splitting distances are above the critical value of 3,34 μm, where the in-well wave-function presents a zero between the individual wells [179]. As we are using a constant RF amplitude ramp, the critical splitting distance is reached only at the very and of the process (13 ms of the 15 ms ramp for the largest double well separations realized). The actual separation takes place on a timescale of $\approx 0,5$ ms. We expect this to be fast with respect to any tunnel dynamics and the coupling to break down immediately after passing the critical distance (compare section 2.2 for a theoretical discussion of the dynamic splitting process). Therefore, both situations shown in figure (9.7) present individual condensates, the phase relation is not mediated by tunnel coupling.

The width of the relative phase distribution has been monitored throughout an entire splitting sequence as indicated in figure (9.8 bottom). We observe a continuous increase of phase spread until the relative phase is almost random for the largest splitting distances. We also observe a coinciding loss of contrast, both effects are not yet fully understood and under investigation: we are able to obtain narrower relative phase distributions for the large double well trap separations by performing faster splitting ramps (to identical final value). The process of

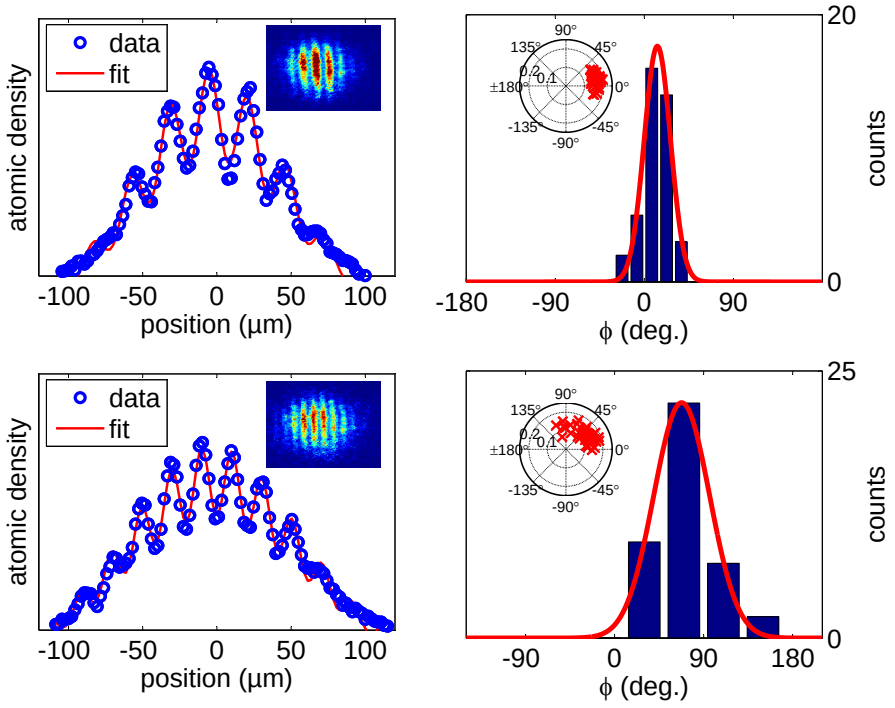

Figure 9.7: Left: a cosine function with gaussian envelope (see text) is fitted to integrated atomic density profiles, obtained from absorption images of matter wave interference patterns (inset). Information on fringe spacing, contrast and relative phase is extracted from each fit. Right: relative phase and contrast for 40 repetitions of the experiment in a polar plot (inset). A histogram of the measured relative phase shows a narrow phase distribution (13 ° and 28 ° respectively), indicating a coherent splitting process. The upper data set corresponds to a double well separation of 3,45 μm, the lower one to 3,85 μm trap distance.

phase randomization and the disappearance of contrast seems to take place in a fixed timescale of $\approx 2,5\,\mathrm{ms}$, independent of the final double well splitting. We would like to point out, that the measured lifetime of the condensates in the double well is at least 500 ms (compare previous section).

We believe longitudinal phase fluctuations in the elongated condensates to be the reason for the vanishing phase signal [57]. They have been observed at any stage of the splitting process in the transverse imaging. Once the splitting is complete and tunnel coupling suppressed, the longitudinal phase evolves individually in each condensate with a specific timescale τ. For splitting times $\Gamma \ll \tau$, the longitudinal phase modulation is essentially identical in both condensates, giving rise to an identical relative phase in the transverse direction. As the longitudinal imaging integrates the identical transverse interference patterns along the cloud, these patterns sum up and allow for high contrast and a measurement of a well defined phase. For slower splittings $\Gamma \simeq \tau$, the longitudinal phase has evolved independently in each individual condensate, leading to a local relative phase, which varies along the condensates. This leads to a broadening of the overall measured phase distribution and a loss of contrast in the individual longitudinal absorption images, until the interference pattern completely vanishes for $\Gamma \gg \tau$.

The "diffusion time" τ of the longitudinal phase can be calculated for the homogeneous 1D system following equation 2.30. Not being totally in this regime and with some uncertainty on the temperature, we estimate $\tau \simeq 1 - 3\,\mathrm{ms}$, which is consistent with our experimental observations. However, a thorough investigation of this processes is under way, analyzing the influence of atom

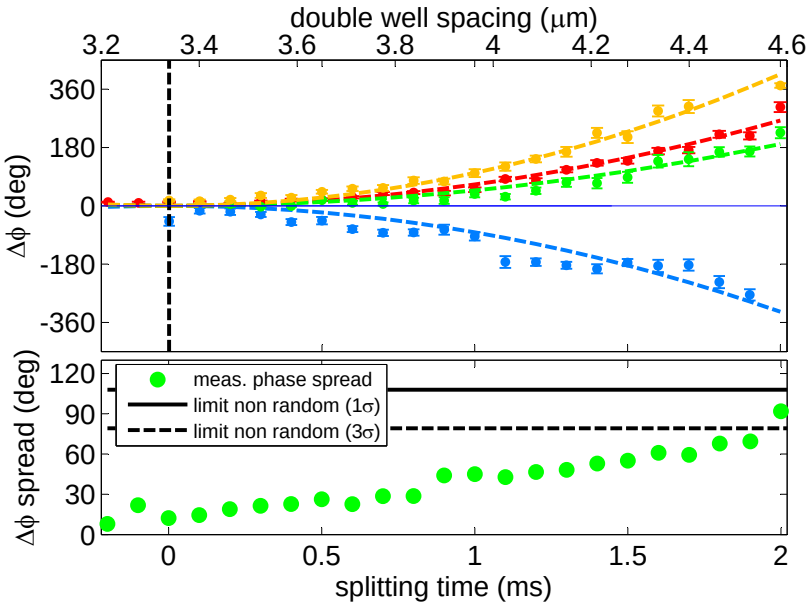

Figure 9.8: Top: evolution of the relative phase throughout the splitting process (15 ms constant ramp time, increasing final splitting distance). The dashed vertical line indicates the critical trap separation of 3,34 μm from which on both condensates are fully separated. To affect the phase evolution, the position of the static magnetic trap has been slightly changed, deliberately introducing a double well imbalance (different trap positions are distinguished by color). The error bars indicate the statistical variance of the mean of the measured relative phase. The dashed colored lines show the result of a numerical simulation of the splitting process, where the initial double well imbalance has been adjusted to fit the data. Bottom: width of the relative phase distribution throughout the splitting as shown in figure (9.7) for two specific settings. The data points correspond to the green curve in the upper plot. The solid (dashed) line indicates the level, below which the measured phase distribution can be distinguished from a random phase by one (three) sigma [180].

number, temperature and longitudinal confinement on the phase distribution. Additionally, a direct interferometric way of monitoring the longitudinal phase is currently implemented. This research will present a major part of the thesis of S. Hofferberth.

Phase evolution

Apart from the phase distribution broadening throughout the splitting process, we observe a deterministic evolution of the (mean) relative phase as depicted in figure (9.8 top, green curve). This is attributed to a small residual energy imbalance in the double well potential, leading to a different evolution of the phases in the individual wells. To test this hypothesis, we deliberately imbalance the double well by displacing the position of the static magnetic trap (by changing the wire current in 10 mA steps). As can be seen from figure (9.8), the phase evolution can be accelerated (red, yellow curves) or reversed in direction (blue curve). To compare with the numerical simulations, we add an artificial imbalance to the dressed adiabatic double well potential. This imbalance increases (linearly) during the splitting process leading to a quadratic evolution of the relative phase in time. The dashed curves in figure (9.8) represent the result of the numerical simulation, where only the initial double well imbalance has been adjusted to fit the data.

We note, that the evolution of the relative phase is sensitive to the experimental settings below the percent level (e.g. 0,8 % changes in wire current between the different curves). The results shown in figure (9.8) represent several days of continuous data taking, significant technical effort is employed to obtain sufficient long-time stability.

9.3 Outlook

The experiments presented in section 9.2 realize RF induced double well potentials in the different regimes of the underlying static magnetic trap, as theoretically described in chapter 7 of this manuscript. We could show, that Bose-Einstein condensates can be split by adiabatically deforming a single magnetic wire trap to a dressed double well potential. This splitting turned out to be rather insensitive to ramp timescales or technical fluctuations, heating or excitations could be avoided almost completely. We could show, that the splitting process does not significantly disturb the phase relation between the condensates and hence the splitting can be considered coherent. We observe a deterministic evolution of the relative phase which could be controlled by experimental parameters.

These experiments have to be considered as a proof of principles, arising many new questions which necessitate careful study. We will briefly list a few of the topics to be addressed in the following months, more long-term perspectives will be outlined in section XYZ.

Dynamics and stability of the splitting process The timings of the splitting sequences have been adjusted to minimize heating and excitations, which we only could detect in a qualitative way. For fast splitting ramps in the harmonic regime, an excitation of collective center of mass modes has been observed as a periodic modulation of fringe spacing. However, the splitting process appears to be very robust, once adiabaticity with respect to the external dynamics timescales (*e.g.* oscillation frequencies) is guaranteed [29]. Surprisingly, stopping the splitting process turned out by far more delicate: Excitations were observed when bringing the separation to a sudden halt, using linear amplitude ramps. More elaborate ramp shapes are currently being investigated.

For the larger separations in the linear regime of the static trap, hold time experiments were prohibited by technical limitations of the radio frequency source, a new dedicated RF generator, based on a direct digital synthesizer (DDS) module is being designed.

Once the atoms can be held in static double well configuration, a thorough investigation of heating processes becomes possible. If these processes are moderate or negligible (as we expect from preliminary measurements), the creation of independent Bose condensates by evaporative cooling in the double well potential can be envisaged. Reversing the splitting process and establishing a tunnel coupling between initially separate BECs should lead to the built up of a collective phase and allow for experiments complementary to the coherent splitting.

The role of interactions Atom-atom interaction play a significant role in almost any stage of the splitting experiment: the chemical potential sets the energy scale, on which a double well imbalance is tolerable. Although being close to the 1D regime, the transverse shape of the wave function is significantly modified by interactions compared to the ideal gas (see section 1.3.2). As described in section 9.2.3, matter wave interference patterns are likewise altered by interaction effects. The local chemical potential in each individual well is predicted to influence the evolution of the relative phase of both condensates (compare section 1.4.3). To reveal this effect, the splitting sequence has been performed with different initial atom numbers, the data remains to be analyzed.

Dynamics of phase coherence As described in section 9.2.4, the distribution of the relative phase broadens, the contrast diminishes and completely vanishes after $\approx 2,5\,\mathrm{ms}$ in interferometric experiments performed in the harmonic splitting regime. We attribute this effect to the presence of longitudinal phase fluctuations in the elongated Bose-Einstein condensates. The creation of more isotropic clouds seem an obvious next step but has turned out to be complicated with the current atom chip wire layout (a new dedicated

atom chip is currently being fabricated by S. Groht at the Weizmann Institute of Science in israel) exclusively using magnetic fields. An additional "dimple" potential created by a local static electric field [166] has shown to allow for low aspect ratio traps, however, the combination with the RF induced double well remains problematic in the current design.

If longitudinal phase fluctuations were the reason for vanishing phase signal, the "diffusion" time should scale in an appropriate way with temperature and atom number. However, a precise measurement of atom number and temperature in the presence of phase fluctuations is a research project in itself [27, 28].

We have therefore chosen an alternative approach to directly monitor transverse and longitudinal relative phase at once, which is currently being implemented: using two RF magnetic fields of orthogonal linear polarization and a relative phase of $\pi/2$, the creation of a balanced vertically orientated double well potential is possible [181]. In an interference experiment, this gives rise to horizontal fringe patterns, parallel to the chip surface, which can be observed in both imaging systems. A fluctuation of the longitudinal phase should be directly visible as a (transverse) displacement of the fringe pattern (in transverse imaging).

Annex

Annex: publications

In the framework of the collaborative Phd. thesis ("Cotutelle de thèse") between the *Laboratoire Charles Fabry à l'Institut d'Optique de L'Université Paris Sud* and the *Institut für Experimentalphysik der Universität Heidelberg*, the following papers were published:

Orsay

- J. Estève, J.-B. Trebbia, T. Schumm, A. Aspect, C. Westbrook, and I. Bouchoule, **Observations of density fluctuations in an elongated Bose gas: ideal gas and quasicondensate**, *arXiv:cond-mat/0510397*

- J. Estève, T. Schumm, J.-B. Trebbia, I. Bouchoule, A. Aspect, and C. I. Westbrook, **Realizing a stable magnetic double-well potential on an atom chip**, *Eur. Phys. J. D* **35**, 141-146 (2005)

- T. Schumm, J. Estève, C. Figl, J.-B. Trebbia , C. Aussibal, H. Nguyen, D. Mailly, I. Bouchoule, C. I. Westbrook, and A. Aspect, **Atom chips in the real world: the effects of wire corrugation**, *Eur. Phys. J. D* 32, 171-180 (2005)

- J. Estève, C. Aussibal, T. Schumm, C. Figl, D. Mailly, I. Bouchoule, C. Westbrook, and Alain Aspect, **The role of wire imperfections in micro magnetic traps for atoms**, *Phys. Rev. A* **70**, 043629(1-4) (2004)

Heidelberg

- I. Lesanovsky, T. Schumm, S. Hofferberth, L. M. Andersson, P. Krüger, and J. Schmiedmayer, **Adiabatic radio frequency potentials for the coherent manipulation of matter waves**, *arXiv:physics/0510076*

- L. M. Andersson, T. Schumm, I. Lesanovsky, S. Hofferberth, P. Krüger, and J. Schmiedmayer, **Comment on "Two-Dimensional Atom Trapping in Field-Induced Adiabatic Potentials"**, submitted to *Phys. Rev. Lett.*

- T. Schumm, S. Hofferberth, L. M. Andersson, S. Wildermuth, S. Groth, I. Bar-Joseph, J. Schmiedmayer, and P. Krüger, **Matter wave interferometry in a double well on an atom chip**, *Nature Physics*, **1**, 57-62 (2005)

- S. Schneider, A. Kasper, Ch. vom Hagen, M. Bartenstein, B. Engeser, T. Schumm, I. Bar-Joseph, R. Folman, L. Feenstra, and J. Schmiedmayer, **Bose-Einstein Condensation in a simple Micro trap**, *Phys. Rev. A* **67**, 023612(1-4) (2003)

- A. Kasper, S. Schneider, Ch. vom Hagen, M. Bartenstein, B. Engeser, T. Schumm, I. Bar-Joseph, R. Folman, L. Feenstra, and J. Schmiedmayer, **A Bose-Einstein condensate in a microtrap**, *J. Opt. B: Quantum Semiclass. Opt.* **5**, 143-149 (2003)

References

Bibliography

[1] A. Einstein, Zur Elektrodynamik bewegter Körper, Ann. Phys. **17**, 891 (1905).

[2] A. Einstein, Über die von der molekularkinetischen Theorie der Wärme geforderte Bewegung von in ruhenden Flüssigkeiten suspendierten Teilchen, Ann. Phys. **17**, 549 (1905).

[3] A. Einstein, Über einen die Erzeugung und Verwandlung des Lichts betreffenden heuristischen Gesichtspunkt, Ann. Phys. **17**, 132 (1905).

[4] N. R. A. Einstein, B. Podolski, Can quantum-mechanical description of physical reality considered complete?, Phys. Rev. **47**, 777 (1935).

[5] A. Einstein, Quantentheorie des einatomigen idealen Gases, Sitzungsber. Preuss. Akad. Wiss. **Bericht 22**, 261–267 (1924).

[6] A. Einstein, Quantentheorie des einatomigen idealen Gases. II, Sitzungsber. Preuss. Akad. Wiss. **Bericht 1**, 3–14 (1925).

[7] S. N. Bose, Plancks Gesetz und Lichtquantenhypothese, Z. Phys. **26**, 178 (1924).

[8] M. H. Anderson, J. R. Ensher, M. R. Matthews, C. E. Wieman, and E. A. Cornell, Observation of Bose-Einstein Condensation in a Dilute Atomic Vapor, Science **269**, 198 (1995).

[9] M. R. Andrews, M.-O. Mewes, N. J. van Druten, D. S. Durfee, D. M. Kurn, and W. Ketterle, Direct, Non-Destructive Observation of a Bose Condensate, Science **273**, 84–87 (1996).

[10] K. B. Davis, M.-O. Mewes, M. R. Andrews, N. J. van Druten, D. S. Durfee, D. M. Kurn, and W. Ketterle, Bose-Einstein Condensation in a Gas of Sodium Atoms, Phys. Rev. Lett. **75**, 3969–3973 (1995).

[11] M. O. Mewes, M. R. Andrews, N. J. van Druten, D. M. Kurn, D. S. Durfee, and W. Ketterle, Bose-Einstein condensation in a tightly confining DC magnetic trap, Phys. Rev. Lett. **77**, 416–19 (1996).

[12] M. Holland and J. Cooper, Expansion of a Bose-Einstein condensate in a harmonic potential, Phys. Rev. A **53**, R1954–R1957 (1996).

[13] F. Dalfovo and S. Stringari, Bosons in anisotropic traps: Ground state and vortices, Phys. Rev. A **53**, 2477–85 (1996).

[14] M. Holland, D. S. Jin, M. L. Chiofalo, and J. Cooper, Emergence of interaction effects in Bose-Einstein condensation, Phys. Rev. Lett. **78**, 3801 (1997).

[15] S. Grossman and M. Holthaus, Bose-Einstein Condensation and Condensate Tunneling, Z. Naturforsch. **50a**, 323–326 (1995).

[16] S. Grossmann and M. Holthaus, On Bose-Einstein condensation in harmonic traps, Physics Letters A **208**, 188 (1995).

[17] W. Ketterle and N. J. van Druten, Bose-Einstein condensation of a finite number of particles trapped in one or three dimensions, Phys. Rev. A **54**, 656–660 (1996).

[18] K. Kirsten and D. J. Toms, Bose-Einstein condensation of atomic gases in a general harmonic-oscillator confining potential trap, Phys. Rev. A **54**, 4188 (1996).

[19] J. M. Kosterlitz and D. J. Thouless, Ordering, metastability and phase transitions in two dimensional systems, J. Phys. C: Solid State Physics **6**, 1181–1203 (1973).

[20] E. Donley, N. R. Claussen, S. L. Cornish, J. L. Roberts, E. A. Cornell, and C. E. Wieman, Dynamics of collapsing and exploding Bose-Einstein condensates, Nature **412**, 295 (2001).

[21] N. N. Bogoliubov, On the theory of superfluidity, J. Phys. (USSR) **11**, 23 (1947).

[22] S. Giorgini, L. P. Pitaevskii, and S. Stringari, Condensate fraction and critical temperature of a trapped interacting Bose gas, Phys. Rev. A **54**, R4633–R4636 (1996).

[23] V. Dunjko, V. Laurent, and M. Olshanii, Bosons in cigar-shaped traps: Thomas-Fermi regime, Tonks-Girardeau regime, and in between, Phys. Rev. Lett. **86**, 5413 (2001).

[24] A. L. Zubarev and Y. E. Kim, Approximation for nonlinear dynamics of trapped Bose-Einstein condensates, Phys. Rev. A. **65**, 035601 (2002).

[25] S. Dettmer, D. Hellweg, P. Ryytty, J. J. Arlt, K. Stengstock, D. S. Petrov, G. V. Shlyapnikov, H. Kreutzmann, L. Santos, and M. Lewenstein, Observation of phase fluctuations in elongated Bose-Einstein condensates, Phys. Rev. Lett. **87**, 160406 (2001).

[26] F. Gerbier, J. H. Thywissen, S. Richard, M. Hubgart, P. Bouyer, and A. Aspect, Momentum distribution and correlation function of quasicondensates in elongated traps, Phys. Rev. Lett. **67**, 051602 (2003).

[27] S. Richard, spectroscopie en impulsion des fluctuations de phase de condensats de Bose-Einstein très allongés, Thèse de doctorat, Université de Paris XI (2004).

[28] F. Gerbier, Condensats de Bose-Einstein dans un piège anisotrope, Thèse de doctorat, Université de Paris XI (2003).

[29] C. Menotti and S. Stringari, Collective oscillations of a one-dimensional trapped Bose-Einstein gas, Phys. Rev. A **66**, 043610 (2002).

[30] This treatment is incorrect for traps of low aspect ratio. For strongly anharmonic traps of $\Re > 100$ as they are considered here, the longitudinal shape of the wafe function only differs by a few percent from the standard Thomas-Fermi profile (justifying the name *Thomas-Fermi 1D regime*).

[31] D. S. Petrov, G. V. Shlyapnikov, and J. T. M. Walraven, Phase-fluctuating 3D condensates in elongated traps, Phys. Rev. Lett. **87**, 050404 (2001).

[32] D. S. Petrov, G. V. Shlyapnikov, and J. T. M. Walraven, Regimes of Quantum Degeneracy in Trapped 1D Gases, Phys. Rev. Lett. **85**, 3745 (2000).

[33] F. Gerbier, Quasi-1D Bose-Einstein condensates in the dimensional crossover regime, Europhys. Lett. **66**, 771 (2004).

[34] D. Hellweg, S. Dettmer, P. Ryyty, J. J. Arlt, W. Ertmer, K. Sengstock, D. S. Petrov, G. V. Shlyapnikov, H. Kreutzmann, L. Santos, and M. Lewenstein, Phase-fluctuations in Bose-Einstein condensates, Appl. Phys. B **73**, 781 (2001).

[35] Z. Hadzibabic, S. Stock, B. Battelier, V. Bretin, and J. Dalibard, Interference of an Array of Independent Bose-Einstein Condensates, Phys. Rev. Lett. **93**, 180403 (2004).

[36] M. Greiner, O. Mandel, T. Esslinger, T. W. Hänsch1, and I. Bloch, Quantum phase transition from a superfluid to a Mott insulator in a gas of ultracold atoms, Nature **415**, 39–44 (2002).

[37] M. R. Andrews, C. G. Townsend, H.-J. Miesner, D. S. Durfee, D. M. Kurn, and W. Ketterle, Observation of interference between two Bose condensates, Science **275**, 637–641 (1997).

[38] Y. Castin and J. Dalibard, Relative phase of two Bose-Einstein condensates, Phys. Rev. A **55**, 4330–4337 (1997).

[39] R. H. Brown and R. Q. Twiss, Correlation between photons in two coherent beams of light, Nature **177**, 27 (1956).

[40] M. Lewenstein and L. You, Quantum Phase Diffusion of a Bose-Einstein Condensate, Phys. Rev. Lett. **77**, 3489–3493 (1996).

[41] J. Javanainen and M. Wilkens, Phase and phase diffusion of a split Bose-Einstein condensate, Phys. Rev. Lett. **78**, 4675–4678 (1997).

[42] A. J. Leggett and F. Sols, Comment on.

[43] Y. Shin, M. Saba, T. A. Pasquini, W. Ketterle, D. E. Pritchard, and A. E. Leanhardt, Atom Interferometry with Bose-Einstin Condensates in a Double-Well Potential, Phys. Rev. Lett. **92**, 050405 (2004).

[44] J. Javaneinen and M. Y. Ivanoc, Splitting a trap containing a Bose-Einstein condensate: Atom number fluctuations, Phys. Rev. A **60**, 2351 (1999).

[45] P. Villain and M. Lewenstein, Dephasing of Josephson oscillations between two coupled Bose-Einstein condensates, Phys. Rev. A **59**, 2250 (1999).

[46] Here, we use the energy of the 2D harmonic oscillator $\Delta E = 2 \times \frac{1}{2}\hbar\omega$, as our experimental system are (to first order) invariant to translation in the third direction. The tunnel coupling is nevertheless purely one-dimensional.

[47] G. J. Milburn, J. Corney, E. M. Wright, and D. F. Walls, Quantum synamics of an atomic Bose-Einstein condensate in a double-well potential, Phys. Rev. A **55**, 4318 (1997).

[48] J. R. Anglin, P. Drummond, and A. Smerzi, Exact quantum phase model for mesoscopic Josephson junctions, Phys. Rev. A **64**, 063605 (2001).

[49] A. Smerzi, S. Fantoni, S. Giovanazzi, and S. R. Shenoy, Quantum coherent atomic tunneling between two trapped Bose-Einstein condensates, Phys. Rev. Lett. **79**, 4950 (1997).

[50] S. Raghavan, A. Smerzi, and V. M. Kenkre, Coherent oscillations between two weakly coupled Bose-Einstein condensates: Josephson effects, pi oscillations, and macroscopic quantum self trapping, Phys. Rev. A **59**, 620 (1999).

[51] S. Raghavan, A. Smerzi, and V. M. Kenkre, Transitions in coheren oscillations between two trapped Bose-Einstein condensates, Phys. Rev. A **60**, R1787 (1999).

[52] Y. B. Zhang and H. J. W. Müller-Kirsten, Instanton approach to Josephson tunneling between trapped condensates, Eur. Phys. J. D **17**, 351 (2001).

[53] I. Marino, S. Raghavan, S. Fantoni, S. R. Shenoy, and A. Smerzi, Bose-condensate tunneling dynamics: Momentum-shortened pendulum with damping, Phys. Rev. Lett. **60**, 487 (1999).

[54] T. A. Fulton, *Superconductor Applications,*, Plenum„ New York, 1976, edited by B. Schwarz and S. Fower.

[55] M. Albiez, R. Gati, J. Fölling, S. Hunsmann, M. Cristiani, and M. K. Oberthaler, Direct Observation of Tunneling and Nonlinear Self-Trapping in a Single Bosonic Josephson Junction, Phys. Rev. Lett. **95**, 010402 (2004).

[56] F. Meier and W. Zwerger, Josephson tunneling between weakly interacting Bose-Einstein condensates, Phys. Rev. A **64**, 033610 (2001).

[57] N. K. Whitlock and I. Bouchoule, Relative phase fluctuations of two coupled one-dimensional condensates, Phys. Rev. A **68**, 053609 (2003).

[58] I. Bouchoule, Modulational instabilities in Josephson oscillations of elongated coupled condensates, Eur. Phys. J. D **32**, 171 (2005).

[59] L. Pezzé, A. Smerzi, G. P. Berman, A. R. Bishop, and L. A. Collins, Dephasing and breakdown of adiabaticity in the splitting of Bose-Einstein condensates, New Journal of Physics **7**, 85 (2005).

[60] K. W. Mahmud, H. Perry, and W. Reinhardt, Quantum phase space picture of Bose-Einstein Condensates in a double well: Proposals for creating macroscopic quantum superposition states and a study of quantum chaos, Phys. Rev. A **71**, 023615 (2005).

[61] By internal dynamics we mean an evolution of the conjugated coordinates phase and double well imballance, external dynamics describe the center of mass motion of the wave packets throughout the splitting.

[62] Note that the Bargmann representation uses a non-standard inner product: $\langle\phi|\theta\rangle = \cos^N\left(\frac{\phi-\theta}{2}\right)$.

[63] A. Smerzi and S. Raghavan, Macroscopic quantum fluctuations in the Josephson dynamics of two weakly linked Bose-Einstein condensates, Phys. Rev. A **61**, 063601 (2000).

[64] As we are dealing with relatively low magnetic fields ($< 100\,\mathrm{G}$), the quadratic Zeemann effect can be neglected here.

[65] W. H. Wing, On neutral particle trapping in quasistatic electromagnetic fields, Prog. Quant. Electr. **8**, 181–199 (1984).

[66] D. E. Pritchard, Cooling Neutral Atoms in a Magnetic Trap for Precision Spectroscopy, Phys. Rev. Lett. **51**, 1336 (1983).

[67] E. Majorana, 'Majorana flops', Nuovo Cimento **9**, 43 (1932).

[68] W. Petrich, M. H. Anderson, J. R. Ensher, and E. A. Cornell, A Stable, Tightly Confining Magnetic Trap for Evaporative Cooling of Neutral Atoms, Phys. Rev. Lett. **74**, 3352 (1995).

[69] S. Gov, S. Shtrikmann, and H. Thomas, Magnetic trapping of neutral particles: Classical and Quantum-mechanical study of a Ioffe-Pritchard type trap, J. Appl. Phys. D **87**, 3989 (2000).

[70] K. Dieckmann, Bose-Einstein Condensation with High Atom Number in a Deep Magnetic Trap, PhD thesis (2001).

[71] Y. V. Gott, M. S. Ioffe, and V. G. Tel'kovskii, 'Ioffe trap', Nuclear Fusion Supplement **3**, 1045 (1962).

[72] C. Cohen-Tannoudji, Piégeage non dissipatif et refroidissement évaporatif, 1996-1997, Cours du Collège de France, disponible sur `http://www.phys.ens.fr/cours/college-de-france/index.html`.

[73] J. Esteve, Du miroir au guide d'onde atomique: Effets de rugosité, Thèse de doctorat, Université de Paris XI (2004).

[74] J. D. Weinstein and K. G. Libbrecht, Microscopic magnetic traps for neutral atoms, Phys. Rev. A **52**, 4004–9 (1995).

[75] J. Schmiedmayer, A wire trap for neutral atoms, Appl. Phys. B **60**, 169 (1995).

[76] J. Fortagh, A. Grossmann, C. Zimmermann, and T. W. Hänsch, Miniaturized Wire Trap for Neutral Atoms, Phys. Rev. Lett **81**, 5310 (1998).

[77] J. Denschlag, D. Cassettari, and J. Schmiedmayer, Guiding Neutral Atoms with a Wire, Phys. Rev. Lett. **82**, 2014 (1999).

[78] J. Denschlag, D. Cassettari, A. Chenet, S. Schneider, and J. Schmiedmayer, A Neutral Atom and a Wire: Towards Mesoscopic Atom Optics, Appl. Phys. B **69**, 291–301 (1999).

[79] A. Haase, D. Cassettari, B. Hessmo, , and J. Schmiedmayer, Trapping neutral atoms with a wire, Phys. Rev. a **64**, 043405 (2001).

[80] W. Hänsel, P. Hommelhoff, T. W. Hänsch, and J. Reichel, Bose-Einstein condensation on a microelectronic chip, Nature **413**, 498 (2001).

[81] H. Ott, J. Fortagh, G. Schlotterbeck, A. Grossmann, and C. Zimmermann, Bose Einstein condensation in a surface microtrap, Phys. Rev. Lett. **87**, 230401 (2001).

[82] S. Schneider, A. Kasper, C. vom Hagen, M. Bartenstein, B. Engeser, T. Schumm, I. Bar-Joseph, R. Folman, L. Feenstra, and J. Schmiedmayer, Bose-Einstein Condensation in a simple Micro trap, Phys. Rev. A **67**, 023612 (2003).

[83] S. Groth, P. Krüger, S. Wildermuth, R. Folman, T. Fernholz, J. Schmiedmayer, D. Mahalu, and I. Bar-Joseph, Atom chips: Fabrication and thermal properties, Appl. Phys. Lett. **85**, 2980 (2004).

[84] As the Orsay setup uses a slightly thinner insolation layer (200 nm instead of 500 nm), we therfore expect the heat dissipation in this setup to be equal or better than in the Heidelberg case.

[85] R. Folman, P. Krüger, J. Schmiedmayer, J. Denschlag, and C. Henkel, Microscopic Atom Optics: From Wires To An Atom Chip, Adv. Atom. Mol. Opt. Phys. **48**, 263 (2002).

[86] $\mathbf{e}_y$ is not effected, as no additional fields are produced in this direction on the $(x = z = 0)$ line.

[87] C. Aussibal, Réalisation d'un condensat de Bose-Einstein sur une microstructure, Thèse de doctorat, Université de Paris XI (2003).

[88] A. E. Leanhardt, A. P. Chikkatur, D. Kielpinski, Y. Shin, T. L. Gustavson, W. Ketterle, and D. E. Pritchard, Propagation of Bose-Einstein Condensates in a Magnetic Waveguide, Phys. Rev. Lett. **89**, 40401 (2002).

[89] X. Lou, P. Krüger, M. W. Klein, K. Brugger, S. Wildermuth, S. Groth, I. Bar-Joseph, R. Folman, and J. Schmiedmayer, An atom fiber for omni-directional guidung of cold neutral atoms, Optics Lett. **29**, 2145 (2004).

[90] X. Lou, P. Krüger, M. W. Klein, K. Brugger, S. Wildermuth, S. Groth, I. Bar-Joseph, R. Folman, and J. Schmiedmayer, Two Wire Guides and Traps with Vertical Bias Field on Atom Chips, Phys. Rev. A **72**, 023607 (2005).

[91] N. H. Dekker, C. S. Lee, V. Laurent, J. H. Thywissen, S. P. Smith, M. Drndić, R. M. Westervelt, and M. Printiss, Guiding Neutral Atoms on a Chip, Phys. Rev. Lett. **84**, 1124 (2000).

[92] J. Esteve, T. Schumm, J.-B. Trebbia, I. Bouchoule, A. Aspect, and C. I. Westbrook, Realizing a stable magnetic double-well potential on an atom chip, Eur. Phys. J. D **35**, 141 (2005).

[93] D. Müller, D. Z. Anderson, R. J. Grow, P. D. D. Schwindt, and E. C. Cornell, Guiding Neutral Atoms Around Curves with Lithography Pattterned Current-Carrying Wires, Phys. Rev. Lett. **83**, 5194 (1999).

[94] W. Hänsel, P. Hommelhoff, T. W. Häansch, and J. Reichel, Magnetic conveyor belt for transporting and merging trapped atom clouds, Phys. Rev. Lett. **86**, 608 (2001).

[95] A. Günther, M. Kemmler, S. Kraft, C. J. Vale, C. Zimmermann, and J. Fortagh, Combined chips for atom-optics, Phys. Rev. A **71**, 063619 (2005).

[96] E. A. Hinds, C. J. Vale, and M. G. Boshier, Two-wire waveguide and interferometer for cold atoms, Phys. Rev. Lett. **86**, 1462 (2001).

[97] W. Hänsel, J. Reichel, P. Hommelhoff, and T. W. Hänsch, Rapped atom interferometer in a magnetic microtrap, Phys. Rev. A **64**, 063607 (2001).

[98] Y.-J. Wang, D. Z. Anderson, V. M. Bright, E. A. Cornell, Q. D., T. Kishimoto, M. Prentiss, R. A. Saravanan, S. R. Segal, and S. Wu, Atom Michelson Interferometer on a Chip Using a Bose-Einstein Condensate, Physical Review Letters **94**(7), 090405 (2005).

[99] O. Zobay and B. M. Garraway, Two-Dimensional Atom Trapping in Field-Induced Adiabatic Potentials, Phys. Rev. Lett. **86**, 1195 (2001).

[100] O. Zobay and B. M. Garraway, Atom trapping and two-dimensional Bose-Einstein condensates in field-induced adiabatic potentials, Phys. Rev. A. **69**, 023605 (2004).

[101] T. Schumm, S. Hofferberth, L. M. Andersson, S. Wildermuth, S. Groth, I. Bar-Joseph, J. Schmiedmayer, and P. Krüger, Matter wave interferometry in a double well on an atom chip, Nature Phys. **1**, 57–62 (2005).

[102] C. Henkel and M. Wilkens, Heating of trapped atoms near thermal surfaces, Europhys. Lett. **47**, 414 (1999).

[103] C. Henkel, S. Pötting, and M. Wilkens, Loss and heating of particles in small and noisy traps, Appl. Phys. B **69**, 379 (1999).

[104] C. Henkel and S. Pötting, Coherent transport of matter waves, Appl. Phys. B **72**, 73 (2001).

[105] C. Henkel, P. Krüger, R. Folman, and J. Schmiedmayer, Fundamental limits for coherent manipulation on atom chips, Appl. Phys. B **76**, 173 (2003).

[106] B. Zhang, C. Henkel, E. Haller, S. Wildermuth, S. Hofferberth, P. Krüger, and J. Schmiedmayer, Relevance of sub-surface chip layers for the lifetime of magnetically trapped atoms, Eur. Phys. J. D **35**, 97 (2005).

[107] D. M. Harber, J. M. McGuirk, J. M. Obrecht, and E. A. Cornell, Thermally induced losses in ultra-cold atoms magnetically trapped near room temperature surfaces, J. Low. Temp. Phys. **113**, 229 (2003).

[108] M. P. A. Jones, C. J. Vale, B. V. Hall, and E. A. Hinds, Spin coupling beween cold atoms and the thermal fluctuations of a metal surface, Phys. Rev. Lett. **91**, 080401 (2003).

[109] J. Fortágh, H. Ott, S. Kraft, A. Günther, and C. Zimmermann, Surface effects in magnetic microtraps, Phys. Rev. A **66**, 41604 (2002).

[110] S. Kraft, A. Günther, H. Ott, D. Wharam, C. Zimmermann, and J. Fortàgh, Anomalous longitudinal magnetic field near the surface of copper conductors, J. Phys. B **35**, L469 (2002).

[111] M. P. A. Jones, C. J. Vale, D. Sahagun, B. V. Hall, C. C. Eberlein, B. E. Sauer, K. Furusawa, D. Richardson, and E. A. Hinds, Cold atoms probe the magnetic field near a wire, J. Phys. B: At. Mol. Opt. Phys. **37**, L15 (2004).

[112] D.-W. Wang, M. D. Lukin, and E. Demler, Disordered Bose-Einstein Condensates in Quasi-One-Dimensional Magnetic Microtraps, Physical Review Letters **92**(7), 076802 (2004).

[113] Of course, additional effect contributing to potential roughness such as bulk inhomogeneities and patch effects can not be excluded. Nevertheless, the excellent quantitative egreement of our experimental findings to the theory identifies the edge effects as dominatig over other effects by at least one order of magnitude in our system.

[114] T. Schumm, J. Estève, C. Figl, J.-B. Trebbia, C. Aussibal, H. Nguyen, D. Mailly, I. Bouchoule, C. I. Westbrook, and A. Aspect, Atom chips in the real world: the effects of wire corrugation, Eur. Phys. J. D **32**, 171 (2005).

[115] *Mathematical methods for physicists*, Academic Press, London.

[116] This assumption is motivated by the fact, that a lithographic process essentially is 3D realization of a initially 2D pattern (the lithographic mask, the photoresist or the seed layer for electroplating). This is also in agreement with our experimental findings presented in part 2.

[117] A. E. Leanhardt, A. Görlitz, A. P. Chikkatur, D. Kielpinski, Y. Shin, D. E. Pritchard, and W. Ketterle, Imprinting vortices in a Bose-Einstein condensate using topological phases, Phys. Rev. Lett. **89**, 190403 (2002).

[118] Y. Lin, I. Teper, C. Chin, and V. Vuletic, Impact of Casimir-Polder Potential and Johnson Noise on Bose-Einstein Condensate Stability near Surfaces, Phys. Rev. Lett. **92**, 050404 (2004).

[119] D. Cassettari, B. Hessmo, R. Folman, T. Maier, and J. Schmiedmayer, Beam Splitter for Guided Atoms, Phys. Rev. Lett. **85**, 5483 (2000).

[120] The approximation of white spectral noise in edge or surface roughness is used to obtain simple scaling laws and to demonstrate the importance of the effect of wire corrugation as a whole. This approximation is of course to be used with precaution, as the noise spectrum of a micro wire strongly depends on material properties and fabrication technique.

[121] The points corresponding to $x < W/2$ lie outside the range of the previous calculation and their values have been obtained by a numerical integration for each x.

[122] P. Krüger, L. M. Andersson, S. Wildermuth, S. Hofferberth, E. Haller, S. Aigner, S. Groth, I. Bar-Joseph, and J. Schmiedmayer, Disorder Potentials near Lithographically Fabricated Atom Chips, eprint arXiv:cond-mat/0504686 (2005).

[123] L. P. Pitaevskii and S.Stringari, Thermal vs. Quantum Decoherence in Double-Well Trapped Bose-Einstein Condensates, Phys. Rev. Lett. **87**, 180402 (2001).

[124] J. D. Davis, 2D magnetic traps for ultra-cold atoms: a simple theory using complex numbers, Eur. Phys. J. D **18**, 27–36 (2002).

[125] S. Wildermuth, P. Krüger, C. Becker, M. Brajdic, S. Haupt, A. Kasper, R. Folman, and J. Schmiedmayer, Optimized magneto-optical trap for experiments with ultracold atoms near surfaces, Phys. Rev. A **69**, 030901(R) (2004).

[126] The new chip was designed when our analysis on the random potential roughness was not yet finalized. Within this analysis, we found wire edge corrugation to be the dominant source of potential roughness in our system, which could not be reduced by using smaller wires (see [114]).

[127] This photoresist can be easily used for negative lithography, without multiple curing and UV flooding. Unfortunately, it does not resist to ion etching and therefore could not be used in the first lithographic procedure.

[128] J. Fortagh, A. Grossmann, T. W. Hänsch, and C. Zimmermann, Fast loading of a magneto-optical trap from a pulsed thermal source, J. Appl. Phys. **84**, 6499 (1998).

[129] U. D. R. A. Wasan and V. Natarajan, Loading of a Rb magneto-optic trap from a getter source, Phys. Rev. A **64**, 023402 (2001).

[130] C. Wieman and L. Hollberg, Using doide lasers for atom physics, Rev. Sci. Instr. **62**, 1 (1991).

[131] L. Ricci, M. Weidemüller, T. Esslinger, A. Hemmerich, C. Zimmermann, V. Vuletic, W. König, and T. W. Hänsch, A compact grating-stabilized diode laser system for atomic physics, Opt. Comm. **117**, 541 (1995).

[132] W. Ketterle, D. S. Durfree, and D. M. Stamper-Kurn, Making, probing and understanding Bose-Einstein condensates, Contribution to the proceedings of the 1998 Enrico Fermi summer school on Bose-Einstein condensation in Varenna, Italy, page 1, Academic Press, 1998, and references therein.

[133] C. C. Bradley, C. A. Sackett, J. J. Tollet, and R. G. Hulet, Evidence of Bose-Einstein Condensation in an Atomic Gas with Attractive Interactions, Phys. Rev. Lett. **75**, 1687 (1995).

[134] J. Reichel, F. Bardou, M. B. Dahan, E. Peik, S. Rand, C. Salomon, and C. Cohen-Tannoudji, Raman Cooling of Cesium below 3 nK: New Approach Inspired by Lévy Flights Statistics, Phys. Rev. Lett. **75**, 4575 (1995).

[135] E. A. Hinds and I. G. Hughes, Magnetic atom optics : mirrors, guides, traps, and chips for atoms, J. Phys. D: Appl. Phys. **32**, R119 (1999).

[136] C. J. Vale, B. Upcroft, M. J. Davis, N. R. Heckenberg, and H. Rubinsztein-Dunlop, Foil-based atom chip for Bose-EInstein condensates, J. Phys. B: At. Mol. Opt. Phys. **37**, 2959–2967 (2004).

[137] S. Aubin, M. H. T. Extavour, S. Myrskog, L. J. LeBlanc, J. Esteve, S. Singh, P. Scrutton, D. McKay, R. McKenzie, I. D. Leroux, A. Stummer, and J. H. Thywissen, Trapping Fermionic ^{40}K and Bosonic ^{87}Rb on a Chip, J. Low Temp. Phys. **140**, 377–396 (2005).

[138] S. Chu, L. Hollberg, J. E. Bjorkholm, A. Cable, and A. Ashkin, Three-Dimensional Viscous Confinement and Cooling of Atoms by Resonance Radiation Pressure, Phys. Rev. Lett. **55**, 48 (1985).

[139] J. Dalibard and C. Cohen-Tannoudji, Laser cooling below the Doppler limit by polarization gradients: simple theoretical models, J. Opt. Soc. Am. B **6**, 2023 (1989).

[140] P. D. Lett, R. N. Watts, C. I. Westbrook, W. D. Phillips, P. L. Gould, and H. J. Metcalf, Observation of Atoms Laser Cooled below the Doppler Limit, Phys. Rev. Lett. **61**, 169 (1988).

[141] P. D. Lett, W. D. Phillips, S. L. Rolston, C. E. Tanner, R. N. Watts, and C. I. Westbrook, Optical Molasses, J. Opt. Soc. Am. B **6**, 2084 (1989).

[142] This number is based on the assumption, that the atomic states will be equally distributed among all five Zeemann levels and that only the $m_F = 2$ state will be magnetically trapped.

[143] O. J. Luiten, M. W. Reynolds, and J. T. M. Walraven, Kinetic Theory of evaporative cooling of a trapped gas, Phys. Rev. A **53**, 381 (1996).

[144] This value takes into account the heigth of the chip surface above the trapping wire, due to the BCB layer and the thickness of the thin Si wafer carrying the five wire structure. This height is estimated (and experimentally varified) to 120 μm.

[145] K. B. Davis, M.-O. Mewes, M. A. Joffe, M. R. Andrews, and W. Ketterle, Evaporative Cooling of Sodium Atoms, Phys. Rev. Lett. **74**, 5202–5205 (1995).

[146] C. A. Sackett, C. C. Bradley, and R. G. Hulet, Optimization of evaporative cooling, Phys. Rev. A **55**, 3797 (1997).

[147] Y. Castin and R. Dum, Bose-Einstein condensation in time dependent traps, Phys. Rev. Lett. **77**, 5315–5319 (1996).

[148] J. Esteve, J.-B. Trebbia, T. Schumm, A. Aspect, C. I. Westbrook, and I. Bouchoule, Observations of density fluctuations in an elongated Bose gas: ideal gas and quasi-condensate regimes, cond-mat/0510397 (2005).

[149] Y. Colombe, E. Knyazchyan, O. Morizot, B. Mercier, V. Lorent, and H. Perrin, Ultracold atoms confined in rf-induced two-dimensional trapping potentials, Europhys. Lett. **67**, 593 (2004).

[150] Y. Colombe, B. Mercier, H. Perrin, and V. Lorent, Loading a dressed Zeeman trap with cold atoms, J. Phys. IV France **116**, 247–252 (2004).

[151] This approximation may become incorrect when using RF fields generated by chip wires. The $1/r$ dependence of the magnetic field leads to strong spatial variations of the RF amplitude, which may be considerable over the size of the ADP trap, especially in widely spread double well configurations.

[152] I. I. Babi, N. F. Ramsey, and J. Schwinger, Use of rotating coordinates in magnetic resonance problems, Rev. Mod. Phys. **26**, 167 (1954).

[153] Here, the quantum number m_F is excerpted from the square root to visulize the potential shapes. This assumes a positive g factor, for negetive g, this operation is incorrect.

[154] L. D. Landau, Zur Theory der Energieübertragung - II, Phys. Z. Sowjetunion **2**, 46–51 (1932).

[155] C. Zener, Non-adiabatic crossing of energy levels, Proc. R. Soc. London Ser. A **137**, 696 (1932).

[156] N. V. Vitanov and K.-A. Suominen, Time-dependent control of ultracold atoms in magnetic traps, Phys. Rev. A **56**, 4377 (1997).

[157] Strictly speaking, at this position all Zeemann levels are resonantly coupled with vanishing level repulsion.

[158] For the ^{87}Rb atom in the $|F = m_F = 2\rangle$ state.

[159] This gives rise to the impression, that the approximated adiabatic potential (7.36) can be expressed in terms of ground state size a_0 and douple well separation $2r_0$ as in the purely magnetic system described in chapter 2. Such an exression could not be found.

[160] A. Kasper, Bose-Einstein condensation in a robust microtrap - the compination of wire traps and atom chips, Phd thesis, University of Heidelberg (2003).

[161] S. Schneider, Bose-Einstein Kondensation in einer magnetischen Z-Falle, Phd thesis, University of Heidelberg (2003).

[162] P. Krüger, Coherent matter waves near surfaces, Phd thesis, University of Heidelberg (2004).

[163] S. Wildermuth, One-dimensional Bose-Einstein condensates in micro-traps, Phd thesis, University of Heidelberg (2005).

[164] A. Kasper, S. Schneider, C. vom Hagen, M. Bartenstein, B. Engeser, T. Schumm, I. Bar-Joseph, R. Folman, L. Feenstra, and J. Schmiedmayer, A Bose-Einstein condensate in a microtrap, J. Opt. B: Quantum Semiclass. Opt. **5**, 143–149 (2003).

[165] S. Groth, Phd thesis, University of Heidelberg (2006), to be published.

[166] P. Krüger, X. L. andM. W. Klein, K. Brugger, A. Haase, S. Wildermuth, S. Groth, I. Bar-Joseph, R. Folman, and J. Schmiedmayer, Trapping and Manipulating Neutral Atoms with Electrostatic Fields, Phys. Rev. Lett. **91**, 233201 (2003).

[167] C. Becker, Eine neuartige magneto-optische Falle für Atomchip-Experimente, diploma thesis, University of Heidelberg (2002).

[168] C. G. Bjorklund, Frequency-modulation spectroscopy: a new method for measuring weak absorptions and dispersions, Opt. Lett. **5**, 15 (1980).

[169] The entire optical system is fixed to an optical bench, that can be extracted from the apparatus. Looking at targets of known dimensions, the magnification and resolition were determined.

[170] This resolution is a theoretical value assuming the diffraction limit, it could not be directly measured. Comparing small atom clouds with both imaging systems indicates a reduced resolution of about $12\,\mu$m, which we attribute to astigmatisms introduced by additional optical elements (beam splitter cubes).

[171] M. Brajdic, Entwicklung einer Computersteuerung und ihre Anwendung in einem Experiment zur vereinfachten Bose-Einstein condensation in einer Oberflächenfalle, diploma thesis, University of Heidleberg (2003).

[172] S. Hofferberth, Experiments with ultracold atoms and Bose-Einstein condensated in microtraps near surfaces, diploma thesis, University of Heidelberg (2004).

[173] Absolute atom numbers could not be determined in the first stages of the magneto optical trap, as the sice of the atomic cloud largely exceeds the field of view of all imaging system. It is roughly estimated to 5×10^8.

[174] The direct analog amplitude controll of the SRS345 turned out to be rather noisy for low amplitudes. In the experiment it is therefore favorable to increase the RF (frequency) detuning and work with higher amplitudes.

[175] The measured time, the RF switch needs to extinguish the oscillating current is about $10\,\mu$s, which aparently is sufficiently slow with respect to the Lamor frequency to retransfer all atoms to the $|F = 2, m_F = 2\rangle$ state. A projection on different states and a Stern-Gerlach-like behaviour has been observed when rapidly changing the frequency of the RF field.

[176] D. S. Rokhsar, Vortex stability and persistent currents in trapped Bose gases, Phys. Rev. Lett. **79**, 2164–2167 (1997).

[177] C. M. deSterke and J. E. Sipe, Application of the split opertor fourier transform method to the solution of the nonlinear schrödinger equation, AIP conference proceedings , 160–269 (1986).

[178] Y. Shin, C. Sanner, G.-B. Jo, T. A. Pasquini, M. Saba, W. Ketterle, D. E. Pritchard, M. Vengalattore, and M. Prentiss, Interference of Bose-Einstein condensates split with an atom chip, Phys. Rev. A **72**, 021604 (2005).

[179] A vanishing probability density of the wafe function in the center of the double well and consequently a full splitting of the condensate translates to the appearance of a third order fringe in the interference pattern, indendent of the actual shape of the wave packets.

[180] This sigma arises from the fact, that only a finite amount of measurements (40 in the presented case) has been performed.

[181] I. Lesanovsky, T. Schumm, S. Hofferberth, L. M. Andersson, P. Krüger, and J. Schmiedmayer, Adiabatic radio frequency potentials for the coherent manipulation of matter waves, arXiv:physics/0510076 (2005).